A Computational Study of Robust Formation of Spatial Protein Patterns

This thesis was reviewed by:

prof.dr. M. Dogterom
prof.dr. P. G. Bolhuis
prof.dr. F. C. MacKintosh
dr. A. M. Walczak
dr. K. Takahashi

The research described in this thesis was performed at *FOM Institute AMOLF*, Amsterdam, The Netherlands. This work is part of the research programme of the *Foundation for Fundamental Research on Matter* (FOM), which is part of the *Netherlands Organisation for Scientific Research* (NWO).

A digital copy of this thesis is available online at www.ubvu.nl/dissertations and www.amolf.nl.

Printed copies may be obtained upon request via e-mail to the AMOLF library (library@amolf.nl).

Nederlandse titel:
"Een numerieke studie naar de robuuste vorming van ruimtelijke eiwit patronen."

ISBN 978-90-77209-72-1

Typesetting was done with LaTeX, graphics with *gnuplot*, *Inkscape* and *GIMP*.

Printed by CPI Wöhrmann Print Service, Zutphen, The Netherlands.

VRIJE UNIVERSITEIT

A Computational Study of Robust Formation of Spatial Protein Patterns

ACADEMISCH PROEFSCHRIFT

ter verkrijging van de graad Doctor aan
de Vrije Universiteit Amsterdam,
op gezag van de rector magnificus
prof.dr. F.A. van der Duyn Schouten,
in het openbaar te verdedigen
ten overstaan van de promotiecommissie
van de Faculteit der Exacte Wetenschappen
op vrijdag 14 juni 2013 om 9.45 uur
in de aula van de universiteit,
De Boelelaan 1105

door

Thomas Robert Sokolowski

geboren te Siemianowice Śląskie (Laurahütte), Polen

promotor: prof.dr. P. R. ten Wolde

"Potykamy się nie o góry, ale o kamyki."

(Aleksander Kumor)

Quote translation: *"Not over mountains we stumble, but over pebbles."*

The work described in this thesis partly has been published in the following publications:

Sokolowski T. R., Erdmann T. and ten Wolde P. R. (2012) Mutual Repression Enhances the Steepness and Precision of Gene Expression Boundaries.
PLoS Comput Biol **8**(8): e1002654. (doi:10.1371/journal.pcbi.1002654)

Sokolowski T. R., ten Wolde P. R. and Becker N. B. (2013) The Stability of Gap Gene Patterns without Morphogen Gradients
Under review with PLoS Comput Biol.

Sokolowski T., Bossen L., Miedema T. and Becker N. (2010) Green's Function Reaction Dynamics–An Exact and Efficient Way To Simulate Intracellular Pattern Formation
AIP Conf Proc **1281**: 1342-1345. (doi:10.1063/1.3497970)

Contents

1 Introduction **1**

2 1D-eGFRD **7**

2.1 Introduction to eGFRD 7

2.1.1 Working principle of eGFRD 8

2.1.2 Single domains 11

2.1.3 Pair domains 13

2.1.4 Brownian Dynamics provides a fallback-system 16

2.1.5 Practical aspects 18

2.2 Introducing 1D transport into eGFRD 19

2.2.1 Structures, surfaces and interactions 19

2.2.2 Interactions with cylinders 20

2.2.3 Diffusion, drift and reactions on cylinders 22

2.2.4 Unbinding from cylinders 23

2.3 1D Green's functions with drift 24

2.3.1 Coordinate separation for the Smoluchowski equation 24

2.3.2 Solution for the 1D-diffusion-reaction problem with drift with different boundary conditions 25

2.4 Finite cylindrical structures 36

2.5 Green's function for 1D diffusion with a reactive sink 39

2.6 Acknowledgements 41

2.A Appendix: Detailed coordinate-separation transform 42

2.B Appendix: Domains in eGFRD 46

2.B.1 Domain classtree 46

2.B.2 Domain making in eGFRD 47

2.B.3 Convergence issues affecting domain construction 54

2.C Appendix: Dynamical cylinders 55

2.C.1 Abstracting dynamical properties of microtubules 55

2.C.2 Including growth and catastrophies into eGFRD 55

2.C.3 Summarized cylinder growth sampling algorithm 57

3 2D-eGFRD **59**

3.1 Introduction 59

3.2 2D structures in eGFRD 60

3.2.1 Interactions with planar surfaces . . . 60
3.2.2 Direct binding: Interactions of particles with particles bound to planes . . . 62
3.2.3 Diffusion and reactions on planar surfaces . . . 63
3.2.4 Finite planes and transitions between them . . . 63
3.3 Green's functions . . . 66
3.3.1 Green's function with absorbing outer boundary in polar coordinates . . . 66
3.3.2 Green's function for the 2D diffusion-reaction problem . . . 67
3.3.3 Green's function for binding to a cylindrical membrane . . . 72
3.4 Generalized linear coordinate transform for direct binding . . . 72
3.4.1 Rewriting the Laplace operator in matrix notation . . . 72
3.4.2 Writing the linear coordinate transform in matrix notation . . . 73
3.4.3 Transforming the Laplace operator . . . 74
3.4.4 Particular transform for the direct binding scenario . . . 75
3.4.5 Inverse transform . . . 77
3.4.6 Using known Green's Functions for the transformed problem . . . 78
3.5 Acknowledgements . . . 79
3.A Appendix: Deflection transform . . . 80
3.B Appendix: Green's function for binding to an outer cylinder . . . 81

4 Simulating polarized growth factor delivery in fission yeast 87
4.1 Introduction . . . 87
4.2 Experimental facts . . . 88
4.3 Model . . . 90
4.3.1 Parameters . . . 92
4.3.2 Simulations and analysis . . . 93
4.4 Results . . . 94
4.5 Discussion . . . 96
4.6 Acknowledgements . . . 98

5 Mutual repression in early Drosophila embryogenesis 99
5.1 Introduction . . . 99
5.2 Results . . . 102
5.2.1 Model . . . 102
5.2.2 Characteristics of gap-gene expresson boundaries . . . 105
5.2.3 Robustness to intra-embryonic fluctuations . . . 108
5.2.4 Robustness to inter-embryonic variations . . . 114
5.2.5 Boundaries shift upon uncorrelated variations in morphogen levels, yet intrinsic noise remains unaltered . . . 121
5.2.6 Mutual repression with one morphogen gradient . . . 123
5.3 Discussion . . . 123
5.4 Methods . . . 127
5.5 Acknowledgements . . . 129
5.A Appendix: Details of parameter choice and measurements . . . 130
5.A.1 Number of cortical nuclei at cell cycle 14 . . . 130

5.A.2 Predicted copy numbers and effective protein lifetime 130
5.A.3 Measurement of the boundary width 131
5.A.4 Measurement of the profile steepness 132
5.B Appendix: Supplementary analysis 134
5.B.1 Poissonian limit with dimerization 134
5.B.2 Bifurcation analysis 135
5.B.3 Estimation of switching times 137
5.B.4 Analysis of statistical properties of the boundary 138
5.C Appendix: Supplementary simulations 142
5.C.1 Influence of the Hill coefficient 142
5.C.2 Influence of the expression level 147
5.C.3 Activation of both gap genes by a single gradient 151

6 Robust gap gene patterns without morphogen gradients 155
6.1 Introduction 155
6.2 Results 157
6.2.1 Pattern stability is maximized at intermediate nearest-neighbor repression strength 157
6.2.2 In the maximally stable regime a restoring force exists 162
6.2.3 The phase-space velocity field reveals a metastable basin 164
6.2.4 Stability enhancement does not require pinning 166
6.2.5 Pinning introduces strong restoring forces 167
6.2.6 Pathways to destruction 167
6.2.7 Fixed point analysis helps understanding the origin of domain stability 170
6.3 Discussion 172
6.4 Methods 174
6.4.1 Details of the model 174
6.4.2 Simulations 174
6.4.3 Parameter choice 176
6.4.4 Data analysis 178
6.4.5 Perturbation experiments 179
6.5 Acknowledgements 180
6.A Appendix: Supplementary Information 181
6.A.1 Estimation of phase space diffusion coefficient from overdamped Langevin dynamics 181
6.A.2 Supplementary velocity field figures 182
6.A.3 Stability analysis of a mutually repressing four gene system . . 188

References 195

Summary 211

Samenvatting 215

Index 221

List of abbreviations **223**

List of persons **225**

Image references **229**

Acknowledgements **231**

Chapter 1

Introduction

Cells are the elementary building blocks of life and therefore could be regarded as the atoms of living matter. Recent advances in high-throughput techniques have made it possible to identify and characterize the components of the living cell on an unprecedented scale. Moreover, single-molecule techniques such as optical tweezers have allowed us to elucidate the dynamics of individual components with impressive detail. Yet, cellular function does not emerge at the level of individual molecules, but rather at the collective level of many molecules acting together. Computer simulations and mathematical modeling have an important role to play in advancing our understanding of the collective behavior of cellular components, and hence cellular function. The interactions between the components are often not only highly non-linear, but also act at multiple length- and time scales, making it difficult to predict and interpret their behavior by intuition. In parallel, experiments in cell biology have in recent years become increasingly quantitative, calling for quantitative models. In this thesis, we develop and apply numerical techniques to understand how spatial patterns of protein activity are robustly formed and maintained.

Information processing in cells

Cells could be viewed as self-assembling information processing devices. Since the discovery of DNA by Avery, MacLeod and McCarty [1] and the establishment of its structural model by Watson and Crick [2] molecular biology and genetics have seen enormous advances. Genes encode information; more specifically, they constitute construction plans for the functional molecules that perform specific tasks in the cell. However, proteins usually are not produced from their DNA continually; gene expression is regulated, i.e. activated or suppressed, by transcription factors which themselves are proteins expressed from genes, as demonstrated by the pioneering work of Jacob and Monod [3]. Gene regulation in addition is influenced by external signals sensed by the cell. The DNA code thus can be regarded as a "program" that is "processed" by the cell, depending on the specific composition of the DNA and external stimuli. Cells therefore can be fairly considered "living computers" that contain internally wired logics capable of processing "protein input" to produce other

proteins as "output" [4] in order to make situational decisions, either as a single cell or in groups. In fact, even the most simple bacterial organisms can successfully detect gradients in order to bias their movement towards increasing nutrient concentration (chemotaxis) [5] or temperature (thermotaxis) [6, 7], and "count" how many of their fellow bacteria surround them via quorum sensing [8, 9]. In essentially all organisms an autonomous internal clock is maintained via circadian rhythms, which can reach a surprisingly high precision and moreover adapt their pace in response to external cues [10]. Finally, in a process which perhaps most elegantly reflects the notion of "the wonder of life", all higher organisms exhibit an astonishing reproducibility and robustness in the course of their development from one single cell that contains the blueprint of their body towards a complete organism, consisting of up to trillions of diversified and well-positioned cells [11, 12, 13].

Only in the recent decades, however, it became clear that gene regulation is an intrinsically stochastic process [14, 15, 16, 17]. This is due to the fact that, while there is an enormous diversity of proteins in cells, the typical copy number per cell of a specific protein is very low, sometimes reaching down to the order of 10-100 copies. Their sparseness and the fact that transcription factors predominantly move via diffusion renders their arrival times at binding sites on the DNA highly irregular, causing protein production to occur in random bursts of varying size. In that respect, cells fundamentally differ from man-made information processing devices because signal propagation is subject to permanent intrinsic uncertainty, effectively resulting in noisy output at each step of a signalling cascade. This leads to the question: How can cells, being genuinely stochastic systems, produce a behavior that, on a larger scale, appears deterministic and well-coordinated? Ultimately, this is part of the major question how chemistry converts to behavior, or matter to life, which already haunted such distinguished scientists as SCHRÖDINGER and TURING [18, 19].

Spatially resolved stochastic models help understanding how cells control noise

The issue of noise control in cells has been addressed by a broad range of theoretical approaches, using techniques from statistical physics and information and signalling theory. While these efforts yielded elegant results on limiting and optimizing factors of information processing by biochemical systems [20, 21, 22, 23, 24, 25, 26, 27, 28], often, for ease of solvability, they do not explicitly account for spatial aspects, assuming well-stirred chemical conditions or even instantaneous action of components on each other. However, in the recent years it is becoming increasingly evident that space plays a prominent role in cellular information processing. Importantly, the obsevation that time-averaging–as a straightforward noise-control mechanism–often is incompatible with the timescales of cellular processes, and that protein-based signalling in many cases is localized to specific parts of the cell, such as the cell membrane or scaffold proteins, lead to the idea that cellular systems use space as an additional degree of freedom in their effort to control protein noise [29, 30, 31, 32]. Whether and how cells employ space to attenuate stochasticity in protein dynamics is the main theme of this theoretical study. More specifically, we focus on one particular function that proteins fulfill: the establishment of spatially confined, well-localized gene expression patterns

that are stable, precise and robust. Such patterns play an indispensable role in cell morphogenesis, confining growth to particular regions of the cell, and in organism development, where they specify different cell fates on the tissue level.

A fundemental difficulty that arises here is the following: On the one hand, typical protein copy numbers appear too small to use mean-field techniques, calling for a particle-based approach; on the other hand, however, they are too large to describe the particle-system analytically as a whole. This makes it necessary to resort to particle-based, stochastic chemical simulation techniques. In the recent years the development of numerous numerical schemes that serve this purpose, such as Smoldyn[1], MCell[2] and ChemCell[3] [33, 34, 35, 36, 37, 38], has been put forward. All of these are, ultimately, based on Brownian Dynamics, in which particle diffusion is simulated by large series of small random steps. Since, as a consequence of low protein numbers, interparticle distances typically are large, simulation schemes based on Brownian Dynamics necessarily spend a major part of computation time on simulating diffusive trajectories, whereas truly interesting events, such as particle reactions, are rare. For that reason, the use of next-event driven schemes, which are able to step from reaction to reaction, is much more preferable.

eGFRD: a powerful particle-based scheme for stochastic simulation of biochemical networks

Arguably, the only event-driven particle-based simulation algorithm that is currently in active development is enhanced Green's Function Reaction Dynamics (eGFRD) [39, 40, 41, 42]. Based on analytical solutions (Green's functions) for the one- and two-particle reaction-diffusion problem (Smoluchowski equation), it implements an exact and outstandingly efficient way to simulate chemical reaction-diffusion systems on the single-particle level. Under biologically relevant conditions, eGFRD can be up to 4-6 orders of magnitude more efficient than Brownian Dynamics. It was successfully applied to simulate gene regulation and enzyme dynamics in space, revealing that rapid rebindings of reactants can fundamentally alter the noise characteristics, and even the qualitative behavior of the system [41, 42]. eGFRD is part of the E-Cell Project[4], which aims at creating a comprehensive whole-cell simulation platform that retains molecular-level detail.

In spite of its paramount computational power, until now eGFRD was limited to systems of particles that diffuse and interact in an unbounded three-dimensional volume. As such, it did not account for well-known intracellular features that chiefly contribute to symmetry breaking, patterning and signal processing in cells, like two-dimensional diffusion and reactions on the cell membrane and one-dimensional active transport on linear polymer filaments, such as microtubules [43, 44, 45, 29, 46, 47]. The incorporation of particle transport and interparticle reactions in 1D and 2D into eGFRD is one of the principal achievements of this work. Indeed the first, more technical chapters of this thesis are completely devoted to describe how we extended

[1] http://www.smoldyn.org
[2] http://www.mcell.cnl.salk.edu
[3] http://chemcell.sandia.gov
[4] http://www.e-cell.org

eGFRD towards 1D (chapter 2) and 2D (chapter 3). Since eGFRD owes its virtue to the full knowledge of the Green's functions, which have to be recalculated from scratch for the reaction-diffusion problems in the lower dimensions, a fair part of these chapters deals with the associated mathematical derivations. A thorough introduction into the basic principles of eGFRD will be given at the beginning of chapter 2. Chapters 2 and 3 converge towards chapter 4, where we use the newly implemented features of eGFRD to simulate a stochastic whole-cell model, studying the polarization of growth factors in fission yeast morphogenesis. The latter is a widely studied–yet poorly understood–symmetry breaking process that involves active transport on microtubules, diffusion in the cytoplasm and on the membrane, and shuttling of particles between these transport modes. We identify conditions that optimize polarity in this system and find that recruitment of polarity agents to the membrane via a second, purely membrane-bound species significantly enhances polarization.

Mutual repression: a beneficial gene interaction motif that makes early fruit fly development more robust

In the second half of this thesis (chapters 5 and 6) the focus is shifted to another organism which became a paradigm of developmental biology: the fruit fly *Drosophila melanogaster*. Since the pioneering work of WIESCHAUS, LEWIS and NÜSSLEIN-VOLHARD [48, 49] the early embryogenesis of the fruit fly, which is driven by successive appearance of spatial gene expression patterns that locally determine cell fates and thus specify divergent development of different body parts, has been the subject of extensive experimental and theoretical endeavor. Morphogen gradients, i.e. spatially decreasing transcription factor profiles that locally activate and suppress the expression of downstream target genes in a concentration-dependent manner, play a crucial role in this process. For a long time, the common model of early tissue development assumed that local patterns are successfully confined only via morphogen gradients ("French-flag model") [50] This picture originally ignored the noisy nature of gene expression. More recent work, however, revealed the intriguing observation that the level of noise in the gradients is markedly higher than the uncertainty in their target gene patterns [51, 30, 52]. This again lead to the question how to overcome intrinsic stochasticity of genetics in order to generate highly reproducible and precise patterns. The insight that the timescale of rapidly progressing fly embryogenesis simply does not allow for time-averaging that is sufficient to reduce noise [30] prompted the search for better-suited noise-control mechanisms in the context of this multi-cellular system. Mutual regulatory interactions between different of the downstream patterning genes have been identified experimentally and put forward as a candidate for such mechanism. While noise reduction via negative autoregulation has been well studied, how mutual repression between pairs of genes enhances the precision of spatial gene-expression patterns is poorly understood.

In chapters 5 and 6 we present two studies in which we conducted extensive stochastic simulations of a spatially-resolved model of the early fruit fly embryo in order to elucidate how mutual interactions between developmental patterning genes help to increase pattern precision and robustness. While these chapters thus follow the main theme of this thesis, they differ from the preceding chapters by employ-

ing other simulation techniques: a clear separation of length- and timescales in the Drosophila embryo allowed us to opt for a spatial variant of the Stochastic Simulation Algorithm by GILLESPIE [53, 54]. We use this highly efficient next-event driven scheme to simulate a setup in which the embryo is represented as a cylindrical array of well-stirred biochemical reactors coupled by diffusion between neighboring volumes.

Chapter 5 focuses on mutual repression between two patterning genes under the control of upstream morphogen gradients. Our main finding here is that mutual repression and spatial averaging together provide a noise-reduction mechanism that can produce patterning gene profiles which are both precise and steep. Mutual repression is also the subject of chapter 6; here, however, we ask whether a stripe pattern of gene expression domains can be maintained in a robust way *without* morphogen gradients. To answer this question we study interactions between four genes whose expression domains are arranged in a particular order along the embryo, in which mutual repression between adjacent stripes is weak, whereas long-range mutual repression is strong, as observed in experiment [12]. Importantly, this model explicitly does not include any morphogen gradients. By combining the spatial GILLESPIE simulation with Non-Stationary Forward Flux Sampling (NS-FFS), a recently developed rare-event sampling technique, we quantify the stability of the pattern as a function of a crucial system parameter, the strength of repression between adjacent gene expression domains. We find that there exists an optimal repression strength that maximizes pattern stability, resulting in persistence times well beyond the biologically relevant timescales, in the abscence of morphogen gradients.

Chapter 2

1D-eGFRD

2.1 Introduction to eGFRD

Green's Function Reaction Dynamics, in short GFRD, is a next-event driven stochastic simulation algorithm for chemical reactions in time and space that retains spatial information on the particle level. The original motivation for GFRD was the limited availability of techniques that combine the efficiency of zero-dimensional next-event driven algorithms, such as the Stochastic Simulation Algorithm by Gillespie [53, 54], with the richness of detail provided by particle-based schemes like Brownian Dynamics, which however are computationally demanding. At its heart, GFRD decomposes the simulated volume into geometrically simple subvolumes ("domains") that contain at most two particles in order to sample next-events from Green's functions, i.e. exact analytical solutions of the reaction-diffusion problem. The Green's functions are used to compute next-event times and particle positions in runtime, updating the individual domains in an asynchronous fashion. Thanks to the complete knowledge of the expected spatio-temporal evolution of the probability density within each domain, large jumps in time and space can be performed and sampling of particle trajectories is unneccessary. In terms of computational effort, GFRD is orders of magnitudes more efficient than brute-force Brownian Dynamics for biologically relevant particle concentrations ($c \leq 1\ \mu M$) [42].

Originally, GFRD was developed by van Zon and ten Wolde in 2005 [39, 40, 41]. While this first version successfully implemented the basic idea of GFRD, it employed Green's functions that were calculated under the assumption that interacting particles can separate infinitely far. This required the definition of a maximum time step and distance-cutoff, in order to ensure that interactions with particles further away than the closest particle indeed can be neglected. Hence, the original scheme was event-driven, but not exact, and updates were synchronous. In 2010 Tănase-Nicola, Takahashi and ten Wolde presented an improved version of the algorithm, called eGFRD (e for enhanced) [42], inspired by earlier work [55, 56]. Here the necessity for a time cutoff was eliminated by the use of Green's functions with absorbing boundary conditions on the outer radii of the spherical domains. While this approach demands the calculation of Green's functions that are more complicated, it guarantees that

any sampled next-event occurs within the domain, and thus truly breaks down the N-particle problem into independent one- and two-particle problems. This makes eGFRD an exact, event-driven, asynchronous algorithm.

GFRD proved an extremly powerful tool to simulate diffusion and reactions of spherical particles in an unbounded three-dimensional volume [42, 41]. However, as yet it did not allow for the simulation of transport on one- and two-dimensional structures, which play a prominent role in many intracellular processes, such as DNA sliding and active transport on microtubules or actin filaments, and reactions at the cell membrane. Here we present work that extends eGFRD in a way that enables the simulation of transport and particle reactions on finite structures in 1D, 2D and 3D, and transitions between the 3D bulk and the lower-dimensional structures.

The following content is organized as follows: First we describe the working principles of eGFRD in more detail. Thereby we introduce common GFRD terminology. After that, in section 2.2 we explain how we include transport and reactions on 1D structures into eGFRD, introducing new, cylindrical domain types. These require new Green's functions, and a large part of this chapter is indeed devoted to their mathematical derivation. This will be conducted in detail for the most important case in section 2.3 and provides an exemplary reference for other cases presented in this and later chapters. Where instructive, methodic details of Green's function calculation will be mentioned. For a complete overview of the use of Green's functions in solving the diffusion/heat equation we refer to the classical book by Carslaw & Jaeger [57] and [58, 59], which are excellent sources. Section 2.4 briefly introduces additional modifications that are necessary to model linear tracks of finite length. To end with, in section 2.5 we present a Green's function used to model diffusive transport in 1D in the presence of a reactive sink.

The implementation of 2D transport into eGFRD is discussed separately in Chapter 2 and partly builds on what follows in this chapter.

2.1.1 Working principle of eGFRD

Imagine a random constellation of N particles of different chemical species that diffuse and react in a 3D volume. Let us assume that the particles are well-represented by solid spherical spheres and completely characterized by their radius, diffusion constant, rates of interaction with each other and their decay rate. Even with these simplifications, in general it is hard–if not impossible–to find an analytical prediction for future particle species and positions given that the system started from a certain initial condition. Nonetheless, as often in physics, exact analytical solutions can be obtained for the case $N \leq 2$. eGFRD capitalizes on this fact by dividing the 3D volume into subvolumes, called protective domains, that contain at most two particles, in order to isolate the content of each domain from the influence of surrounding particles up to a certain (domain-specific) time $\tau_{\mathcal{D}}$. This way the N-particle problem is reduced to $M < N$ independent one- or two-particle problems. $\tau_{\mathcal{D}}$ is the time at which a reconstruction of the domain becomes necessary, e.g. when one of the particles hits a domain boundary or experiences a reaction that changes its properties. Figure 2.1 illustrates this principle.

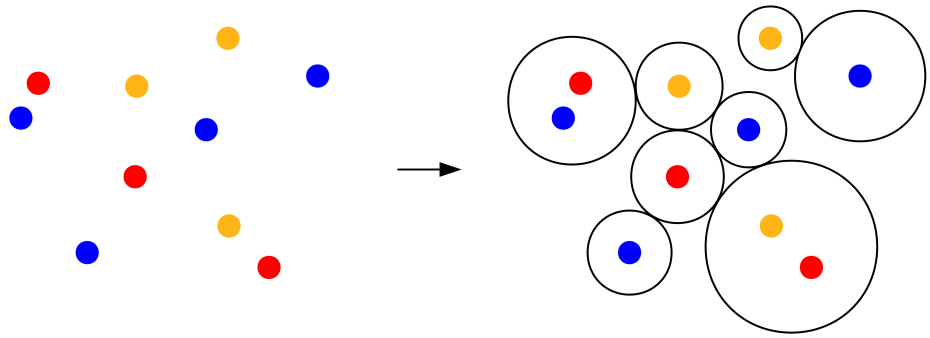

Figure 2.1: Protective domains separate the N-particle problem into one- and two-particle problems. The drawing illustrates how eGFRD constructs protective domains that contain at most two particles in order to isolate these from the influence of other particles, starting from a random particle constellation. Subsequently, analytical solutions are calculated for each domain individually and used to propagate the domains in an event-driven, asynchronous fashion. We show here a 2D projection for the standard scenario in which particles diffuse and react in unbounded 3D space. In this case protective domains are spherical. Different colors mark different chemical species.

For sufficiently simple domain geometries, such as spheres or cylinders, the Green's functions for the isolated reaction-diffusion problems, i.e. the density function $p(\mathbf{r}, t|\mathbf{r}_0)$ for the probability that a particle is at position $\mathbf{r}$ at time t given that it started at position $\mathbf{r}_0$, can be calculated analytically with exact results. Here the confining character of the domain is taken into account by imposing specific boundary conditions to $p(\mathbf{r}, t|\mathbf{r}_0)$. Quantities that derive from the Green's function can be used to generate tentative next-event times for each domain individually. Most importantly, since $p(\mathbf{r}, t|\mathbf{r}_0)$ completely describes the transient dynamics within the domain, it enables the sampling of new particle positions at $\tau_{\mathcal{D}}$, rendering the sampling of particle trajectories unnecessary. If collected in an global scheduler list, the sampled times can be used to update the domains sequentially, i.e. asynchronously, and to set up an event-driven scheme. While updates result in particle displacements and possibly species changes, by construction these remain confined to the respective domain and thus do not interfere with the situation in neighboring domains. After each domain update the domain is removed, the new constellation of particles is reanalysed and new domains are constructed around the displaced particles. The newly calculated next-event times are inserted into the ordered scheduler in the right place and the domain with the foremost next-event time is updated next. To enhance the formation of two-particle domains, recently updated particles can force a premature update of domains in their proximity, called "bursting". A bursted domain is propagated towards a time prior to its originally scheduled update; the new particle position at that time sampled form the associated Green's function. If bursting causes particles to move close enough, creation of a two-particle domain will be attempted. A compact overview over the basic eGFRD algorithm is given by Algorithm 1.

Algorithm 1 Basic outline of the eGFRD algorithm. Symbols $\mathcal{D}_\mathrm{x}$ denote domains, τ_x next-event times. The scheduler S is the list of all next-event times in the system, ordered by increasing time. List U collects all particles that have been updated at a given time τ_x and require construction of a new domain. t_sim is the time that passed since simulation start.

Initialize:
$t_\mathrm{sim} \leftarrow 0$, scheduler $S \leftarrow \{\}$
for all particles p_i **do**
  if not p_i already in domain **then**
    $\mathcal{D}_\mathrm{j} \leftarrow$ create domain for p_i
    $\tau_\mathrm{j} \leftarrow$ draw next-event time for $\mathcal{D}_\mathrm{j}$
    insert τ_j into S ordered by increasing time
  end if
end for

Main loop:
while $S \neq \{\}$ **and** $t_\mathrm{sim} < t_\mathrm{end}$ **do**
  $t_\mathrm{sim} \leftarrow \tau_\mathrm{n} =$ topmost element in S
  remove τ_n from S
  propagate $\mathcal{D}_\mathrm{n}$ to τ_n and remove $\mathcal{D}_\mathrm{n}$
  reset particle update list: $U \leftarrow \{\}$
  $U \leftarrow U \cup \{p_{\mathrm{n}_\mathrm{i}}\}$ **for all** particles $p_{\mathrm{n}_\mathrm{i}} \in \mathcal{D}_\mathrm{n}$
  while $U \neq \{\}$ **do**
    $p_\mathrm{u} \leftarrow$ next particle in U
    for all domains $\mathcal{D}_{\mathrm{u}_\mathrm{j}}$ close to p_u **do**
      burst: propagate $\mathcal{D}_{\mathrm{u}_\mathrm{j}}$ to τ_n and remove $\mathcal{D}_{\mathrm{u}_\mathrm{j}}$
      remove $\tau_{\mathrm{u}_\mathrm{j}}$ from S
      $U \leftarrow U \cup \{p_{\mathrm{u}_\mathrm{jk}}\}$ **for all** particles $p_{\mathrm{u}_\mathrm{jk}} \in \mathcal{D}_{\mathrm{u}_\mathrm{j}}$
    end for
  end while
  for all $p_\mathrm{u} \in U$ **do**
    if not p_u already in domain **then**
      $\mathcal{D}_\mathrm{u} \leftarrow$ create domain for p_u
      $\tau_\mathrm{u} \leftarrow$ draw next-event time for $\mathcal{D}_\mathrm{u}$
      insert τ_u into S
    end if
  end for
end while

In the following we will call domains that contain one particle *Single* domains or *Singles* and domains that contain two particles *Pair* domains or *Pairs*. We will now explain how Green's functions may be used to sample next-event times for the two domain types specifically.

2.1.2 Single domains

Two types of next-events can happen within a *Single* domain $\mathcal{D}_1$: either the particle undergoes a monomolecular reaction, which can mean decay or species change, or it hits the boundary of the domain by diffusion. In eGFRD, the former is called a *Single Reaction*, the latter a *Single Escape*.

If we assume that monomolecular reactions are a Poissonian process independent of particle diffusion, the propensity function for the next reaction is simply an exponential distribution

$$q_{\mathrm{m}}(t) = k_{\mathrm{m}} e^{-k_{\mathrm{m}} t} \tag{2.1}$$

where k_{m} is the rate of the specific monomolecular reaction. A tentative next-event time τ_{m} for a monomolecular reaction then can be sampled via the inversion method as

$$\tau_{\mathrm{m}} = -k_{\mathrm{m}} \ln(\mathcal{R}_{\mathrm{m}}) \tag{2.2}$$

where $\mathcal{R}_{\mathrm{m}} \in [0, 1]$ is a uniformely distributed random number.

Let $p(\mathbf{r}, t|\mathbf{r}_0)$ be the density function for the probability that a diffusing particle will be located at $\mathbf{r}$ at time t given that it started at $\mathbf{r}_0$ at time $t_0 = 0$. Within an unbounded volume, the evolution of $p(\mathbf{r}, t|\mathbf{r}_0)$ is well-described by the diffusion equation

$$\partial_{\mathrm{t}} p(\mathbf{r}, t|\mathbf{r}_0) = D\nabla^2 p(\mathbf{r}, t|\mathbf{r}_0) + \delta(\mathbf{r} - \mathbf{r}_0)\delta(t - t_0) \quad . \tag{2.3}$$

Note that due to the delta-peak inhomogeneity that represents the initial condition, the solution $p(\mathbf{r}, t|\mathbf{r}_0)$ technically is a Green's function.

To sample a first-passage time for the particle to reach the outer shell $\partial\mathcal{D}_1$ of a domain $\mathcal{D}_1$ constructed around $\mathbf{r}_0$, additionally an absorbing boundary condition may be imposed as follows:

$$p(\mathbf{r}, t|\mathbf{r}_0) = 0 \quad \text{for} \quad \mathbf{r} \in \partial\mathcal{D}_1 \tag{2.4}$$

In the simplest case, for a spherical domain with radius R:

$$p(|\mathbf{r} - \mathbf{r}_0| = R, t|\mathbf{r}_0) = 0 \tag{2.5}$$

For more complicated domain geometries, e.g. cylinders, the problem has to be transformed into a coordinate system that captures specific symmetries, and boundary conditions have to be imposed for each coordinate separately.

Given that the Green's function $p(\mathbf{r}, t|\mathbf{r}_0)$ for the above boundary-value problem can be found, integration of $p(\mathbf{r}, t|\mathbf{r}_0)$ over the whole domain yields its survival probability $S(t)$, i.e. the probability for the particle(s) to still remain within $\mathcal{D}_1$ at time t.

Note that $S(t_0) = 1$. The survival probability is linked to the propensity function $q(t)$, which is the probability for hitting $\partial\mathcal{D}_1$ within the time interval $[t, t+dt]$, via:

$$q(t) = -\partial_t S(t) = -\partial_t \int_{\mathcal{D}_1} p(\mathbf{r}, t|\mathbf{r}_0) d\mathbf{r} \tag{2.6}$$

In other words, $1 - S(t) = \int_{t_0}^{t} q(t')dt' = Q(t)$ is equal to the cumulative distribution function of $q(t)$ and may be used to sample a next-event time τ_e for exiting the domain via the inversion method as follows:

$$\tau_e = Q^{-1}(\mathcal{R}_e) = S^{-1}(1 - \mathcal{R}_e) \tag{2.7}$$

Here $\mathcal{R}_e \in [0, 1]$ again is a uniformely distributed random number. In general, it may be difficult to calculate S^{-1} analytically. Then τ_e can be obtained by solving the equation $S(\tau_e) - \mathcal{R}_e = 0$ with a numerical rootfinder[1].

After construction of an eGFRD *Single* domain, first both τ_e and τ_m are sampled as described. Since we presuppose that diffusion and monomolecular reactions are occuring independently, the next-event time for the domain is set as:

$$\tau_{\mathcal{D}_1} = \min(\tau_e, \tau_m) \tag{2.8}$$

This automatically determines the event type to be either a *Single Escape* or a *Single Reaction*. For reasons discussed earlier and in appendix section 2.B.2, eGFRD also allows for "bursting", i.e. update of the domain at times $\tau_b < \tau_{\mathcal{D}_1}$. Here we make use of the fact that eGFRD is capable to generate a new particle position $\mathbf{r}_\nu$ from the Green's function for an arbitrary update time $\tau_\nu \leq \tau_{\mathcal{D}_1}$. Since in these cases the PDF $p(\mathbf{r}, \tau_\nu|\mathbf{r}_0)$ is not normalized within $\mathcal{D}_1$, precisely because probability leaked out through $\partial\mathcal{D}_1$ during the time $\tau_\nu - t_0$, it is important to sample $\mathbf{r}_\nu$ from the conditional PDF $p_{S(\tau_\nu)}(\mathbf{r}, \tau_\nu|\mathbf{r}_0) \equiv \frac{1}{S(\tau_\nu)} p(\mathbf{r}, \tau_\nu|\mathbf{r}_0)$. How this is done in detail depends on the geometry of the domain. For a spherical domain with radius R the angles $\theta \in [0, \pi]$ and $\phi \in [0, 2\pi]$ in $\mathbf{r}_\nu = (r_\nu, \theta, \phi)$ are sampled from uniform distributions over the respective intervals, employing existing symmetry. If the next-event type is a *Single Escape*, $r_\nu = R$ with certainty and no further steps are required. For the other event types, i.e. *Single Reaction* or bursting, the new radial distance r_ν is sampled from

$$r_\nu = P^{-1}_{S(\tau_\nu)}(\mathcal{R}_S) \tag{2.9}$$

with a uniform random number $\mathcal{R}_S \in [0, 1]$ and the cumulative conditional PDF

$$P_{S(\tau_\nu)}(r_\nu) = \frac{1}{S(\tau_\nu)} \int_0^{r_\nu} \int_0^{2\pi} \int_0^{\pi} p(r, \theta, \phi, \tau_\nu|\mathbf{r}_0) r^2 \sin(\theta) d\theta d\phi dr \quad . \tag{2.10}$$

If a *Single Reaction* event produces two particles from one, these are put at contact at the sampled position $\mathbf{r}_\nu$ with random spatial orientation. If it is a true decay event the particle is removed from the system together with its domain. Finally, when a *Single Reaction* induces a change the particle species from s_0 to s, the s_0 particle is removed and a new s-particle is created at $\mathbf{r}_\nu$. In any other event the particle is simply moved to $\mathbf{r}_\nu$.

[1] As a matter of course, using $1 - \mathcal{R}_e$ and $\mathcal{R}_e$ is equivalent if both are uniform random numbers from $[0, 1]$.

2.1.3 Pair domains

Sampling of next-event times for a *Pair* domain $\mathcal{D}_2$ follows the same principles as for *Singles*. However, here the two particles can react at contact, which creates an additional channel of exit from the domain and a new next-event type.

Let us denote by $p_2(\mathbf{r}_\mathrm{A}, \mathbf{r}_\mathrm{B}, t|\mathbf{r}_\mathrm{A0}, \mathbf{r}_\mathrm{B0})$ the PDF for the likelihood of finding two diffusing particles A and B initially located at positions $\mathbf{r}_\mathrm{A0}$ and $\mathbf{r}_\mathrm{B0}$ at $t = t_0$ at positions $\mathbf{r}_\mathrm{A}$ and $\mathbf{r}_\mathrm{B}$ at a later time t. The time-evolution of p_2 is governed by the SMOLUCHOWSKI equation:

$$\partial_\mathrm{t} p_2 = [D_\mathrm{A}\nabla_\mathrm{A}^2 + D_\mathrm{B}\nabla_\mathrm{B}^2]p_2 \tag{2.11}$$

Here D_A and D_B are the diffusion constants of particles A and B. As demonstrated later for a more general case, this problem can be simplified by transforming coordinates $\mathbf{r}_\mathrm{A}$ and $\mathbf{r}_\mathrm{B}$ to $\mathbf{r}$ and $\mathbf{R}$, where $\mathbf{r}$ is the interparticle vector and $\mathbf{R}$ the (weighted) center-of-mass of the particles. A separation ansatz $p_2 = p_\mathrm{r}(\mathbf{r})p_\mathrm{R}(\mathbf{R})$ then yields two separate, uncoupled diffusion equations for $\mathbf{r}$ and $\mathbf{R}$, which are equivalent to (2.11):

$$\partial_\mathrm{t} p_\mathrm{r} = D_\mathrm{r}\nabla_\mathrm{r}^2 p_\mathrm{r}\ , \qquad \partial_\mathrm{t} p_\mathrm{R} = D_\mathrm{R}\nabla_\mathrm{R}^2 p_\mathrm{R} \quad . \tag{2.12}$$

The constants D_r and D_R depend only on D_A and D_B. The uncoupling allows for the calculation of two Green's function solutions $p_\mathrm{r}(\mathbf{r}, t|\mathbf{r}_0)$ and $p_\mathrm{R}(\mathbf{R}, t|\mathbf{R}_0)$ on two subdomains $\mathcal{D}_\mathrm{r}$ and $\mathcal{D}_\mathrm{R}$ of $\mathcal{D}_2$, respectively, with boundary conditions adapted to the problem as described further below. $\mathcal{D}_\mathrm{r}$ and $\mathcal{D}_\mathrm{R}$ must be defined in a way that all possible positions constructed from sampled values of $\mathbf{r}$ and $\mathbf{R}$ remain within the protective domain $\mathcal{D}_2$. Figure 2.2A shows a valid definition of the subdomains for a (projected) spherical pair domain.

The Green's function p_R for the $\mathbf{R}$ diffusion is calculated in precisely the same way as the Green's function for the one-particle problem in *Single* domains, with an absorbing boundary condition $p_\mathrm{R}(\mathbf{R}, t) = 0$ for $\mathbf{R} \in \partial\mathcal{D}_\mathrm{R}$. This yields a next-event time τ_R for first-arrival of $\mathbf{R}$ to $\partial\mathcal{D}_\mathrm{R}$, called *Center of Mass Escape* or *CoM Escape*.

Reactions between A and B are modelled via a radiating boundary condition to p_r at the particle contact radius $\sigma = R_\mathrm{A} + R_\mathrm{B}$:

$$q_\sigma(t) \equiv \int_{\partial\mathcal{D}_\mathrm{r}^\sigma} -D\nabla_\mathbf{r} p_\mathrm{r}(\mathbf{r}, t|\mathbf{r}_0)d\mathbf{r} = kp_\mathrm{r}(|\mathbf{r}| = \sigma, t) \tag{2.13}$$

Here, k is the intrinsic particle reaction rate, which is the rate at which the particles react given that they are in contact, and $p_\mathrm{r}(|\mathbf{r}| = \sigma, t)$ is the probability that the particles are indeed at contact at time t. The integral on the left is the total probability (out)flux through the "contact surface" or inner boundary of the $\mathbf{r}$-subdomain, which is the set of all points at which A and B are in contact: $\partial\mathcal{D}_\mathrm{r}^\sigma = \{\mathbf{r}\big||\mathbf{r}| = \sigma\}$. At the outer boundary of the $\mathbf{r}$-subdomain $\partial\mathcal{D}_\mathrm{r}^a$ absorbing boundary conditions are imposed. The initial condition for this boundary value problem is set by the inital separation of the two particles, $p_\mathrm{r}(\mathbf{r}, t = 0|\mathbf{r}_0) = \delta(\mathbf{r} - (\mathbf{r}_\mathrm{B0} - \mathbf{r}_\mathrm{A0}))$. A tentative next-event time τ_r can be sampled from the survival probability $S_\mathrm{r}(t) = \int_{\mathcal{D}_\mathrm{r}} p_\mathrm{r}(\mathbf{r}, t|\mathbf{r}_0)d\mathbf{r}$ in the same way as before. With this, however, it remains undetermined by which boundary the particle escaped. To specify whether the exit from $\mathcal{D}_\mathrm{r}$ happens through the radiating (*Pair Reaction* event) or through the absorbing boundary (*IV Escape*[2]), the probability

[2] IV = interparticle vector

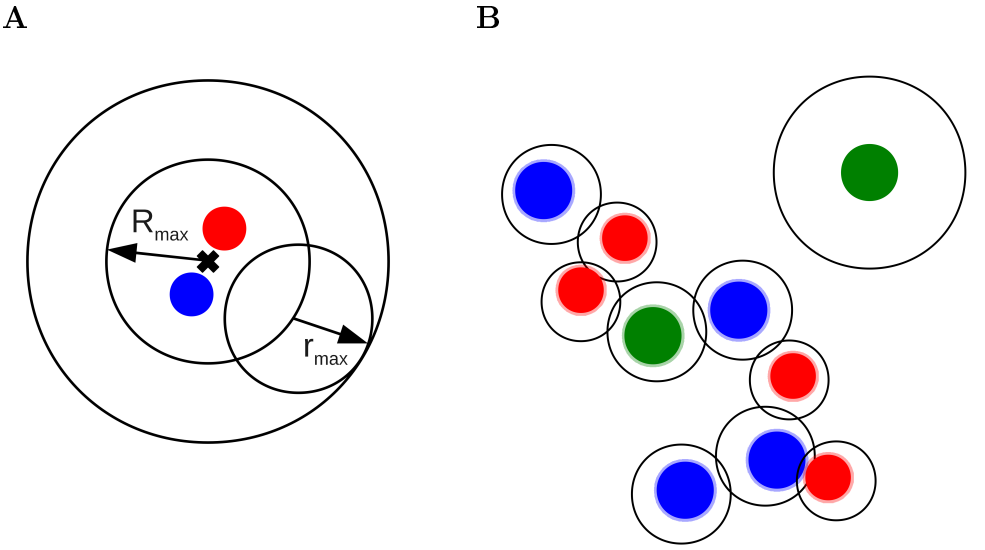

Figure 2.2: Pair and Multi domains in eGFRD. (A) Decomposition of a (projected) spherical *Pair* domain into subdomains for the center-of-mass vector **R** and the interparticle vector **r**. (B) An exemplary *Multi* domain. Here we show the situation in which particles inside the *Multi* have been already propagated by earlier updates (and thus are offset with respect to the shells), but none of them reached its outer shell yet. Thin faint-color rings around the particles indicate their reaction volume. A blue and a red particle in the lower-right part of the Multi overlap with their reaction volumes and will attempt a reaction. Since enough space was available, the top-right green particle formed a regular *Single* domain.

fluxes through the boundaries at time τ_r are compared: If a uniformly distributed random number $\mathcal{R}_r \in [0,1]$ is smaller than the fractional propensity

$$q_{\mathrm{frac}}(\tau_r) = \frac{q_\sigma(\tau_r)}{q_\sigma(\tau_r) + q_a(\tau_r)} = \frac{q_\sigma(\tau_r)}{-\partial_t S_r(\tau_r)} \tag{2.14}$$

the next-event is a *Pair Reaction*; otherwise it is a *IV Escape*.

In general, particles A and B additionally can undergo monomolecular reactions, for which next-event times τ_A and τ_B are calculated in the same manner as for *Singles*. Thus, during *Pair* domain construction, altogether four next-event times τ_r, τ_R, τ_A, τ_B with different next-event types are determined. Since the four stochastic processes again are independent of each other, the tentative next-event time for the *Pair* domain is defined as:

$$\tau_{\mathcal{D}_2} = \min\left(\{\tau_r, \tau_R, \tau_A, \tau_B\}\right) \tag{2.15}$$

The precise procedure of sampling new positions for A and B at next-event time $\tau_{\mathcal{D}_2}$ depends on the type of the next event and the coordinate system in which the problem is considered. We present here the classical treatment for two interacting

particles in 3D, which employs spherical coordinates, for each possible event-type respectively:

- *Pair Reaction*: Here the CoM position $\mathbf{R}_\nu(\tau_\mathrm{r})$ is sampled in the same manner as the new position $\mathbf{r}_\nu(\tau < \tau_{\mathcal{D}_1})$ in *Singles*. A particle with the product species is created at $\mathbf{R}_\nu(\tau_\mathrm{r})$.

- *IV Escape*: In this case $|\mathbf{r}_\nu| = a$ with certainty, but the escape angle θ_ν yet remains undetermined. It is sampled from the propensity function for leaving the **r**-subdomain at the **r**-escape time τ_r through its outer boundary at an angle θ, given by

$$q_\mathrm{a}(\theta) = -\frac{a\sin(\theta)}{Q} D_\mathrm{r} \int_0^{2\pi} \left[\partial_\mathrm{r} p_\mathrm{r}(r,\theta,\phi,\tau_\mathrm{r}|\mathbf{r}_0)\right]_{\mathrm{r=a}} a d\phi \; .$$

  Here the normalization factor is the total flux through the outer boundary $Q = \int_0^\pi q_\mathrm{a}(\theta) d\theta$. The second angle $\phi_\nu \in [0, 2\pi]$ is drawn from a uniform distribution.

- *CoM Escape*: A new center-of-mass position $\mathbf{R}_\nu(\tau_\mathrm{R})$ is sampled as $\mathbf{r}_\nu(\tau_{\mathcal{D}_1})$ in the *Single*. To determine $\mathbf{r}_\nu(\tau_\mathrm{R})$, first a new radius r_ν is sampled from the conditional probability

$$\tilde{p}_\mathrm{r}(r,\tau_\mathrm{R}) \equiv \frac{r^2}{S_\mathrm{r}(\tau_\mathrm{R})} \int_0^\pi \int_0^{2\pi} p_\mathrm{r}(r,\theta,\phi,\tau_\mathrm{R}|\mathbf{r}_0)\sin(\theta) d\theta d\phi \; .$$

  Subsequently, a new angle θ_ν is sampled from the density $p_{\mathrm{r},\theta}(\theta, r_\nu, \tau_\mathrm{R}) \equiv \frac{r_\nu \sin(\theta)}{\tilde{p}_\mathrm{r}(r_\nu,\tau_\mathrm{R})} \int_0^{2\pi} p_\mathrm{r}(r_\nu,\theta,\phi,\tau_\mathrm{R}|\mathbf{r}_0) d\phi$ and $\phi_\nu \in [0, 2\pi]$ from the uniform distribution.

- *Monomolecular reaction* (of A)[3]: The new CoM position $\mathbf{R}_\nu(\tau_\mathrm{A})$ is sampled as in the case *Pair Reaction*, the new interparticle vector $\mathbf{r}_\nu(\tau_\mathrm{A})$ as in the case *CoM Escape*. From this we obtain $\mathbf{r}_{\mathrm{A},\nu}(\tau_\mathrm{A})$ and $\mathbf{r}_{\mathrm{B},\nu}(\tau_\mathrm{A})$. Particle B is simply moved to $\mathbf{r}_{\mathrm{B},\nu}(\tau_\mathrm{A})$, while A is treated as described for the monomolecular reactions in *Singles*.

[3] An identical procedure applies, with A and B interchanged, to the case in which B undergoes a monomolecular reaction.

2.1.4 Brownian Dynamics provides a fallback-system

The strength of eGFRD is that–due to the knowledge of the Green's function–detailed sampling of diffusive trajectories inside the domains can be omitted and particles are propagated with large jumps in time and space. This, however, comes at the cost of increased computational effort per update, because drawing times and positions from Green's functions is significantly more expensive than sampling of simple Gaussian displacements. Therefore eGFRD becomes more costly than Brownian Dynamics (BD) when particles get such crowded that the maximal size of protective domains becomes comparable to particle radii. This may be due to the presence of more than one other particle or other, static obstacles. In such situations, eGFRD seamlessly switches to a simulation mode in which particles are propagated by Brownian Dynamics within specialized domains, called *Multis*.

Multi domains

Whenever particle distances fall below a predefined threshold and regular domain types cannot be constructed, the algorithm prompts the construction of *Multi* domains, which can contain more than two particles. An exemplary *Multi* domain is shown in Figure 2.2B. *Multis* are composed of intersecting spherical shells with shell radii ρ_n proportional to particle radii R_n, i.e. $\rho_\mathrm{n} = \mu R_\mathrm{n}$, where the "multi-shell factor" $\mu > 1$ is a simulation parameter. Each *Multi* constitutes an autonomous BD simulator isolated from its surroundings. Within their shells, particles are propagated, one at a time, by sampling displacements $\Delta\mathbf{r}$ from the free Gaussian propagator with a fixed, sufficiently small timestep Δt that ensures $|\Delta\mathbf{r}| \ll \rho_\mathrm{n}$. Particle propagation continues until either one of the particles hits its surrounding shell or two overlapping particles react. Then, the *Multi* is broken apart and the new constellation is evaluated de novo, possibly resulting in *Multi* reconstruction. Particles that moved away sufficiently far from the particle crowd or obstacle at that moment reform *Single* domains and revert to propagation via Green's functions.

When and how *Multis* are constructed is explained in more detail in section 2.B.2 in the appendix.

Reactions in BD fulfill detailed balance

Particles that create overlaps within *Multis* are tested for reactions. Reaction events in BD mode are sampled such that detailed balance is obeyed. Let $\mathbf{r}_{12}$ be the interparticle vector of the two interacting particles. Detailed balance demands that, for any $\mathbf{r}_{12}$, the probability of the unbound configuration at distance $|\mathbf{r}_{12}|$ times the transition probability to move into the bound state from $\mathbf{r}_{12}$ equals the likelihood to be in the bound state times the probability of the inverse transition:

$$p_\mathrm{u}(\mathbf{r}_{12})\pi_{\mathrm{u}\to\mathrm{b}}(\mathbf{r}_{12}) = p_\mathrm{b}\pi_{\mathrm{b}\to\mathrm{u}}(\mathbf{r}_{12}) \tag{2.16}$$

The occupancy ratio $p_\mathrm{b}/p_\mathrm{u}(\mathbf{r}_{12}) = K_\mathrm{eq}$ is fixed by the equilibrium constant of the reaction and $\pi_{\mathrm{u}\to\mathrm{b}}(\mathbf{r}_{12})$ depends on algorithmic details of particle propagation. This leaves us with the task to prescribe a backward move in a way that $\pi_{\mathrm{b}\to\mathrm{u}}(\mathbf{r}_{12})$ obeys (2.16). Originally, eGFRD employed the Reaction Brownian Dynamics algorithm by

MORELLI and TEN WOLDE [60]. While this scheme yields excellent results for diffusing spheres in 3D, it proved troublesome to extend it to arbitrary dimensions and non-spherical objects. In recent eGFRD we therefore implemented a conceptually similar but more versatile scheme. Its key assumption is that reactive objects, be it other particles or static structures, are surrounded by a small "reaction volume" V^* within which the precise shape of the density $p_{\mathrm{u}}(\mathbf{r}_{12})$ may be ignored. Reaction attempts only occur within V^*, and at the inverse reaction the particle is placed uniformely back into V^*. The binding process is thus broken apart into a displacement and a reaction step. As in [60], it proves useful to rewrite the transition probabilities as a product of a proposal (i.e. move generation) density and (reaction) acceptance probability:

$$\begin{aligned}\pi_{\mathrm{u}\to\mathrm{b}}(\mathbf{r}_{12}) &= P^{\mathrm{gen}}_{\mathrm{u}\to\mathrm{V}^*}(\Delta t)P^{\mathrm{acc}}_{\mathrm{V}^*\to\mathrm{b}} \\ \pi_{\mathrm{b}\to\mathrm{u}}(\mathbf{r}_{12}) &= P^{\mathrm{gen}}_{\mathrm{V}^*\to\mathrm{u}}(\Delta t)P^{\mathrm{acc}}_{\mathrm{b}\to\mathrm{V}^*}\end{aligned} \tag{2.17}$$

Herein $P^{\mathrm{gen}}_{\mathrm{u}\to\mathrm{V}^*}(\Delta t)$ is the probability to move diffusively into the reaction volume V^* from a distance $\mathbf{r}_{12}$ in the unbound state within a time Δt, whereas $P^{\mathrm{gen}}_{\mathrm{V}^*\to\mathrm{u}}(\Delta t)$ is the probability of the inverse move. It can be shown that these probabilities only differ by a factor V^*: $P^{\mathrm{gen}}_{\mathrm{V}^*\to\mathrm{u}}(\Delta t) = V^* P^{\mathrm{gen}}_{\mathrm{u}\to\mathrm{V}^*}(\Delta t)$. Together with the assumption that unbinding occurs with Possonian statistics, i.e. $P^{\mathrm{acc}}_{\mathrm{b}\to\mathrm{V}^*} = k_{\mathrm{u}}\Delta t$, one finds that detailed balance is fulfilled when forward reaction attempts are accepted with a rate

$$P^{\mathrm{acc}}_{\mathrm{V}^*\to\mathrm{b}} = \frac{k_{\mathrm{b}}\Delta t}{V^*} \quad . \tag{2.18}$$

In practice V^* depends on the given situation and it is convenient to tune the magnitudes of specifically occuring reaction volumes via a global "reaction length" parameter δ. For two spherical particles with contact radius σ we have $V^* = \frac{4}{3}\pi\left((\sigma+\delta)^2 - \sigma^2\right)$. For the particle-surface interactions that we introduce later V^* is calculated similarly, taking into account the particular geometry of the contact region. This is described in more detail in [61].

The reaction length δ and the propagation time step Δt are set for each *Multi* domain individually, subject to the following two constraints:

$$D_{\max}\Delta t \leq (\phi R_{\min})^2 \tag{2.19}$$

$$\frac{k_{\mathrm{b,max}}\Delta t}{\delta} \leq P^{\mathrm{acc}}_{\max} \tag{2.20}$$

Here $D_{\max}$ is the maximal diffusion constant of a particle in the *Multi*, $R_{\min}$ the minimal particle radius, $k_{\mathrm{b,max}}$ the fastest intrinsic forward rate (divided by dimension-specific contact-surface factors) and $\phi \leq 1$ a tuneable step size fraction. The first requirement limits the maximal displacement within timestep Δt to a fraction of the smallest particle size; the second ensures that the acceptance probability remains bounded by a value ≤ 1 also for fast reactions. The standard choice in eGFRD is $P^{\mathrm{acc}}_{\max} = 0.01$ and $\delta = \phi R_{\min}$ with $\phi = 0.05 - 0.10$.

2.1.5 Practical aspects

On the practical level, additional attention has to be devoted to some further aspects. In particular, we were not concerned about details of creating protective domain shells given a certain constellation of surrounding shells. While it is clear that in principle one would like to size them up as much as possible, precisely because this makes it possible to make large jumps in time and space, in practice it turns out that this directive by itself may provoke unfavorable behavior that hampers efficiency. Specifically, a domain that is sized up to the boundary of a rather small neighboring domain is likely to be bursted shortly afterwards, when the small domain is updated; this forces domain reconstruction from scratch from almost the same situation as before, wasting computational effort. Moreover, while we explained in section 2.1.4 that it is advantageous to locally propagate particles by Brownian Dynamics when they get crowded, it is not a priori clear when precisely the transition between the two simulation modes should be done. We give a full account of measures that deal with these issues in section 2.B.2 in the appendix, where we present a detailed description of domain making rules in eGFRD.

Implementation

eGFRD is implemented with a core-system written in *C++* and a *Python*-based annex part. The core system is embedded into *Python* via *Boost.Python*. While the usage of *C++* at the core level ensures high computation efficiency, the attached *Python* interface provides a user-friendly scripting environment. eGFRD makes intense use of *GNU Scientific Library*, *Numpy*, *Scipy*, *Automake* and *GNU Libtool*. In later 2012 eGFRD surpassed the 150k linecount. The open-source code is stored in an online *git* repository accessible from the eGFRD website (http://gfrd.org).

Performance

eGFRD has demonstrated hitherto unmatched computational efficiency as a truly particle-based stochastic simulation environment in simulations of reacting hard spheres. It clearly outperforms classical Brownian Dynamics up to μM particle concentrations [39, 42], which is well within the biologically relevant regime. At higher particle densities BD becomes favorable for the reasons explained in section 2.1.4. For particles in a finite, constant 3D volume with periodic boundary conditions the CPU time scales as $N^{5/3}$ with the particle number N. For the extended simulator with the new features that we present in the forthcoming sections and chapters, detailed benchmarking remains yet to be performed.

2.2 Introducing 1D transport into eGFRD

In cells, 1D transport is common. There are two princpal types of 1D transport: diffusion on linear structures, an example of which is DNA sliding [62, 63, 64], and cytoskeletal active transport [65, 66]. In active transport, cargo such as proteins, vesicles or virus vectors, is transported via molecular motors on linear macropolymer tracks like microtubules and actin filaments. Molecular motors consist of a stalk domain that bind the cargo and two foot domains that can attach to the polymer track. There are two major classes of molecular motors: processive and non-processeive motors [67]. Processive motors can move preferentially into one direction in a walking-like fashion while remaining bound to the filament. This is achieved through an ATP-powered sequence of reactions that induce periodic allosteric changes of the motor structure, in a way that one foot remains bound to the track while the other one is first protruded towards and then anchored to a neighboring lattice site on the track. In spite of reaction reversibility, permanent consumption of ATP makes the forward-step reaction more probable than the backward-step. This way, a biased random walk of the motor towards a specific end of the linear track is created. Although non-processive motors also can change their confirmation upon binding to a filament, they are incapable of taking successive steps. Nevertheless, multiple groups of non-processive motors can create a step-like movement and drag cargo along the filament collectively. However, the resulting movement is much more irregular as compared to processive motors, with diffusion dominating over drift.

GFRD heavily relies on the availability of exact analytical solutions for the diffusion-reaction problem in simple geometries. Under this constraint, details like motor structure and filament curvature, which massively complicate mathematical calculations, have to be abandoned. In order to implement 1D transport into GFRD we therefore devised a minimal model of diffusive and active transport on linear tracks: Tracks are represented as thin, long cylinders with a reactive surface. Sliding proteins and motor-cargo complexes are assumed to be well-represented by perfectly spherical (single) particles. The biased 1D random walk is described by a modified diffusion equation that contains an additional drift term. These simplifications enables us to introduce (cylindrical) domains that produce next-event times for binding to and displacements on the cylinders, using the associated Green's functions.

In what follows, after introducing some new terminology, we first describe how we treat binding of particles from the cytosol to the reactive cylindrical structures and the reverse process. We then explain modelling of 1D movement of particles on the cylinders. The mathematical derivation of the required Green's functions is subject of the subsequent section 2.3.

2.2.1 Structures, surfaces and interactions

Here we briefly clarify the use of new terminology.

We will call static objects on which particles can exist "structures". This may be the 3D volume, called the "bulk" structure, or submanifolds of the 3D space, like cylinders and planes, referred to as "surfaces".

Further, we will distinguish between "reactions", i.e. the binding of particles to particles, and "interactions", which is the binding of particles to surfaces. Instant transfer of particles from one surface to another is called "transitions". Accordingly, in addition to the basic classification into *Singles* and *Pairs*, we distinguish between "*Interaction*" and "*Transition*" domains, in which, respectively, particles can bind to surfaces or jump from one surface to another. The four domain categories are not necessarily mutually exclusive: *Transitions* can be *Singles* or *Pairs*, whereas *Interactions* are always *Single* domains. For completeness, we refer to *Singles* that are not *Interactions* as "*Non-Interaction Singles*". Note that *Non-Interaction Singles* may also exist on surfaces.

A domain class tree illustrating the categorization of domain types, which also includes new domain types introduced in the next chapter, is shown in Figure S2.1 in appendix section 2.B.1.

2.2.2 Interactions with cylinders

Let us assume a situation in which a spherical particle that diffuses in 3D is close to a long cylinder with a reactive surface to which the particle can bind with an intrinsic forward rate k. To isolate the particle-surface association problem from the influence of surrounding particles and surfaces we construct a cylindrical protective domain, with an axis that coincides with the axis of the reactive surface and such that it contains only the proximate particle. A sketch of such a "*Cylindrical Surface Interaction*" domain is shown in Figure 2.3A. For the one-particle surface-binding problem an analytical solution can be readily obtained.

Diffusion of the particle within the cylindrical domain is described by the diffusion equation in cylindrical coordinates $\mathbf{r} = (r, \phi, z)$:

$$\partial_{\mathrm{t}} p(\mathbf{r}, t|\mathbf{r}_0) = D\nabla^2 p(\mathbf{r}, t|\mathbf{r}_0) = D\left[\frac{1}{r}\partial_{\mathrm{r}}\left(r\partial_{\mathrm{r}}\right) + \frac{1}{r^2}\partial_{\phi}^2 + \partial_{\mathrm{z}}^2\right] p(\mathbf{r}, t|\mathbf{r}_0) \tag{2.21}$$

Since here diffusion in the direction parallel to the cylinders and diffusion in the direction orthogonal to the cylinders are not correlated, the above 3D diffusion equation can be uncoupled into a 1D and 2D problem using a separation ansatz $p(\mathbf{r}, t|\mathbf{r}_0) = p_{\mathrm{r}}(r, \phi, t)p_{\mathrm{z}}(z, t)$. This yields:

$$\partial_{\mathrm{t}} p_{\mathrm{r}}(r, \phi, t) = D\left[\frac{1}{r}\partial_{\mathrm{r}}\left(r\partial_{\mathrm{r}}\right) + \frac{1}{r^2}\partial_{\phi}^2\right] p_{\mathrm{r}}(r, \phi, t) \tag{2.22}$$

$$\partial_{\mathrm{t}} p_{\mathrm{z}}(z) = D\partial_{\mathrm{z}}^2 p_{\mathrm{z}}(z, t) \tag{2.23}$$

Let the particle initially be located at $\mathbf{r}_0 = (r_0, \phi_0, z_0 = 0)$. Then we may write the initial condition as:

$$p(r, \phi, z, t = 0) = \delta(\mathbf{r} - \mathbf{r}_0) = \underbrace{\frac{1}{r}\delta(r - r_0)\delta(\phi - \phi_0)}_{p_{\mathrm{r}}(r,\phi,t=0)} \underbrace{\delta(z)}_{p_{\mathrm{z}}(z,t=0)} \tag{2.24}$$

To include the new domain into the existing eGFRD framework we have to compute the expected times of particle exit from the domain. Here exit can either happen

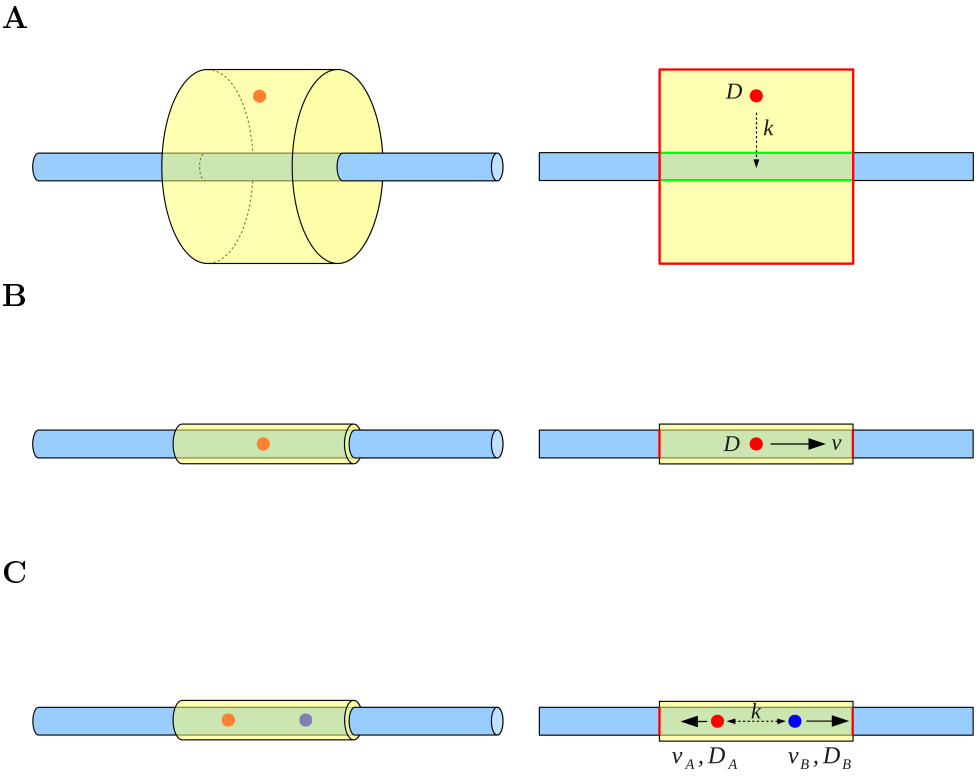

Figure 2.3: New protective domain types for interactions with and transport and reactions on 1D structures. (A) *Cylindrical Surface Interaction* domain; (B) *Cylindrical Surface Single* domain; (C) *Cylindrical Surface Pair* domain. Right panels show sections of 3D objects along the common cylinder axis. Absorbing boundaries are highlighted by red, radiative boundaries by green. Note that drift velocities (v, v_{A}, v_{B}) can be towards any cylinder end.

by hitting the absorbing outer boundary of the cylindrical domain or by reacting with the cylindrical structure enclosed by the domain. Let R_{D} and L be the radius and the length of the cylindrical domain, respectively, R_0 the radius of the reactive cylinder representing the filament and R the particle radius. Then the two aforementioned exit channels can be included into the model by imposing the following boundary conditions:

$$p_{\mathrm{z}}(-L/2,t) = 0, \qquad p_{\mathrm{z}}(+L/2,t) = 0 \tag{2.25}$$

$$p_{\mathrm{r}}(R_{\mathrm{D}},\phi,t) = 0 \tag{2.26}$$

$$2\pi\sigma D\partial_{\mathrm{r}}p_{\mathrm{r}}(r,\phi,t)\big|_{\mathrm{r}=\sigma} = kp_{\mathrm{r}}(|\mathbf{r}| = \sigma, t) \tag{2.27}$$

Here $\sigma = R + R_0$ is the contact radius, i.e. the radius of the cylindrical surface that

comprises all positions in which the particle is in contact with the reactive cylinder. $2\pi\sigma D\partial_r p_r(r,\phi,t)\big|_{r=\sigma}$ is the total outward probability flux in radial direction through the radiative boundary at $r=\sigma$ at time t, while $p_r(|\mathbf{r}|=\sigma,t)$ is the probability to be at contact with the reactive cylinder for the given t.

Clearly, the original 3D diffusion-reaction problem can be broken down into two problems that can be solved separately: Equations (2.22) with (2.26), (2.27) and the respective part of (2.24) constitute a boundary value problem for 2D diffusion of a point particle with a radiating boundary condition at $r=\sigma$ and an absorbing boundary condition at $r=R_D$. We present the Green's function for this problem in section 3.3.2. Equations (2.23) with (2.25) and the initial condition for p_z in (2.24) describe diffusion of a point particle in one dimension with two absorbing boundaries. The Green's function for this scenario follows as a special case of the Green's Function derived later in this chapter, as described in section 2.3.2.

2.2.3 Diffusion, drift and reactions on cylinders

Once a particle has bound to the cylindrical surface it can diffuse and drift along its axis and interact with other particles. To calculate next-event times for this scenario we again construct a protective domain around the particle. Here specifically we seek a domain that isolates cylinder-bound (1D) particles both from bulk (3D) particles and from other 1D particles simultaneously. While it certainly would be possible to take into account the finite thickness of the filament and rotational diffusion around the cylinder axis, we ignore these microscopic dynamics here; we argue that for most biological processes the dynamics at this molecular scale can be coarse-grained. Therefore we assume that the spherical particles in their bound state localize onto the axis of the cylinder. Then cylindrical domain geometry again is a natural choice, with a cylinder radius R_D equal to or greater than the particle radius. The length of the cylindrical domain is determined by the available free space, which in turn is limited by already present protective domains of other particles or the ends of the cylindrical surface if it is finite. In section 2.4 we describe in more detail how finite linear tracks are treated. Again we allow for one- (*Cylindrical Surface Single*, Fig. 2.3B) and two-particle domains (*Cylindrical Surface Pair*, Fig. 2.3C); the latter are formed when two cylinder-bound particles are close to each other. In addition, we introduce a special *Single* domain that encloses a reactive sink (*Cylindrical Surface Sink* domain, Fig. 2.5D) which may be used to model, for example, a reactive promoter site on DNA. More detail on the *Cylindrical Surface Sink* follows in sections 2.4 and 2.5.

The new domain types differ by their associated Green's functions. For the *Single* domains the Green's Function $p(x,t|x_0)$ is calculated from the diffusion-drift equation

$$\partial_t p(\mathbf{r},t|\mathbf{r}_0) = D\nabla^2 p(\mathbf{r},t|\mathbf{r}_0) - \mathbf{v}\nabla p(\mathbf{r},t|\mathbf{r}_0) \tag{2.28}$$

with two absorbing boundary conditions. Here the constant parameter $\mathbf{v}$ is the drift velocity of the particle and D the diffusion coefficient of the 1D diffusion process.

Similarly, in the *Pair* domains the spatio-temporal evolution of the combined probability density p_2 for two particles with diffusion constants D_A and D_B and (constant) drift velocities $\mathbf{v}_\mathrm{A}$ and $\mathbf{v}_\mathrm{B}$, respectively, may be described by the following SMOLUCHOWSKI equation [68, 39]:

$$\partial_\mathrm{t} p_2 = [D_\mathrm{A}\nabla_\mathrm{A}^2 + D_\mathrm{B}\nabla_\mathrm{B}^2 - \mathbf{v}_\mathrm{A}\nabla_\mathrm{A} - \mathbf{v}_\mathrm{B}\nabla_\mathrm{B}]p_2 \tag{2.29}$$

Herein $p_2 = p_2(\mathbf{r}_\mathrm{A}, \mathbf{r}_\mathrm{B}, t|\mathbf{r}_\mathrm{A0}, \mathbf{r}_\mathrm{B0})$ is the probability density function for the probability to find particle A at postion $\mathbf{r}_\mathrm{A}$ and particle B at $\mathbf{r}_\mathrm{B}$ at time t given that they started at $\mathbf{r}_\mathrm{A0}$ and $\mathbf{r}_\mathrm{B0}$ at $t = 0$. In section 2.3.1 we demonstrate that via an adequate coordinate transform we can decompose the combined diffusion-drift movement of both particles into two independent diffusion-drift processes for the center-of-mass and the interparticle vector, as already described in general for *Pairs* in section 2.1.3. This yields two equations of the same form as (2.28).

The fact that the required Green's function solutions follow from the same partial differential equation (2.28) facilitates further effort: In the following we will first derive the Green's function for the 1D diffusion-drift problem with one radiating and one absorbing boundary and then obtain the corresponding solution for the situation with two absorbing boundaries as a limit (section 2.3.2). The Green's function for the *Cylindrical Surface Sink* domain is treated as a special case in section 2.5.

2.2.4 Unbinding from cylinders

Unbinding from the cylindrical surfaces is treated in the same way as monomolecular reactions in standard eGFRD. A next-unbinding time τ_u is again sampled from an exponential distribution. Upon unbinding at time τ_u the cylindrical protective domain of the particle is bursted, i.e. particles are propagated until τ_m using the associated Green's function. After that, the unbinding particle is put at contact with the cylindrical surface at a random unbinding angle $\phi_\mathrm{u} \in [0, 2\pi]$. Of course, also monomolecular reactions that leave the particle on the cylinder or annihilate it are possible, and technically treated in the same way.

2.3 Green's functions for the diffusion-drift-reaction problem in 1D

In the following we derive Green's functions that are needed to sample next-event times for particles diffusing, drifting and interacting in 1D.

First we present the coordinate transform that is necessary to treat the two-particle problem.

2.3.1 Coordinate separation for the Smoluchowski equation

Starting from the SMOLUCHOWSKI equation [68] for two particles with diffusion coefficients D_A, D_B and drift velocities $\mathbf{v}_A$, $\mathbf{v}_B$

$$\partial_t p_2 = [D_A \nabla_A^2 + D_B \nabla_B^2 - \mathbf{v}_A \nabla_A - \mathbf{v}_B \nabla_B] p_2 \tag{2.30}$$

we define the interparticle vector $\mathbf{r}$ and the weighted center-of-mass vector $\mathbf{R}$ as follows:

$$\begin{aligned} \mathbf{r} &\equiv \mathbf{r}_B - \mathbf{r}_A \\ \mathbf{R} &\equiv \gamma \mathbf{r}_A + \delta \mathbf{r}_B \end{aligned} \tag{2.31}$$

γ and δ are constant coefficients that will be specified later.

In section 2.A of the appendix we show that operators ∇_A and ∇_B may be rewritten in terms of ∇_r and ∇_R as follows:

$$\begin{aligned} \nabla_A &= \gamma \nabla_R - \nabla_r \\ \nabla_B &= \delta \nabla_R + \nabla_r \end{aligned} \tag{2.32}$$

With the constraint $D_A \gamma = D_B \delta$, which causes mixed derivative terms $\sim \nabla_r \nabla_R$ to vanish, and after some intermediate steps one arrives at:

$$\begin{aligned} \partial_t p_2 =& \big[(D_A + D_B) \nabla_r^2 + (\gamma^2 D_A + \delta^2 D_B) \nabla_R^2 \\ & - \mathbf{v}_A (\gamma \nabla_R - \nabla_r) - \mathbf{v}_B (\delta \nabla_R + \nabla_r) \big] p_2 \\ =& \big[(D_A + D_B) \nabla_r^2 + (\gamma^2 D_A + \delta^2 D_B) \nabla_R^2 \\ & + (\mathbf{v}_A - \mathbf{v}_B) \nabla_r - (\gamma \mathbf{v}_A + \delta \mathbf{v}_B) \nabla_R \big] p_2 \end{aligned} \tag{2.33}$$

Via the separation ansatz $p_2 \equiv p_r p_R$ we can rewrite the above equation in terms of two diffusion-drift equations, one for $\mathbf{r}$ and one for $\mathbf{R}$, with diffusion and drift constants made up from the corresponding constants of the individual particles:

$$\begin{aligned} \partial_t p_r =& \big[\underbrace{(D_A + D_B)}_{D_r} \nabla_r^2 - \underbrace{(\mathbf{v}_B - \mathbf{v}_A)}_{\mathbf{v}_r} \nabla_r \big] \; p_r \\ \partial_t p_R =& \big[\underbrace{(\gamma^2 D_A + \delta^2 D_B)}_{D_R} \nabla_R^2 - \underbrace{(\gamma \mathbf{v}_A + \delta \mathbf{v}_B)}_{\mathbf{v}_R} \nabla_R \big] \; p_R \end{aligned} \tag{2.34}$$

The interpretation of the new drift constants is straightforward: $\mathbf{v}_\mathrm{r}$ describes the relative velocity of the particles (as in the case without diffusive motion) while $\mathbf{v}_\mathrm{R}$ is an effective weighted center-of-mass drift.

As explained in section 2.A, there is some freedom in choosing γ and δ as long as the constraint imposed above remains fulfilled. Here we make the same choice as in eGFRD:

$$\gamma = \frac{D_\mathrm{B}}{D_\mathrm{A} + D_\mathrm{B}}, \qquad \delta = \frac{D_\mathrm{A}}{D_\mathrm{A} + D_\mathrm{B}} \tag{2.35}$$

which implies:

$$D_\mathrm{R} = \frac{D_\mathrm{A} D_\mathrm{B}}{D_\mathrm{A} + D_\mathrm{B}}, \qquad \mathbf{v}_\mathrm{R} = \frac{D_\mathrm{B}\mathbf{v}_\mathrm{A} + D_\mathrm{A}\mathbf{v}_\mathrm{B}}{D_\mathrm{A} + D_\mathrm{B}} \tag{2.36}$$

With the definition of 1D structures and domains introduced in section 2.2 movement of the particles is restricted to a straight line. Then vectors $\mathbf{r}$, $\mathbf{R}$, $\mathbf{v}_\mathrm{r}$ and $\mathbf{v}_\mathrm{R}$ are collinear, and we can pass from the vector equation to a scalar equation.

2.3.2 Solution for the 1D-diffusion-reaction problem with drift with different boundary conditions

With the assumptions made in the previous section the 1D diffusion-drift equation takes the common form, where x stands for either the inter-particle distance r or the center-of-mass position R:

$$\partial_\mathrm{t} p_\mathrm{x} = \left[D_\mathrm{x}\partial_\mathrm{x}^2 - v_\mathrm{x}\partial_\mathrm{x}\right]\ p_\mathrm{x} \tag{PDE}$$

In both cases the initial condition is $p_\mathrm{x}(x, t_0 = 0) = \delta(x - x_0)$. In the following we will drop the index and simply use $p = p(x, t|x_0, t_0)$ to denote the Green's function. Following the standard treatment in eGFRD, we model chemical reactions between particles A and B on the cylinder by imposing a radiating boundary condition to r at particle contact, while the R-equation has to be solved subject to absorbing boundary conditions. For completeness, we will also give the solutions for the half-bounded problems.

To summarize, in the following we will derive the Green's function for (PDE) on an interval $[\sigma, a]$ of length $L = a - \sigma$ or on a one-sided interval $[\sigma, \infty)$, and the following boundary conditions, respecitvely:

- Rad-Abs: radiating left boundary at σ, absorbing right boundary at $a > \sigma$.
- Abs-Abs: absorbing left boundary at σ, absorbing right boundary at $a > \sigma$.
- Rad-Inf: radiating left boundary at σ, no right boundary.
- Abs-Inf: absorbing left boundary at σ, no right boundary.

The Green's Functions are used to derive the resulting survival probability $S(t|x_0, t_0) = \int_\mathrm{a}^{b \text{ or } \infty} p(x, t|x_0, t_0)dx$, the corresponding propensity function $\pi(t|x_0, t_0) = -\partial_\mathrm{t} S(t|x_0, t_0)$ and expressions for the transient boundary fluxes.

Free solution

It is easily verified that "free", i.e. unbounded, diffusion-drift equation (PDE) with initial condition $p(x, t = 0) = \delta(x - x_0)$ is solved by

$$p_{\text{free}}(x, t|x_0) = \frac{1}{\sqrt{4\pi Dt}} e^{-\frac{1}{4Dt}[(x-x_0)-vt]^2} \tag{2.37}$$

which describes a Gaussian distribution with a width that increases in time, centered around a mean value that moves with the drift velocity v.

Green's function for 1D-diffusion with drift, Rad-Abs case

We start with the most general of the four cases, with the perspective of deriving other cases as special limits.

The radiation boundary condition relates the probability flux $j(x = \sigma, t)$ at the radiating boundary to the intrinsic reaction rate k via:

$$j(x = \sigma, t) = -kp(x = \sigma, t) \tag{2.38}$$

Here the flux contains a contribution from diffusion and a contribution from the drift:

$$j(x, t) = -D\partial_{\text{x}} p(x, t) + vp(x, t) \tag{2.39}$$

The correct boundary condition for the boundary at $\sigma < a$ therefore is:

$$\begin{aligned} -D\partial_{\text{x}} p(x, t)\big|_{\text{x}=\sigma} + vp(\sigma, t) &= -kp(\sigma, t) \\ \Leftrightarrow \qquad \partial_{\text{x}} p(x, t)\big|_{\text{x}=\sigma} &= \frac{v + k}{D} p(\sigma, t) \end{aligned} \tag{BCr}$$

The minus sign on the right side of the equation is due to the fact that at the left boundary the flux out of the system is negative with respect to the x-axis.

The absorbing boundary at $x = a$ requires:

$$p(a, t) = 0 \qquad \forall t \tag{BCa}$$

Dedimensionalization

Before we attempt to solve the PDE with these boundary conditions it is convenient to perform a dedimensionalization. The natural length scale is given by the length $L = a - \sigma$ of the interval $[\sigma, a]$, while $T \equiv L^2/D$ defines a corresponding natural time scale. We thus rescale our variables via

$$\begin{aligned} \xi \equiv \frac{x - \sigma}{a - \sigma} = \frac{x - \sigma}{L}, \quad &\Rightarrow \partial_\xi \equiv L\partial_{\text{x}} \\ \tau \equiv \frac{t}{T} = \frac{Dt}{L^2}, \quad &\Rightarrow \partial_\tau \equiv T\partial_{\text{t}} = \frac{L^2}{D}\partial_{\text{t}} \end{aligned} \tag{2.40}$$

to obtain the following boundary value problem to solve:

$$\partial_\tau p(\xi,\tau) = \left[\partial_\xi^2 - \frac{vL}{D}\partial_\xi\right]\ p(\xi,\tau) \tag{PDE}$$

$$\partial_\xi p(\xi,\tau)\big|_{\xi=0} = \frac{(v+k)L}{D}p(0,\tau) \tag{BCr}$$

$$p(1,\tau) = 0 \tag{BCa}$$

$$p(\xi,\tau=0) = \frac{1}{L}\delta\left(\xi-\xi_0\right) \tag{IC}$$

The last equation represents the starting condition for a particle initially located at position $L\xi_0$ (or a pair having an initial separation $L\xi_0$), where for convenience we set $t_0 = 0 = \tau_0$. Note that we have to scale the delta function by $1/L$ because the integration norm scales as $d\xi = Ldx$.

Unfortunately the linear operator $\Lambda \equiv \left[\partial_\xi^2 - \frac{vL}{D}\partial_\xi\right]$ is non-Hermitian. Therefore we can not apply straightforward techniques like eigenfunction expansion to calculate the solution. As we will see, a simple transform can resolve this issue.

Simplifying the problem with the help of an integrating factor

The difficulties imposed by the non-Hermiticity of the operator can be overcome by introducing an integrating factor $\phi(\xi) \equiv e^{\frac{vL}{2D}\xi} = e^{\frac{\nu}{2}\xi}$ (depending explicitly on ξ)[4]. This technique was already used by Smoluchowski himself [69]. Multiplying (PDE) with $1/\phi(\xi) = e^{-\frac{\nu}{2}\xi}$ and completing the square yields ($\nu \equiv \frac{vL}{D}$):

$$\begin{aligned}
\partial_\tau\left[e^{-\frac{\nu}{2}\xi}p(\xi,\tau)\right] &= e^{-\frac{\nu}{2}\xi}\left[\partial_\xi^2 - \nu\partial_\xi\right]\ p(\xi,\tau) \\
&= \left[e^{-\frac{\nu}{2}\xi}\partial_\xi^2 - 2\frac{\nu}{2}e^{-\frac{\nu}{2}\xi}\partial_\xi + \frac{\nu^2}{4}e^{-\frac{\nu}{2}\xi}\right. \\
&\qquad\qquad \left. -\frac{\nu^2}{4}e^{-\frac{\nu}{2}\xi}\right]\ p(\xi,\tau) \\
&= \partial_\xi^2\left[e^{-\frac{\nu}{2}\xi}p(\xi,\tau)\right] - \frac{\nu^2}{4}e^{-\frac{\nu}{2}\xi}p(\xi,\tau)
\end{aligned} \tag{2.41}$$

Thus, by writing the solution with an ansatz

$$p(\xi,\tau) = \phi(\xi)\pi(\xi,\tau) = e^{\frac{\nu}{2}\xi}\pi(\xi,\tau) \tag{2.42}$$

which means defining a new function

$$\pi(\xi,\tau) \equiv e^{-\frac{\nu}{2}\xi}p(\xi,\tau) \tag{2.43}$$

equation (PDE) is equivalent to:

$$\partial_\tau\pi(\xi,\tau) = \partial_\xi^2\pi(\xi,\tau) - \frac{\nu^2}{4}\pi(\xi,\tau) \tag{2.44}$$

[4] Λ is non-Hermitian with respect to the usual Cartesian integration norm $d\xi$. However it is Hermitian with respect to the integration norm $d\phi = \frac{\nu}{2}e^{\frac{\nu}{2}\xi}d\xi$.

Alternatively, this can be seen by plugging the new ansatz for p into (PDE) and applying the operators accordingly.

As a next step, also the boundary conditions and the initial condition have to be transformed analogously to yield an equivalent of the whole problem. Clearly, $\pi(\xi,\tau) = 0$ whenever $p(\xi,\tau) = 0$. Thus, $\pi(\xi,\tau)$ fulfills the boundary condition at $\xi = 1$ trivially if $p(\xi,\tau)$ does so. Because of

$$\partial_\xi \pi(\xi,\tau) = \left[\partial_\xi e^{-\frac{\nu}{2}\xi}\right] p(\xi,\tau) + e^{-\frac{\nu}{2}\xi}\partial_\xi p(\xi,\tau)$$

we have

$$\begin{aligned}
\partial_\xi \pi(\xi,\tau)\big|_{\xi=0} &= -\frac{\nu}{2}p(0,\tau) + \left[e^{-\frac{\nu}{2}\xi}\partial_\xi p(\xi,\tau)\right]_{\xi=0} \\
&= -\frac{\nu}{2}p(0,\tau) + \frac{(v+k)L}{D}p(0,\tau) \\
&= \left[\frac{\nu}{2} + \frac{kL}{D}\right]\pi(0,\tau)
\end{aligned}$$

where in the last step we use $p(0,\tau) = \pi(0,\tau)$ and $\nu = \frac{vL}{D}$.

The initial condition becomes:

$$\pi(\xi,0) = e^{-\frac{\nu}{2}\xi}p(\xi,0) = e^{-\frac{\nu}{2}\xi}\frac{1}{L}\delta(\xi-\xi_0)$$

In the prefactor of the delta function ξ only takes values other than ξ_0 when the delta function is zero, so we can set $\xi = \xi_0$ here. This facilitates further calculations.

In summary, after multiplication with the integrating factor ϕ the initial problem for $p(\xi,\tau)$ is equivalent to the following problem for $\pi(\xi,\tau)$:

$$\partial_\tau \pi(\xi,\tau) = \left[\partial_\xi^2 - \frac{\nu^2}{4}\right]\pi(\xi,\tau) \tag{PDE}$$

$$\partial_\xi \pi(\xi,\tau)\big|_{\xi=0} = \left[\frac{\nu}{2} + \frac{kL}{D}\right]\pi(0,\tau) \tag{BCr}$$

$$\pi(1,\tau) = 0 \tag{BCa}$$

$$\pi(\xi,0) = e^{-\frac{\nu}{2}\xi_0}\frac{1}{L}\delta(\xi-\xi_0) \tag{IC}$$

This result reveals that the diffusion-drift problem is mathematically equivalent to a diffusion-decay problem with a slightly modified radiative boundary condition. The strategy now is to solve (PDE) for $\pi(\xi,t)$ and reconstruct the solution $p(\xi,t)$ afterwards using (2.42).

Solving the PDE via Laplace transform

Applying the Laplace transform by integrating $\int_0^\infty \pi(\xi,\tau)e^{-s\tau}d\tau \equiv \hat{\pi}(\xi,s)$ on both sides of (PDE) yields:

$$\begin{aligned}
& s\hat{\pi}(\xi,s) - e^{-\frac{\nu}{2}\xi_0}\frac{1}{L}\delta(\xi-\xi_0) = \left[\partial_\xi^2 - \frac{\nu^2}{4}\right]\hat{\pi}(\xi,s) \\
\Leftrightarrow \quad & \left[\partial_\xi^2 - \kappa^2\right]\hat{\pi}(\xi,s) = -\phi_0\delta(\xi-\xi_0)
\end{aligned} \tag{2.45}$$

where we abbreviate $\kappa^2 \equiv \frac{\nu^2}{4} + s \geq 0$ and $\phi_0 \equiv \frac{1}{L} e^{-\frac{\nu}{2}\xi_0} > 0$. According to transformation rules, the time derivative $\partial_\tau \pi(\xi, \tau)$ converts to $\hat{\pi}(\xi, s) - \pi(\xi, \tau = 0)$ in LAPLACE space.

To solve the transformed equation we first calculate the solution of the homogenous problem. This will be used to obtain two different specific solutions on the two parts of the underlying space separated by the delta peak, i.e. $[0, \xi_0]$ and $[\xi_0, 1]$, employing the boundary conditions and a continuity/discontinuity condition at $\xi = \xi_0$. The general solution to the homogenous problem $\partial_\xi^2 = \kappa^2 \hat{\pi}(\xi, s)$ can be written as $\hat{\pi}_\mathrm{h}(\xi, s) = \alpha \sinh(\kappa x) + \beta \cosh(\kappa x)$. We thus make an ansatz for each part of the interval $[0, 1]$ as follows:

$$\hat{\pi}(\xi, s) = \hat{\pi}_-(\xi, s) \equiv \alpha_- \sinh(\kappa\xi) + \beta_- \cosh(\kappa\xi) \qquad \text{for} \quad \xi < \xi_0 \tag{2.46}$$

$$\hat{\pi}(\xi, s) = \hat{\pi}_+(\xi, s) \equiv \alpha_+ \sinh(\kappa\xi) + \beta_+ \cosh(\kappa\xi) \qquad \text{for} \quad \xi > \xi_0 \tag{2.47}$$

with constant, yet arbitrary, real coefficients α_+, β_+ and α_-, β_-. Let us first apply the absorbing boundary condition at $\xi = 1$ to (2.47):

$$\hat{\pi}_+(1) = 0 \quad \Rightarrow \qquad \alpha_+ \sinh(\kappa) = -\beta_+ \cosh(\kappa) \tag{2.48}$$

where we neglect the unphysical solution $\alpha_+ = 0,\ \beta_+ = 0$.

Applying the transformed radiating boundary condition at $\xi = 0$ to (2.46) yields:

$$\begin{aligned}
&\partial_\xi \hat{\pi}_-(\xi, s)\big|_{\xi=0} = \underbrace{\left[\frac{\nu}{2} + \frac{kL}{D}\right]}_{\Omega} \hat{\pi}_-(0, s) \\
&\Leftrightarrow \left[\alpha_- \kappa \cosh(\kappa\xi) + \beta_- \kappa \sinh(\kappa\xi)\right]_{\xi=0} \\
&\qquad\qquad = \Omega \left[\alpha_- \sinh(\kappa\xi) + \beta_- \cosh(\kappa\xi)\right]_{\xi=0} \\
&\Leftrightarrow \kappa\alpha - = \Omega\beta_-
\end{aligned} \tag{2.49}$$

Reinsertion into (2.46) and (2.47) leads to:

$$\hat{\pi}_-(\xi, s) = \alpha_- \left(\sinh(\kappa\xi) + \frac{\kappa}{\Omega} \cosh(\kappa\xi)\right) \tag{2.50}$$

$$\hat{\pi}_+(\xi, s) = \alpha_+ \left(\sinh(\kappa\xi) - \tanh(\kappa) \cosh(\kappa\xi)\right) \tag{2.51}$$

In order to determine coefficients α_+ and α_- we, firstly, impose continuity of $\hat{\pi}(\xi, s)$ at $\xi = \xi_0$, i.e. $\hat{\pi}_-(\xi_0, s) = \hat{\pi}_+(\xi_0, s)$ for all s. Secondly, by integrating equation (2.45) over $[\xi_0 - \epsilon, \xi_0 + \epsilon]$ and taking the limit $\epsilon \to 0$, we obtain the following discontinuity condition for the left- and right-hand derivative $\partial_\xi \hat{\pi}(\xi, s)\big|_{\xi=\xi_0}$:

$$\begin{aligned}
&\int_{\xi_0-\epsilon}^{\xi_0+\epsilon} \left[\partial_\xi^2 \hat{\pi}(\xi, s) - \kappa^2 \hat{\pi}(\xi, s)\right] d\xi = -\int_{\xi_0-\epsilon}^{\xi_0+\epsilon} \phi_0 \delta(\xi - \xi_0) d\xi \qquad \Leftrightarrow \\
&\left[\partial_\xi \hat{\pi}(\xi, s)\big|_{\xi_0+\epsilon} - \partial_\xi \hat{\pi}(\xi, s)\big|_{\xi_0-\epsilon}\right] - \kappa^2 \left[\hat{\Pi}(\xi_0 + \epsilon, s) - \hat{\Pi}(\xi_0 - \epsilon, s)\right] = -\phi_0 \\
&\overset{\epsilon \to 0}{\Rightarrow} \qquad \partial_\xi \hat{\pi}_+(\xi, s)\big|_{\xi_0} - \partial_\xi \hat{\pi}_-(\xi, s)\big|_{\xi_0} = -\phi_0
\end{aligned} \tag{2.52}$$

The term $[\hat{\Pi}(\xi_0+\epsilon,s)-\hat{\Pi}(\xi_0-\epsilon,s)]$ vanishes for $\epsilon\to 0$ because continuity of $\hat{\pi}(\xi,s)$ at $\xi=\xi_0$ implies continuity of the stem function $\hat{\Pi}(\xi,s)=\int\hat{\pi}(\xi,s)d\xi$ at this point.

Applying the two additional constraints to (2.50) and (2.51) determines, after some algebraic steps, the coefficients α_- and α_+:

$$\begin{aligned}\alpha_- &= \frac{-\phi_0}{\kappa\left(\frac{\kappa}{\Omega}+\tanh(\kappa)\right)}\left(\sinh(\kappa\xi_0)-\tanh(\kappa)\cosh(\kappa\xi_0)\right)\\ \alpha_+ &= \frac{-\phi_0}{\kappa\left(\frac{\kappa}{\Omega}+\tanh(\kappa)\right)}\left(\sinh(\kappa\xi_0)+\frac{\kappa}{\Omega}\cosh(\kappa\xi_0)\right)\end{aligned} \tag{2.53}$$

Hence,

$$\begin{aligned}\hat{\pi}_-(\xi,s) &= \frac{-\phi_0}{\kappa\left(\frac{\kappa}{\Omega}+\tanh(\kappa)\right)}\times\\ &\qquad\left(\sinh(\kappa\xi)+\frac{\kappa}{\Omega}\cosh(\kappa\xi)\right)\left(\sinh(\kappa\xi_0)-\tanh(\kappa)\cosh(\kappa\xi_0)\right)\\ \hat{\pi}_+(\xi,s) &= \frac{-\phi_0}{\kappa\left(\frac{\kappa}{\Omega}+\tanh(\kappa)\right)}\times\\ &\qquad\left(\sinh(\kappa\xi_0)+\frac{\kappa}{\Omega}\cosh(\kappa\xi_0)\right)\left(\sinh(\kappa\xi)-\tanh(\kappa)\cosh(\kappa\xi)\right)\end{aligned} \tag{2.54}$$

or, after multiplying numerator and denominator by $\cosh(\kappa)$:

$$\begin{aligned}&\hat{\pi}_-(\xi,s) =\\ &\quad\frac{\phi_0}{\kappa}\frac{\left(\sinh(\kappa\xi)+\frac{\kappa}{\Omega}\cosh(\kappa\xi)\right)\left(\sinh(\kappa)\cosh(\kappa\xi_0)-\cosh(\kappa)\sinh(\kappa\xi_0)\right)}{\sinh(\kappa)+\frac{\kappa}{\Omega}\cosh(\kappa)}\\ &\hat{\pi}_+(\xi,s) =\\ &\quad\frac{\phi_0}{\kappa}\frac{\left(\sinh(\kappa\xi_0)+\frac{\kappa}{\Omega}\cosh(\kappa\xi_0)\right)\left(\sinh(\kappa)\cosh(\kappa\xi)-\cosh(\kappa)\sinh(\kappa\xi)\right)}{\sinh(\kappa)+\frac{\kappa}{\Omega}\cosh(\kappa)}\end{aligned} \tag{2.55}$$

Here we shall not forget that $\kappa=\kappa(s)=\sqrt{s+\frac{\nu^2}{4}}$.

With this we have determined unique solutions to the diffusion-drift-reaction problem for the left ($\xi\le\xi_0$) and right ($\xi\ge\xi_0$) part of the spatial domain in Laplace space. Now we can attempt the back transform to the time domain, where we will find that the solution becomes symmetric in ξ and ξ_0 again.

Inverse Laplace transform via residue formula

Having $\hat{\pi}(\xi,s)$ we can obtain the corresponding function in the time domain via the Bromwich / Fourier-Mellin integral:

$$\pi(\xi,t)=\mathcal{L}^{-1}\left[\hat{\pi}(\xi,z)\right]=\frac{1}{2\pi i}\lim_{\mathrm{T}\to\infty}\int_{\gamma-\mathrm{iT}}^{\gamma+iT}\hat{\pi}(\xi,z)e^{zt}dz \tag{2.56}$$

Herein $\hat{\pi}(\xi, z)$ is the extension of $\hat{\pi}(\xi, s)$ to the complex plane. The integration has to be performed on a line perpendicular to the real axis at the positive real value γ, which must be greater than the real part of any singularity of the complex function $\hat{\pi}(\xi, z)$. Usually this is a daunting task. It is simplified a lot if $\hat{\pi}(\xi, z)$ is a holomorphic function. In that case we can apply residue calculus to compute the line integral via a contour integral. To that purpose we close the line path from $\gamma - iT$ to $\gamma + iT$ by a half-circle in the space left to it ($\{z|\mathrm{Re}(z) \leq \gamma\}$) to obtain contour $\gamma'(T)$. In the limit $T \to \infty$ the half-circle contribution vanishes, i.e. $\lim_{\mathrm{T}\to\infty} \oint_{\gamma'(\mathrm{T})} \hat{\pi}(\xi, z)dz = \lim_{\mathrm{T}\to\infty} \int_{\gamma-\mathrm{iT}}^{\gamma+iT} \hat{\pi}(\xi, z)dz$. The residue formula states that the integral of $\hat{\pi}(\xi, z)$ along the contour is equal to the sum of residues at the singularities of $\hat{\pi}(\xi, z)$ enclosed by the contour times $2\pi i$. Thus, if all singularities of $\hat{\pi}(\xi, z)$ are to the left of γ, the inverse LAPLACE transform can be calculated as:

$$\pi(\xi, t) = \frac{1}{2\pi i} \lim_{\mathrm{T}\to\infty} \oint_{\gamma'(\mathrm{T})} \hat{\pi}(\xi, z)e^{zt}dz = \sum_{\mathrm{n}} \mathrm{Res}_{\hat{\pi}(\xi,\mathrm{z})e^{\mathrm{zt}}}(z_{\mathrm{n}}) \tag{2.57}$$

Since $\hat{\pi}_-(\xi, s)$ and $\hat{\pi}_+(\xi, s)$ only differ by the fact that ξ and ξ_0 are interchanged it is sufficient to carry out the inverse transform for $\hat{\pi}_+(\xi, s)$ and obtain $\pi_-(\xi, t)$ by substituting $\xi \leftrightarrow \xi_0$.

As a first step we reinsert $\kappa = \sqrt{s + \frac{\nu^2}{4}}$ and substitute $s = z - \frac{\nu^2}{4}$ in $\hat{\pi}_+(\xi, s)$ where z is a complex variable now:

$$\hat{\pi}_+(\xi, z) = \frac{\phi_0}{\sqrt{z}} \frac{\left(\sinh(\xi_0\sqrt{z}) + \frac{1}{\Omega}\sqrt{z}\cosh(\xi_0\sqrt{z})\right)}{\sinh(\sqrt{z}) + \frac{1}{\Omega}\sqrt{z}\cosh(\sqrt{z})} \times \\ \left(\sinh(\sqrt{z})\cosh(\xi\sqrt{z}) - \cosh(\sqrt{z})\sinh(\xi\sqrt{z})\right) \tag{2.58}$$

Later, instead of reinserting $z = s + \frac{\nu^2}{4}$, we will apply the standard LAPLACE-inversion rule $\mathcal{L}^{-1}[\hat{f}(s + c)] = e^{-ct}f(t)$ for $c = const.$

The fact that $\hat{\pi}_+(\xi, z)$ contains $\sqrt{z}$ which is non-holomorphic on the negative real branch recommends testing holomorphicity of the function. By TAYLOR-expanding the $\sinh(const \cdot \sqrt{z})$ and $\cosh(const \cdot \sqrt{z})$ functions one can show that $\hat{\pi}_+(\xi, z)$ can be written as a sum over purely integer powers z^n and thus is indeed a holomorphic (even entire) function. Its complex roots z_{n} are found by setting the denominator to zero, which yields:

$$\tanh(\sqrt{z_{\mathrm{n}}}) = -\frac{1}{\Omega}\sqrt{z_{\mathrm{n}}} \tag{2.59}$$

It can be shown that all z_{n} lie on the negative real axis and that there is no singularity at $z = 0$. Since $\hat{\pi}_+(\xi, z)$ can be written as $\hat{\pi}_+(\xi, z) = g(z)/h(z)$ with functions $g(z)$ and $h(z)$ that are holomorphic in the neighborhood of each z_{n}, we may calculate the residue of $\hat{\pi}_+(\xi, z)$ at z_{n} via the well-known formula $\mathrm{Res}_{\hat{\pi}_+(\xi,\mathrm{z})e^{\mathrm{zt}}}(z_{\mathrm{n}}) = g(z_{\mathrm{n}})/h'(z_{\mathrm{n}})$. Here we find, with $h(z) = \sinh(\sqrt{z}) + \frac{1}{\Omega}\sqrt{z}\cosh(\sqrt{z})$:

$$h'(z_{\mathrm{n}}) = \frac{1}{2\sqrt{z_{\mathrm{n}}}} \left[\left(1 + \frac{1}{\Omega} - \frac{z_{\mathrm{n}}}{\Omega^2}\right)\cosh(\sqrt{z_{\mathrm{n}}})\right] \tag{2.60}$$

In the next step we additionally substitute the square roots via $\sqrt{z_\mathrm{n}} \equiv \pm i\zeta_\mathrm{n}$ with $\zeta_\mathrm{n} \in \mathbb{R}^+$. Taking into account $\sinh(\pm ix) = \pm\sin(x)$ and $\cosh(\pm ix) = \cos(x)$ and cancelling multiplicative minus signs, the solution in the time domain as a sum of residues reads:

$$\begin{aligned}
\pi_+(\xi,\xi_0,t) &= \sum_\mathrm{n} \mathrm{Res}_{\hat{\pi}_+(\xi,\mathrm{z})e^{\mathrm{z}t}}(z_\mathrm{n}) \\
&= e^{-\frac{\nu^2}{4}t} \cdot 2\phi_0 \sum_\mathrm{n} e^{z_\mathrm{n}t} \frac{\sinh(\xi z_\mathrm{n}^{\frac{1}{2}}) + \frac{z_\mathrm{n}^{\frac{1}{2}}}{\Omega}\cosh(\xi z_\mathrm{n}^{\frac{1}{2}})}{\left(1+\frac{1}{\Omega}-\frac{z_\mathrm{n}}{\Omega^2}\right)\cosh(z_\mathrm{n}^{\frac{1}{2}})} \\
&\qquad \times \left(\sinh(z_\mathrm{n}^{\frac{1}{2}})\cosh(\xi_0 z_\mathrm{n}^{\frac{1}{2}}) - \cosh(z_\mathrm{n}^{\frac{1}{2}})\sinh(\xi_0 z_\mathrm{n}^{\frac{1}{2}})\right) \\
&= -\frac{2}{L} e^{-\frac{\nu^2}{4}t - \frac{\nu}{2}\xi_0} \cdot \sum_\mathrm{n} e^{-\zeta_\mathrm{n}^2 t} \frac{\sin(\xi\zeta_\mathrm{n}) + \frac{\zeta_\mathrm{n}}{\Omega}\cos(\xi\zeta_\mathrm{n})}{\left(1+\frac{1}{\Omega}+\frac{\zeta_\mathrm{n}^2}{\Omega^2}\right)\cos(\zeta_\mathrm{n})} \\
&\qquad \times \left(\sin(\zeta_\mathrm{n})\cos(\xi_0\zeta_\mathrm{n}) - \cos(\zeta_\mathrm{n})\sin(\xi_0\zeta_\mathrm{n})\right)
\end{aligned} \tag{2.61}$$

where the n-summation goes over the (positive) roots of the implicit equation

$$\tanh(\sqrt{z_\mathrm{n}}) = -\frac{1}{\Omega}\sqrt{z_\mathrm{n}} \quad \Leftrightarrow \quad \tan(\zeta_\mathrm{n}) = -\frac{1}{\Omega}\zeta_\mathrm{n} \tag{2.62}$$

with $\Omega = \frac{\nu}{2} + \frac{kL}{D} = \left(\frac{v}{2}+k\right)\frac{L}{D}$. Using the root equation (2.62) we can further simplify

$$\begin{aligned}
&\frac{\left(\sin(\zeta_\mathrm{n})\cos(\xi_0\zeta_\mathrm{n}) - \cos(\zeta_\mathrm{n})\sin(\xi_0\zeta_\mathrm{n})\right)}{\cos(\zeta_\mathrm{n})} = \\
&\qquad \tan(\zeta_\mathrm{n})\cos(\xi_0\zeta_\mathrm{n}) - \sin(\xi_0\zeta_\mathrm{n}) = -\left(\sin(\xi_0\zeta_\mathrm{n}) + \frac{\zeta_\mathrm{n}}{\Omega}\cos(\xi_0\zeta_\mathrm{n})\right)
\end{aligned} \tag{2.63}$$

and realize that the denominator of the summation terms in the time domain is completely symmetric in ξ and ξ_0. Hence, the solution in the time domain is invariant to interchanging ξ and ξ_0. After taking into account the integrating factor via $p(\xi,\xi_0,t) = e^{\frac{\nu}{2}\xi}\pi(\xi,\xi_0,t)$ and reverting dedimensionalization we can write the final solution for both sides of the spatial domain as:

$$p_\mathrm{RA}(x,x_0,t) \equiv$$

$$p(x,x_0,t) = \frac{2}{L} e^{\frac{v}{2D}(x-x_0) - \frac{v^2}{4D}t} \sum_\mathrm{n} e^{\frac{-\zeta_\mathrm{n}^2 Dt}{L^2}} \frac{F_\mathrm{n}(x)F_\mathrm{n}(x_0)}{\Omega^2+\Omega+\zeta_\mathrm{n}^2} \tag{2.64}$$

with

$$F_\mathrm{n}(x) \equiv \Omega\sin(\zeta_\mathrm{n}\frac{x-\sigma}{L}) + \zeta_\mathrm{n}\cos(\zeta_\mathrm{n}\frac{x-\sigma}{L}) \tag{2.65}$$

$$\Omega = \left(\frac{v}{2}+k\right)\frac{L}{D} \qquad \text{and} \tag{2.66}$$

$$\zeta_\mathrm{n} \quad \text{positive roots of} \qquad \tan(\zeta_\mathrm{n}) = -\frac{1}{\Omega}\zeta_\mathrm{n} \tag{2.67}$$

It can be easily verified that this function fulfills the imposed boundary conditions. Also the initial condition at $t = 0$ is recovered, which can be seen by expanding the delta function into the orthogonal functions $F_{\mathrm{n}}(x)$ and utilizing the straightforwardly proven orthogonality relation:

$$\int_{\sigma}^{a} F_{\mathrm{n}}(x)F_{\mathrm{m}}(x)dx = \begin{cases} \frac{L}{2}\left(\zeta_{\mathrm{n}}^2 + \Omega^2 + \Omega\right) & \text{for} \quad n = m \\ 0 & \text{for} \quad n \neq m \end{cases} \tag{2.68}$$

In the limit $v \to 0$ the solution reproduces the well-known solution for the case without drift, which can be found in [57, 14.3II, p. 360]. To verify this, set $\zeta_{\mathrm{n}} = \alpha_{\mathrm{n}} L$ in (2.64) and $k_1 = 1$, $k_2 = 0$, $h_1 = \frac{k}{D}$, $h_2 = 1$ in the reference formula.

Exemplary time evolution plots of $p_{\mathrm{RA}}(x, x_0, t)$ are shown in Figure 2.4 for different values of diffusion coefficient D, drift velocity v and intrinsic reaction rate k.

Green's function for 1D-diffusion with drift, Abs-Abs case

From (2.64) we can easily obtain the Green's function for 1D-diffusion with drift on a finite domain with two absorbing boundaries by taking the limit $k \to \infty$. The originally radiating boundary condition at $x = \sigma$ (BCr) then becomes

$$p(\sigma, t) = \frac{D\partial_{\mathrm{x}} p(x,t)\big|_{\mathrm{x}=\sigma} - vp(\sigma, t)}{k} \underset{k\to\infty}{\longrightarrow} 0 \quad . \tag{2.69}$$

First notice that because of $\Omega = \left(\frac{v}{2} + k\right)\frac{L}{D} \underset{k\to\infty}{\longrightarrow} 0$ the root equation (2.67) in the limit $k \to \infty$ reads:

$$\begin{aligned} &\tan(\zeta_{\mathrm{n}}) = -\frac{1}{\Omega}\zeta_{\mathrm{n}} \underset{k\to\infty}{\longrightarrow} 0 \\ &\Rightarrow \quad \zeta_{\mathrm{n}} = n\pi, \quad n \in \mathbb{N} \quad \text{for} \quad k \to \infty \end{aligned} \tag{2.70}$$

To obtain the limit of (2.64) we multiply the numerator and denominator of the summation terms by $1/k^2$. Because of

$$\frac{\Omega}{k} = \left(1 + \frac{v}{2k}\right)\frac{L}{D} \underset{k\to\infty}{\longrightarrow} \frac{L}{D} \tag{2.71}$$

we have

$$\frac{\Omega}{k}\sin\left(\zeta_{\mathrm{n}}\frac{x-\sigma}{L}\right) + \frac{\zeta_{\mathrm{n}}}{k}\cos\left(\zeta_{\mathrm{n}}\frac{x-\sigma}{L}\right) \underset{k\to\infty}{\longrightarrow} \frac{L}{D}\sin\left(\zeta_{\mathrm{n}}\frac{x-\sigma}{L}\right) \tag{2.72}$$

$$\frac{\Omega^2}{k^2} + \underbrace{\frac{\Omega}{k^2} + \frac{\zeta_{\mathrm{n}}^2}{k^2}}_{\to 0} \underset{k\to\infty}{\longrightarrow} \frac{L^2}{D^2} \tag{2.73}$$

and therefore:

$$\begin{aligned} &p_{\mathrm{AA}}(x, x_0, t) = p_{\mathrm{RA}}(x, x_0, t)\big|_{\mathrm{k}\to\infty} \\ &= \frac{2}{L} e^{\frac{v}{2D}(x-x_0) - \frac{v^2}{4D}t} \sum_{\mathrm{n}} e^{-\left(\frac{n\pi}{L^2}\right)^2 Dt} \sin\left(n\pi\frac{x-\sigma}{L}\right)\sin\left(n\pi\frac{x_0-\sigma}{L}\right) \end{aligned} \tag{2.74}$$

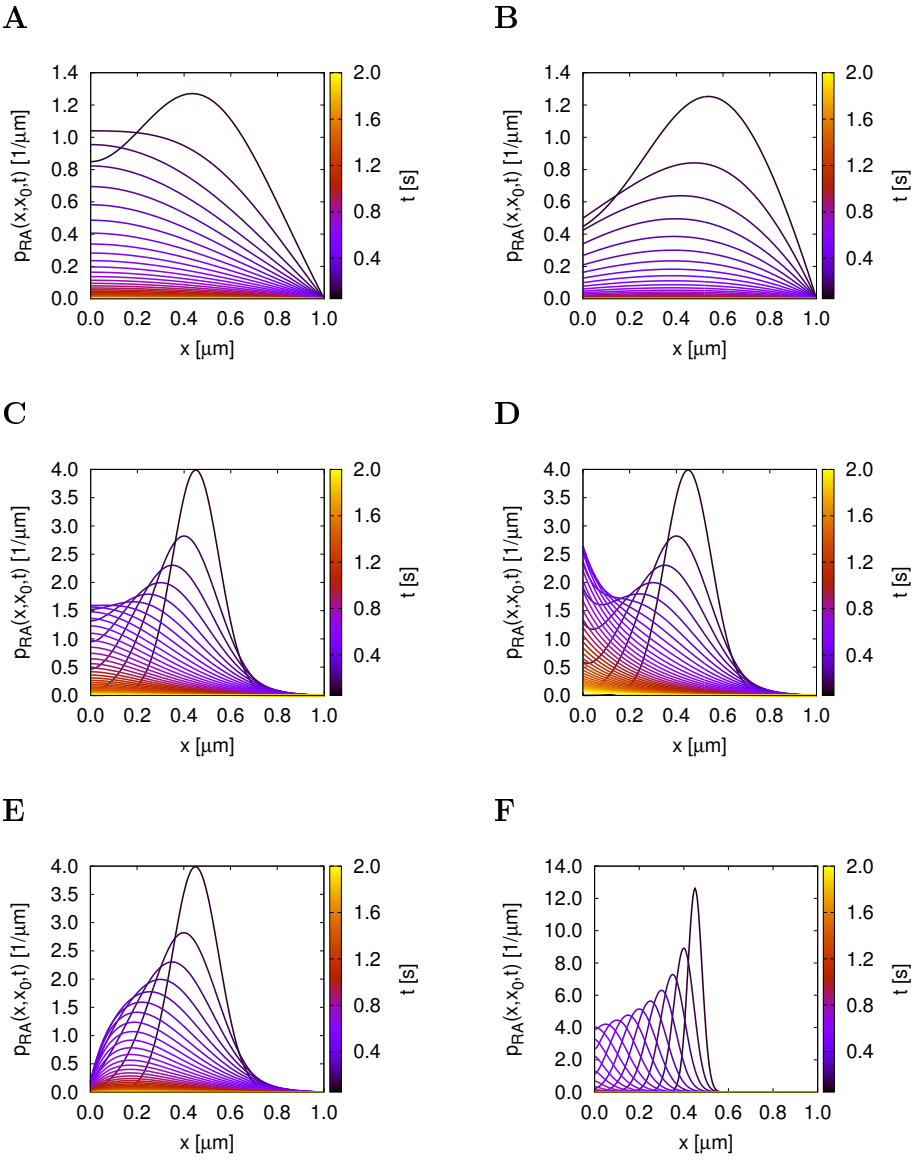

Figure 2.4: Green's function for the 1D diffusion-drift problem with radiating ($x = 0$) and absorbing ($x = 1$) boundary. (A) $D = 1.0$, $v = -1.0$, $k = |v|$; (B) $D = 1.0$, $v = +1.0$, $k = v$; (C) $D = 0.1$, $v = -1.0$, $k = |v|$; (D) $D = 0.1$, $v = -1.0$, $k = \frac{|v|}{2}$; (E) $D = 0.1$, $v = -1.0$, $k = 10|v|$; (F) $D = 0.01$, $v = -1.0$, $k = |v|$. Values are in $[\frac{\mu m^{(2)}}{s}]$. $x_0 = 0.5$ μm.

Green's function for 1D-diffusion with drift, Rad-Inf case

For completeness, we also mention here the Green's functions for the corresponding half-bounded problems. A solution for the case with only one radiating boundary at $x = 0$ and constant drift was already published by Lamm and Schulten [70] and reads:

$$\begin{aligned} & p_{\mathrm{R}\infty}(x,t|x_0,t=0) \\ &= \frac{1}{\sqrt{4\pi Dt}}\left(e^{-\frac{(x-x_0-vt)^2}{4Dt}} + e^{-\frac{vx_0}{D}}e^{-\frac{(x+x_0-vt)^2}{4Dt}}\right) \\ &\quad - \frac{v/2+k}{D}e^{\frac{vx_0}{D}}e^{\frac{k}{D}[(x+x_0)+(k+v)t]}\operatorname{erfc}\left(\frac{x+x_0}{\sqrt{4Dt}} + \frac{v/2+k}{D}\sqrt{Dt}\right) \end{aligned} \tag{2.75}$$

Green's function for 1D-diffusion with drift, Abs-Inf case

For the situation with only one absorbing boundary at $x = a \geq 0$ the Green's function for the 1D-diffusion-drift problem can be straightforwardly obtained via the method of images: Since any linear combination of the free solution $p_{\mathrm{free}}(x,t|x_0)$ fulfills the diffusion-drift equation, we can easily construct a solution $p_{\mathrm{A}\infty}(x,t|x_0)$ that will obey $p_{\mathrm{A}\infty}(a,t|x_0) = 0\ \forall t$ by subtracting from the free solution the antisymmetric solution for a particle starting from a distance $x_0 - a$ to the left of the boundary and with inverted drift $v \to -v$:

$$\begin{aligned} p_{\mathrm{A}\infty}(x,t|x_0) &= p_{\mathrm{free,v_+}}(x,t|x_0) - p_{\mathrm{free,v_-}}(x,t|a-(x_0-a)) \\ &= \frac{1}{\sqrt{4\pi Dt}}\left(e^{-\frac{1}{4Dt}[(x-x_0)-vt]^2} - e^{-\frac{1}{4Dt}[(x-2a+x_0)+vt]^2}\right) \end{aligned} \tag{2.76}$$

We verified that the above solution is equivalent to the solution for this problem calculated explicitly by applying the boundary conditions in Laplace space and inverting via the Residue formula, following the workflow described in section 2.3.2.

Survival probabilities

The survival probability is calculated by integration of the Green's function over the whole interval on which it is defined:

$$S(t) = \int_{\mathrm{a}}^{b} p(x,t|x_0)dx \tag{2.77}$$

For the half-bounded solutions $b = \infty$. The cumulative distribution function $P(x,t|x_0) = \int_{\mathrm{a}}^{x} p(x',t|x_0)dx'$ is needed besides $S(t)$ to sample positions at next-event times τ_ν. It is therefore convenient to first calculate $P(x,t|x_0)$ and then $S(t) = P(b,t|x_0)$ as a special case.

The Green's functions presented in this section all have the the form

$$p(x,t|x_0) = C_0 e^{\frac{v(x-x_0)}{2D}} \sum_{\mathrm{n}} c_{\mathrm{n}} f_{\mathrm{n}}(x) \tag{2.78}$$

where C_0 and c_n do not depend on x and $f_n(x)$ are either trigonometric or GAUSS functions. To calculate $P(x,t|x_0)$ the integration is most conveniently performed term-wise, i.e. by computing $\int_a^x e^{\frac{v(x'-x_0)}{2D}} f_n(x')dx'$ with the help of partial integration and reassembling the sum. Differentiation of the survival probability gives the propensity function $q(t) \equiv -\partial_t S(t)$. These are all straightforward calculations and therefore omitted here.

Boundary fluxes

With drift $v \neq 0$ the probability flux at position $x = x'$ is calculated from the Green's function $p(x,t|x_0)$ as follows:

$$q_{x'}(t) = -D\partial_x p(x,t|x_0)\big|_{x=x'} + vp(x',t|x_0) \tag{2.79}$$

Note that for an absorbing boundary at $x' = a$ we have $p(a,t|x_0) = 0$ and the drift-dependent term vanishes.

For a radiating boundary at $x' = \sigma$ with intrinsic reaction rate k it is more convenient to calculate the flux directly from

$$q_\sigma(t) = kp(\sigma,t|x_0) \tag{2.80}$$

which equals (2.79) with $x' = \sigma$ by construction of the problem.

For the Green's functions introduced in this chapter these expressions are again easily calculated and therefore not shown here. A complete collection of the surivival probabilities, cumulative distribution functions and boundary fluxes for all Green's functions presented in this chapter is available as part of the eGFRD technical documentation.

2.4 Finite cylindrical structures

Throughout this chapter until now we have assumed an infinite length for the cylindrical structures that particles interact with and are transported on. In many applications, however, we seek to study systems with finite 1D tracks, such as microtubules that canalize transported cargo to one of their ends preferentially, where it may unbind at a certain rate. Moreover, particles can behave differently after reaching the ends of microtubules by, for example, forming tip clusters [71, 72].

In order to include these features into eGFRD we introduce a new structure type, the disk structure, which is used to mark a special interaction site on a 1D cylindrical structure. A disk may be placed at the ends of a cylindrical structure of finite length to model reactive tip sites, or in any other place on the cylinder to model a point of interaction, e.g. a transcription-factor binding pocket on DNA. Within our framework a disk located at the end of a cylindrical structure is called a "cap", a disk located in between the ends a "sink". Particles on disks are immobilized. We allow particles on the cylinder to bind with a certain affinity both to disk structures and to particles already immobilized on caps. Unbinding from a cap returns the particle into the bulk, whereby the particle is moved in radial direction and placed at contact with

the disk. When unbinding from a sink, the particle transfers back to the cylindrical structure, i.e. becomes mobile again. Concerning implementation, particles bound to caps or sinks are treated as individual species, which enables the definition of different parameters and reactions for cylinder-bound and disk-bound species. This may be used, for example, to introduce cap-bound species representing particle clusters that "grow" by successively absorbing particles from the cylinder via a cascade of reactions, in order to model particle clustering at filament tips.

Since the problem of a diffusing 1D particle that interacts with a disk is mathematically equivalent to the problem of two interacting particles that move in 1D, here we may re-use the 1D Green's function with drift (2.64).

To model interactions with disks we introduce the following new domain types:

- *Cap Interaction* domain: a cylindrical domain that encloses an empty cap and a nearby cylinder-bound 1D particle. Next-event times are calculated from the 1D Green's function with drift and Rad-Abs boundary conditions.
- *Disk Surface Single* domain: a cylindrical domain that encloses a particle bound to a disk surface. The only possible next-events are unbinding reactions which are sampled from exponential distributions.
- *Mixed Pair 1D-Cap* domain: a cylindrical domain that encloses a cap with a bound particle and a nearby cylinder-bound 1D particle. Next-event times are calculated as for the *Cylindrical Surface Pair*, with drift and diffusion coefficient of the cap-bound partner set to zero.
- *Cylindrical Surface Sink* domain: a cylindrical domain that contains a sink and a proximate cylinder-bound particle. For this case we calculate the Green's function explicitly in section 2.5.

Sketches of these new domain types are shown in Figure 2.5.

Dynamical cylinders

While the aforementioned modifications allow for the inclusion of finite cylindrical structures into eGFRD, these are still assumed to be static. In reality, macromolecular filaments are dynamical structures which exhibit interchanging phases of growth and shrinkage. For microtubules, this mechanism is known as dynamic instability and has been extensively studied in both experiment [73, 74, 75, 76] and theory [77, 78, 79, 80].

We present a concept to include cylinders with length dynamics into eGFRD, with detailed description of required new domain and event types, in appendix section 2.C. The concept will be fully implemented in future work.

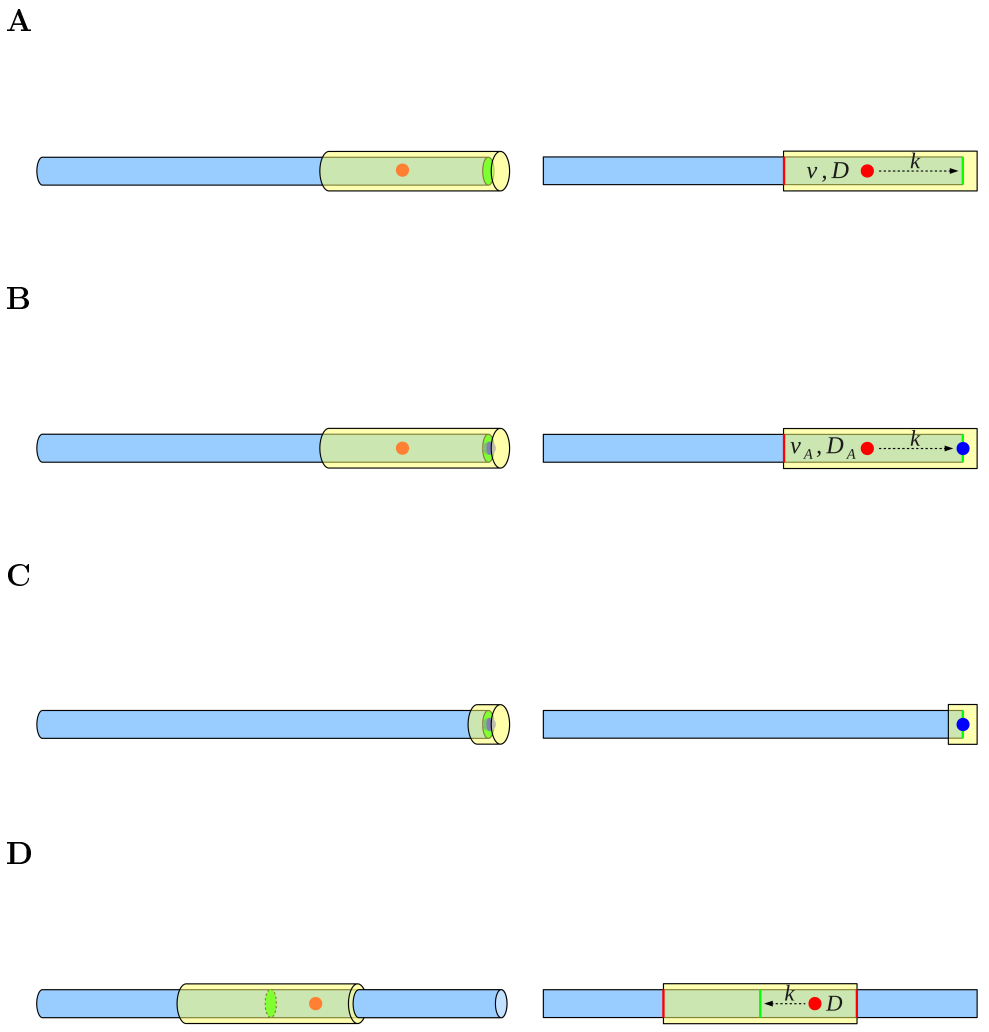

Figure 2.5: New protective domain types on finite 1D structures. The cylindrical surface is limited by a reactive cap at its right end (green colour). (A) *Cap Interaction* domain; (B) *Mixed Pair 1D-Cap* domain; (C) *Disk Surface Single* domain, here shown for a particle on a cap; (D) *Cylindrical Surface Sink* domain. Right panels show sections of 3D objects along the common cylinder axis. Absorbing boundaries are highlighted by red, radiative boundaries by green. Note that drift velocities (v, v_{A}, v_{B}) can be towards any cylinder end.

2.5 Green's function for 1D diffusion with a reactive sink

In transcription activation, transcription factors can perform a diffusive search for their binding site on the DNA [62, 63, 64]. To be able to model such and similar 1D random search processes in GFRD, we introduced sink structures that mark point-sites at which particles can react while diffusing over the cylindrical structure that they are bound to. In order to isolate this interaction from interactions with other particles on the cylinder we further introduced new domains (*Cylindrical Surface Sink* domains) that only contain a sink and the closeby particle. Exits from these domains then can happen via two different events: either the particle hits the (absorbing) boundaries of the domain, or it binds to the sink. For the case without particle drift, we present here the Green's function for this problem. One complication here is that the particle may diffuse over the sink without being absorbed. It is, however, possible to incorporate this feature into the mathematical derivation by imposing the correct probability flux balance at the sink position.

Assuming that the particle, starting from initial position $x = x_0$, can attach to the sink located at position x_s with an intrinsic rate k, the diffusive dynamics of the particle may be described via the modified diffusion equation:

$$\partial_t p(x,t|x_0) = D\nabla^2 p(x,t|x_0) - k\delta(x-x_s)p(x,t|x_0) \tag{2.81}$$

with absorbing boundaries at $x = a$ and $x = b > x_s > a$

$$p(a,t|x_0) = 0\ , \qquad p(b,t|x_0) = 0 \tag{2.82}$$

and initial condition

$$p(x,t=0|x_0) = \delta(x-x_0) \quad . \tag{2.83}$$

As with the 1D-Rad-Abs Green's function calculated in section 2.3.2, this problem may be solved separately for the subintervals of $[a,b]$ divided by the delta peaks, imposing continuity of $p(x,t|x_0)$ and discontinuity of its derivative at the junction points. Here it is convenient to consider the intervals left and right to the sink and to account for the initial condition directly by an adequate ansatz for the part that contains the starting point x_0. Continuity-discontinuity relations then only have to be imposed at x_s.

Let us denote the solution on interval $[a, x_s]$ by $p_-(x,t|x_0)$ and the solution on $[x_s, b]$ by $p_+(x,t|x_0)$. By integrating (2.81) over an ϵ-interval around the sink and taking the limit $\epsilon \to 0$ we obtain the discontinuity condition for the probability flux at $x = x_s$:

$$\partial_x p_-(x,t|x_0)\big|_{x=x_s} - \partial_x p_+(x,t|x_0)\big|_{x=x_s} = -\frac{k}{D} p_-(x_s,t|x_0) \tag{2.84}$$

This equation simply states that the flux from/towards the left of the sink equals the flux from/towards the region right of it minus the reactive flux through the sink. Moreover, continuity requires:

$$p_-(x_s,t|x_0) = p_+(x_s,t|x_0) \tag{2.85}$$

Again this problem is most conveniently solved in LAPLACE space. The homogenous version of the LAPLACE-transformed PDE reads:

$$s\hat{p}(x,s|x_0) = D\nabla^2\hat{p}(x,s|x_0) \tag{2.86}$$

Let us without loss of generality assume $x_0 \in [x_s, b]$ and that the sink is located at $x = x_s = 0$, implying $a = -|a| < 0$. Then we can make the following ansatz in LAPLACE space ($q \equiv \sqrt{\frac{s}{D}}$):

$$\begin{aligned}
\hat{p}_-(x,s|x_0) &= A_- \sinh(qx) + B_- \cosh(qx), && x < 0 \\
\hat{p}_+(x,s|x_0) &= A_+ \sinh(qx) + B_+ \cosh(qx) + \underbrace{\frac{1}{2Dq} e^{-q|x-x_0|}}_{\hat{p}_{\mathrm{free}}(x,s|x_0)}, && x > 0
\end{aligned} \tag{2.87}$$

Function $\hat{p}_+(x,s|x_0)$ contains the (LAPLACE-transformed) free solution for a point particle starting from $x = x_0$ and thus fulfills the initial condition by construction.

The coefficients $A_\pm$ and $B_\pm$ are calculated by applying the boundary and continuity-discontinuity conditions. Subsequently, the solution can be transformed back into the time-domain via the residue formula. This procedure is precisely the same as in 2.3.2 and therefore omitted here. The final solution reads, with $L \equiv b - a = b + |a|$,

$$p_-(x,t|x_0) = -2D \sum_{n=1}^{\infty} e^{-D\zeta_n^2 t} \sin\left(\zeta_n(|a|+x)\right) \frac{\zeta_n \sin\left(\zeta_n(b-x_0)\right)}{\Xi_n} \tag{2.88}$$

$$\begin{aligned}
p_+(x,t|x_0) = -2D \sum_{n=1}^{\infty} e^{-D\zeta_n^2 t} \sin\left(\zeta_n(b-\hat{x})\right) \times \\
\frac{D\zeta_n \sin\left(\zeta_n(|a|+\check{x})\right) + k \sin(\zeta_n(|a|) \sin(\zeta_n \check{x})}{\Xi_n}
\end{aligned} \tag{2.89}$$

with $\hat{x} \equiv \max(x, x_0)$, $\check{x} \equiv \min(x, x_0)$ and a common denominator:

$$\begin{aligned}
\Xi_n = D\left[L\zeta_n \cos(\zeta_n L) + \sin(\zeta_n L)\right] \\
+ k\left[b\cos(\zeta_n b)\sin(\zeta_n|a|) + |a|\cos(\zeta_n|a|)\sin(\zeta_n b)\right]
\end{aligned} \tag{2.90}$$

The numbers ζ_n are all real and positive and the roots of the equation

$$D\zeta_n \sin\left(\zeta_n L\right) + k \sin\left(\zeta_n|a|\right) \sin\left(\zeta_n b\right) = 0 \tag{2.91}$$

which, with the help of trigonometric relations and setting $\Delta L \equiv b - |a|$, may be written in the more convenient form:

$$D\zeta_n \sin\left(\zeta_n L\right) = \frac{k}{2}\left[\cos\left(\zeta_n L\right) - \cos\left(\zeta_n \Delta L\right)\right] \tag{2.92}$$

The necessity of interchanging x and x_0 in (2.89) when the sign of $(x - x_0)$ changes arises from the presence of $|x - x_0|$ in the ansatz for $p_+(x,s|x_0)$.

The survival probability for the whole domain $[a, b]$ is given by

$$S(t) = \int_{\mathrm{a}}^{x_\mathrm{s}=0} p_-(x, t|x_0)dt + \int_{x_\mathrm{s}=0}^{b} p_+(x, t|x_0)dt \tag{2.93}$$

and easily obtained by simple integration.

The next-event time τ_ν for the associated *Cylindrical Surface Sink* domain is sampled from $1 - S(t)$, as usual. The next-event type, i.e. whether the particle exits the domain by being absorbed at the sink or at one of the boundaries, is determined by comparing the probability fluxes through these exit channels at τ_ν. These are most conveniently calculated via:

$$\begin{aligned} q_\mathrm{s} &= kp_-(x_\mathrm{s}, \tau_\nu|x_0) = kp_+(x_\mathrm{s}, \tau_\nu|x_0) \\ q_\mathrm{a} &= -D\partial_\mathrm{x} p_-(x, \tau_\nu|x_0)\big|_{\mathrm{x=a}} \\ q_\mathrm{b} &= -D\partial_\mathrm{x} p_+(x, \tau_\nu|x_0)\big|_{\mathrm{x=b}} \end{aligned} \tag{2.94}$$

2.6 Acknowledgements

The calculations for the 1D Green's function with sink presented in section 2.5 were carried out together with J. PAIJMANS as part of his master's project. The author also thanks him for performing additional tests of the other 1D Green's functions presented in this chapter and for fruitful discussions.

J. PAIJMANS further is credited with the elaboration of the two-step Brownian Dynamics scheme sketched in section 2.1.4.

The authors thanks A. HOFFMANN for critical reading of this chapter.

2.A Appendix: Detailed coordinate-separation transform

The SMOLUCHOWSKI equation for the probability density function $p = p(\mathbf{r}_\mathrm{A}, \mathbf{r}_\mathrm{B}, t|\mathbf{r}_\mathrm{A0}, \mathbf{r}_\mathrm{B0}, t_0)$ of two diffusing particles A and B that can interact via a force $\mathbf{F}$ depending on their distance and move with different diffusion constants D_A and D_B is given by [68, 39]

$$\partial_\mathrm{t} p = \left[D_\mathrm{A}\nabla_\mathrm{A}^2 + D_\mathrm{B}\nabla_\mathrm{B}^2 + D_\mathrm{A}\nabla_\mathrm{A}\cdot\varphi\mathbf{F}(\mathbf{r}) - D_\mathrm{B}\nabla_\mathrm{B}\cdot\varphi\mathbf{F}(\mathbf{r})\right] p \tag{S2.1}$$

where $\mathbf{r}$ denotes the interparticle vector:

$$\mathbf{r} = \mathbf{r}_\mathrm{B} - \mathbf{r}_\mathrm{A} \tag{S2.2}$$

We define the weighted center-of-mass vector $\mathbf{R}$ as follows:

$$\mathbf{R} = \gamma\mathbf{r}_\mathrm{A} + \delta\mathbf{r}_\mathrm{B} \tag{S2.3}$$

Equations (S2.2) and (S2.3) define new coordinates $\mathbf{r}(\mathbf{r}_\mathrm{A}, \mathbf{r}_\mathrm{B})$ and $\mathbf{R}(\mathbf{r}_\mathrm{A}, \mathbf{r}_\mathrm{B})$. Notice that this is not a coordinate transformation in the strict sense, as in general $\mathbf{r}$ and $\mathbf{R}$ will not be orthogonal.

Moreover, we define the operators:

$$\nabla_\mathrm{r} \equiv \frac{\partial}{\partial\mathbf{r}} = \begin{pmatrix}\partial_{\mathrm{r}_1}\\ \partial_{\mathrm{r}_2}\\ \partial_{\mathrm{r}_3}\end{pmatrix}, \qquad \nabla_\mathrm{R} \equiv \frac{\partial}{\partial\mathbf{R}} = \begin{pmatrix}\partial_{\mathrm{R}_1}\\ \partial_{\mathrm{R}_2}\\ \partial_{\mathrm{R}_3}\end{pmatrix}. \tag{S2.4}$$

If the differential operator on the right side of (S2.1) equation can be written as a sum of ∇_r^2, ∇_r, ∇_R^2 and ∇_R, we may separate (S2.1) into two independent PDEs for $\mathbf{r}$ and $\mathbf{R}$ by a product ansatz for p. In the following we will calculate different options for the choice of coefficients γ and δ with which the above objective is reached.

Rewriting ∇_A and ∇_B

First we rewrite ∇_A and ∇_B in terms of ∇_r and ∇_R. Let $r_{\mathrm{A,i}} = r_{\mathrm{A,i}}(\mathbf{r}, \mathbf{R})$ denote the i-th component of the vector $\mathbf{r}_\mathrm{A}$, and r_j, R_k components of $\mathbf{r}$ and $\mathbf{R}$ respectively. Then the derivative of p with respect to $r_{\mathrm{A,i}}$ is

$$\begin{aligned}\frac{\partial p}{\partial r_{\mathrm{A,i}}} &= \sum_\mathrm{j}\frac{\partial p}{\partial r_\mathrm{j}}\frac{\partial r_\mathrm{j}}{\partial r_{\mathrm{A,i}}} + \sum_\mathrm{k}\frac{\partial p}{\partial R_\mathrm{k}}\frac{\partial R_\mathrm{k}}{\partial r_{\mathrm{A,i}}}\\ &= \sum_\mathrm{j}(-1)\delta_\mathrm{ij}\frac{\partial p}{\partial r_\mathrm{j}} + \sum_\mathrm{k}\gamma\delta_\mathrm{ik}\frac{\partial p}{\partial R_\mathrm{k}}\\ &= \gamma\frac{\partial p}{\partial R_\mathrm{i}} - \frac{\partial p}{\partial r_\mathrm{i}} = \left(\gamma\frac{\partial}{\partial\mathbf{R}} - \frac{\partial}{\partial\mathbf{r}}\right)_\mathrm{i} p\end{aligned} \tag{S2.5}$$

because r_i and R_i only depend on the component $r_{\mathrm{A,i}}$ with the same index i. Since this holds for every i, we have:

$$\nabla_\mathrm{A} = \gamma\nabla_\mathrm{R} - \nabla_\mathrm{r} \tag{S2.6}$$

Analogously, one obtains:

$$\nabla_{\mathrm{B}} = \delta\nabla_{\mathrm{R}} + \nabla_{\mathrm{r}} \tag{S2.7}$$

From this it follows that:

$$\begin{aligned}\nabla_{\mathrm{A}}^2 &= \gamma^2\nabla_{\mathrm{R}}^2 + \nabla_{\mathrm{r}}^2 - 2\gamma\nabla_{\mathrm{r}}\nabla_{\mathrm{R}} \\ \nabla_{\mathrm{B}}^2 &= \delta^2\nabla_{\mathrm{R}}^2 + \nabla_{\mathrm{r}}^2 + 2\delta\nabla_{\mathrm{r}}\nabla_{\mathrm{R}}\end{aligned} \tag{S2.8}$$

Here we use $\nabla_{\mathrm{r}}\nabla_{\mathrm{R}} = \nabla_{\mathrm{R}}\nabla_{\mathrm{r}}$, assuming the 2nd derivative of p with respect to any of its variables to be a continuous function in $\mathbb{R}^3$. The partial derivatives then may be interchanged by the theorem of CLAIRAUT & SCHWARZ.

Now that we have expressed ∇_{A} and ∇_{B} in terms of ∇_{r} and ∇_{R}, we can also rewrite the right side of the SMOLUCHOWSKI equation. First, for the case $\varphi = 0$, we get:

$$\begin{aligned}D_{\mathrm{A}}\nabla_{\mathrm{A}}^2 + D_{\mathrm{B}}\nabla_{\mathrm{B}}^2 = &\left(D_{\mathrm{A}} + D_{\mathrm{B}}\right)\nabla_{\mathrm{r}}^2 \\ &+ \left(\gamma^2 D_{\mathrm{A}} + \delta^2 D_{\mathrm{B}}\right)\nabla_{\mathrm{R}}^2 \\ &+ 2\left(\delta D_{\mathrm{B}} - \gamma D_{\mathrm{A}}\right)\nabla_{\mathrm{r}}\nabla_{\mathrm{R}}\end{aligned} \tag{S2.9}$$

Rewriting the force term separately yields:

$$\left(D_{\mathrm{A}}\nabla_{\mathrm{A}} - D_{\mathrm{B}}\nabla_{\mathrm{B}}\right)\cdot\varphi\mathbf{F} = \left[\left(\gamma D_{\mathrm{A}} - \delta D_{\mathrm{B}}\right)\nabla_{\mathrm{R}} - \left(D_{\mathrm{A}} + D_{\mathrm{B}}\right)\nabla_{\mathrm{r}}\right]\cdot\varphi\mathbf{F} \tag{S2.10}$$

To get rid of the mixed term containing $\nabla_{\mathrm{r}}\nabla_{\mathrm{R}}$ we can make any choice for γ and δ that fulfills

$$\delta = \frac{D_{\mathrm{A}}}{D_{\mathrm{B}}}\gamma \quad . \tag{S2.11}$$

Note that with this choice the force contribution (S2.10) only depends on the derivative with respect to the interparticle vector (∇_{r}).

Coefficient choice as in original GFRD

One possible choice for γ and δ, which is the the same as in the original version of GFRD, is the following:

$$\gamma \equiv \sqrt{\frac{D_{\mathrm{B}}}{D_{\mathrm{A}}}}, \qquad \delta \equiv \sqrt{\frac{D_{\mathrm{A}}}{D_{\mathrm{B}}}} \tag{S2.12}$$

This yields

$$\mathbf{R} = \sqrt{\frac{D_{\mathrm{B}}}{D_{\mathrm{A}}}}\cdot\mathbf{r}_{\mathrm{A}} + \sqrt{\frac{D_{\mathrm{A}}}{D_{\mathrm{B}}}}\cdot\mathbf{r}_{\mathrm{B}} \tag{S2.13}$$

and

$$D_{\mathrm{A}}\nabla_{\mathrm{A}}^2 + D_{\mathrm{B}}\nabla_{\mathrm{B}}^2 = \left(D_{\mathrm{A}} + D_{\mathrm{B}}\right)\left(\nabla_{\mathrm{r}}^2 + \nabla_{\mathrm{R}}^2\right) \quad . \tag{S2.14}$$

The same prefactor also appears in the force term

$$(D_\mathrm{A}\nabla_\mathrm{A} - D_\mathrm{B}\nabla_\mathrm{B}) \cdot \varphi\mathbf{F} = -\left(D_\mathrm{A} + D_\mathrm{B}\right)\nabla_\mathrm{r} \cdot \varphi\mathbf{F} \tag{S2.15}$$

so that equation (S2.1) simplifies as follows:

$$\partial_\mathrm{t} p = \left(D_\mathrm{A} + D_\mathrm{B}\right)\left(\nabla_\mathrm{r}^2 + \nabla_\mathrm{R}^2 - \nabla_\mathrm{r} \cdot \varphi\mathbf{F}\right) p \tag{S2.16}$$

Here we can separate the equation by the product ansatz $p(\mathbf{r}, \mathbf{R}, t|\mathbf{r}_0, \mathbf{R}_0, t_0) = p_\mathrm{r}(\mathbf{r}, t|\mathbf{r}_0, t_0)p_\mathrm{R}(\mathbf{R}, t|\mathbf{R}_0, t_0)$ into two equations describing two independent diffusion processes (here with the same diffusion constant $D_\mathrm{A} + D_\mathrm{B}$):

$$\partial_\mathrm{t} p_\mathrm{r} = \underbrace{\left(D_\mathrm{A} + D_\mathrm{B}\right)}_{D_\mathrm{r}}\left(\nabla_\mathrm{r}^2 - \nabla_\mathrm{r} \cdot \varphi\mathbf{F}\right) p_\mathrm{r} \tag{S2.17}$$

$$\partial_\mathrm{t} p_\mathrm{R} = \underbrace{\left(D_\mathrm{A} + D_\mathrm{B}\right)}_{D_\mathrm{R}}\nabla_\mathrm{R}^2\, p_\mathrm{R} \tag{S2.18}$$

Note that, as expected, the force contribution is present only in the equation for the interparticle vector $\mathbf{r}$.

Coefficient choice as in eGFRD

The following slightly different choice for γ and δ

$$\gamma \equiv \frac{D_\mathrm{B}}{D_\mathrm{A} + D_\mathrm{B}}, \qquad \delta \equiv \frac{D_\mathrm{A}}{D_\mathrm{A} + D_\mathrm{B}} \tag{S2.19}$$

leads to:

$$\begin{aligned} D_\mathrm{A}\nabla_\mathrm{A}^2 + D_\mathrm{B}\nabla_\mathrm{B}^2 &= \left[\frac{D_\mathrm{A}D_\mathrm{B}^2 + D_\mathrm{B}D_\mathrm{A}^2}{\left(D_\mathrm{A} + D_\mathrm{B}\right)^2}\right]\nabla_\mathrm{R}^2 + \left(D_\mathrm{A} + D_\mathrm{B}\right)\nabla_\mathrm{r}^2 \\ &= \left(\frac{D_\mathrm{A}D_\mathrm{B}}{D_\mathrm{A} + D_\mathrm{B}}\right)\nabla_\mathrm{R}^2 + \left(D_\mathrm{A} + D_\mathrm{B}\right)\nabla_\mathrm{r}^2 \end{aligned} \tag{S2.20}$$

Everything that has been said for the previous choice of γ and δ also applies to this case, except for the fact that $\mathbf{R}(\mathbf{r}_\mathrm{A}, \mathbf{r}_\mathrm{B})$ now has a different weighting as before:

$$\mathbf{R} = \frac{D_\mathrm{B}\mathbf{r}_\mathrm{A} + D_\mathrm{A}\mathbf{r}_\mathrm{B}}{D_\mathrm{A} + D_\mathrm{B}} \tag{S2.21}$$

Therefore, also the diffusion constant D_R now is different from D_r. Using the same separation ansatz as before we arrive at:

$$\begin{aligned} \partial_\mathrm{t} p_\mathrm{r} &= \left(D_\mathrm{A} + D_\mathrm{B}\right)\left(\nabla_\mathrm{r}^2 - \nabla_\mathrm{r} \cdot \varphi\mathbf{F}\right) p_\mathrm{r} \\ \partial_\mathrm{t} p_\mathrm{R} &= \left(\frac{D_\mathrm{A}D_\mathrm{B}}{D_\mathrm{A} + D_\mathrm{B}}\right)\nabla_\mathrm{R}^2\, p_\mathrm{R} \end{aligned} \tag{S2.22}$$

Prescribing an arbitrary centre-of-mass diffusion constant

For completeness we briefly describe how to choose γ and δ in order to ensure that D_R is equal to an arbitrary prescribed diffusion constant D_C, if desired. D_C might be, for example, the diffusion constant of the product of the $A + B \to C$ reaction.

In this case γ and δ have to obey the two equations:

$$D_\mathrm{R} = \gamma^2 D_\mathrm{A} + \delta^2 D_\mathrm{B}, \qquad \delta = \frac{D_\mathrm{A}}{D_\mathrm{B}}\gamma \tag{S2.23}$$

Combining these we obtain:

$$D_\mathrm{R} = \gamma^2 D_\mathrm{A}\left[1 + \frac{D_\mathrm{A}}{D_\mathrm{B}}\right] \stackrel{!}{=} D_\mathrm{C} \tag{S2.24}$$

Since all involved quantities are positive real numbers, it follows that:

$$\gamma = \sqrt[+]{\frac{D_\mathrm{C}}{D_\mathrm{A}\left(1 + \frac{D_\mathrm{A}}{D_\mathrm{B}}\right)}} \qquad \Rightarrow \qquad \delta = \frac{D_\mathrm{A}}{D_\mathrm{B}}\gamma = \sqrt[+]{\frac{D_\mathrm{C}}{D_\mathrm{B}\left(1 + \frac{D_\mathrm{B}}{D_\mathrm{A}}\right)}} \tag{S2.25}$$

This combination of γ and δ indeed leads to:

$$\begin{aligned} D_\mathrm{R} = D_\mathrm{A}\gamma^2 + D_\mathrm{B}\delta^2 &= \frac{D_\mathrm{C}}{1 + \frac{D_\mathrm{A}}{D_\mathrm{B}}} + \frac{D_\mathrm{C}}{1 + \frac{D_\mathrm{B}}{D_\mathrm{A}}} \\ &= \frac{D_\mathrm{B}D_\mathrm{C} + D_\mathrm{A}D_\mathrm{C}}{D_\mathrm{A} + D_\mathrm{B}} = D_\mathrm{C} \end{aligned} \tag{S2.26}$$

Since γ and δ are always real and positive, except for the (usually uninteresting) cases $D_\mathrm{A} = 0$ or $D_\mathrm{B} = 0$, one can indeed always find a coordinate transform for which D_R matches an arbitrary diffusion coefficient, while $D_\mathrm{r} = D_\mathrm{A} + D_\mathrm{B}$.

2.B Appendix: Domains in eGFRD

2.B.1 Domain classtree

Figure S2.1 shows the complete class tree of the domain classes employed by the new version of eGFRD that features transport and reactions in 1D and 2D, including the new domain types introduced in chapters 2 and 3.

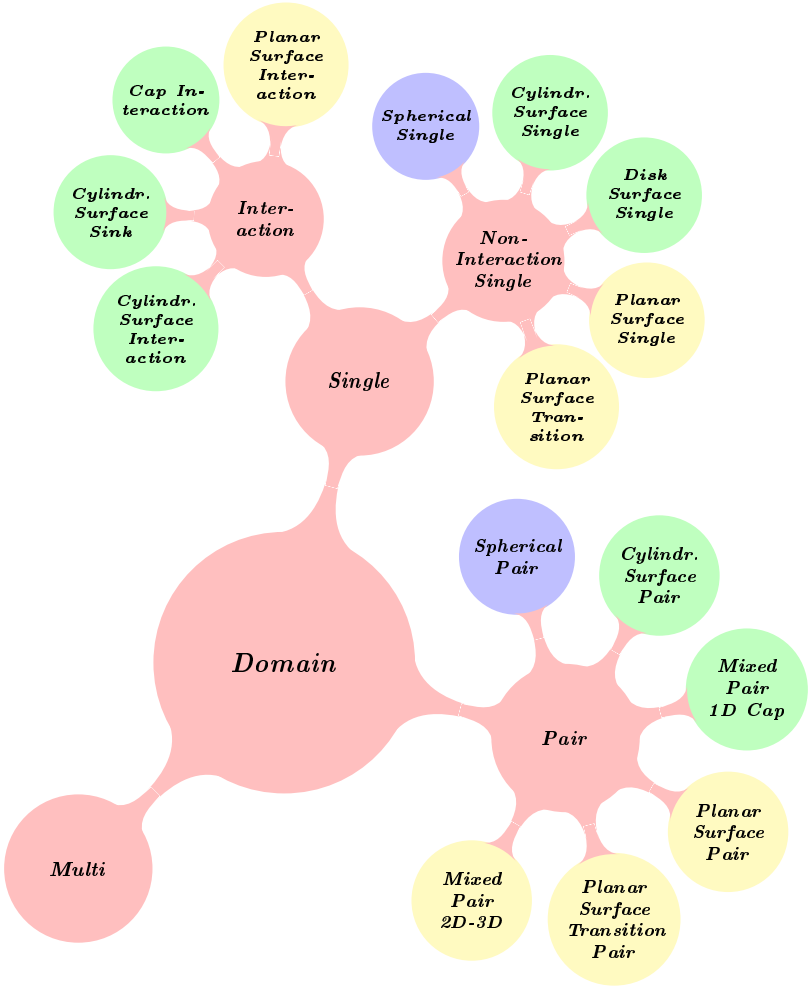

Figure S2.1: Domain class tree. Blue circles are domain types used to simulate reactions and diffusion purely in 3D. Domain types employed for interactions with and reaction-diffusion on 1D rods are in green, whereas yellow marks domain types used for 2D interactions and reaction-diffusion. Red color marks abstract superclasses.

2.B.2 Domain making in eGFRD

Principal domain making strategy

The governing principle in constructing and sizing of domains in eGFRD is to minimize the computational cost associated with this process. Domain making consists of the following successive steps:

1. Determine which type of domain to construct.
2. Determine the available space for the domain (i.e. its shell).
3. Construct the domain with an optimally sized shell.
4. Draw the next-event time and type for the newly constructed domain.
5. Re-schedule the domain in the central scheduler.

While the cost of the first and last step is roughly the same for all domains, it may vary among different domain types for the other steps. In general, cylindrical domains are more expensive to construct than spherical domains because of the increased computational effort for scaling up cylinders within a constellation of other cylinders and spheres. Similarly, *Pair* domains are more expensive than *Single* domains because they require an additional coordinate transform and employ Green's functions which are mathematically more complex.

It is unfeasible to foresee all possible constellations that may occur during eGFRD simulations as required for a real quantitative optimization of the domain making rules. The strategy in defining a unique set of functional rules therefore is to minimize the likelihood of situations that lead to the waste of computational cost, such as repeated reconstruction of domains and construction of expensive domains when it is not strictly advantageous.

Social upsizing prevents premature and mutual bursting

Particular care must be put into determining the optimal size of the domain. In principle we want to construct domains as big as possible because their next-event time directly correlates with their size. However, when we size up a large domain such that it will protrude into the direct vicinity of a very small domain, the latter will most likely be updated long before the next event time of the freshly constructed large domain. This may induce premature bursting of the large domain which then has to be reconstructed from an almost identical situation as before after insignificant time progress, wasting the initial investment of domain making cost. Therefore domains should not be sized up to the maximal available space in any given situation but in a "social" manner, i.e. leave some space for their neighbour domains to avoid very small domains in their own direct vicinity.

In particular it is important to prevent repeated mutual bursting of two newly constructed adjacent *Single* domains, which may even result in an infinite cycle of domain (re)construction and bursting. Repeated mutual bursting can occur when two particles are at a small distance, yet sufficiently far away to enable the construction

of two *Single* domains, and the formation of a *Pair* is disallowed for other reasons (e.g. presence of obstacles). Since domains are sized up in a successive order, using the maximally available space for the first *Single* domain (A) would result in a very small size of the second (B), causing immediate update of B with negligible particle displacement. This in turn would force bursting of domain A in order to size up the B domain again, which would restart the whole process all over from B. This example demonstrates that maximizing domain size is not the same as optimizing it.

A minimal Single domain size controls switching to Brownian Dynamics

In section 2.1.4 we explain why it is necessary to switch from eGFRD to Brownian Dynamics when propagating particles under crowded conditions. Yet, it is not a priori clear when this switch should be performed. In principle it should be done when the computational cost for *Single* construction divided by the maximal displacement within the domain, which is correlated to domain size, becomes larger than the cost to sample a trajectory covering the same distance with Brownian Dynamics. Since in GFRD *Single* construction cost is variable, it is hard to devise a general rule. Notwithstanding, it is clear that a minimal *Single* has to be defined for proper working of the algorithm. We decided to make this a simulation parameter, the details of which will be described in more detail in the following text.

Summarized domain making objectives

The abovementioned compiles into the following set of simple objectives for efficient domain making rules:

- Construct *Pair* and *Interaction* domains only when interaction is likely, i.e. when particles are close to other particles or reactive surfaces.
- Construct domains socially, i.e. reserve some space for neighbouring domains in order to prevent premature or mutual bursting.
- Construct *Multi* domains (i.e. fall back into Brownian dynamics) if construction of a minimal-size *Single* is impossible.

In order to transform these rules into an applicable algorithm we introduced two length factors which will determine when to start constructing *Pairs* or *Interactions* and when to go into the Brownian dynamics mode during runtime.

Two length factors balance the domain making behaviour

Let us define the following two dimensionless constants:

- $\beta \equiv$ "single-shell factor"
- $\mu \equiv$ "multi-shell factor"

For a given particle radius R these two factors define the half-size βR of the minimal *Single* shell and the radius μR of the (always spherical) *Multi* shell of that

particle, respectively. Note that the minimal *Single* shell can be either a sphere or a cylinder, depending on whether the particle is a 3D, 2D or 1D species. The requirements $\beta \geq 1$ and $\mu \geq 1$ are obvious. Since a *Multi* shell shall never be constructed when there is enough space for a minimal *Single* shell, we also require $\beta > \mu$.

Let R_0 be the radius of a particle P_0 for which we want to construct a domain, R_1 the radius of its nearest neighbour particle P_1 and $\sigma \equiv R_0 + R_1$. Then, based on β and μ, we define the following lengths for P_0:

- the "reaction horizon" $\equiv \beta R_0$
- the "multi horizon" $\equiv \mu R_0$

and, as specializations of the above:

- the "pair horizon" $\equiv \beta\sigma$
- the "surface horizon" $\equiv$ "reaction horizon" $= \beta R_0$
- the "burst horizon" $\equiv$ "burst radius" $\equiv$ "reaction horizon" $= \beta R_0$
- the "multi-partner horizon" $\equiv \mu\sigma$

Different naming highlights different purpose for these of the above quantities that are equal to each other.

The reaction horizon is used to determine when a *Pair* or *Interaction* domain should be constructed instead of a *Single* domain. The multi horizon defines when *Single* construction should be dropped in favor of *Multi* construction. The pair horizon and surface horizon are specifications of the reaction horizon for *Pair* and *Interaction Single* formation: while an *Interaction* is formed when a surface is within the reaction horizon, a *Pair* construction is attempted only when the reaction horizons of the two involved particles overlap, i.e. when the center of mass of P_1 is within the pair horizon of P_0. Similarly, the algorithm will switch into Brownian Dynamics mode when a surface is within the multi horizon of P_0 or when the multi horizons of P_0 and P_1 overlap, i.e. when P_1 is within the multi-partner horizon of P_0.

The burst horizon defines the volume within which a particle will burst neighbouring domains. Since the objective of bursting is to generate space for at least a minimal *Single* shell the burst horizon should be at least as big as the reaction horizon. Since there is no evident necessity to make it bigger than the reaction horizon, we conveniently set these lengths to be equal.

Practically β and μ can be used to tune the overall behaviour and performance of domain making: Increasing μ will prompt the simulation to switch to Brownian Dynamics earlier. Whether this is advantageous or not depends the crossover radius at which construction of small *Single* domains yields a smaller average simulation time advance per computational cost unit than the construction of *Multi* domains. In a similar way, whether a larger or smaller β is favorable depends on the average likelihood of reactions in the system. Since the latter depend on the parameters, there is no obviously optimal choice for β and μ. We find that $\beta \in [2, 3]$ and $\mu \in [\sqrt{3}, 2]$ gives reasonable performance.

Domain making algorithm

We can now compile the abovementioned postulations and definitions into a well-defined algorithm for domain making. Let us imagine a particle which just exited from whatever domain type after an update. An update can be either triggered by a next-event picked from the scheduler (i.e. a reaction, domain exit or surface interaction) or by premature bursting of neighbouring particles induced in the aftermath of such scheduler event. The particle by default is put into the system as a *Non-Interaction Single* with a shell that just envelopes the particle. Note that this "zero-shell" is spherical for 3D particles and cylindrical for 2D and 1D particles. We will call a *Single* with a zero-shell a "*Zero-Single*". Each *Zero-Single* is put into the scheduler with zero next-event time ($dt = 0$) in order to reconstruct its domain immediately after it was produced.

We then perform the following order of actions to construct a new domain:

1. **Bursting**: Burst any neighbouring "intruder", i.e. a domain that intrudes into the burst radius of the particle, with the exception of *Multi* domains and other *Zero-Singles*, i.e. domains which are yet to pass through the domain making procedure themselves. By default the burst radius is equal to the reaction horizon. Burst recursively, i.e. whenever a bursted intruder has intruders within its own reaction horizon, also burst these. The following steps then are repeated for each *Zero-Single* present in the system after bursting.

2. **Reaction/interaction attempt**: Compile a list of all potential interaction partners (particles or reactive surfaces). Pick the closest interaction partner and try a reaction (with particles) or interaction (with surfaces) if the closest partner is within the specified reaction or interaction horizon. If a minimal reaction (*Pair*) domain or *Interaction* domain can be constructed, size it up socially to the maximal available space and go directly to step (4.).

3. ***Single* domain upsizing attempt**: If a *Pair* or *Interaction* could not be constructed, yet the closest partner is within the multi horizon of the *Non-Interaction Single*, then (recursively) construct a *Multi* domain (as specified further below) and proceed directly to step (4.). Else, size up the *Non-Interaction Single* domain socially to the maximally available space and continue.

4. **Re-scheduling**: For the constructed domain type determine the next-event time and type and reinsert this information into the scheduler.

5. **Repeat** the whole procedure for the next *Zero-Single* until there are no more *Zero-Singles* in the scheduler.

The pseudo-code of the domain making algorithm is shown in Algorithm S1.

Algorithm S1 The eGFRD domain making algorithm.

$Z \leftarrow$ *Zero-Single*
while $z \in Z$ **do**

  for all domain in burst radius of z **do**
    if domain is **not** *Multi* **and** $\mathrm{dt}(\mathrm{domain}) > 0$ **then**
      $Z_{\mathrm{bursted}} \leftarrow$ burst domain recursively
      $Z \cup Z_{\mathrm{bursted}}$
    end if
  end for

  $S \leftarrow \{$neighbouring surfaces of $z\}$
  $P \leftarrow \{$neighbouring particles of $z\}$
  $c \leftarrow$ closest object $n \in S \cup P$

  if $c \in S$ **and** c in surface horizon of z **then**
    successful $\leftarrow$ try interaction of z with c
  else if not successful **and** $c \in P$ **and** c in pair horizon of z **then**
    successful $\leftarrow$ try to form *Pair* (z, c)
  else if not successful **and** c out of multi horizon of z **then**
    successful $\leftarrow$ try to scale up shell of z
  else if not successful **then**
    form *Multi* from z with c recursively
  end if

  re-schedule z
  remove z from Z

end while

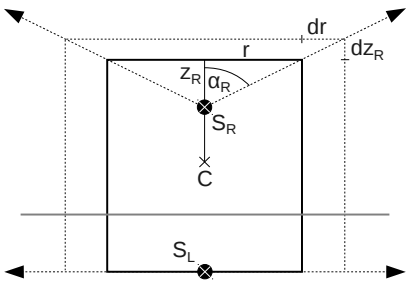

Figure S2.2: Cylinder scaling in eGFRD. The cylinder is scaled differently on its two sides (L and R) from two separate scale centers S_{L} and S_{R} which here do not coincide with the center point (C). For each side, the scale angle (α_{L}, α_{R}) defines the aspect ratio at scaling, i.e. how the respective height (z_{L}, z_{R}) scales with the cylinder radius (r). In the given example, $\alpha_{\mathrm{L}} = \pi/2$, meaning that z_{L} ($= 0$) remains constant upon changing r.

Multi construction

In eGFRD *Multis* are contingent three-dimensional objects made up from either one spherical *Multi* shell or a set of overlapping spherical *Multi* shells. The radius of a *Multi* shell is equal to the particle radius plus the reaction length multiplied by the multi-shell factor $\mu > 1$. *Multi* domains are constructed recursively: When a *Zero-Single* z has been determined to form a *Multi* object it checks for objects within its surroundings. Any other *Zero-Single* z' that is within the common multi horizon $\mu(R_z + R_{z'})$ will be added to the *Multi*. Then, for each z' that was added, the same check is performed for its surroundings, ignoring z. This is repeated until no further *Zero-Singles* can be added to the *Multi* object. Note that *Multi* shells in such constellations in principle can overlap with more than one other *Multi* shells. If there are only surfaces within the horizon the *Multi* will consist of only one *Multi* shell, the one around z.

The test-shell concept

In order to prevent double effort, in eGFRD the sizing of a domain shell upon domain (re)construction is decoupled from sampling of next-event information from the Green's function. This is achieved by using "test shells". In a particular situation in which a new domain has to be created, the simulator first attempts to determine the maximal size of the tentative test shell of the domain, taking into account the required shell geometry (cylinderical or spherical) and particular scaling parameters (e.g. the scale aspect ratio of cylinders). Starting from a (predefined) maximal shell size, the test shell then is scaled down successively with respect to each neighboring shell via collision detection. During the collision detection step the maximal dimensions of the test shell that does not lead to an overlap with the particular other domain shell are calculated (see subsequent section for more detail). If at the end of the scaling procedure the dimensions of the test shell are not smaller than the required minimal dimensions (determined by the factors β and μ defined further above and particle radii) a new domain object is parametrized with the test shell, and only after this step its next-event information is sampled. In the opposite case the construction of the respective domain type is rejected and the algorithm proceeds by attempting the construction of another domain type (e.g. *Single* or *Multi*).

Shell collision detection

Considerable computational effort has to be put into detection of collisions between a scaled test shell and another (static) shell. While this problem is trivial when scaling spheres or cylinders against spheres or parallel cylinders against each other, it is, maybe surprisingly, less straightforward for arbitrarily oriented and even orthogonal cylinders. Note that in eGFRD cylinder scaling is performed subject to a fixed (but in principle arbitrary) "scale aspect ratio" (defining a certain "scale angle"), which links the change in cylinder height to the change in the radius. The aspect ratio is usually set by the requirement of equalizing expected first passage times of the enclosed particle towards the cap and the tube of the cylindrical shell; as illustrated

by Figure S2.2, the scale angle may differ for the two opposite sides of the cylinder[1]. In general, also the reference points of the scaling ("scale centers") do not coincide with the midpoint of the cylinder, particularly in cases in which scale angles are indeed different on both sides. Thus, scaling a cylindrical shell in eGFRD conceptually consists of scaling the two sides of the cylinder separately, albeit linked via the common radius.

To scale orthogonal cylinders against each other in eGFRD we consider the two-cylinder problem in a standardized cartesian coordinate system centered at the midpoint of the scaled cylinder, with x-base-vector pointing towards the midpoint of the static cylinder and z-base-vector coinciding with the axis of the scaled cylinder. We then determine the specific type of collision that may occur upon scaling up the cylindrical test shell. There are seven possible collision types:

1. TF: the tube of the scaled cylinder hits the flat side of the static cylinder.
2. TT: the tube of the scaled cylinder hits the tube of the static cylinder.
3. TE: the tube of the scaled cylinder hits the edge[2] of the static cylinder.
4. FT: the flat side of the scaled cylinder hits the tube of the static cylinder.
5. ET: the edge of the scaled cylinder hits the tube of the static cylinder.
6. EE: the edge of the scaled cylinder hits the edge of the static cylinder.
7. None: no collision possible in the given scenario[3].

Identification of the collision type is facilitated by comparing the location of the projected midpoint of the scaled cylinder to the projected edges of the static cylinder in the xy-plane of the standardized coordinate system (in which the scaled cylinder appears circular and the static cylinder rectangular). Certain respective locations exclude certain collision types; for example, if the midpoint of the scaled cylinder is within the rectangular projection of the static cylinder, the collision must be of type FT (given that the height is scaled). Once the collision type is known, the maximal dimensions of the scaled cylinder are determined taking into account its "intrinsic" scaling properties (scale angle, location of scale center, minimal size). This is mostly achieved via straightforward geometric calculations. For collision type EE a closed form for the new dimensions could not be obtained; the values are therefore calculated from an implicit equation using a numerical rootfinder. The detailed calculations are part of the eGFRD technical documentation and beyond the scope of this thesis.

A concise scheme for scaling arbitrarily oriented eGFRD-type cylinders against each other is yet to be devised.

[1] This is e.g. the case for the shell of the *Planar Surface Interaction* domain (see section 3.2.1), the height of which is scaled only on the side of the planar surface facing the particle, while the height on the opposite side is kept fixed when the radius is scaled. This is the example shown in Fig. S2.2, where the gray line represents a planar surface.

[2] defined as the circular line that separates cylinder tube and flat side

[3] This e.g. may occur in cases in which only the radius or height are scaled.

2.B.3 Convergence issues affecting domain construction

The Green's functions, survival probabilities, cumulative PDFs and the expressions for the boundary fluxes used in eGFRD typically have the common form

$$C \cdot \sum_{\mathrm{n}=0}^{\infty} e^{-\zeta_{\mathrm{n}}^2 Dt} X_{\mathrm{n}} \tag{S2.27}$$

where C is constant and X_{n} does not depend on t. It can be shown that ζ_{n}^2, to a good approximation, scales linearly with n and inversely with the domain size L, while typically $|X_{\mathrm{n}}| \sim 1$. Convergence of these sums thus is dominated by the exponential terms. We found that it is severly hampered for evaluation times t which are small on the typical timescale of the domain, i.e. the mean time required to traverse it by diffusion with diffusion constant D. This is the case when the distance Δ of the particle to the closest boundary becomes very small. Then evaluation times are of the order of $t_\Delta = \Delta^2/2dD$, where d is the dimensionality. A fair estimate for the number n of summation terms needed to reach a desired convergence threshold ε follows from:

$$e^{-\left(\frac{cn}{L}\right)^2 Dt} < \varepsilon \qquad \Leftrightarrow \qquad n > \frac{L\sqrt{1/\varepsilon}}{c\sqrt{Dt}} \tag{S2.28}$$

where we approximate $\zeta_{\mathrm{n}} = cn/L$ with $c = const.$ Inserting t_Δ into the above equation yields

$$n_\Delta > \frac{L}{\Delta} \cdot const \tag{S2.29}$$

showing that the required number of terms to reach a predefined convergence accuracy scales inversely with the distance Δ to the closest boundary. Therefore it should be avoided to construct domains in a way that Δ/L is small; optimally domains should be constructed in a way that distances between the starting point of the diffusing particle and the domain boundaries are approximately equal.

In practice this is handled in two ways: Whenever particles start very close to radiating or absorbing boundaries we construct a domain that does not use all available space but is only sized up to $L \simeq 2\Delta$. While this requires the succesive creation of undersized domains (resulting in minor next-event times) in order to elongate the distance between the reactive boundary and the particle, it overcomes the above-mentioned convergence issues by keeping Δ/L constant. Alternatively, we scale domains up as much as possible and, where available, employ Green's functions that are bounded unilaterally, i.e. neglect the distant second boundary. These Green's functions typically are finite sums, which facilitates their implementation and computation, and in the above case approximate the double-bounded solutions very well.

2.C Appendix: Dynamical cylinders

2.C.1 Abstracting dynamical properties of microtubules

A further step towards a more accurate representation of microtubules in eGFRD is to allow for dynamical cylindrical surfaces which–in a coarse-grained fashion–reflect the dynamics of microtubules. Here we present a concept to incorporate dynamical cylinders into eGFRD.

Microtubule dynamics are characterized by permanent length changes via a process called dynamic instability [73, 74, 75, 76]: The microtubule tip alternates between phases of growth and shrinkage; the latter are induced by sporadic "microtubule catastrophies" that lead to an almost instantaneous shortening of the microtubule by a large fraction of its length, occasionally even to its complete disappearance. Catastrophies are–to a good approximation–Poissonian events that happen with a certain frequency which may depend on other factors, such as forces exerted onto the microtubule [81] and the presence of tip-tracking proteins [82, 83, 44].

The arguably most simple way to implement dynamic instability into eGFRD is to allow for length fluctuations of cylindrical surfaces that grow at a constant speed v_g and retract instantaneously to zero length at a constant catastrophy rate k_c. Next-event times for catastrophy events then can be sampled from an exponential distribution, while growth is linear and future length therefore easy to predict. However, since the cylinders typically carry particles enclosed by domains with well-defined next-event times, which moreover may interact with the growing tip, more care is required to integrate growth and shrinkage events with events produced by particle domains. In the following sections we first describe how catastrophies of dynamical cylinders can be treated within the current eGFRD framework. We then introduce growth events, produced by several new "growth" domain types that take into account particles bound to or interacting with a growing cylinder cap, as described in more detail further below. Finally, we give a brief summary of the dynamical cylinder concept elaborated here.

2.C.2 Including growth and catastrophies into eGFRD

We assume that the succession of microtubule catastrophies is a Poisson process with constant catastrophy rate k_c. Next-event times for catastrophies then are easily sampled via $\tau_c = -k_c \ln(\mathcal{R})$, where $\mathcal{R}$ is a random number from the uniform distribution on $[0, 1]$. For each cylindrical surface, τ_c is the lifetime of the cylinder and as such an upper cut-off for growth next-event times.

In the event of a catastrophy (*"Cylindrical Surface Catastrophy"*) the length of the cylindrical surface is immediately set to zero and all domains associated with that surface are bursted, i.e. their position is propagated up to the time of catastrophy τ_c before they are converted to cytoplasmic zero-singles.

Cylinders grow at constant speed within cylindrical growth domains

In order to shield the growing cylinder tip from interference by particles that are in the way we construct cylindrical growth domains in the extension of the cylinder surface

beyond its growing end ("growth volume"), with a certain length L_g determined by the specific constellation in the neighborhood of the growth domain. Here we first consider the most simple growth domain, the *"Cylindrical Surface Cap Growth"* domain, which encloses only the growing tip and the growth volume; further growth domains that also contain cylinder-bound particles are the subject of the forthcoming sections. We define the *"Cylindrical Surface Growth"* event to occur when the growing cap of the cylindrical surface reaches the distant end of the growth domain. For constant growth velocity v_g we can easily calculate the length $L(t|t < \tau_c)$ of the cylinder at any future time t given that a catastrophy did not happen until that time. The next-event time of the growth event then simply is given by $\tau_g \equiv L_g/v_g$. To avoid that the growth domain becomes an artificial obstacle for diffusing particles we allow the growth domain to be bursted by nearby particles when the growth domain is within the burst radius of the particles. This results in a length change $\Delta L < L_g$ and creates a situation in which the particles close to the growing cylindrical surface correctly detect the free space available to them.

Whenever obstacles such as surfaces or particle domains are in the way of the growing cylinder, the growth domain is constructed up to the closest interfering object in the direction of cylinder growth (i.e. along the extended cylinder axis). When a growth domain with minimal size cannot be constructed any more, both the length changes of the cylinder and–if the obstacles are particle domains–the displacements and reactions of intruding particles are simulated via Brownian dynamics. Once the intruders have moved out of the growth volume of the cylindrical surface, construction of a new growth domain may be attempted. To avoid instantaneous re-bursting of a newly constructed growth domain, it is wise to propagate the particles in BD mode until their distance is larger than their burst radius (reaction horizon).

Binding to a growing cylinder cap

In section 2.4 we have described how the 1D Green's function with drift derived in section 2.3 is used to sample next-event times and positions for a particle that diffuses (with diffusion constant D) and drifts (with velocity v) on a finite, static cylindrical surface and binds to the cylinder cap with an intrinsic reaction rate. This principle can be straightforwardly extended to the case of dynamical cylinders. For constant cylinder growth velocity v_g, the problem can be easily transformed into the reference frame of the moving cap by substituting the drift velocity v in the Green's function with $v - v_g$. Note that this then also assumes that the absorbing boundary of the cap binding domain is not static any more, but trails behind the particle at a velocity v_g. This has to be taken into account when sampling a new particle position x on the cylinder axis at a time τ: position x has to be post-processed by adding $\Delta x = v_g\tau$, the length increase of the growing cylinder until time τ. Note that τ may be a time at which the domain is bursted, and thus arbitrary.

To isolate the problem from exterior influence, we can encapsulate the particle and the growing cap by a (cylindrical) *"Cylindrical Surface Growing Cap Interaction"* domain that extends beyond the cap as far as possible, i.e. using up all available space in the direction of the growing cylindrical surface. As described for the *Cylindrical Surface Cap Growth* domain (see previous subsection), the length of this extension

defines the next-event time τ_g for the *Cylindrical Surface Growth* event. The next-event time τ_ν for the *Cylindrical Surface Growing Cap Interaction* domain then is given by the minimum of τ_{dd}, the next-event time sampled from the diffusion-drift Green's function with the modified drift, τ_g and τ_s, which is the tentative time of the next monomolecular reaction of the particle.

Similarly, we can define a *"Cylindrical Surface Growing Cap Single"* domain for a particle that is bound to the cap of a growing cylinder. Again we construct a cylindrical domain that encloses the particle and as much of the space in the direction of the growing cylinder as possible. Here the next-event time τ_ν is the minimum of τ_g (cylinder growth) and τ_s (monomolecular reaction). For any τ_ν, both the cap and the particle are displaced by $\Delta x = v_g \tau_\nu$; when $\tau_\nu = \tau_s$, the particle in addition is displaced orthogonally and placed at contact with the cap at a random angle.

To end with, the case of a cylinder-bound particle interacting with a particle on the growing cylinder cap can be treated in analogy to the *Cylindrical Surface Growing Cap Interaction* defined above. As before, we can create a cylindrical domain (*"Mixed Pair 1D-Growing Cap"*) that encloses both particles and the available growth volume. There are two minor differences: First, for any next-event time τ the cap-bound particle is displaced deterministically with the growing cap by $\Delta x = v_g \tau$, while the position of the other particle is sampled from the 1D Green's function before Δx is added, as described above. Second, since here both particles can undergo monomolecular reactions with tentative next-event times τ_{s1} and τ_{s2}, the next-event time τ_ν of the domain is the minimum of τ_g, τ_{dd}, τ_{s1} and τ_{s2}.

2.C.3 Summarized cylinder growth sampling algorithm

The concept presented in the preceding sections can be compiled into the following algorithm for growth domain construction in eGFRD.

Starting from the situation in which a growing cylinder with growth velocity v_g and catastrophy rate k_c just exited from its last update we first sample a next-catastrophy time τ_c from an exponential distribution with decay rate k_c. Depending on whether there are particles on and/or close to the cylinder cap, we construct a domain that surrounds the cap and the particles associated or interacting with the cap and the available growth volume in the direction of the growing cylindrical surface. Possible growth domain types are:

- *Cylindrical Surface Cap Growth*: contains only the growing cap, no particles.
- *Cylindrical Surface Growing Cap Single*: contains the growing cap and a cap-bound particle.
- *Cylindrical Surface Growing Cap Interaction*: contains the growing cap and a nearby particle diffusing and drifting on the cylinder.
- *Mixed Pair 1D/Growing Cap*: contains the growing cap, a cap-bound particle and a nearby particle diffusing and drifting on the cylinder.

We then calculate a next-event time τ_g for the growth event which is directly determined by the length of the "free path" L_g available to the growth domain in growth

direction, $\tau_g = L_g/v_g$. If the domain contains a mobile particle that is not bound to the cap, we calculate a next-event time for particle association to the cap (or cap-bound particle) or for exit through the absorbing boundary from the 1D Green's function with drift (section 2.3) in which the drift v is substituted via $v \to (v - v_g)$. In the following this function is denoted by p_{v-v_g}. For all of the above domain types that contain a particle, we finally also compute the next-event time of a monomolecular particle reaction τ_s, where τ_s is the smaller of the two tentative monomolecular reaction times if there are two particles involved. The next-event time for the growth domain then is defined as $\tau_\nu = \min(\tau_c, \tau_g, \tau_{dd}, \tau_s)$; this automatically determines the scheduled next-event type. The possible events produced by growth domains require slightly different update procedures:

- *Cylindrical Surface Catastrophy* ($\tau_\nu = \tau_c$): If the next event is a catastrophy we burst all associated domains and shorten the cylinder down to zero length. The cylindrical single and pair domains that enclose cylinder-bound particles are bursted in the regular fashion; bursting of growth domains, which also contain the growing cylinder end, is described further below.

- *Cylindrical Surface Growth* ($\tau_\nu = \tau_g$): In this case we first extend the length of the growing cylinder by $\Delta L_g = v_g \tau_g$. If the domain contains a cylinder-bound mobile particle, a new particle position x_ν is sampled from $p_{v-v_g}(x, \tau_g)$ and ΔL_g added to x_ν afterwards.

- Particle exit ($\tau_\nu = \tau_{dd}$): here first the length of the cylindrical surface is enlarged by $\Delta L_{dd} = v_g \tau_{dd}$. The cap and an eventual cap-bound particle are displaced by ΔL_{dd}. Then, if the exit of the diffusing cylinder-bound particle is through the reactive boundary, it is removed and a new cap-bound product particle is placed at the updated position of the cap, which will subsequently result in the creation of a *Cylindrical Surface Growing Cap Single*. If the exit is through the absorbing boundary, the sampled new particle position x_ν has to be transformed via $x_\nu \to x_\nu + v_g \tau_{dd}$.

- Particle monomolecular reaction ($\tau_\nu = \tau_s$): again, first the cylinder length should be enlarged by $\Delta L_s = v_g \tau_s$. The cap and an eventual cap-bound particle are displaced accordingly. The new position x_ν of a diffusing particle is sampled from $p_{v-v_g}(x, \tau_s)$ and post-transformed via $x_\nu \to x_\nu + \Delta L_s$. The particle that underwent the monomolecular reaction is placed at contact with the cylinder at a random angle.

- Bursting $\tau \leq \tau_\nu$: If any of the domains is bursted at an arbitrary time τ, the cap and cap-bound particles have to be displaced by $\Delta L = v_g \tau$. For the diffusing particles new positions are sampled from $p_{v-v_g}(x, \tau)$ and ΔL is added afterwards.

Note that growth, binding and monomolecular reaction events are conditioned on the fact that a catastrophy did not yet happen. The above prescription exploits the fact that catastrophy times are Poissonian, which precisely means that the probability of an catastrophy event to happen within the time interval $[t, t + dt]$ is independent of the fact that it did not occur until time t.

Chapter 3

2D-eGFRD

3.1 Introduction

It has long been known that the cell membrane serves to maintain an intracellular environment that is different from its surroundings. The membrane acts both as a barrier and as an interface: not only does it prevent unwanted exchange of molecules between cell and environment, it also allows for controlled exchange of proteins and ions via endo- and exocytosis and ion channels. In addition, it is now becoming increasingly clear that the membrane is also a central platform for cellular signal processing. It is not only the place where extra-cellular signals are detected, but also amplified and integrated [29, 46, 47].

Not surprisingly, a broad range of proteins is able to anchor to the membrane in order to perform specialized tasks or to act as membrane-bound reaction sites for other proteins. In eukaryotic cells, up to 50% of the membrane mass consists of proteins, and in yeast about one third of all genes code for membrane-bound proteins [84, 85, 86]. Therefore, a scheme that aims at constituting a generic and versatile cell simulation environment must take into account membrane-associated processes.

Here we describe the inclusion of membrane-binding and two-dimensional diffusion into eGFRD. In the first part of this chapter we explain how we use planar structures to represent the cell membrane in eGFRD, defining new domain types which model interactions between bulk and membrane and diffusion-reaction processes on the membrane. There we also introduce the concept of "transitions", i.e. instant particle transfer between adjacent planes, which is used to define closed compartments consisting of interlinked planes.

While many concepts already introduced in the first chapter also apply here, it is necessary to calculate new Green's functions for the newly introduced domain types, to which the second, mathematical part of this chapter is devoted. Since many of the calculations employ polar coordinates in which the diffusion equation translates to Bessel's equation, we make extensive use of the theory of Bessel functions; while we briefly mention related details where necessary, we refer the reader to [87] for a comprehensive treatise and to [88] for an excellent concise introduction to this topic.

We end by describing a generalized coordinate transform which is needed to treat the case of a bulk particle that directly interacts with a membrane-bound particle, to which we refer by "direct binding".

3.2 2D structures in eGFRD

In order to render eGFRD capable of simulating diffusion and reactions on the cell membrane we introduce two-dimensional structures into the scheme. In vivo, membranes are closed, irregularly curved shapes, which in addition undergo dynamical fluctuations. However, in many systems shape fluctuations and deformations are not essential for cellular signaling. We therefore represent membranes as static reactive planes, neglecting curvature. Bulk particles may bind to any position on the plane that is not yet occupied by another particle with a certain rate, and unbind back to the bulk. We also allow for "direct binding" of a (3D) bulk particle to a (2D) particle that is already bound to a plane. In addition, particles may diffuse and react on the membrane.

In order to permit modelling of a finite, fully membrane-enclosed volume representative of a whole cell, we implemented a box structure consisting of six finite, orthogonal planar surfaces that are connected at their common edges. Particles that diffuse on one plane can instantly change to a neighboring plane at edge contact via special *"Transition"* domains that enclose tentative new positions on both planes and account for the necessary geometric transform. Alternatively, a closed cell could be represented by a spherical or cylindrical outer surface, to which particles can bind and diffuse in curvilinear coordinates. While we did not implement this variant here, a Green's function for binding to such a (cylindrical) curved surface was derived and is briefly presented in section 3.3.3.

In the following we first describe how binding to planar surfaces is treated. Then we present the treatment of diffusion and reactions of particles on the planes. A third subsection explains the concept of transitions and associated geometric transforms. In all cases, new domain types will be introduced. The mathematical derivation of the new Green's functions employed by these domains is described separately in the subsequent sections.

3.2.1 Interactions with planar surfaces

Binding of a bulk particle to a reactive planar structure is treated in a similar way as binding to a reactive cylinder, as described in section 2.2.2. Following the usual principle, we construct a protective domain that isolates the bulk particle and a region on the reactive plane from exterior influence. For that purpose we introduce a new cylindrical domain type, the *"Planar Surface Interaction"* domain, shown in Figure 3.1A. Cylindrical geometry was chosen because it facilitates scaling of the domain with respect to the other cylindrical domains for plane-bound particles that we will introduce further below. The domain is created in a way that its cylinder axis is perpendicular to the plane and congruent with the line that projects the particle onto the plane. Its height over the plane $h = \delta + \beta R_0$ is determined by the distance δ between plane and interacting particle plus βR_0, where R_0 is the particle radius and

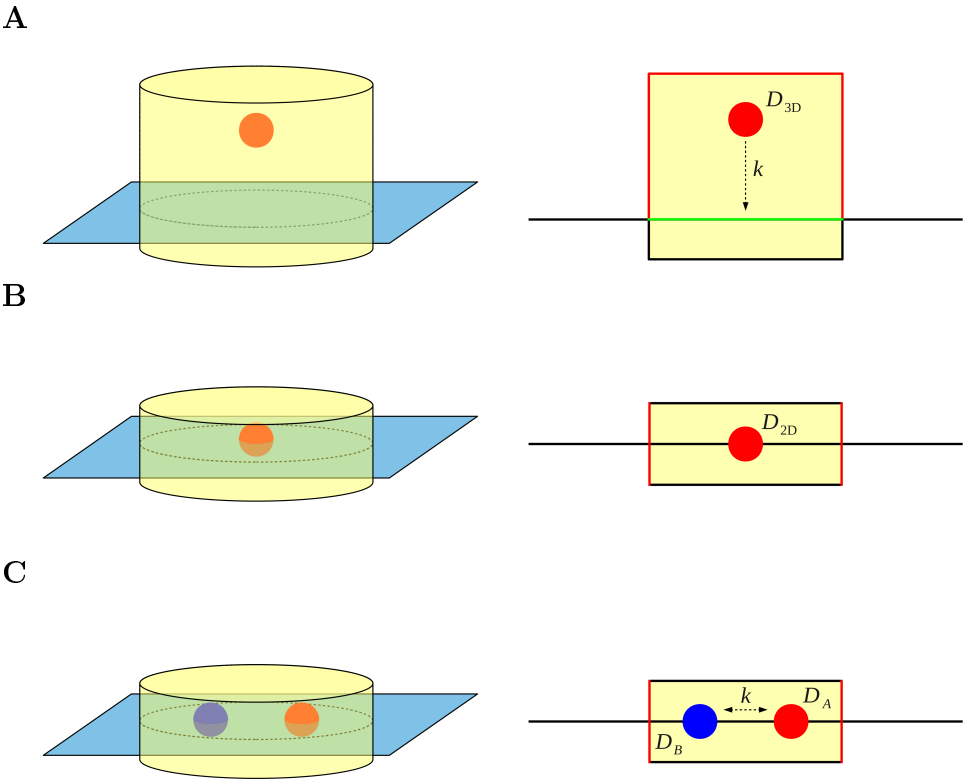

Figure 3.1: New protective domain types for interaction with and reaction-diffusion on planar surfaces. (A) *Planar Surface Interaction* domain; (B) *Planar Surface Single* domain; (C) *Planar Surface Pair* domain. Right panels show sections of 3D objects. Absorbing boundaries are highlighted by red, radiative boundaries by green.

$\beta > 1$ the single-shell factor (as defined in section 2.B.2 of the appendix). Note that the domain slightly extends behind the reactive plane by a length $h' = \beta R_0$; this is to prevent the bound particle from overlapping with particles on the opposite side of the plane–a prerequisite for modelling intracellular compartments. Association to the plane is modeled via a radiating boundary condition at particle-plane contact. Here, the spherical particles are thought to interact with the infinitely thin plane not with their outer shell but with their centers; concomitantly, in the bound state particle centers coincide with the plane. By default we allow for binding to both sides of the plane; binding can be restricted to one side as a species property.

The particle can exit the interaction domain by either reacting with the plane or by hitting one of the domain's absorbing boundaries, i.e. the cylinder tube or the cytoplasmic cylinder cap. Let $p(r, \phi, z, t|r_0, \phi_0, z_0)$ be the probability density function for this problem, written in cylindrical coordinates $\mathbf{r} = (r, \phi, z)$. As in section 2.2.2, we can separate diffusion along the cylinder axis from diffusion in the polar

plane via the ansatz $p(r, \phi, z, t|r_0, \phi_0, z_0) = p_r(r, \phi, t|r_0, \phi_0)p_z(z, t|z_0)$, which yields a one-dimensional diffusion equation for p_z and BESSEL's equation for p_r. The 1D-problem for p_z has to be solved with a radiating boundary at $z = 0$ and an absorbing boundary at $z = h$. Here we simply reuse the 1D Green's function (2.64) calculated in section 2.3.2 with drift $v = 0$, $\sigma = 0$ and $a = h$. The equation for p_r has perfect radial symmetry by construction and describes 2D diffusion in polar coordinates for a particle starting at $r = 0$ and a circular absorbing boundary at $r = R$. The solution to this problem is well-known and presented in section 3.3.1.

From the two Green's functions p_r and p_z we sample next-event times τ_r and τ_z in the usual way and take their minimum as the next-event time τ_ν of the interaction domain. In the case $\tau_\nu = \tau_z$, i.e. when the particle exits the cylindrical domain through one of its caps, we compare the fluxes through the opposite boundaries to determine whether the particle left through the absorbing (*IV Escape* event, particle is put into the cytoplasm) or through the radiating boundary (*IV Interaction*, particle associates with the membrane). For $\tau_\nu = \tau_r$ we know with certainty that a (radial) escape through the cylinder tube occured. In both cases the respective other coordinate is sampled from the corresponding Green's function normalized by the respective survival probability.

3.2.2 Direct binding: Interactions of particles with particles bound to planes

Instead of binding to the plane, a bulk (3D) particle may bind to a (2D) particle that is already associated with the plane. We call this process "direct binding", in the sense that the 3D particle directly interacts with the 2D particle without prior binding to the membrane. Within the framework of eGFRD direct binding constitutes a pair-reaction. When the cytoplasmic particle can bind the particle on the membrane, but not the membrane itself, the membrane acts as a reflecting surface. We can then exploit the fact that trajectories that are reflected from the plane are simply the mirror image of the trajectories that would continue through the plane if the plane would not exist. This conceptual trick enables us to use the Green's functions that we have already derived for pairs of particles that interact in 3D. However, here in addition the fact that movement of the 2D particle is restricted to the plane must be taken into account. More specifically, since the bound particle is immobile in the direction perpendicular to the plane, the interparticle diffusion constant in this direction is equal to the diffusion constant of the 3D particle, whereas in the orthogonal directions it is given by the sum of the 2D and 3D diffusion constants. This renders interparticle diffusion anisotropic. In section 3.4 we show that by defining the interparticle and center-of-mass coordinates such that they account for the anisotropy, the problem can be transformed in a way that known Green's functions may be employed to sample the next event. The sampled new positions then are post-processed via the corresponding inverse coordinate transform. For the specific transform that we choose, the new interparticle positions lie within an oblate spheroid centered around the new center-of-mass position. To facilitate scaling of domain shells against each other, we enclose the mathematical domains by adequately sized cylindrical shells, as for regular binding. We show such a *"Mixed Pair 2D-3D"* domain in Figure 3.2A.

3.2.3 Diffusion and reactions on planar surfaces

We treat diffusion of particles on the plane and reactions between two such particles in the same manner as in 3D. Here, however, instead of spheres we use flat cylinders for single and pair domains and consequently the corresponding Green's functions are calculated in polar instead of spherical coordinates. Figures 3.1B and 3.1C, respectively, show a *"Planar Surface Single"* and a *"Planar Surface Pair"* domain.

In the *Planar Surface Single* the particle starts out from the center of the domain and the only exit channel is the absorbing boundary at its outer radius. The Green's function for this problem is precisely the one that describes planar movement in the *Planar Surface Interaction* domain (see section 3.2.1), which is presented in section 3.3.1.

The same Green's function is also used to sample next-event information for the center-of-mass diffusion in the *Planar Surface Pair* domain, after the 2D pair problem has been transformed into center-of-mass and interparticle diffusion; this is achieved via precisely the same transform as in 3D and 1D (see calculations in section 2.3.1 with drift $v = 0$). The respective interparticle vector problem is solved subject to an outer absorbing boundary and an inner radiating boundary at particle contact which models the reaction. While this is completely analogous to the treatment in 3D, mathematically the problem has to be reconsidered from scratch for the polar coordinate system used here. The derivation of the corresponding Green's function is summarized in section 3.3.2. Next-event times and new positions for the *Planar Surface Pair* are sampled in the regular fashion, as described in section 2.1.3.

3.2.4 Finite planes and transitions between them

When introducing the new domain types for membrane-interaction and -diffusion we implicitly assumed that particles interact with a single unbounded planar surface. An extension towards bounded planes does not require significant changes: domains associated to the plane must simply be constructed such that they do not reach out of it. In contrast, the implementation of particle transitions between two bordering orthogonal planes within the box-arrangement that we introduced earlier requires new domain types. We imagine that the two connected planes–in an abstract fashion–represent a continuous part of the membrane. This means that the edge does not constitute an obstacle for the diffusing particle; when it reaches the edge its movement is instantly redirected into the orthogonal direction imposed by the bordering plane. Under the assumption that this holds for each diffusive trajectory, we devised the following procedure for transitions of a particle between orthogonal planes: First we construct a spherical *"Planar Surface Transition"* domain in a way that it contains the particle on the surface of origin and an empty region on the target surface. The domain is centered around the original particle position $\mathbf{r}_0$. This construction is shown in Figure 3.2B. As a second step a next-event time τ_ν and a new position $\mathbf{r}_\nu$ is sampled in the same way as for the *Planar Surface Single*, where the radius of the absorbing outer circle is equal to the radius of the spherical transition domain. If $\mathbf{r}_\nu$ is inside the finite plane of origin, the particle is moved to that point at τ_ν. If, in contrast, $\mathbf{r}_\nu$ lies beyond the boundaries of the original plane, the new position is deflected onto the orthogonal target plane; this is done by rotating the part of the

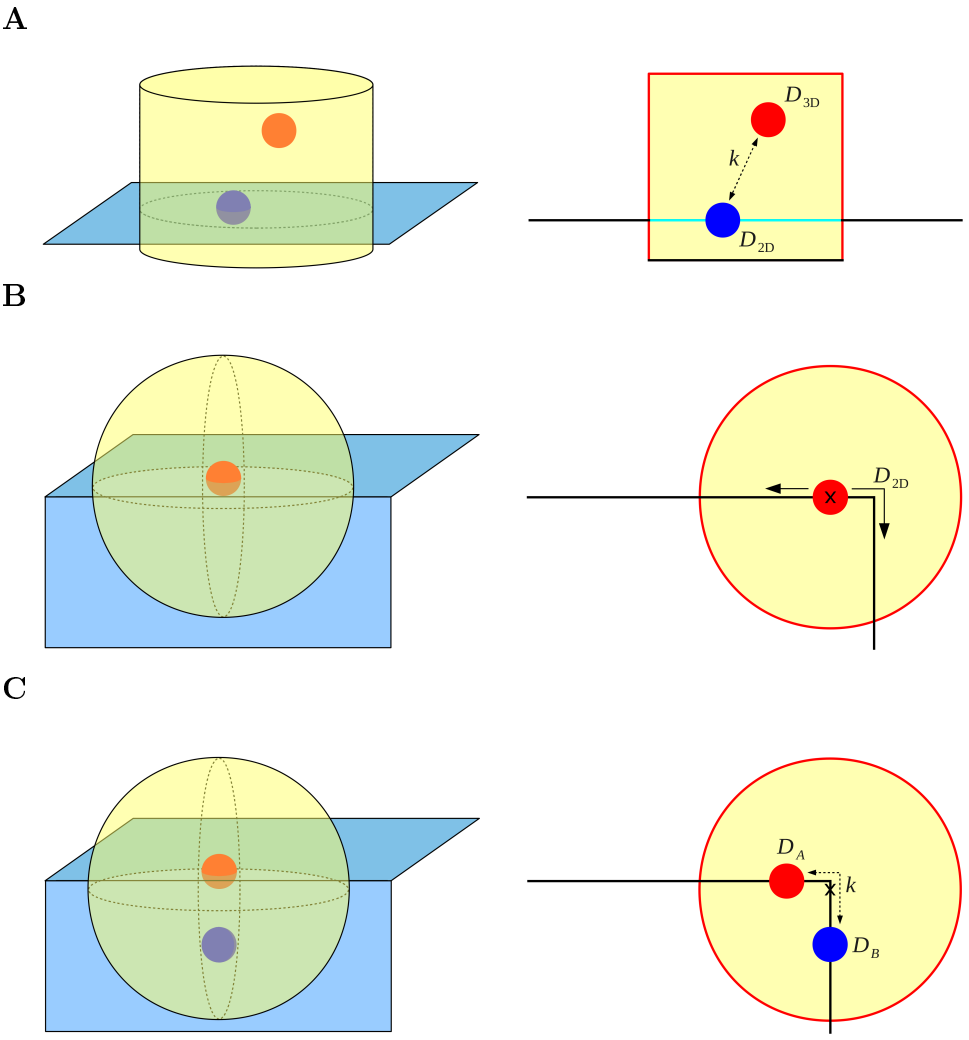

Figure 3.2: Special protective domains for particles on planar surfaces. (A) *Mixed Pair 2D-3D* domain; (B) *Planar Surface Transition* domain; (C) *Planar Surface Transition Pair* domain. Right panels show sections of 3D objects. Here, absorbing boundaries are highlighted by red, reflective boundaries by cyan color. The center of spherical domains is indicated by a black cross.

displacement vector $\Delta\mathbf{r} = \mathbf{r}_\nu - \mathbf{r}_0$ that reaches out of the original plane about the line that marks the edge between the planes by an angle of $\pi/2$. Details of this simple geometrical transform are described in section 3.A in the appendix.

The above principle can be straightforwardly extended to the case of a pair of particles that reside on different neighboring planes and interact "around the edge". Let us assume that particle A is located at position $\mathbf{r}_\mathrm{A}$ on plane A and and particle B at $\mathbf{r}_\mathrm{B}$ on plane B. Here first position $\mathbf{r}_\mathrm{B}$ is transformed into plane A via the inverse of the deflection transform (appendix section 3.A). Then a next-event time and new particle positions are determined in plane A, following the procedure for the *Planar Surface Pair*. Finally, new positions that lie beyond the boundaries of plane A are transformed into plane B. Also the construction of the protective domain is slightly different as compared to the case with one particle: We encapsulate the pair constellation with a spherical *"Planar Surface Transition Pair"* domain centered around the weighted center-of-mass $\mathbf{R}$ of the particles, as shown in Figure 3.2C. Note that here vector $\mathbf{R}$ is calculated as follows: First $\mathbf{r}_\mathrm{B}$ is transformed into plane A, yielding $\mathbf{r}'_\mathrm{B}$, and the weighted center-of-mass $\mathbf{R}'$ is computed in plane A from $\mathbf{r}'_\mathrm{B}$ and $\mathbf{r}_\mathrm{A}$. If $\mathbf{R}'$ is within the bounds of plane A, we set $\mathbf{R} = \mathbf{R}'$; otherwise $\mathbf{R}$ is obtained by deflecting $\mathbf{R}'$ back into plane B. The latter case is shown in the example situation in Figure 3.2C.

Special treatment is required in the rare event that two particles end up very close to each other in the proximity of an edge between two planes. This may happen due to a single reaction, in which the products are put at contact with a random angle, but also when a *Planar Surface Transition Pair* is bursted and its two particles happen to end up close to each other. In these cases constellations are possible in which one of the particles reaches out of the plane, but application of the deflection transform would lead to particle overlap, because the transform shortens the effective distance between the two particles. Therefore particles are slightly moved apart in such situations, introducing a minor error.

3.3 Green's functions

3.3.1 Green's function with absorbing outer boundary in polar coordinates

We now sketch the calculation of the Green's function in polar coordinates $\mathbf{r} = (r, \phi)$ for a diffusing particle starting at radius $r = 0$ with a symmetric absorbing boundary at a radial distance $r = a$; this function is used to sample next-event times and new positions in the *Planar Surface Interaction* domain (section 3.2.1), *Planar Surface Single* and *Planar Surface Pair* domains (section 3.2.3), and the transition domains derived from the latter two (section 3.2.4).

Since we assume perfect radial symmetry here, the Green's function $p_{\mathrm{s}}(r,t)$ does not depend on the angular coordinate ϕ, so that the corresponding boundary value problem can be written as follows:

$$\partial_{\mathrm{t}} p_{\mathrm{s}}(r,t) = D\left[\frac{1}{r}\partial_{\mathrm{r}}\left(r\partial_{\mathrm{r}}\right)\right] p_{\mathrm{s}}(r,t) \tag{3.1}$$

$$p_{\mathrm{s}}(r, t_0 = 0) = \frac{1}{2\pi r}\delta(r) \tag{3.2}$$

$$p_{\mathrm{s}}(a,t) = 0 \tag{3.3}$$

The solution to this problem is well-known [57, p. 368f] and, for the above initial condition, reads

$$p_{\mathrm{s}}(r,t|r_0 = 0) = \frac{1}{\pi a^2}\sum_{\mathrm{n}=1}^{\infty} e^{-\rho_{\mathrm{n}}^2 Dt}\frac{J_0(r\rho_{\mathrm{n}})}{J_1^2(a\rho_{\mathrm{n}})} \tag{3.4}$$

where J_0 and J_1 are regular Bessel functions and ρ_{n} the roots of the equation:

$$J_0(a\rho_{\mathrm{n}}) = 0 \tag{3.5}$$

The corresponding survival probability $S_{\mathrm{s}}(t)$ and (radial) cumulative PDF $P_{\mathrm{s}}(r,t)$ follow by integration of $p_{\mathrm{s}}(r,t)$ over the considered circular domain:

$$S_{\mathrm{s}}(t) = \int_0^a \int_0^{2\pi} p(r,t|r_0) r d\phi dr = \frac{2}{a}\sum_{\mathrm{n}=1}^{\infty} e^{-\rho_{\mathrm{n}}^2 Dt}\frac{1}{\rho_{\mathrm{n}} J_1(a\rho_{\mathrm{n}})} \tag{3.6}$$

$$P_{\mathrm{s}}(r,t) = \int_0^r \int_0^{2\pi} p(r',t|r_0) r' d\phi dr' = \frac{2}{a^2}\sum_{\mathrm{n}=1}^{\infty} e^{-\rho_{\mathrm{n}}^2 Dt}\frac{rJ_1(r\rho_{\mathrm{n}})}{\rho_{\mathrm{n}} J_1^2(a\rho_{\mathrm{n}})} \tag{3.7}$$

Here the standard formula $\int_0^r r' J_0(r')dr' = rJ_1(r)$ is used.

Next-event times τ_ν are sampled from $p_{\mathrm{s}}(r,t)$ in the usual way by comparing a uniform random number from $[0,1]$ with $S_{\mathrm{s}}(t)$ via the inversion method. For an arbitrary time τ, a new radius $r_\nu(\tau)$ is obtained from $\frac{1}{S_{\mathrm{s}}(\tau)}P_{\mathrm{s}}(r,\tau)$, whereas a new angle $\phi_\nu(\tau)$ is sampled from the uniform distribution on $[0, 2\pi]$. If $\tau = \tau_\nu$, we directly set $r_\nu(\tau_\nu) = a$.

3.3.2 Green's function for the 2D diffusion-reaction problem

In this section we describe the derivation of the Green's function in polar coordinates $\mathbf{r} = (r, \phi)$ for a particle starting at an arbitrary position $\mathbf{r}_0 = (r_0, \phi_0)$ within an annular region bounded by a radiating inner and absorbing outer boundary. This Green's function is required for next-event sampling in the *Planar Surface Pair* domain (section 3.2.3), but also for the *Cylindrical Surface Interaction* domain (section 2.2.2).

We assume here that the problem of two particles that interact on a plane has been transformed correctly into a diffusion problem for their center-of-mass vector $\mathbf{R}$ and a diffusion-reaction problem for their interparticle vector $\mathbf{r} = (r, \phi)$, with a radiating boundary at particle contact, i.e. $r = |\mathbf{r}| = \sigma = R_\mathrm{A} + R_\mathrm{B}$, and an absorbing boundary at $r = a$. While the problem for $\mathbf{R}$ is solved by the Green's function presented in section 3.3.1, the spatio-temporal evolution of $\mathbf{r}$ is goverened by the following diffusion equation in polar coordinates

$$\begin{aligned}\partial_\mathrm{t} p_\mathbf{r}(r, \phi, t|r_0, \phi_0) &= D_\mathrm{r} \nabla^2_\mathbf{r} p_\mathbf{r}(r, \phi, t|r_0, \phi_0) \\ &= D_\mathrm{r} \left[\partial^2_\mathrm{r} + \frac{1}{r}\partial_\mathrm{r} + \frac{1}{r^2}\partial^2_\phi\right] p_\mathbf{r}(r, \phi, t|r_0, \phi_0) \qquad \text{(PDE)}\end{aligned}$$

subject to boundary conditions

$$2\pi\sigma D_\mathrm{r} \partial_\mathrm{r} p_\mathbf{r}(r, \phi, t|r_0, \phi_0)\big|_{\mathrm{r}=\sigma} = k p_\mathbf{r}(|\mathbf{r}| = \sigma|r_0, \phi_0) \qquad \text{(BCr)}$$

$$p_\mathbf{r}(r, \phi, t|r_0, \phi_0)\big|_{\mathrm{r}=\mathrm{a}} = 0 \qquad \text{(BCa)}$$

and initial condition

$$p_\mathbf{r}(r, \phi, t = 0|r_0, \phi_0) = \frac{1}{r}\delta(r - r_0)\delta(\phi - \phi_0) \qquad \text{(IC)}$$

where k is the intrinsic particle reaction rate.

Solution in Laplace space

The above boundary value problem is again solved most conveniently in LAPLACE space. Applying the LAPLACE transform $\hat{p}_\mathbf{r}(r, \phi, s|r_0, \phi_0) \equiv \int_{-\infty}^{\infty} p_\mathbf{r}(r, \phi, s|r_0, \phi_0) e^{-st} dt$ on both sides of the equations yields:

$$s\hat{p}_\mathbf{r}(r, \phi, s|r_0, \phi_0) - p_\mathbf{r}(r, \phi, t = 0|r_0, \phi_0) = D_\mathrm{r} \nabla^2_\mathbf{r} \hat{p}_\mathbf{r}(r, \phi, s|r_0, \phi_0) \quad \Leftrightarrow$$

$$\left[\partial^2_\mathrm{r} + \frac{1}{r}\partial_\mathrm{r} + \frac{1}{r^2}\partial^2_\phi - \frac{s}{D_\mathrm{r}}\right] \hat{p}_\mathbf{r}(r, \phi, s|r_0, \phi_0) = \frac{-1}{D_\mathrm{r} r}\delta(r - r_0)\delta(\phi - \phi_0) \qquad \text{(PDE)}$$

$$2\pi\sigma D_\mathrm{r} \partial_\mathrm{r} \hat{p}_\mathbf{r}(r, \phi, s|r_0, \phi_0)\big|_{\mathrm{r}=\sigma} = k\hat{p}_\mathbf{r}(\mathbf{r} = \sigma|r_0, \phi_0) \qquad \text{(BCr)}$$

$$\hat{p}_\mathbf{r}(r, \phi, s|r_0, \phi_0)\big|_{\mathrm{r}=\mathrm{a}} = 0 \qquad \text{(BCa)}$$

As usual we first attempt to find a general solution to the homogenous problem corresponding to (PDE) and specialize it afterwards by applying the initial and

boundary conditions. Let us set $s/D_\mathrm{r} \equiv q^2 \geq 0$. The homogenous problem then reads:

$$\left[\partial_\mathrm{r}^2 + \frac{1}{r}\partial_\mathrm{r} + \frac{1}{r^2}\partial_\phi^2 - q^2\right] \hat{p}_{\mathbf{r},\mathrm{h}}(r,\phi,q) = 0 \tag{3.8}$$

Via the separation ansatz $\hat{p}_{\mathbf{r},\mathrm{h}}(r,\phi,q) = R(r)\Phi(\phi)$ one can show that the above PDE is equivalent to the following two differential equations coupled by a positive parameter m^2:

$$\partial_\phi^2 \Phi(\phi) = -m^2\Phi(\phi) \tag{3.9}$$

$$\left[r^2\partial_\mathrm{r}^2 + r\partial_\mathrm{r} - (r^2q^2 - m^2)\right] R(r) \tag{3.10}$$

The solution to (3.9) is readily obtained as $\Phi(\phi) = \alpha\cos(m(\phi-\phi_0))$ where we exploit that $\Phi(\phi)$ must be an even function because the operator ∂_ϕ^2 conserves the symmetry of $\delta(\phi-\phi_0)$. α is a yet undetermined real constant. With $rq \equiv \rho$ equation (3.10) is equivalent to the modified Bessel equation:

$$\left[\rho^2\partial_\rho^2 + r\partial_\rho - (\rho^2 - m^2)\right] R(\rho) \tag{3.11}$$

which is solved by any linear combination of the modified Bessel functions $R(\rho) = \beta I_\mathrm{m}(\rho) + \gamma K_\mathrm{m}(\rho)$. The solution to (3.8) thus reads

$$\begin{aligned}
&\hat{p}_{\mathbf{r},\mathrm{h}}(r,\phi,q) \\
&\quad = (\alpha\beta)\cos\left(m(\phi-\phi_0)\right) I_\mathrm{m}(\rho) + (\alpha\gamma)\cos\left(m(\phi-\phi_0)\right) K_\mathrm{m}(\rho) \\
&\quad \equiv A\cos\left(m(\phi-\phi_0)\right) I_\mathrm{m}(qr) + B\cos\left(m(\phi-\phi_0)\right) K_\mathrm{m}(qr)
\end{aligned} \tag{3.12}$$

with constants A and B.

We now can construct an ansatz for the inhomogenous problem. For further calculation it is convenient to write the ansatz as

$$\hat{p}_\mathbf{r} = \hat{p}_\mathrm{f} + \hat{p}_\mathrm{c} \tag{3.13}$$

where $\hat{p}_\mathrm{f}(\mathbf{r},q|\mathbf{r}_0) = \frac{1}{2\pi D_\mathrm{r}} K_0(q(\mathbf{r}\cdot\mathbf{r}_0))$ is the "free" solution to the unbounded 2D diffusion problem for a point particle starting at (r_0,ϕ_0), written in Laplace space, and $\hat{p}_\mathrm{c}$ a correction resulting from the boundaries. Although $\hat{p}_\mathrm{f}$ fulfills the initial condition by construction, this does not automatically apply to the entire ansatz and must be separately proven later on. Since until now m^2 is an arbitrary constant, we shall construct the ansatz as a sum over all possible m. For $\hat{p}_\mathrm{c}$ we thus write

$$\hat{p}_\mathrm{c}(r,\phi,q|r_0,\phi_0) = \sum_{\mathrm{m}=-\infty}^{\infty} \cos\left(m(\phi-\phi_0)\right)\left[A_\mathrm{m} I_\mathrm{m}(qr) + B_\mathrm{m} K_\mathrm{m}(qr)\right] \tag{3.14}$$

with real coefficients A_m and B_m. Now it is also convenient to expand $\hat{p}_\mathrm{f}$ into functions that resemble (3.12), using a formula from [57, 87, p. 365]:

$$\hat{p}_\mathrm{f}(\mathbf{r},q|\mathbf{r}_0) = \begin{cases} \frac{1}{2\pi D_\mathrm{r}} \sum_{\mathrm{m}=-\infty}^{\infty} \cos\left(m(\phi-\phi_0)\right) I_\mathrm{m}(qr) K_\mathrm{m}(qr_0)\,, & r < r_0 \\ \frac{1}{2\pi D_\mathrm{r}} \sum_{\mathrm{m}=-\infty}^{\infty} \cos\left(m(\phi-\phi_0)\right) I_\mathrm{m}(qr_0) K_\mathrm{m}(qr)\,, & r > r_0 \end{cases} \tag{3.15}$$

This yields the combined ansatz:

$$\hat{p}_{\mathbf{r}}(r,\phi,q|r_0,\phi_0) = \begin{cases} \frac{1}{2\pi D_{\mathrm{r}}} \sum_{\mathrm{m}=-\infty}^{\infty} \cos\left(m(\phi-\phi_0)\right) \times \\ \qquad \left[I_{\mathrm{m}}(qr)K_{\mathrm{m}}(qr_0) + A_{\mathrm{m}}I_{\mathrm{m}}(qr) + B_{\mathrm{m}}K_{\mathrm{m}}(qr)\right], \\ \qquad\qquad \text{for } r < r_0 \\ \frac{1}{2\pi D_{\mathrm{r}}} \sum_{\mathrm{m}=-\infty}^{\infty} \cos\left(m(\phi-\phi_0)\right) \times \\ \qquad \left[I_{\mathrm{m}}(qr_0)K_{\mathrm{m}}(qr) + A_{\mathrm{m}}I_{\mathrm{m}}(qr) + B_{\mathrm{m}}K_{\mathrm{m}}(qr)\right], \\ \qquad\qquad \text{for } r > r_0 \end{cases} \tag{3.16}$$

By applying the boundary conditions at $r = \sigma$ and $r = a$ term-wise for each m we find, after some algebraic steps

$$\begin{aligned} A_{\mathrm{m}} &= K_{\mathrm{m}}(qa)\frac{\mathcal{I}_{\mathrm{m}}(q)K_{\mathrm{m}}(qr_0) - \mathcal{K}_{\mathrm{m}}(q)I_{\mathrm{m}}(qr_0)}{\mathcal{K}_{\mathrm{m}}(q)I_{\mathrm{m}}(qa) - \mathcal{I}_{\mathrm{m}}(q)K_{\mathrm{m}}(qa)} \\ B_{\mathrm{m}} &= \mathcal{I}_{\mathrm{m}}(q)\frac{I_{\mathrm{m}}(qr_0)K_{\mathrm{m}}(qa) - K_{\mathrm{m}}(qr_0)I_{\mathrm{m}}(qa)}{\mathcal{K}_{\mathrm{m}}(q)I_{\mathrm{m}}(qa) - \mathcal{I}_{\mathrm{m}}(q)K_{\mathrm{m}}(qa)} \end{aligned} \tag{3.17}$$

where we abbreviated:

$$\begin{aligned} \mathcal{I}_{\mathrm{m}}(q) &= \kappa I_{\mathrm{m}}(q\sigma) + qI'_{\mathrm{m}}(q\sigma) \\ \mathcal{K}_{\mathrm{m}}(q) &= \kappa K_{\mathrm{m}}(q\sigma) + qK'_{\mathrm{m}}(q\sigma) \end{aligned} \tag{3.18}$$

With these coefficients the particular solution to the initial problem is completely determined in LAPLACE space.

Inverse Laplace transform

We may transform the solution back into the time domain as usual by calculating the BROMWICH integral

$$\begin{aligned} p_{\mathbf{r}}(r,\phi,t|r_0,\phi_0) &= \lim_{\mathrm{T}\to\infty} \int_{\gamma-\mathrm{iT}}^{\gamma+iT} \hat{p}_{\mathbf{r}}(r,\phi,s|r_0,\phi_0)e^{st}ds \\ &= \lim_{\mathrm{T}\to\infty} \int_{\gamma-\mathrm{iT}}^{\gamma+iT} \hat{p}_{\mathbf{r}}(r,\phi,q|r_0,\phi_0)e^{q^2D_{\mathrm{r}}t}(2D_{\mathrm{r}}q)dq \end{aligned} \tag{3.19}$$

where the integration as usual occurs on a line through a real constant γ located to the right of all singularities of function $\hat{p}_{\mathbf{r}}(r,\phi,q|r_0,\phi_0)$ extended to the complex plane. Assuming convergence of the sum, we can perform the integration term-wise.

This somewhat lengthy calculation shall be omitted here. It ultimately yields:

$$p_{\mathbf{r}}(r,\phi,t|r_0,\phi_0) = \frac{\pi}{4}\sum_{\mathrm{m}=-\infty}^{\infty}\cos\left(m(\phi-\phi_0)\right)\sum_{\mathrm{n}=1}^{\infty}\frac{\zeta_{\mathrm{mn}}^2\mathcal{R}_{\mathrm{m}}^2(\zeta_{\mathrm{mn}})\mathcal{J}_{\mathrm{mn}}(r)\mathcal{J}_{\mathrm{mn}}(r_0)}{\mathcal{R}_{\mathrm{m}}^2(\zeta_{\mathrm{mn}})-\zeta_{\mathrm{mn}}^2-\kappa^2-\frac{m^2}{\sigma^2}}e^{-\zeta_{\mathrm{mn}}^2 D_{\mathrm{r}}t} \tag{3.20}$$

where ζ_{mn} are the roots of the implicit equation

$$\begin{aligned}\frac{\kappa J_{\mathrm{m}}(\sigma\zeta_{\mathrm{mn}})-\zeta_{\mathrm{mn}}J'_{\mathrm{m}}(\sigma\zeta_{\mathrm{mn}})}{J_{\mathrm{m}}(a\zeta_{\mathrm{mn}})} &= \frac{\kappa Y_{\mathrm{m}}(\sigma\zeta_{\mathrm{mn}})-\zeta_{\mathrm{mn}}Y'_{\mathrm{m}}(\sigma\zeta_{\mathrm{mn}})}{Y_{\mathrm{m}}(a\zeta_{\mathrm{mn}})}\\ &\equiv \mathcal{R}_{\mathrm{m}}(\zeta_{\mathrm{mn}})\end{aligned} \tag{3.21}$$

with $\kappa = \frac{k}{D_{\mathrm{r}}}$ and

$$\mathcal{J}_{\mathrm{mn}}(r) \equiv J_{\mathrm{m}}(r\zeta_{\mathrm{mn}})Y_{\mathrm{m}}(a\zeta_{\mathrm{mn}}) - Y_{\mathrm{m}}(r\zeta_{\mathrm{mn}})J_{\mathrm{m}}(a\zeta_{\mathrm{mn}}) \tag{3.22}$$

As demonstrated in [89], the above function fulfills the diffusion equation (PDE), the boundary conditions (BCr) and (BCa) and the initial condition (IC).

By separating out the $m = 0$ term from the sum and unifying the summation over $m < 0$ and $m > 0$ with the help of cosine and BESSEL function (anti)symmetry relations, the Green's function (3.20) can be rewritten into a form that proves more convenient for further usage:

$$\begin{aligned}p_{\mathbf{r}}(r,\phi,t|r_0,\phi_0) = &\\ &\frac{\pi}{4}\sum_{\mathrm{n}=0}^{\infty}\frac{\zeta_{0\mathrm{n}}^2\mathcal{R}_0^2(\zeta_{0\mathrm{n}})\mathcal{J}_{0\mathrm{n}}(r)\mathcal{J}_{0\mathrm{n}}(r_0)}{\mathcal{R}_0^2(\zeta_{0\mathrm{n}})-\zeta_{0\mathrm{n}}^2-\kappa^2}e^{-\zeta_{0\mathrm{n}}^2 D_{\mathrm{r}}t}\\ &+\frac{\pi}{2}\sum_{\mathrm{m}=1}^{\infty}\sum_{\mathrm{n}=1}^{\infty}\cos\left(m(\phi-\phi_0)\right)\frac{\zeta_{\mathrm{mn}}^2\mathcal{R}_{\mathrm{m}}^2(\zeta_{\mathrm{mn}})\mathcal{J}_{\mathrm{mn}}(r)\mathcal{J}_{\mathrm{mn}}(r_0)}{\mathcal{R}_{\mathrm{m}}^2(\zeta_{\mathrm{mn}})-\zeta_{\mathrm{mn}}^2-\kappa^2-\frac{m^2}{\sigma^2}}e^{-\zeta_{\mathrm{mn}}^2 D_{\mathrm{r}}t}\end{aligned} \tag{3.23}$$

The advantage of this form of the Green's function is that here the double-sum term vanishes under the $\int_0^{2\pi} d\phi$ integral, which significantly facilitates the calculation of the survival probability and the boundary fluxes.

Survival probability

The survival probability $S(t)$ here is obtained by integrating the Green's function over the entire circular domain on which the 2D diffusion takes place:

$$S_{\mathbf{r}}(t) = \int_{\sigma}^{a} \int_{0}^{2\pi} p_{\mathbf{r}}(r, \phi, t | r_0, \phi_0) r d\phi dr \tag{3.24}$$

This is done most conveniently starting from (3.23), where the part with the sum over $m > 0$ disappears under the ϕ-integral because of $\int_0^{2\pi} \cos(m(\phi - \phi_0))\, d\phi = 0$. Hence, after interchanging the order of summation and integration:

$$\begin{aligned} S_{\mathbf{r}}(t) &= 2\pi \cdot \frac{\pi}{4} \sum_{\mathrm{n}=0}^{\infty} e^{-\zeta_{0\mathrm{n}}^2 D_{\mathrm{r}} t} \frac{\zeta_{0\mathrm{n}}^2 \mathcal{R}_0^2(\zeta_{0\mathrm{n}}) \mathcal{J}_{0\mathrm{n}}(r_0)}{\mathcal{R}_0^2(\zeta_{0\mathrm{n}}) - \zeta_{0\mathrm{n}}^2 - \kappa^2} \int_{\sigma}^{a} r \mathcal{J}_{0\mathrm{n}}(r) dr \\ &= \frac{\pi^2}{2} \sum_{\mathrm{n}=0}^{\infty} e^{-\zeta_{0\mathrm{n}}^2 D_{\mathrm{r}} t} \frac{\mathcal{R}_0^2(\zeta_{0\mathrm{n}}) \mathcal{J}_{0\mathrm{n}}(r_0)}{\mathcal{R}_0^2(\zeta_{0\mathrm{n}}) - \zeta_{0\mathrm{n}}^2 - \kappa^2} \left[\frac{2}{\pi} + \sigma \mathcal{J}'_{0\mathrm{n}}(\sigma) \right] \\ &\text{with } \mathcal{J}'_{0\mathrm{n}}(r) = \frac{d}{dr} \mathcal{J}_{0\mathrm{n}}(r) = \zeta_{0\mathrm{n}} \left[J_1(r\zeta_{0\mathrm{n}}) Y_0(a\zeta_{0\mathrm{n}}) - Y_1(r\zeta_{0\mathrm{n}}) J_0(a\zeta_{0\mathrm{n}}) \right] \end{aligned} \tag{3.25}$$

To calculate the integral we have employed the well-known relations $\int r J_0(r) dr = r J_1(r)$ and $J_1'(r) = -J_0(r)$ which analogously apply to $Y_0(r)$. The $\frac{2}{\pi}$ term within the brackets originates from $\mathcal{J}'_{0\mathrm{n}}(a) = -\frac{2}{\pi a}$ which can be shown with the help of the boundary conditions.

Boundary fluxes

We can calculate the probability fluxes through the radiative ($q_{\mathbf{r},\sigma}$) and absorbing ($q_{\mathbf{r},\mathrm{a}}$) domain boundaries at time t by integrating the probability density gradient over the two circular contours that constitute the boundaries:

$$\begin{aligned} q_{\mathbf{r},\sigma}(t) &= \int_0^{2\pi} +D_{\mathrm{r}} \partial_{\mathrm{r}} p_{\mathbf{r}}(r, \phi, t | r_0, \phi_0) \big|_{\mathrm{r}=\sigma} r d\phi \\ q_{\mathbf{r},\mathrm{a}}(t) &= \int_0^{2\pi} -D_{\mathrm{r}} \partial_{\mathrm{r}} p_{\mathbf{r}}(r, \phi, t | r_0, \phi_0) \big|_{\mathrm{r}=\mathrm{a}} r d\phi \end{aligned} \tag{3.26}$$

Here the signs account for opposite flux directions. In the modified form of the Green's function (3.23) again the $m \neq 0$ terms vanish under the ϕ-integral. The only r-dependent part of the $m = 0$ term is $\mathcal{J}_{0\mathrm{n}}(r)$, the derivative of which we have calculated in (3.25). With this we arrive at:

$$\begin{aligned} q_{\mathbf{r},\sigma}(t) &= 2\pi D_{\mathrm{r}} \cdot \frac{\pi}{4} \sum_{\mathrm{n}=0}^{\infty} e^{-\zeta_{0\mathrm{n}}^2 D_{\mathrm{r}} t} \frac{\zeta_{0\mathrm{n}}^2 \mathcal{R}_0^2(\zeta_{0\mathrm{n}}) \mathcal{J}_{0\mathrm{n}}(r_0)}{\mathcal{R}_0^2(\zeta_{0\mathrm{n}}) - \zeta_{0\mathrm{n}}^2 - \kappa^2} \sigma \mathcal{J}'_{0\mathrm{n}}(\sigma) \\ q_{\mathbf{r},\mathrm{a}}(t) &= 2\pi D_{\mathrm{r}} \cdot \frac{\pi}{4} \sum_{\mathrm{n}=0}^{\infty} e^{-\zeta_{0\mathrm{n}}^2 D_{\mathrm{r}} t} \frac{\zeta_{0\mathrm{n}}^2 \mathcal{R}_0^2(\zeta_{0\mathrm{n}}) \mathcal{J}_{0\mathrm{n}}(r_0)}{\mathcal{R}_0^2(\zeta_{0\mathrm{n}}) - \zeta_{0\mathrm{n}}^2 - \kappa^2} \underbrace{(-a \mathcal{J}'_{0\mathrm{n}}(a))}_{\frac{2}{\pi}} \end{aligned} \tag{3.27}$$

3.3.3 Green's function for binding to a cylindrical membrane

In order to faciliate the calculation of Green's functions, here we opted to implement binding to and diffusion on membranes in the arguably most straightforward way, representing the membrane with planar surfaces. In reality, however, cells typically have curved shapes. In particular, a cylindrical outer membrane would represent many types of yeast and bacteria more accurately. As a first step towards implementing curved membrane shapes into eGFRD we derived a Green's function for binding of a particle to a region on a cylindrical outer membrane. This is achieved by solving the diffusion equation on a cylindrical wedge domain, with a radiating boundary at the outer radius and absorbing boundary conditions elsewhere. While this function is not yet further used, for completeness we present it together with the resulting survival probability function in the appendix, in section 3.B.

3.4 Generalized linear coordinate transform for direct binding

In this section we present a generalization of the linear coordinate transform that maps two arbitrary particle positions $\mathbf{r}_\mathrm{A}$ and $\mathbf{r}_\mathrm{B}$ onto a (generalized) interparticle vector $\mathbf{r}$ and weighted center-of-mass vector $\mathbf{R}$ in a way that the diffusion anisotropy which arises in the direct binding scenario disappears in the transformed coordinates. To this end we pursue the following approach: First, we rewrite the linear operator (Laplacian) of the diffusion equation in a generic matrix notation in order to account for anisotropic diffusion, starting from the well-known form of the Smoluchowski equation. As a second step, we write down the linear coordinate transform in its most general form and apply it to both the linear operator and the original coordinates $\mathbf{r}_\mathrm{A}$ and $\mathbf{r}_\mathrm{B}$ in order to decouple the equation. Finally, the generic result will be used to specify a particular transform for the direct binding scenario. This involves some freedom in the choice of transformation coefficients. We therefore postulate the following criteria to constrain the result: First, the transformed Laplacian should not contain any mixed derivatives because this complicates the solution of the transformed equation. Second, the new coordinates should capture existing symmetries and, moreover, resemble the previously defined interparticle vector and center of mass as much as possible, so that we can use previously derived Green's functions.

3.4.1 Rewriting the Laplace operator in matrix notation

Let us recall the Smoluchowski equation for the density of the probability $p \equiv p(\mathbf{r}_\mathrm{A}, \mathbf{r}_\mathrm{B}, t|\mathbf{r}_\mathrm{A0}, \mathbf{r}_\mathrm{B0}, t_0)$ to find two diffusing particles A and B with diffusion constants D_A and D_B at positions $\mathbf{r}_\mathrm{A}$ and $\mathbf{r}_\mathrm{B}$, given that they started from $\mathbf{r}_\mathrm{A0}$ and $\mathbf{r}_\mathrm{B0}$ (compare to section 2.1.3):

$$\partial_\mathrm{t} p = [D_\mathrm{A}\nabla_\mathrm{A}^2 + D_\mathrm{B}\nabla_\mathrm{B}^2]\; p \tag{3.28}$$

Here for simplicity we neglect the force-interaction term, i.e. $F(\mathbf{r}_\mathrm{A} - \mathbf{r}_\mathrm{B}) = 0$.

By introducing

$$\nabla_{\mathrm{X}} \equiv \begin{pmatrix} \nabla_{\mathrm{A}} \\ \nabla_{\mathrm{B}} \end{pmatrix} \tag{3.29}$$

and its transpose $\nabla_{\mathrm{X}}^T \equiv (\nabla_{\mathrm{A}}, \nabla_{\mathrm{B}})$ the linear operator $\mathcal{L}^2 \equiv D_{\mathrm{A}}\nabla_{\mathrm{A}}^2 + D_{\mathrm{B}}\nabla_{\mathrm{B}}^2$ may be written in vector-matrix-notation as

$$\mathcal{L}^2 = \nabla_{\mathrm{X}}^T \begin{pmatrix} \mathcal{D}_{\mathrm{A}} & \\ & \mathcal{D}_{\mathrm{B}} \end{pmatrix} \nabla_{\mathrm{X}} \equiv \nabla_{\mathrm{X}}^T \mathcal{D} \nabla_{\mathrm{X}} \tag{3.30}$$

where the sub-matrices

$$\mathcal{D}_{\mathrm{A(B)}} \equiv \begin{pmatrix} D_{\mathrm{A(B)}} & & \mathbb{O} \\ & D_{\mathrm{A(B)}} & \\ \mathbb{O} & & D_{\mathrm{A(B)}} \end{pmatrix} \tag{3.31}$$

define a diffusion matrix $\mathcal{D}$. While here the entries of matrices $\mathcal{D}_{\mathrm{A}}$ and $\mathcal{D}_{\mathrm{B}}$ are equal along their diagonals, in general they may differ if diffusion is anisotropic. Importantly, the Laplacian $\mathcal{L}^2$ has no mixed derivatives only if $\mathcal{D}$ is diagonal.

3.4.2 Writing the linear coordinate transform in matrix notation

A generic linear coordinate transform $\mathcal{M} : \mathbb{R}^6 \to \mathbb{R}^6$ for two arbitrary $\mathbb{R}^3$-vectors $\mathbf{r}_{\mathrm{A}}$ and $\mathbf{r}_{\mathrm{B}}$ is described via:

$$\mathbf{r} \equiv a\mathbf{r}_{\mathrm{A}} + b\mathbf{r}_{\mathrm{B}} \,, \qquad \mathbf{R} \equiv c\mathbf{r}_{\mathrm{A}} + d\mathbf{r}_{\mathrm{B}} \,. \tag{3.32}$$

In matrix notation this reads

$$\mathbf{Y} \equiv \begin{pmatrix} \mathbf{r} \\ \mathbf{R} \end{pmatrix} = \mathcal{M} \begin{pmatrix} \mathbf{r}_{\mathrm{A}} \\ \mathbf{r}_{\mathrm{B}} \end{pmatrix} \equiv \mathcal{M}\mathbf{X} \tag{3.33}$$

with

$$\mathcal{M} = \begin{pmatrix} a & 0 & 0 & b & 0 & 0 \\ 0 & a & 0 & 0 & b & 0 \\ 0 & 0 & a & 0 & 0 & b \\ c & 0 & 0 & d & 0 & 0 \\ 0 & c & 0 & 0 & d & 0 \\ 0 & 0 & c & 0 & 0 & d \end{pmatrix} \equiv \begin{pmatrix} \mathcal{A} & \mathcal{B} \\ \mathcal{C} & \mathcal{D} \end{pmatrix} \,. \tag{3.34}$$

We may generalize this transform further by allowing the nonzero coefficients to differ from each other as long as the full rank of the matrix is preserved. In the following we therefore assume that $\mathcal{M}$ has the form:

$$\mathcal{M} = \begin{pmatrix} \mathcal{A} & \mathcal{B} \\ \mathcal{C} & \mathcal{D} \end{pmatrix} = \begin{pmatrix} a_1 & 0 & 0 & b_1 & 0 & 0 \\ 0 & a_2 & 0 & 0 & b_2 & 0 \\ 0 & 0 & a_3 & 0 & 0 & b_3 \\ c_1 & 0 & 0 & d_1 & 0 & 0 \\ 0 & c_2 & 0 & 0 & d_2 & 0 \\ 0 & 0 & c_3 & 0 & 0 & d_3 \end{pmatrix} \tag{3.35}$$

3.4.3 Transforming the Laplace operator

Let us now apply the generalized transform to the linear operator $\mathcal{L}^2$. This means expressing the derivatives ∂_{X_i} of the original coordinates in terms of derivatives ∂_{Y_i} of the new, transformed coordinates. The chain rule of differentiation yields:

$$\frac{\partial}{\partial X_i} = \frac{\partial Y_j}{\partial X_i}\frac{\partial}{\partial Y_j} \equiv N_{ij}\frac{\partial}{\partial Y_j} \tag{3.36}$$

The coefficeints $N_{ij} = \frac{\partial Y_j}{\partial X_i}$ define a new matrix $\mathcal{N}$. Since the considered transform is linear these coefficients must be constants and related to the entries of the matrix $\mathcal{M}$ via

$$\frac{\partial Y_i}{\partial X_j} = (\mathcal{M})_{ij} = N_{ji} \; . \tag{3.37}$$

Since for a linear transform the Jacobian and the matrix of the transform are identical, we have:

$$\begin{aligned} \mathcal{N} &= \mathcal{M}^T \\ \nabla_X &= \mathcal{M}^T \nabla_Y \end{aligned} \tag{3.38}$$

With this we may rewrite the linear operator as follows[1]:

$$\begin{aligned} \mathcal{L}^2 &= \nabla_X^T \begin{pmatrix} \mathcal{D}_A & \\ & \mathcal{D}_B \end{pmatrix} \nabla_X \\ &= \nabla_Y^T \mathcal{M} \begin{pmatrix} \mathcal{D}_A & \\ & \mathcal{D}_B \end{pmatrix} \mathcal{M}^T \nabla_Y \equiv \nabla_Y^T \mathcal{D}' \nabla_Y \equiv \Lambda^2 \end{aligned} \tag{3.39}$$

Here $\mathcal{D}'$ is the transformed diffusion matrix in the new coordinates. Recall that Λ^2 will not contain mixed derivatives after the coordinate transform only if $\mathcal{D}'$ is diagonal. By carrying out explicitly the above calculation we arrive at:

$$\mathcal{D}' = \begin{pmatrix} \mathcal{D}_A\mathcal{A}^2 + \mathcal{D}_B\mathcal{B}^2 & \mathcal{D}_A\mathcal{A}\mathcal{C} + \mathcal{D}_B\mathcal{B}\mathcal{D} \\ \mathcal{D}_A\mathcal{A}\mathcal{C} + \mathcal{D}_B\mathcal{B}\mathcal{D} & \mathcal{D}_A\mathcal{C}^2 + \mathcal{D}_B\mathcal{D}^2 \end{pmatrix} \tag{3.40}$$

Since all matrices involved in the above expression are diagonal by definition, the diagonality condition reduces to:

$$\begin{aligned} & \mathcal{D}_A\mathcal{A}\mathcal{C} + \mathcal{D}_B\mathcal{B}\mathcal{D} = \mathbb{O} \\ \Leftrightarrow \forall j: \quad & (\mathcal{D}_A)_{jj}a_j c_j + (\mathcal{D}_B)_{jj} b_j d_j = 0 \end{aligned} \tag{3.41}$$

We have now established a condition for transforming the Laplacian in a way that mixed derivatives disappear in the new coordinates. This is a generalization of the condition already mentioned in section 2.3.1. However note that we still can choose the transform coefficients freely as long as the above equation is fulfilled. We will now determine a specific choice that is appropriate for the considered direct binding scenario.

[1] We denote the new representation of the operator with a different sign, but formally $\Lambda^2 = \mathcal{L}^2$.

3.4.4 Particular transform for the direct binding scenario

In direct binding one of the particles (A) diffuses on a planar 2D submanifold of the $\mathbb{R}^3$ while the other particle (B) performs a standard isotropic 3D diffusion in $\mathbb{R}^3$. Let us assume that the 2D plane corresponds to the xy-plane of the Cartesian coordinate system, implying $D_{\mathrm{Az}} \equiv (\mathcal{D}_{\mathrm{A}})_{33} = 0$. The diffusion matrix in the original coordinates $\{\mathbf{r}_{\mathrm{A}}, \mathbf{r}_{\mathrm{B}}\}$ then reads:

$$\mathcal{D} = \begin{pmatrix} D_{\mathrm{A}} & 0 & 0 & 0 & 0 & 0 \\ 0 & D_{\mathrm{A}} & 0 & 0 & 0 & 0 \\ 0 & 0 & 0 & 0 & 0 & 0 \\ 0 & 0 & 0 & D_{\mathrm{B}} & 0 & 0 \\ 0 & 0 & 0 & 0 & D_{\mathrm{B}} & 0 \\ 0 & 0 & 0 & 0 & 0 & D_{\mathrm{B}} \end{pmatrix} \tag{3.42}$$

We now specify the coefficients of the transformation matrix $\mathcal{M}$ such that (3.41) holds and the off-diagonal elements of $\mathcal{D}'$ vanish. The latter requires either $b_3 = 0$ or $d_3 = 0$ because of $D_{\mathrm{Az}} = 0$ and $D_{\mathrm{Bz}} \neq 0$. To ensure that the z-component of the generalized interparticle vector $\mathbf{r}$ is nonzero, as in previous definitions, we opt for $d_3 = 0$. The transformed diffusion matrix $\mathcal{D}' = \mathcal{M}\mathcal{D}\mathcal{M}^T$ then becomes:

$$\mathcal{D}' = \begin{pmatrix} D_{\mathrm{A}}^2 a_1^2 + D_{\mathrm{B}}^2 b_1^2 & 0 & 0 & 0 & 0 & 0 \\ 0 & D_{\mathrm{A}}^2 a_2^2 + D_{\mathrm{B}}^2 b_2^2 & 0 & 0 & 0 & 0 \\ 0 & 0 & D_{\mathrm{B}} b_3^2 & 0 & 0 & 0 \\ 0 & 0 & 0 & D_{\mathrm{A}}^2 c_1^2 + D_{\mathrm{B}}^2 d_1^2 & 0 & 0 \\ 0 & 0 & 0 & 0 & D_{\mathrm{A}}^2 c_2^2 + D_{\mathrm{B}}^2 d_2^2 & 0 \\ 0 & 0 & 0 & 0 & 0 & 0 \end{pmatrix} \tag{3.43}$$

With this we may rewrite the Laplacian as follows:

$$\begin{aligned} \Lambda^2 &= \nabla_{\mathrm{Y}}^T (\mathcal{M}^T \mathcal{D} \mathcal{M}) \nabla_{\mathrm{Y}} \\ &= (D_{\mathrm{A}} a_1^2 + D_{\mathrm{B}} b_1^2) \partial_{\mathrm{r}_1}^2 + (D_{\mathrm{A}} a_2^2 + D_{\mathrm{B}} b_2^2) \partial_{\mathrm{r}_2}^2 + D_{\mathrm{B}} b_3^2 \partial_{\mathrm{r}_3}^2 \\ &\quad + (D_{\mathrm{A}} c_1^2 + D_{\mathrm{B}} d_1^2) \partial_{\mathrm{R}_1}^2 + (D_{\mathrm{A}} c_2^2 + D_{\mathrm{B}} d_2^2) \partial_{\mathrm{R}_2}^2 \end{aligned} \tag{3.44}$$

The fact that the prefactor of $\partial_{\mathrm{r}_3}^2$ is different from the prefactors of the other two components prevents us from regrouping the separate differential operators into a closed form. This is precisely the signature of anisotropic diffusion. Provided that we do not change the (full) rank of $\mathcal{M}$ we may choose the yet undetermined coefficients freely. Here we set

$$a_{1,2} = -1 \qquad b_{1,2} = +1 \tag{3.45}$$

to ensure that the first two components of $\mathbf{r}$ reproduce the ones of the standard interparticle vector. Then from (3.44) it is evident that setting $b_3 = \pm\sqrt{\frac{D_{\mathrm{A}} + D_{\mathrm{B}}}{D_{\mathrm{B}}}}$ yields equal prefactors for all three derivatives. With this choice we get rid of diffusion anisotropy by adequately rescaling the r_{z}-coordinate.

The corresponding transformation matrix $\mathcal{M}_{\mathrm{DB}}$ has the form

$$\mathcal{M}_{\mathrm{DB}} = \begin{pmatrix} -1 & 0 & 0 & 1 & 0 & 0 \\ 0 & -1 & 0 & 0 & 1 & 0 \\ 0 & 0 & a_3 & 0 & 0 & \pm\sqrt{1+\frac{D_\mathrm{A}}{D_\mathrm{B}}} \\ c_1 & 0 & 0 & d_1 & 0 & 0 \\ 0 & c_2 & 0 & 0 & d_2 & 0 \\ 0 & 0 & c_3 & 0 & 0 & 0 \end{pmatrix} \tag{3.46}$$

and in this particular case the diagonality condition (3.41) reads:

$$\begin{aligned} -D_\mathrm{A} c_\mathrm{j} + D_\mathrm{B} d_\mathrm{j} &= 0\,, \qquad j = 1,2 \\ \underbrace{(\mathcal{D}_\mathrm{A})_{33}}_{=0} a_3 c_3 + D_\mathrm{B} b_3 \underbrace{d_3}_{=0} &= 0 \end{aligned} \tag{3.47}$$

Evidently, the second line is fulfilled for any choice of a_3, b_3 and c_3. However, preserving full rank requires $c_3 \neq 0$. An adequate choice is $c_3 = \frac{1}{D_\mathrm{A}+D_\mathrm{B}}$. Moreover it is convenient to set $a_3 = -b_3$ and

$$c_\mathrm{j} = \frac{D_\mathrm{B}}{D_\mathrm{A}+D_\mathrm{B}}, \quad d_\mathrm{j} = \frac{D_\mathrm{A}}{D_\mathrm{A}+D_\mathrm{B}}, \quad j = 1,2 \quad . \tag{3.48}$$

With this the particular transform is completely determined and we finally arrive at the Laplacian in transformed coordinates:

$$\Lambda^2_{\mathrm{DB}} = \underbrace{(D_\mathrm{A}+D_\mathrm{B})}_{\equiv D_\mathrm{r}} \nabla^2_\mathrm{r} + \underbrace{\left(\frac{D_\mathrm{A} D_\mathrm{B}}{D_\mathrm{A}+D_\mathrm{B}}\right)}_{\equiv D_\mathrm{R}} \left(\partial^2_{\mathrm{R}_1} + \partial^2_{\mathrm{R}_2}\right) \tag{3.49}$$

This is structurally analogous to the operator yielded by the coordinate transform previously defined in section 2.3.1. However, here the transformed coordinates are different. The explicit (forward) transformation rules read:

$$\begin{aligned} \mathbf{r} &= \begin{pmatrix} r_{\mathrm{B}_1} - r_{\mathrm{A}_1} \\ r_{\mathrm{B}_2} - r_{\mathrm{A}_2} \\ b_3 r_{\mathrm{B}_3} + a_3 r_{\mathrm{A}_3} \end{pmatrix} = \begin{pmatrix} r_{\mathrm{B}_1} - r_{\mathrm{A}_1} \\ r_{\mathrm{B}_2} - r_{\mathrm{A}_2} \\ \varepsilon (r_{\mathrm{B}_3} - r_{\mathrm{A}_3}) \end{pmatrix}, \qquad \varepsilon \equiv \pm\sqrt{1+\frac{D_\mathrm{A}}{D_\mathrm{B}}} \\ \mathbf{R} &= \frac{1}{D_\mathrm{A}+D_\mathrm{B}} \begin{pmatrix} D_\mathrm{B} r_{\mathrm{A}_1} + D_\mathrm{A} r_{\mathrm{B}_1} \\ D_\mathrm{B} r_{\mathrm{A}_2} + D_\mathrm{A} r_{\mathrm{B}_2} \\ r_{\mathrm{A}_3} \end{pmatrix} \end{aligned} \tag{3.50}$$

The formula for $\mathbf{r}$ demonstrates that in the new coordinate system anisotropy is cancelled by rescaling the z-component of the interparticle vector. The sign of the scaling factor ε may be chosen freely; in the following we opt for the positive solution. Note that $r_{\mathrm{A}_3} = const$ because the 2D particle (A) is always in the plane by definition.

For completeness we once again explicitly state the final version of the transformation matrix $\mathcal{M}_{\mathrm{DB}}$:

$$\mathcal{M}_{\mathrm{DB}} = \begin{pmatrix} -1 & 0 & 0 & 1 & 0 & 0 \\ 0 & -1 & 0 & 0 & 1 & 0 \\ 0 & 0 & -\varepsilon & 0 & 0 & \varepsilon \\ \varepsilon^{-2} & 0 & 0 & \frac{D_{\mathrm{A}}}{D_{\mathrm{B}}}\varepsilon^{-2} & 0 & 0 \\ 0 & \varepsilon^{-2} & 0 & 0 & \frac{D_{\mathrm{A}}}{D_{\mathrm{B}}}\varepsilon^{-2} & 0 \\ 0 & 0 & D_{\mathrm{r}}^{-1} & 0 & 0 & 0 \end{pmatrix} \tag{3.51}$$

The determinant of this matrix is

$$\det(\mathcal{M}_{\mathrm{DB}}) = \frac{-\varepsilon}{D_{\mathrm{A}} + D_{\mathrm{B}}} = \frac{\mp 1}{\sqrt{D_{\mathrm{B}}(D_{\mathrm{A}} + D_{\mathrm{B}})}} \neq 0 \tag{3.52}$$

confirming that our specific coefficient choice preserves the full-rank property.

3.4.5 Inverse transform

To obtain the inverse transformation rule we simply calculate the inverse of matrix $\mathcal{M}_{\mathrm{DB}}$ (3.51):

$$\mathcal{M}_{\mathrm{DB}}^{-1} = \begin{pmatrix} -\frac{D_{\mathrm{A}}}{D_{\mathrm{B}}}\varepsilon^{-2} & 0 & 0 & 1 & 0 & 0 \\ 0 & -\frac{D_{\mathrm{A}}}{D_{\mathrm{B}}}\varepsilon^{-2} & 0 & 0 & 1 & 0 \\ 0 & 0 & 0 & 0 & 0 & D_{\mathrm{r}} \\ \varepsilon^{-2} & 0 & 0 & 1 & 0 & 0 \\ 0 & \varepsilon^{-2} & 0 & 0 & 1 & 0 \\ 0 & 0 & \varepsilon^{-1} & 0 & 0 & D_{\mathrm{r}} \end{pmatrix} \tag{3.53}$$

This results in the following back-transform rules:

$$\mathbf{r}_{\mathrm{A}} = \begin{pmatrix} R_1 - \frac{D_{\mathrm{A}}}{D_{\mathrm{A}}+D_{\mathrm{B}}} r_1 \\ R_2 - \frac{D_{\mathrm{A}}}{D_{\mathrm{A}}+D_{\mathrm{B}}} r_2 \\ (D_{\mathrm{A}} + D_{\mathrm{B}}) R_3 \end{pmatrix}$$

$$\mathbf{r}_{\mathrm{B}} = \begin{pmatrix} R_1 + \frac{D_{\mathrm{B}}}{D_{\mathrm{A}}+D_{\mathrm{B}}} r_1 \\ R_2 + \frac{D_{\mathrm{B}}}{D_{\mathrm{A}}+D_{\mathrm{B}}} r_2 \\ (D_{\mathrm{A}} + D_{\mathrm{B}}) R_3 + \sqrt{\frac{D_{\mathrm{B}}}{D_{\mathrm{A}}+D_{\mathrm{B}}}} r_3 \end{pmatrix} \tag{3.54}$$

We will now explain how the derived transform may be used to sample next-event information for the direct binding scenario using some of the Green's functions that we have already presented within this thesis.

3.4.6 Using known Green's Functions for the transformed problem

By applying the coordinate transform in the way described we succeeded in transforming the two-particle problem in 3D into two separate diffusion problems, namely a 2D-diffusion of the center-of-mass vector $\mathbf{R}$ and a 3D-diffusion of the interparticle vector $\mathbf{r}$, with a z-axis rescaled by $\varepsilon \geq 1$. Since diffusion of $\mathbf{R}$ in the plane is still isotropic after the transform, we may sample next-event times and new positions for $\mathbf{R}$ in the same way as for the *Planar Surface Pair*, i.e. by imposing a circular absorbing boundary at $|\mathbf{R}| = R_{\max}$ and reusing the Green's function presented in section 3.3.1.

The situation is different for the rescaled interparticle vector $\mathbf{r}$. In 3D, where diffusion of the interparticle vector is isotropic, radiating or absorbing boundary conditions are defined on spheres. Here, by rescaling the z-axis all lengths in z-direction become slightly longer with respect to the other directions in the new coordinate system, meaning that boundaries originally represented by spheres now become prolate spheroids (Figure 3.3). Since it is technically challenging to compute the Green's function for such boundary conditions, we opted for a simpler, approximative approach, in which the prolate spheroidal boundaries in the transformed coordinates are substituted by spherical boundaries. As an evident advantage, with spherical boundaries we may reuse the well-known 3D Green's function for a radiating inner and absorbing outer boundary. Given that the diffusion constant in the plane is significantly smaller than the diffusion constant in the bulk, e.g. $D_{\mathrm{A}} \simeq D_{\mathrm{B}}/10$, the scaling factor $\varepsilon = \sqrt{1 + D_{\mathrm{A}}/D_{\mathrm{B}}}$ is rather small ($\varepsilon \simeq 1.05$), implying only a minor error induced by the substitution.

As a further modification, we choose the radius of the inner, radiating sphere in such a way that its surface area equals the surface area of the prolate spheroidal. The rationale here is that equal surface areas will ensure that the total probability flux through the new, spherical boundary will be approximately equal to the total flux through the original, prolate boundary. Let the radius of the boundary sphere in the untransformed coordinate system be σ. The sphere transforms to a prolate spheroidal with semi-major axis length $A = \varepsilon\sigma$, whereas the semi-minor axis a is identical to the radius σ (Figure 3.3). The surface area of a prolate spheroidal is given by:

$$A_{\mathrm{P}}(a, A) = 2\pi \left[a^2 + \frac{aA \arccos\left(\frac{a}{A}\right)}{\sin\left(\arccos\left(\frac{a}{A}\right)\right)} \right] \tag{3.55}$$

Setting this equal to the surface of a sphere with radius ρ, with the particular values for the half-axes from above, we obtain:

$$\begin{aligned} 4\pi\rho^2 &= 2\pi \left[\sigma^2 + \frac{\sigma(\varepsilon\sigma) \arccos\left(\frac{\sigma}{\varepsilon\sigma}\right)}{\sin\left(\arccos\left(\frac{\sigma}{\varepsilon\sigma}\right)\right)} \right] \\ \rho &= \sqrt[+]{\frac{1}{2}\left(1 + \frac{\varepsilon \arccos\left(\frac{1}{\varepsilon}\right)}{\sin\left(\arccos\left(\frac{1}{\varepsilon}\right)\right)}\right)} \cdot \sigma \end{aligned} \tag{3.56}$$

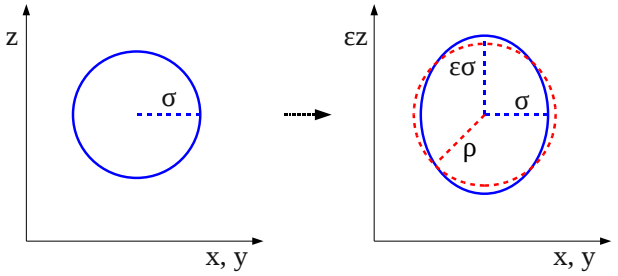

Figure 3.3: Distorsion of a spherical boundary due to the anisotropic coordinate transform.

To facilitate calculations we sample next-event information for the transformed inter-particle vector from the regular Green's function that assumes a spherical boundary, using ρ as defined above for the contact radius. Note that after back-transform sampled positions are located on oblate spheroids. This may cause particle overlap when the sampled new distance between the particles is short (comparable to σ); in this case particles are slightly moved apart, the error of which again is small.

3.5 Acknowledgements

Detailed calculations and tests of the 2D Green's function presented in section 3.3.2 were conducted by L. BOSSEN as part of his master's project.

The author further thanks N. BECKER and L. BOSSEN for fruitful discussions that contributed to the derivation of the generalized coordinate transform in section 3.4.

The author thanks A. HOFFMANN for critical reading of this chapter.

3.A Appendix: Deflection of particle trajectories at the edge between orthogonal planes

Here we describe the mathematical procedure that "deflects" the new position $\mathbf{r}_\nu$ of a plane-bound particle towards an adjacent, orthogonal "target" plane when $\mathbf{r}_\nu$ reaches beyond the boundaries of the original plane.

Imagine that the particle originally was located at position $\mathbf{r}_0$. To transform the trajectory of the diffusing particle towards the target plane first we calculate the point $\mathbf{S}$ at which the edge between the two planes intersects with the line $\mathbf{r}_0 + \lambda\Delta\mathbf{r}$ that links $\mathbf{r}_0$ and the new position $\mathbf{r}_\nu$. Let $\hat{\mathbf{u}}_\mathrm{x}$ and $\hat{\mathbf{u}}_\mathrm{z}$ be the unit vectors that define the orientation of the target plane and $\hat{\mathbf{u}}_\mathrm{z} \equiv \hat{\mathbf{u}}_\mathrm{x} \times \hat{\mathbf{u}}_\mathrm{y}$ the corresponding normal vector. Since $\mathbf{S}$ lies both on the line $\mathbf{r}_0 + \lambda\Delta\mathbf{r}$ and in the target plane, it must obey

$$\mathbf{S} \cdot \hat{\mathbf{u}}_\mathrm{z} = (\mathbf{r}_0 + \lambda_\mathrm{S}\Delta\mathbf{r}) \cdot \hat{\mathbf{u}}_\mathrm{z} = \mathbf{C} \cdot \hat{\mathbf{u}}_\mathrm{z} \tag{S3.1}$$

where $\mathbf{C}$ is the center point of the target plane[1]. With this we find

$$\mathbf{S} = \mathbf{r}_0 + \lambda_\mathrm{S}\Delta\mathbf{r} \qquad \text{with} \qquad \lambda_\mathrm{S} = \frac{(\mathbf{C} - \mathbf{r}_0) \cdot \hat{\mathbf{u}}_\mathrm{z}}{\Delta\mathbf{r} \cdot \hat{\mathbf{u}}_\mathrm{z}} \tag{S3.2}$$

and the protruding part of displacement vector $\Delta\mathbf{r}$:

$$\Delta\mathbf{r}' = (1 - \lambda_\mathrm{S})\Delta\mathbf{r} \tag{S3.3}$$

Instead of applying a rotation transform to $\Delta\mathbf{r}'$, here it is more convenient to construct the deflected position $\mathbf{r}'_\nu$ directly via

$$\mathbf{r}'_\nu = \mathbf{S} + \Delta r'_\parallel \hat{\mathbf{u}}_\parallel + \Delta r'_\perp \hat{\mathbf{u}}_\perp \tag{S3.4}$$

where $\Delta r'_\parallel = \Delta\mathbf{r}' \cdot \hat{\mathbf{u}}_\parallel$ is the component of $\Delta\mathbf{r}'$ parallel to the edge and $\Delta r'_\perp = \Delta\mathbf{r}' \cdot \hat{\mathbf{u}}_\mathrm{z}$ its component perpendicular to the edge. $\hat{\mathbf{u}}_\parallel$ is the target plane's unit vector parallel to the edge, whereas $\hat{\mathbf{u}}_\perp$ is the target plane's second unit vector, which is perpendicular to both $\hat{\mathbf{u}}_\parallel$ and $\hat{\mathbf{u}}_\mathrm{z}$. How precisely $\hat{\mathbf{u}}_\parallel$ and $\hat{\mathbf{u}}_\perp$ map onto the two unit vectors $\hat{\mathbf{u}}_\mathrm{x}$ and $\hat{\mathbf{u}}_\mathrm{y}$ that define the plane depends on the direction from which the particle enters the target plane. To avoid recalculation at each edge crossing, this information is stored in a neighborhood table when the box structure is constructed. It is easily proven that the deflected position is ensured to stay within the circular domain.

For the inverse transform we note that $\mathbf{S}$ is obtained by projecting $\mathbf{r}'_\nu$ onto the original plane. With this $\mathbf{r}_\nu$ is easily constructed via:

$$\mathbf{r} = \mathbf{r}_0 + |\mathbf{r}'_\nu - \mathbf{S}| \cdot \frac{\mathbf{S} - \mathbf{r}_0}{|\mathbf{S} - \mathbf{r}_0|} \tag{S3.5}$$

[1] Note that instead of C, alternatively we could choose any point located in the target plane.

3.B Appendix: Green's function for binding to a cylindrical membrane

Here we present the Green's function in cylindrical coordinates for a particle enclosed by a "wedge" with two reactive surfaces at radii $r = a$ and $r = b$ (with different intrinsic rates k_a, k_b). Thus, the particle is bounded by absorbing conditions at $z = 0$ and $z = L$ and at angles $\theta = 0$ and $\theta = \Theta$, while at radii $r = a$ and $r = b$ we impose radiating boundary conditions. The Green's function for this problem can be calculated by a product ansatz $p(r, \vartheta, z, t|r', \vartheta', z', t') = T(t)R(r)\Theta(\vartheta)$, following the workflow described in [58, p. 125ff], from which we also took the eigenfunctions used here. For brevity, we start by stating the final solution for the Green's function, and directly proceed to the calculation of the survival probability. Note that in eGFRD the solution of interest that models association to a cylindrical outer membrane is the one for the special case $k_\mathrm{a} = 0$.

Green's function

The final result for the Green's function on the reactive wedge domain reads

$$p(r, \vartheta, z, t|r', \vartheta', z', t') = \frac{8}{L\Theta} \sum_{\mathrm{k}} \sum_{\mathrm{m}} \sum_{\rho_{\mathrm{nm}}} \left\{ e^{-D(t-t')\left(\rho_{\mathrm{nm}}^2 + \frac{k^2\pi^2}{L^2}\right)} \sin\left(\frac{k\pi}{L} z\right) \sin\left(\frac{k\pi}{L} z'\right) \sin\left(l_\mathrm{m}\vartheta\right) \sin\left(l_\mathrm{m}\vartheta'\right) \times \frac{R_{l_\mathrm{m}}(\rho_{\mathrm{nm}} r) R_{l_\mathrm{m}}(\rho_{\mathrm{nm}} r')}{b^2 \left[\frac{k_\mathrm{b}^2}{D_\mathrm{b}^2} \frac{1}{\rho_{\mathrm{nm}}^2} + \left(1 - \frac{l_\mathrm{m}^2}{b^2 \rho_{\mathrm{nm}}^2}\right)\right] R_{l_\mathrm{m}}^2(\rho_{\mathrm{nm}} b) - a^2 \left[\frac{k_\mathrm{a}^2}{D_\mathrm{a}^2} \frac{1}{\rho_{\mathrm{nm}}^2} + \left(1 - \frac{l_\mathrm{m}^2}{a^2 \rho_{\mathrm{nm}}^2}\right)\right] R_{l_\mathrm{m}}^2(\rho_{\mathrm{nm}} a)} \right\} \tag{S3.6}$$

where $l_\mathrm{m} \equiv \frac{m\pi}{\Theta}$ are the eigenvalues of the ϑ-eigenfunctions. The radial eigenfunctions $R_{l_\mathrm{m}}(\rho_{\mathrm{nm}} r) \neq R(r)$ are defined as

$$R_{l_\mathrm{m}}(\rho_{\mathrm{nm}} r) = \frac{J_{l_\mathrm{m}}(\rho_{\mathrm{nm}} r)}{D_\mathrm{b} \rho_{\mathrm{nm}} J'_{l_\mathrm{m}}(\rho_{\mathrm{nm}} b) + k_\mathrm{b} J_{l_\mathrm{m}}(\rho_{\mathrm{nm}} b)} - \frac{Y_{l_\mathrm{m}}(\rho_{\mathrm{nm}} r)}{D_\mathrm{b} \rho_{\mathrm{nm}} Y'_{l_\mathrm{m}}(\rho_{\mathrm{nm}} b) + k_\mathrm{b} Y_{l_\mathrm{m}}(\rho_{\mathrm{nm}} b)} \tag{S3.7}$$

and ρ_{nm} are the roots of the transcendental equation

$$\frac{-D_\mathrm{a} \rho_{\mathrm{nm}} J'_{l_\mathrm{m}}(\rho_{\mathrm{nm}} a) + k_\mathrm{a} J_{l_\mathrm{m}}(\rho_{\mathrm{nm}} a)}{D_\mathrm{b} \rho_{\mathrm{nm}} J'_{l_\mathrm{m}}(\rho_{\mathrm{nm}} b) + k_\mathrm{b} J_{l_\mathrm{m}}(\rho_{\mathrm{nm}} b)} - \frac{-D_\mathrm{a} \rho_{\mathrm{nm}} Y'_{l_\mathrm{m}}(\rho_{\mathrm{nm}} a) + k_\mathrm{a} Y_{l_\mathrm{m}}(\rho_{\mathrm{nm}} a)}{D_\mathrm{b} \rho_{\mathrm{nm}} Y'_{l_\mathrm{m}}(\rho_{\mathrm{nm}} b) + k_\mathrm{b} Y_{l_\mathrm{m}}(\rho_{\mathrm{nm}} b)} = 0 \quad . \tag{S3.8}$$

The constants $D_{\mathrm{a/b}}$ and $k_{\mathrm{a/b}}$ originate from the boundary conditions for the radial function $R(r)$ at $r = a$ and $r = b > a$:

$$\begin{aligned} -D_\mathrm{a} \left[\partial_\mathrm{r} R\right]_{\mathrm{r=a}} &= -k_\mathrm{a} R(a) \\ D_\mathrm{b} \left[\partial_\mathrm{r} R\right]_{\mathrm{r=b}} &= -k_\mathrm{b} R(b) \end{aligned} \tag{S3.9}$$

Here we assume isotropic diffusion and therefore $D_\mathrm{a} = D_\mathrm{b} = D$.

Alternatively the solution may be written in terms of another set of eigenfunctions $\tilde{R}_{l_m}(\rho_{nm} r)$, which only differ from $R_{l_m}(\rho_{nm} r)$ by their coefficients and by the fact that they match the boundary condition at $r = a$ already by definition (while R_{l_m} does so with the BC at $r = b$):

$$\tilde{R}_{l_m}(\rho_{nm} r) = \frac{J_{l_m}(\rho_{nm} r)}{D_\mathrm{a}\rho_{nm} J'_{l_m}(\rho_{nm} a) - k_\mathrm{a} J_{l_m}(\rho_{nm} a)} - \frac{Y_{l_m}(\rho_{nm} r)}{D_\mathrm{a}\rho_{nm} Y'_{l_m}(\rho_{nm} a) - k_\mathrm{a} Y_{l_m}(\rho_{nm} a)} \tag{S3.10}$$

Since $R_{l_m}(\rho_{nm} r)$ and $\tilde{R}_{l_m}(\rho_{nm} r)$ are of the same structure, the normalization constant is computed in the same way in both cases.
The solution $\tilde{p}(r, \vartheta, z, t | r', \vartheta', z', t')$ then also has the same structure as before:

$$\begin{aligned}
&\tilde{p}(r, \vartheta, z, t | r', \vartheta', z', t') = \\
&\frac{8}{L\Theta} \sum_\mathrm{k} \sum_\mathrm{m} \sum_{\rho_{nm}} \left\{ e^{-D(t-t')\left(\rho_{nm}^2 + \frac{k^2\pi^2}{L^2}\right)} \sin\left(\frac{k\pi}{L} z\right) \sin\left(\frac{k\pi}{L} z'\right) \sin(l_m \vartheta) \sin(l_m \vartheta') \times \right. \\
&\left. \frac{\tilde{R}_{l_m}(\rho_{nm} r) \tilde{R}_{l_m}(\rho_{nm} r')}{b^2 \left[\frac{k_\mathrm{b}^2}{D_\mathrm{b}^2} \frac{1}{\rho_{nm}^2} + \left(1 - \frac{l_m^2}{b^2 \rho_{nm}^2}\right)\right] \tilde{R}_{l_m}^2(\rho_{nm} b) - a^2 \left[\frac{k_\mathrm{a}^2}{D_\mathrm{a}^2} \frac{1}{\rho_{nm}^2} + \left(1 - \frac{l_m^2}{a^2 \rho_{nm}^2}\right)\right] \tilde{R}_{l_m}^2(\rho_{nm} a)} \right\}
\end{aligned} \tag{S3.11}$$

However, the roots ρ_{nm} this time are to be determined from:

$$\frac{-D_\mathrm{b}\rho_{nm} J'_{l_m}(\rho_{nm} b) + k_\mathrm{b} J_{l_m}(\rho_{nm} b)}{D_\mathrm{a}\rho_{nm} J'_{l_m}(\rho_{nm} a) - k_\mathrm{a} J_{l_m}(\rho_{nm} a)} - \frac{-D_\mathrm{b}\rho_{nm} Y'_{l_m}(\rho_{nm} b) + k_\mathrm{b} Y_{l_m}(\rho_{nm} b)}{D_\mathrm{a}\rho_{nm} Y'_{l_m}(\rho_{nm} a) + k_\mathrm{a} Y_{l_m}(\rho_{nm} a)} = 0 \tag{S3.12}$$

Solution 14.15(3) in [57], in which also the radial boundaries are completely absorbing, can be reconstructed from the above expression by taking $k_\mathrm{a}, k_\mathrm{b} \to \infty$.

Survival probability

To obtain the survival probability from the calculated Green's function we have to integrate the latter on the whole domain of support, thus calculate the integral $\int_0^L \int_0^\Theta \int_\mathrm{a}^b p(r, \vartheta, z, t) r dr d\vartheta dz$.

Since the z- and ϑ-dependend parts are simple trigonometric functions, these integrals are readily obtained:

$$\begin{aligned}
\mathcal{I}_\mathrm{z} &= \int_0^L \sin\left(\frac{k\pi}{L} z\right) dz = \frac{L}{k\pi} \left[1 - \cos(k\pi)\right] = \frac{2L}{(2k'+1)\pi} \\
\mathcal{I}_\vartheta &= \int_0^\Theta \sin\left(\frac{m\pi}{\Theta} \vartheta\right) d\vartheta = \frac{\Theta}{m\pi} \left[1 - \cos(m\pi)\right] = \frac{2L}{(2m'+1)\pi}
\end{aligned} \tag{S3.13}$$

In the last steps we account for the fact that

$$\begin{aligned} 1-\cos(n\pi) &= 2 \quad \text{for } n \text{ odd} \\ 1-\cos(n\pi) &= 0 \quad \text{for } n \text{ even} \end{aligned} \tag{S3.14}$$

so that we can directly replace $k \to (2k'+1) \in 2\mathbb{N}+1$, $m \to (2m'+1) \in 2\mathbb{N}+1$.

While the z- and ϑ-integrations are straightforward, the integral over the r-component is more demanding. It contains a particular type of HANKEL function, which consists of both regular and irregular BESSEL functions of arbitrary order.

Definite integrals over $rJ_\nu(r)$ or $rY_\nu(r)$ typically yield hypergeometric series. Here we use

$$\begin{aligned} &\int rJ_\nu(\rho r)dr = \frac{r^2}{2}\left(\frac{\rho r}{2}\right)^\nu \Gamma(1+\frac{\nu}{2})\,{}_1\tilde{F}_2\left(1+\frac{\nu}{2},\left\{1+\nu,2+\frac{\nu}{2}\right\},-\left(\frac{\rho r}{2}\right)^2\right) \\ &\int rY_\nu(\rho r)dr = \\ &\qquad \cos(\nu\pi)\frac{r^2}{2}\left(\frac{\rho r}{2}\right)^\nu \Gamma(1+\frac{\nu}{2})\,{}_1\tilde{F}_2\left(1+\frac{\nu}{2},\left\{1+\nu,2+\frac{\nu}{2}\right\},-\left(\frac{\rho r}{2}\right)^2\right) \\ &\qquad -\frac{4^\nu}{\sin(\nu\pi)}\frac{r^2}{2}\left(\frac{1}{2\rho r}\right)^\nu \Gamma(1-\frac{\nu}{2})\,{}_1\tilde{F}_2\left(1-\frac{\nu}{2},\left\{1-\nu,2-\frac{\nu}{2}\right\},-\left(\frac{\rho r}{2}\right)^2\right) \end{aligned} \tag{S3.15}$$

where ${}_{\mathrm{p}}\tilde{F}_{\mathrm{q}}(\cdot,\cdot,\cdot)$ is the regularized generalized hypergeometric function. The first part of the Y_ν-integral differs from the J_ν-integral only by the cosine prefactor. The rdr-integral of a HANKEL-type function $\Psi J_\nu(\rho r)+\Upsilon Y_\nu(\rho r)$ (with r-independent prefactors Ψ and Υ) therefore may be written as:

$$\begin{aligned} &\int \left[\Psi J_\nu(\rho r)+\Upsilon Y_\nu(\rho r)\right] rdr = \\ &\qquad \left(\Psi+\Upsilon\cos(\nu\pi)\right)\frac{r^2}{2}\left(\frac{\rho r}{2}\right)^\nu \Gamma(1+\frac{\nu}{2})\,{}_1\tilde{F}_2\left(1+\frac{\nu}{2},\left\{1+\nu,2+\frac{\nu}{2}\right\},-\left(\frac{\rho r}{2}\right)^2\right) \\ &\qquad -\Upsilon\frac{r^2}{2}\frac{4^\nu}{\sin(\nu\pi)}\left(\frac{1}{2\rho r}\right)^\nu \Gamma(1-\frac{\nu}{2})\,{}_1\tilde{F}_2\left(1-\frac{\nu}{2},\left\{1-\nu,2-\frac{\nu}{2}\right\},-\left(\frac{\rho r}{2}\right)^2\right) \end{aligned} \tag{S3.16}$$

The regularized generalized hypergeometric function ${}_{\mathrm{p}}\tilde{F}_{\mathrm{q}}(\cdot,\cdot,\cdot)$ differs from the non-regularized version ${}_{\mathrm{p}}F_{\mathrm{q}}(\cdot,\cdot,\cdot)$ only by some gamma function factors:

$${}_{\mathrm{p}}\tilde{F}_{\mathrm{q}}(\{A_1,A_2,..,A_{\mathrm{p}}\},\{B_1,B_2,..,B_{\mathrm{q}}\},C) = \frac{{}_{\mathrm{p}}F_{\mathrm{q}}(\{A_1,A_2,..,A_{\mathrm{p}}\},\{B_1,B_2,..,B_{\mathrm{q}}\},C)}{\Gamma(B_1)\Gamma(B_2)..\Gamma(B_{\mathrm{q}})} \tag{S3.17}$$

Using this definition and $\Gamma(z+1) = z\Gamma(z)$ for the gamma function we obtain a form of the integral based on ${}_{\mathrm{p}}F_{\mathrm{q}}(\cdot,\cdot,\cdot)$, which facilitates later implementation:

$$\begin{aligned}\mathcal{Y}_\nu(\rho r) \equiv \int \left[\Psi J_\nu(\rho r) + \Upsilon Y_\nu(\rho r)\right] r dr = \\ \left(\Psi + \Upsilon\cos(\nu\pi)\right)\frac{r^2\left(\frac{\rho r}{2}\right)^\nu}{2(1+\frac{\nu}{2})\Gamma(1+\nu)}\ {}_1F_2\left(1+\frac{\nu}{2}, \left\{1+\nu, 2+\frac{\nu}{2}\right\}, -\left(\frac{\rho r}{2}\right)^2\right) \\ -\Upsilon\frac{r^2}{2(1-\frac{\nu}{2})\Gamma(1-\nu)}\frac{4^\nu}{\sin(\nu\pi)}\left(\frac{1}{2\rho r}\right)^\nu\ {}_1F_2\left(1-\frac{\nu}{2}, \left\{1-\nu, 2-\frac{\nu}{2}\right\}, -\left(\frac{\rho r}{2}\right)^2\right)\end{aligned} \tag{S3.18}$$

The above expression is the indefinite integral, whereas we will use the definite integral $\int_{\mathrm{a}}^{b}\left[\Psi J_\nu(\rho r) + \Upsilon Y_\nu(\rho r)\right] r dr = \mathcal{Y}_\nu(\rho b) - \mathcal{Y}_\nu(\rho a)$ in the expression for the survival probability.

Further detailed calculations shall be omitted here for brevity. Ultimately, for the survival probability we obtain the expression presented in the box on the following page. Note that here in contrast to the Green's function $p(r,t)$, the sums go over the odd k and m now, which is accounted for by $l_{\mathrm{m}} \to \hat{l}_{\mathrm{m}} \equiv l_{2\mathrm{m}+1}$.

The roots ρ_{nm} that appear in this function are to be calculated from:

$$\frac{-D_{\mathrm{a}}\rho_{\mathrm{nm}}J'_{\hat{\mathrm{l}}_{\mathrm{m}}}(\rho_{\mathrm{nm}}a) + k_{\mathrm{a}}J_{\hat{\mathrm{l}}_{\mathrm{m}}}(\rho_{\mathrm{nm}}a)}{D_{\mathrm{b}}\rho_{\mathrm{nm}}J'_{\hat{\mathrm{l}}_{\mathrm{m}}}(\rho_{\mathrm{nm}}b) + k_{\mathrm{b}}J_{\hat{\mathrm{l}}_{\mathrm{m}}}(\rho_{\mathrm{nm}}b)} - \frac{-D_{\mathrm{a}}\rho_{\mathrm{nm}}Y'_{\hat{\mathrm{l}}_{\mathrm{m}}}(\rho_{\mathrm{nm}}a) + k_{\mathrm{a}}Y_{\hat{\mathrm{l}}_{\mathrm{m}}}(\rho_{\mathrm{nm}}a)}{D_{\mathrm{b}}\rho_{\mathrm{nm}}Y'_{\hat{\mathrm{l}}_{\mathrm{m}}}(\rho_{\mathrm{nm}}b) + k_{\mathrm{b}}Y_{\hat{\mathrm{l}}_{\mathrm{m}}}(\rho_{\mathrm{nm}}b)} = 0 \tag{S3.19}$$

Possible simplifications

Evidently, the formulae for $p(r,t)$ and $S(t)$ are far from trivial. For an arbitrary wedge angle Θ, they involve the calculation of arbitrary order Bessel functions and hypergeometric series with non-integer arguments. A simple workaround that facilitates calculations is found by choosing rational values for Θ as follows

$$\Theta = \frac{\pi}{N}, \qquad N \in \mathbb{N}\backslash 0 \tag{S3.20}$$

because then

$$\begin{aligned} l_{\mathrm{m}} &= \frac{m\pi}{\Theta} = m\cdot N && \in \mathbb{N} \\ \hat{l}_{\mathrm{m}} &= \frac{(2m+1)\pi}{\Theta} = (2m+1)\cdot N && \in \mathbb{N} \end{aligned} \tag{S3.21}$$

This restriction implies a trade-off between the possible sizes of wedge domains and numerical calculation efficiency. At this point it cannot be predicted whether the above constraint will be advantageous or rather detrimental. However note that by choosing $\Theta = \frac{\pi}{2}, \frac{\pi}{3}, \frac{\pi}{4}, ..$ a fair amount of different cylindrical wedges can be generated.

$$S(t|r',\vartheta',z',t') =$$

$$\frac{32}{\pi^2}\sum_{\mathrm{k}}\sum_{\mathrm{m}}\sum_{\rho_{\mathrm{nm}}}\left\{e^{-D(t-t')\left[\rho_{\mathrm{nm}}^2+\left(\frac{(2k+1)\pi}{L}\right)^2\right]}\frac{\sin\left(\frac{(2k+1)\pi}{L}z'\right)\sin\left(\frac{(2m+1)\pi}{\Theta}\vartheta'\right)}{(2k+1)(2m+1)}\times\right.$$

$$\left.\frac{\left[\mathcal{Y}_{\hat{\mathrm{l}}_{\mathrm{m}}}(\rho_{\mathrm{nm}}b)-\mathcal{Y}_{\hat{\mathrm{l}}_{\mathrm{m}}}(\rho_{\mathrm{nm}}a)\right]R_{\hat{\mathrm{l}}_{\mathrm{m}}}(\rho_{\mathrm{nm}}r')}{b^2\left[\frac{k_{\mathrm{b}}^2}{D_{\mathrm{b}}^2}\frac{1}{\rho_{\mathrm{nm}}^2}+\left(1-\frac{\hat{l}_{\mathrm{m}}^2}{b^2\rho_{\mathrm{nm}}^2}\right)\right]R_{\hat{\mathrm{l}}_{\mathrm{m}}}^2(\rho_{\mathrm{nm}}b)-a^2\left[\frac{k_{\mathrm{a}}^2}{D_{\mathrm{a}}^2}\frac{1}{\rho_{\mathrm{nm}}^2}+\left(1-\frac{\hat{l}_{\mathrm{m}}^2}{a^2\rho_{\mathrm{nm}}^2}\right)\right]R_{\hat{\mathrm{l}}_{\mathrm{m}}}^2(\rho_{\mathrm{nm}}a)}\right\} \tag{S3.22}$$

with

$$R_{\hat{\mathrm{l}}_{\mathrm{m}}}(\rho_{\mathrm{nm}}r') \equiv \Psi J_{\hat{\mathrm{l}}_{\mathrm{m}}}(\rho_{\mathrm{nm}}r')+\Upsilon Y_{\hat{\mathrm{l}}_{\mathrm{m}}}(\rho_{\mathrm{nm}}r')$$
$$=\frac{J_{\hat{\mathrm{l}}_{\mathrm{m}}}(\rho_{\mathrm{nm}}r')}{D_{\mathrm{b}}\rho_{\mathrm{nm}}J'_{\hat{\mathrm{l}}_{\mathrm{m}}}(\rho_{\mathrm{nm}}b)+k_{\mathrm{b}}J_{\hat{\mathrm{l}}_{\mathrm{m}}}(\rho_{\mathrm{nm}}b)}-\frac{Y_{\hat{\mathrm{l}}_{\mathrm{m}}}(\rho_{\mathrm{nm}}r')}{D_{\mathrm{b}}\rho_{\mathrm{nm}}Y'_{\hat{\mathrm{l}}_{\mathrm{m}}}(\rho_{\mathrm{nm}}b)+k_{\mathrm{b}}Y_{\hat{\mathrm{l}}_{\mathrm{m}}}(\rho_{\mathrm{nm}}b)} \tag{S3.23}$$

and

$$\mathcal{Y}_{\mathrm{l}}(\rho b)-\mathcal{Y}_{\mathrm{l}}(\rho a) =$$
$$\frac{\Psi+\Upsilon\cos(l\pi)}{2(1+\frac{l}{2})\Gamma(1+l)}\left[b^2\left(\frac{\rho b}{2}\right)^l{}_1F_2\left(1+\frac{l}{2},\left\{1+l,2+\frac{l}{2}\right\},-\left(\frac{\rho b}{2}\right)^2\right)\right.$$
$$\left.-a^2\left(\frac{\rho a}{2}\right)^l{}_1F_2\left(1+\frac{l}{2},\left\{1+l,2+\frac{l}{2}\right\},-\left(\frac{\rho a}{2}\right)^2\right)\right]$$
$$-\frac{\Upsilon 4^l}{2\sin(l\pi)\left(1-\frac{l}{2}\right)\Gamma(1-l)}\left[b^2\left(\frac{1}{2\rho b}\right)^l{}_1F_2\left(1-\frac{l}{2},\left\{1-l,2-\frac{l}{2}\right\},-\left(\frac{\rho b}{2}\right)^2\right)\right.$$
$$\left.-a^2\left(\frac{1}{2\rho a}\right)^l{}_1F_2\left(1-\frac{l}{2},\left\{1-l,2-\frac{l}{2}\right\},-\left(\frac{\rho a}{2}\right)^2\right)\right]$$

where we further have abbreviated:

$$\rho\equiv\rho_{\mathrm{nm}}\,,\qquad l\equiv\hat{l}_{\mathrm{m}}\equiv l_{2\mathrm{m}+1}=\frac{(2m+1)\pi}{\Theta}\,,$$
$$\Psi\equiv\frac{1}{D_{\mathrm{b}}\rho_{\mathrm{nm}}J'_{\hat{\mathrm{l}}_{\mathrm{m}}}(\rho_{\mathrm{nm}}b)+k_{\mathrm{b}}J_{\hat{\mathrm{l}}_{\mathrm{m}}}(\rho_{\mathrm{nm}}b)},\qquad \Upsilon\equiv\frac{1}{D_{\mathrm{b}}\rho_{\mathrm{nm}}Y'_{\hat{\mathrm{l}}_{\mathrm{m}}}(\rho_{\mathrm{nm}}b)+k_{\mathrm{b}}Y_{\hat{\mathrm{l}}_{\mathrm{m}}}(\rho_{\mathrm{nm}}b)} \tag{S3.24}$$

Chapter 4

Simulating polarized growth factor delivery in fission yeast

4.1 Introduction

How different cell types can produce different shapes is a fundamental question in cell biology. As a relatively simple eukaryotic single-cell organism that is easy to control and manipulate, fission yeast (*Schizosaccharomyces pombe*) became one of the most intensely studied model systems of single-cell morphogenesis. Fission yeast cells have an elongated, rod-like shape with a highly reproducible diameter of ca. 3 μm and a cell-cycle-dependent length on the order of $8 - 14$ μm [90]. The rod-like shape results from restriction of cell growth to two opposite regions on the cell cortex that are marked by accumulations of growth factor proteins. Knock-out experiments have identified many key components of fission yeast polarization. Intriguingly, they suggest that the localization of growth factors to the growing poles of the cell is established via a symmetry-breaking mechanism that combines active transport on the cytoskeleton, diffusion on the membrane and shuttling of proteins between cytoplasm, cytoskeleton and membrane.

To elucidate this interplay we developed a spatially-resolved model of growth factor polarization that features microtubules and a fully membrane-enclosed cell volume, and conducted stochastic simulations of the model with eGFRD. Our model is representative of the Tea1/Mod5-system, which is described in detail in section 4.2. It contains two species: a permanently membrane-bound species M (Mod5) and species T (Tea1), which can diffuse in the cytoplasm, bind microtubules on which it can drift towards the cell poles, and form TM-complexes with M on the membrane. The TM-complexes have a finite lifetime; after TM-complex dissociation T moves back into the cytoplasm. This sets up a cycle in which T is transported actively from the cytoplasm to the membrane at the poles and passively returns from the membrane to the cytoplasm via diffusion on the membrane.

In order to identify the components of the considered system that are critical to establish proper growth factor polarization we compared models with different ways

of TM-complex formation at the membrane and systematically varied the membrane diffusion constant and the lifetime of the TM-complexes. We find that a "direct binding" model, in which growth factors T can bind to their membrane-bound partners M directly, exhibits better polarization properties than a "two-step binding" model, in which a T-particle first binds the membrane and then must find its reaction partner M via membrane diffusion. In the "direct binding" model, the simulations further reveal that cell polarization is enhanced with decreasing membrane diffusion constant of the TM-complexes. Moreover, there exists an optimal lifetime of TM-complexes on the membrane that maximizes both the efficiency of polarization, measured as the ratio between polar and central surface-density of TM-complexes, and the growth factor concentration at the poles.

In this chapter, we first give an overview of the current knowledge on fission yeast morphogenesis, discussing recent experimental findings. We then describe how we model the yeast cell and simulate polarization of growth factors with eGFRD. In the last part of this chapter we present and discuss our results.

4.2 Experimental facts

Elongated growth of fission yeast cells is controlled by polarity markers that agglomerate at the opposite cell poles in a mechanism that involves microtubules, actin and the cell membrane [43, 90, 91]. Once established, the agglomerations persist throughout interphase and promote continuous cell elongation from the poles, until growth stops during mitosis. Directly after cell division, cells only continue growing at the "old" pole opposite of the division site until the growth machinery is reconstituted at the "new" pole in G2 phase ("new end take off" / NETO) [92].

An essential polarity factor is the GTPase Cdc42, whose active form accumulates preferentially at the cell poles; cells with deleted or overexpressed *cdc42* produce under- or oversized round cells, respectively. Cdc42 also plays a crucial role in growth of other yeast types and is thought to activate a range of proteins that promote actin polymerization. Indeed, the growth sites at the cell poles feature patches of actin which are necessary to localize enzymes involved in cell wall synthesis and remodelling [43, 90]. Recently, the active form of Cdc42 was shown to exhibit oscillations between the cell poles [93]. Here, we do not focus on the Cdc42 system, but rather on another polarization system.

Among the most prominent polarity markers are further the proteins of the Tea familiy. While certain Tea protein complexes (Tea1/Tea4) play an essential role in establishing bipolar patterns of Cdc42 [94], the detailed interactions between Tea proteins and Cdc42 are yet poorly understood. Figure 4.1 summarizes the current picture of Tea-protein-based polarization in fission yeast. Proper localization of the Tea-family markers requires interaction with microtubules [45]. In fission yeast, microtubules form dynamic antiparallel bundles emerging from the cell center, with plus-ends growing towards and transiently remaining at the cell poles. The polarity marker Tea1 is delivered directly to the membrane at the poles by microtubule tips, to which it associates with the help of protein Tip1 [44, 95]. Tip1 is rapidly transported by the motor protein Tea2 towards the plus-end, where both proteins

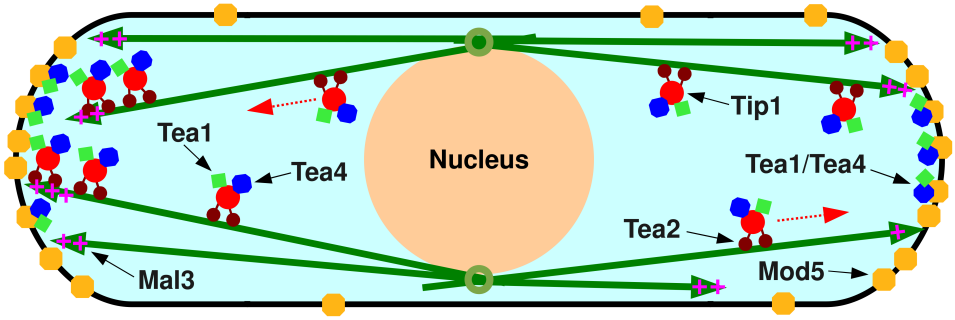

Figure 4.1: Schematic drawing of the currently assumed model of fission yeast growth polarization. Fission yeast forms elongated cells by restricting growth to opposite cell poles. This involves microtubules (dark green), which in fission yeast form dynamic antiparallel bundles with outwards-growing plus ends. Growth is restricted to the cell poles by accumulation of polarity factors Tea1 (green) and Tea4 (blue). Tea1 and Tea4 are transported towards microtubule plus-ends via Tip1 (light red) and kinesin motor protein Tea2 (dark red). These complexes accumulate at the plus-end with the help of tip-tracking protein Mal3 (magenta). Membrane-bound protein Mod5 (yellow) is required for direct delivery of the markers to the membrane at the poles. On the membrane, Tea1 and Tea4 engage in complexes that promote actin assembly and subsequent recruitment of cell-wall-remodelling enzymes. Note that the drawing does not include other prominent polarity factors such as Cdc42, whose connection to the Tea-proteins is yet unclear.

form clusters [96]. To accumulate at the microtubule tip, they require the protein Mal3 [97], which belongs to the EB1 family of tip trackers. Cells with knocked-out *tea1* or its transporter *tea2* fail to establish two oppositely located growth sites; instead, a single growth site forms in a random spot on the cell wall, producing L- or T-shaped cells [98, 99, 100]. The same is observed in cells with shorter or completely depolymerized microtubules [45, 101]. While microtubules thus play a crucial role in Tea-protein polarization, there is also evidence that proper anchoring of Tea1 to the membrane requires the membrane protein Mod5 [102]. Consistently, Mod5 is localized to the cell poles in wild-type, whereas in a *tea1*-knockout it spreads out uniformly over the membrane. Since Mod5-turnover at the cell poles was found to be much faster than Tea1-turnover, it was proposed that Mod5 catalyzes the formation of membrane-bound Tea1-clusters [103]. An important role was also found for Tea4: like Tea1, it associates with growing microtubule plus-ends and together with Tea1 forms membrane-complexes that act as nucleators of actin assembly [94, 95, 104, 105].

Importantly, polarity factors also influence microtubule dynamics. At the microtubule plus-ends Tip1 acts as a stabilizing factor, reducing the microtubule catastrophy rate in the regions far from the cell poles [44]. Increase of the catastrophy rate at the poles was also found to depend on pushing forces and tip-accumulation of motors from the kinesin-8 family, which contribute to depolymerization of long microtubules at their plus-ends [81, 106]. Moreover, microtubules are hampered in directing their growth towards the cell poles in *tea1*-deletion mutants [82, 83].

Taken together, these observations suggest a polarization mechanism that involves 1D active transport on microtubules and diffusion in 2D and 3D: Microtubules recruit polarity markers such as Tea1 and Tea4 from the cytosol and direct them via active transport towards their plus-ends, where the markers accumulate aided by tip-trackers like Mal3. The plus-end clusters have a stabilizing effect on the microtubules, enhancing the probability to reach the cell poles. At the poles, the polarity markers are delivered to the cell membrane, where they bind and anchor with the help of highly mobile membrane-bound proteins such as Mod5. After forming membrane-bound complexes, the markers stimulate actin polymerization, leading to actin-mediated recruitment of wall-remodelling enzymes, and further cell growth.

The overwhelming number of interacting proteins involved in fission yeast growth polarization, which in addition employ different transport modes and partly appear to follow distinct strategies to set up bipolar patterns, prompted us to ask: Which components of this system are indeed critical for efficient polarization? Following a bottom-up approach, we therefore aimed at reconstituting a minimal model of growth factor polarization in fission yeast, i.e. a model that includes as few of the experimentally identified system components as possible while producing a robust bipolar pattern under biologically realistic, meaning stochastic conditions.

4.3 Model

In order to reconstitute a minimal mechanism of fission yeast polarization we developed a model which features 1D active transport on microtubules, 2D diffusion on the cell membrane, cytosolic diffusion in 3D and particle interactions across the different dimensions. Using eGFRD, we performed particle-based stochastic simulations of the spatially-resolved model. We considered the system on the observed timescale of polarization, i.e. minutes. Therefore our model neglects elongation of the cell, focusing on the spatio-temporal dynamics of polarity factors. The cell is thus modelled as a static rectangular box consisting of six interlinked finite planes representing the cell membrane, with an aspect ratio typical of interphase fission yeast; exemplary 3D views of the model geometry are shown in Figure 4.3. At the mid-plane of the long axis of the box, we symmetrically place four pairs of antiparallel capped rods whose orientation vectors point outwards, representing microtubules with plus-ends directed towards the cell poles. Here we considered only static rods, i.e. microtubules with a fixed length; the influence of microtubule dynamics will be studied in forthcoming work. In our model, the microtubule bundles are almost as long as the box, with tips located in proximity to the poles.

As shown in Figure 4.2, the model features two principal chemical species: the cytosolic species T, which represents a polarity factor protein, e.g. Tea1, and the membrane-bound species M, representative of the Mod5 protein. T and M can form membrane-bound complexes TM with diffusion-limited on-rate; the lifetime τ of TM-complexes is a model parameter. The complex diffuses slower than the individual proteins. This is tuned via a "slowdown factor" χ that divides the standard 2D diffusion constant $D_2 = 0.1\ \mu\text{m}^2/\text{s}$ of a single membrane-bound protein. Most importantly, in our model Mod5 (M) acts only as a recruiting agent for Tea1 (T), i.e. the model

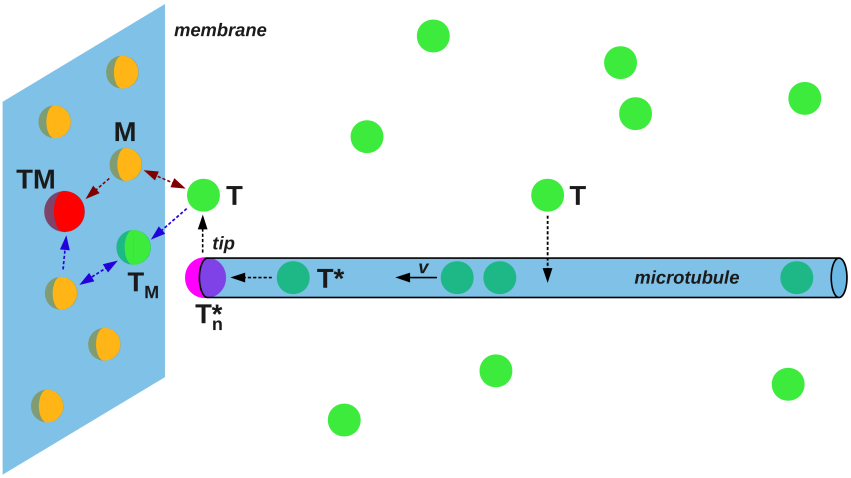

Figure 4.2: Schematic of the simulated fission yeast polarization model. Our model includes two protein species: a bulk species T (green), representative of (e.g.) Tea1, and a membrane-bound species M (yellow), representing Mod5. Upon binding of T to microtubles it is converted to T^* and transported towards the microtubule plus-end (tip) with drift velocity v. T^*-particles can agglomerate at the tip, forming clusters T^*_n (magenta), which "spawn" T-particles back into the cytosol close to the membrane. T and M can form membrane-bound complexes TM (red) which have a reduced mobility, tuned by model parameter s. We compare a "direct binding" scenario, in which T may bind M directly (red arrows), to a "two-stage binding" scenario, in which T first binds to the membrane to create T_M before forming TM (blue arrows).

does not assume a catalytic role for Mod5 in Tea1 polymerization on the membrane, as proposed previously [103]. We assume that species M is tightly bound to the membrane, i.e. never dissociates on the considered timescale. Moreover, we assume that on the given timescale protein production and degradation is negligible. Particle numbers thus only change due to formation and dissociation of TM-complexes. As a further important model feature, T-particles may also bind to the microtubules and convert to species T^*, which is transported outwards with significant drift until it reaches the cylinder cap. T^* represents the whole complex consisting of Tea1 or Tea4, Tip1 and the motor protein Tea2 as a single species. The cylinder cap (microtubule tip) can accumulate T^*-particles via a cascade of reactions of the type $T^*_n + T^* \rightarrow T^*_{n+1}$; for simplicity we represent a cluster of n T^*-particles by a single, immobile particle with increased radius (species T^*_n). A cap-bound cluster particle can "spawn" T particles at a rate k^u_{tip} back into the cytosol. In order to limit the combinatorial explosion of modelled reactions here we only considered a model in which T-particles unbind from the cap-bound cluster one by one.

To assess the role of the membrane-protein Mod5 in the polarization of the polarity markers, we compare a system with "direct binding", in which T directly associates with M, to a system with "two-stage binding", in which T first binds to the membrane to form T_M and then finds its reaction partner M via 2D diffusion.

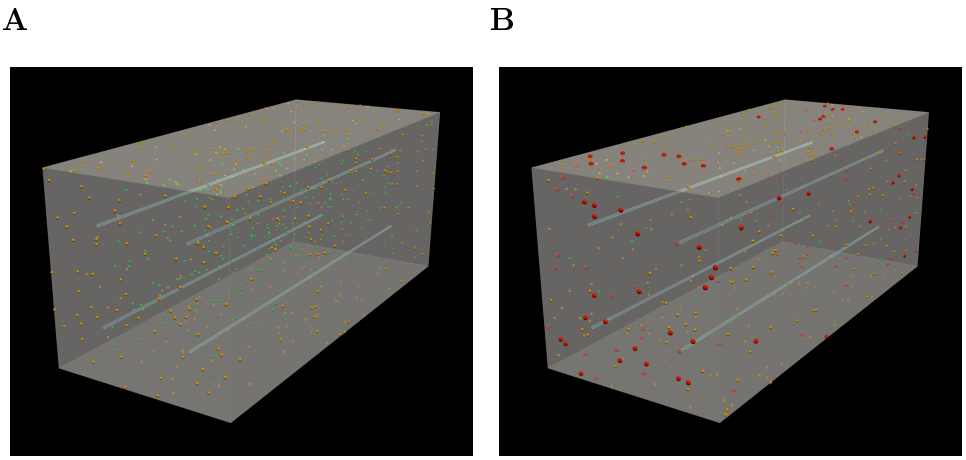

Figure 4.3: Typical 3D views of the polarization model simulated with eGFRD. We show here a typical initial (A) and final, polarized state (B) of the particle-based fission yeast model as simulated with eGFRD. The yeast cell is represented as a box consisting of interlinked finite planes, with lengths and aspect ratio corresponding to wild-type cells in interphase. Four microtubule bundles are modelled by eight pairwise antiparallel static cylinders oriented with their plus-ends outwards, starting from the mid-section of the box. Each bundle spans 95 % of the box length, with cylinder caps close to the two opposite "cell poles". Our model features two principal particle species, cytoplasmic species T (green) and membrane-bound species M (yellow), which can form membrane complexes TM (red; also see Fig. 4.2). T-particles can bind the microtubules to drift outwards, and return to the cytoplasm at the cylinder caps. The shown snapshots are for the system with direct binding, for complex diffusion constant $D_{\mathrm{TM}} = 0.01\ \mu\mathrm{m}^2/\mathrm{s}$ (slowdown factor $\chi = 10$) and complex lifetime $\tau = 10$ s.

4.3.1 Parameters

Here we briefly describe the choice of parameters in our model. Table 4.1 gives an overview of their standard values. Note that modelled species are not thought to represent single molecules but rather larger protein complexes, in particular in the microtubule-bound state.

The dimensions of the simulation box roughly correspond to the dimensions of a fission yeast cell in interphase. With the chosen aspect ratio between box length and width/height the surface-to-volume ratio of the box corresponds well to the surface-to-volume ratio of a spherocylinder of the same size. In our model, microtubules are static and their length is chosen such that their tips are close to the two box ends; the bundles therefore span 95 % of the box length. Particle and rod diameters have typical values for proteins and microtubules.

Since diffusion constants for the involved protein species are unknown we resorted to typical values. Thefore we set $D_3 = 1\ \mu\mathrm{m}^2/\mathrm{s}$ for the cytoplasmic diffusion constant and $D_2 = 0.1\ \mu\mathrm{m}^2/\mathrm{s}$ for the standard diffusion constant on the membrane. The diffusion constant of the membrane-bound TM-complex is equal to D_2/χ, where the slowdown factor $\chi = 1 - 100$ is varied.

Quantity	Symbol	Value	Unit
Geometry			
Simulation box length	l_{X}	9.5	μm
Simulation box width	l_{YZ}	4.0	μm
Microtubule (MT) length	l_{MT}	4.5	μm
Distance of MT axis from box sides	δ_{MT}	1.0	μm
Total membrane surface area	A_{mem}	240	$\mu\mathrm{m}^2$
Particles			
No. of cytoplasmic (T) particles	N_{T}	200	
No. of membrane-bound (M) particles	N_{M}	400	
Particle radius (TM-complexes)	R_{TM}	45	nm
Particle radius (all other species)	R_0	30	nm
Microtubule radius	r_0	25	nm
Mobility			
Cytoplasmic diffusion constant	D_3	1.0	$\mu\mathrm{m}^2/\mathrm{s}$
Standard membrane diffusion constant	D_2	0.1	$\mu\mathrm{m}^2/\mathrm{s}$
Standard 1D diffusion constant	D_1	0.1	$\mu\mathrm{m}^2/\mathrm{s}$
Membrane complex slowdown factor	χ	10–10^3	
Outwards drift velocity on MTs	v	0.5	$\mu\mathrm{m}/\mathrm{s}$
Kinetics			
T^*-unbinding rate from microtubule	$k^{\mathrm{u}}_{\mathrm{MT}}$	0	
$\mathrm{T}^*_{\mathrm{n}}$-dissociation rate from MT tip	$k^{\mathrm{u}}_{\mathrm{tip}}$	1.0	1/s
TM-complex dissociation rate	$k^{\mathrm{u}}_{\mathrm{TM}} = 1/\tau$	0.01–1.0	1/s
Dissociation rate of $\mathrm{T_M}$ from membrane	$k^{\mathrm{u}}_{\mathrm{T_M}} = 1/\tau$	0.01–1.0	1/s
binding rates		diff. ltd.	

Table 4.1: The standard parameters of the simulated fission yeast system.

We assume all binding rates to be diffusion-limited; the binding rates at contact are therefore set to high numerical values. For simplicity we set the unbinding rate from the microtubules to zero. Unbinding thus only happens from the microtubule tips at a rate $k^u_{\mathrm{tip}} = 1.0/\mathrm{s}$. The dissociation rate of TM-complexes is a model parameter that we vary.

4.3.2 Simulations and analysis

We conducted stochastic, particle-based simulations of the simplified yeast model defined in section 4.3 using eGFRD, with the new features defined in chapters 2 and 3. In all simulations, initially we randomly placed N_{T} T-particles in the cytosplasm and N_{M} M-particles on the membrane (the state shown in Fig. 4.3A). The system then was propagated for a fixed number of steps, usually resulting in several hundred seconds of simulated time. Particle data (positions and species) was acquired at approximately regular time points with a measurement interval of $\Delta t = 0.5$ s.

Initial simulations showed that the polarity-complex formation model indeed is capable of establishing polarity along the long axis of the simulation box on a timescale

of minutes. To quantify and compare the extent of polarization we introduced the following protocol: For all recorded time points, raw particle position data was binned into a coarse (six-bin) histogram along the long axis of the system. This was used to compute the average (area) density $\langle\rho\rangle$ of TM-complexes on the membrane for each bin by dividing the total particle number by the total membrane surface area in the bin. We then define the "polarization score" or "polarity" as the ratio between the average density in the two outermost bins at the poles $\langle\rho_{\mathrm{p}}\rangle$ and the average density $\langle\rho_{\mathrm{c}}\rangle$ in the two central bins:

$$\Pi \equiv \frac{\langle\rho_{\mathrm{p}}\rangle}{\langle\rho_{\mathrm{c}}\rangle} \tag{4.1}$$

The polarity Π quantifies the anisotropy of the TM-complex density in a straightforward way. However, high anisotropy does not necessarily imply a sufficiently high density of the complexes at the poles. Indeed, Π could be high, while the overall density at the poles is low. To capture the combined effect of polarization and density enhancement at the poles, we therefore also compute a "combined score" which increases with both TM-complex density and polarity, defined as:

$$\Gamma \equiv \langle\rho_{\mathrm{p}}\rangle\,\Pi = \frac{\langle\rho_{\mathrm{p}}\rangle^2}{\langle\rho_{\mathrm{c}}\rangle} \tag{4.2}$$

4.4 Results

We reasoned that two parameters of our model are crucial for the magnitude of TM-complex polarity: the slowdown of membrane diffusion upon complex formation, characterized by the slowdown factor χ, and τ, the mean lifetime of the complexes on the membrane. Since in our model particle binding to microtubules occurs (quasi) instantly after contact and microtubule-bound particles drift outwards very efficiently without interrupting unbindings, τ is the main determinant of the timescale of polarity marker recycling via cytoplasm and microtubules. To assess the dependence of polarity on χ and τ we performed a parameter sweep over these two quantities and compared the values of polarity Π and combined score Γ. We find that while increasing slowdown is beneficial for proper polarization, there exits an optimal lifetime $\tau_{\mathrm{opt}} = 10$ s of the complexes on the membrane that maximizes Γ.

In Figure 4.4 we plot the time evolution and a time average of the TM-complex surface density along the long (x-) axis of the system; we compare the system in which the cytoplasmic species T binds membrane-bound species M directly (4.4A) to the system in which T first has to associate with the membrane itself before it can form the complex with M (4.4B), for $\tau = 10$ s and $\chi = 10$. In both cases the density of the membrane-bound polarity marker complexes is enhanced at the poles. The systems are capable of establishing polarization on a timescale of $t \simeq 60$ s. However, while in the system with two-stage binding the overall complex density is slightly higher, polarization along the x-axis is significantly more pronounced in the system with direct binding ($\Pi = 4.32$ / $\Gamma = 3.17$ with direct binding vs. $\Pi = 1.64$ / $\Gamma = 1.64$

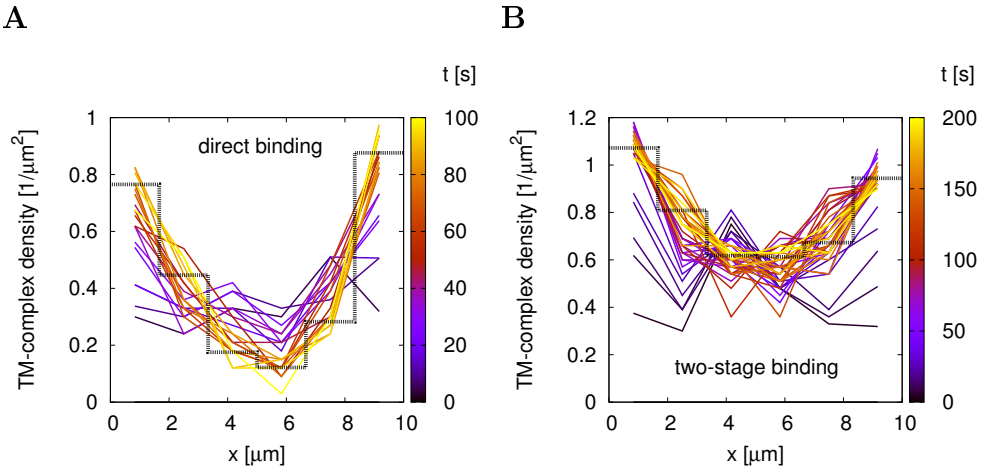

Figure 4.4: Establishment of TM-complex density polarization. Here we plot the time evolution of the average TM-complex surface density along the long (x-) axis of the simulation box for the systems with direct binding (A) and with two-stage binding (B), for complex lifetime $\tau = 10$ s and slowdown factor $\chi = 10$. The black dashed line shows the time average of the density over the last 30 s. Note that initially the complex density is zero because no membrane-complexes have formed yet. The expected system-wide average density when all T-particles have formed membrane complexes is $0.83/\mu\text{m}^2$.

with two-stage binding). Note that in the system with direct binding, membrane-complex density at the midplane of the system initially reaches higher values than at later times, when it is reduced simultaneously with the increase of the pole density. In contrast, in the system with two-stage binding the density at the center remains at the relatively high level that builds up at the onset of polarization.

As a next step we quantified the dependence of polarity on the two principal parameters of our system, the TM-complex lifetime τ and the complex slowdown factor χ. In Figure 4.5 we plot, for the system with direct binding, the polarity Π and the combined score Γ, which is the product of Π and the pole density $\langle\rho_\text{p}\rangle$, as a function of τ for different slowdown factors χ. The figure reveals the requirements for optimizing polarization in the considered system: First, for slowdown factors $\chi \geq 10$, i.e. for membrane-complex diffusion constants $D_\text{TM} \leq 0.01\ \mu\text{m}^2/\text{s}$, the system reaches significantly higher scores than for $\chi = 1$ ($D_\text{TM} = 0.1\ \mu\text{m}^2/\text{s}$). Moreover, figure 4.5A suggests that faster recycling of the complexes, corresponding to short complex lifetimes, leads to more efficient polarization. However, this neglects the fact that with decreasing complex lifetime τ also the complex density on the membrane decreases. Therefore there is a trade-off between polarity and membrane occupancy when reducing τ. This is captured by the combined score $\Gamma = \langle\rho_\text{p}\rangle\,\Pi$ (4.5B), which displays a maximum at $\tau_\text{opt} = 10$ s.

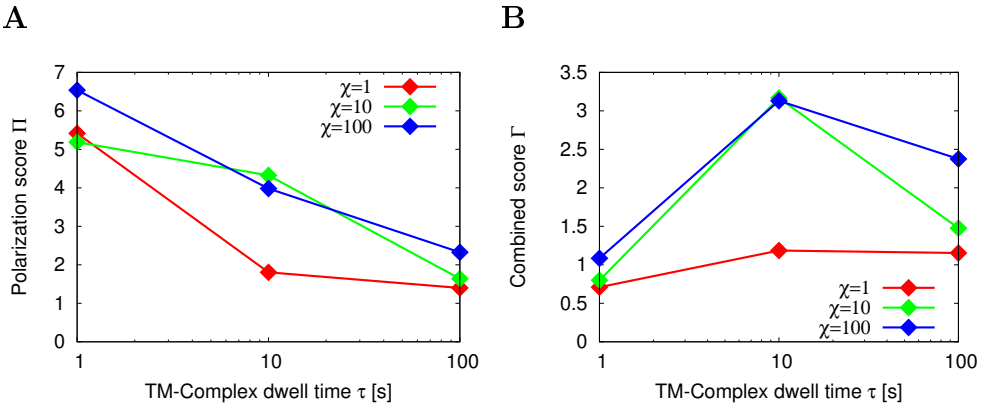

Figure 4.5: An optimal TM-complex dwell time maximizes the product of polarity and pole density in the system with direct binding. Plotted are (A) the polarization score Π and (B) the combined score $\Gamma = \langle \rho_{\mathrm{p}} \rangle \Pi$ as a function of τ, the TM-complex dwell time on the membrane, for different complex slowdown factors χ, in the system with direct binding. Slowdown is beneficial for polarity in general, and polarity increases with decreasing complex lifetime τ (A). Since binding is diffusion-limited, the latter simultaneously reduces the number of bound complexes; hence, there is a trade-off between polarity and pole occupancy that maximizes the combined score Γ for $\tau = 10$ s.

We compared these results to a system in which the ratio between membrane-bound particles (M) and polarity markers (T) was increased in favor of M ($N_{\mathrm{M}} = 600$, $N_{\mathrm{T}} = 200$). We found that while the density at the poles is slightly higher in that system, the principal findings still apply.

4.5 Discussion

In order to reconstitute a minimal model of yeast polarization we conducted stochastic, particle-based eGFRD-simulations of a model that features a cytoplasmic polarity marker species T (representing Tea1), which can bind microtubules which transport it towards the cell poles, and a membrane-bound species M (representing Mod5), with which T can form slow-diffusing heterodimeric polarity complexes TM on the membrane. The results presented in this chapter demonstrate that this simple system, with static microtubules that reach the proximity of the cell poles, is capable of establishing considerable polarity ($\Pi \gtrsim 4$) along the long axis of the cell if two conditions are met: First, for efficient polarization the polarity markers should diffuse slowly ($D \lesssim 0.01\ \mu\mathrm{m}^2/\mathrm{s}$) once bound to the membrane. Second, there is an optimal lifetime of polarity marker complexes on the membrane $\tau_{\mathrm{opt}} = 10$ s that maximizes both polarity and the surface density of the markers at the poles. The optimum arises from a trade-off between two opposing effects: On the one hand, fast complex recycling aids polarization by rapidly returning polarity markers that were "misanchored" at the membrane far from the poles back to the microtubules, and by preventing correctly localized complexes from diffusing too far away from the poles; on the other

hand, it also reduces the overall number of complexes at the membrane. Importantly, in contrast to earlier studies [103, 107], our polarization model does not explicitly assume polymerization, i.e. formation of larger clusters of Tea1 on the membrane.

Interestingly, we find that the two-stage binding scenario, in which T must first associate with the membrane to form TM-complexes with M, performs significantly worse in terms of polarization efficiency than the system in which direct binding of T to M is allowed. Since this is observed for equal slowdown factors, the reduced polarization efficiency in the system with two-stage binding must be the product of reduced recycling efficiency for complexes forming at the central parts of the membrane. In the system with two-stage binding the whole membrane constitutes a reactive surface for cytoplasmic T-particles and thus the probability of a cytoplasmic T-particle to bind the microtubule and be directed to the cell poles is lower than in the direct binding scenario. Moreover, in the two-stage binding scenario T remains bound to the membrane for a certain time after complex dissociation; this enhances the probability to reform the complex with a closeby M-particle.

We believe that in addition the following positive feedback mechanism is at work: The formation of complexes at the poles is accompanied by depletion of freely diffusing M. For high slowdown factors, there is a significant difference between the mobility of M and TM-complexes. This leads to an effective influx of M into the pole regions upon formation of slow complexes; simulataneously, the concentration of M in more remote regions of the membrane is decreased. This way, formation of polarity marker complexes at the poles reduces the probability of complex formation at the central parts of the membrane. The above effect also manifests itself in the density profiles of the two species: If the diffusion constants of species M and TM were to be equal, $D_{\mathrm{M}} = D_{\mathrm{TM}}$, the sum of their average densities $\langle\rho_{\mathrm{M}}\rangle + \langle\rho_{\mathrm{TM}}\rangle$ would be constant, because the total number $N_{\mathrm{M}} + N_{\mathrm{TM}}$ is conserved on the membrane. A rise of $\langle\rho_{\mathrm{TM}}\rangle$ at the poles then would be accompanied by a complementary drop of $\langle\rho_{\mathrm{M}}\rangle$, implying a peak of $\langle\rho_{\mathrm{M}}\rangle$ in the central parts of the cell. In contrast, if $D_{\mathrm{M}} \gg D_{\mathrm{TM}}$, the total density $\langle\rho_{\mathrm{M}}\rangle + \langle\rho_{\mathrm{TM}}\rangle$ can be high at the poles while $\langle\rho_{\mathrm{M}}\rangle$ does not exhibit the central peak because it is annihilated by fast diffusion of M. Indeed, in our simulations with direct binding we observe that while in the polarized state the density of M at the poles is somewhat reduced when compared to its density in the center of the system, this effect is far less pronounced than enhancement of TM-complex density at the poles (data not shown); in fact, to a good approximation, the M-particles equilibrate over the membrane, supporting the existence of the mechanism described above. This gives a rationale for the presence of the membrane-bound reaction partner (M / Mod5) in the system.

A combined theoretical-experimental study on the Pom1 protein [107], another important polarity factor in fission yeast that associates with the membrane to form concentration gradients decreasing from the cell poles, recently uncovered dynamics with striking similarities to our model: It was found that membrane-bound Pom1 molecules permanently change from a clustered to a non-clustered state, defining two separate Pom1 populations with markedly different diffusion speeds (unclustered form: $D_{\mathrm{u}} \simeq 0.026\ \mu\mathrm{m}^2/\mathrm{s}$; clusters: $D_{\mathrm{c}} \simeq 0.006\ \mu\mathrm{m}^2/\mathrm{s}$; cytoplasmic diffusion: $D_1 \simeq 1.5\ \mu\mathrm{m}^2/\mathrm{s}$). While the average cluster lifetime was measured as $\tau_{\mathrm{u}} \simeq 3\ s$, the overall membrane-bound time of Pom1 was $\tau_{\mathrm{m}} \simeq 30\ s$. These findings not only are in very

good agreement with the values at which we find optimal polarization efficiency in our model, they also suggest that slowdown of polarity factors upon binding to the poles is a common ingredient in mechanisms that establish bipolar concentrations along the yeast membrane. While in [107] the authors demonstrate that two different diffusion speeds on the membrane aid in producing more robust Pom1 gradient signals, i.e. making positional information along the membrane more reliable, our results, in particular the uncovered trade-off between polarity and pole occupancy, give a slightly different rationale for the observed slowdown, also offering an explanation for the timescale of membrane association ($\sim 10\ s$). To clarify whether true (i.e. multimeric) membrane clustering as proposed in [107] performs better or worse in terms of polarization reliability than the simpler (hetero-) dimerization considered in our model a direct comparison of these two "slowdown mechanisms" will have to be performed.

Continued simulations which account for the observed microtubule dynamics, and with more realistic copy numbers of the involved reaction partners, will help to further elucidate the mechanisms of fission yeast polarization in forthcoming work.

4.6 Acknowledgements

The author thanks P. RECOUVREUX, A. MUGLER and N. TABERNER for inspiring discussions on the topic presented in this chapter.

The author thanks A. HOFFMANN for critical reading of this chapter.

Chapter 5

Mutual repression in early Drosophila embryogenesis

5.1 Introduction

The development of multicellular organisms requires spatially controlled cell differentiation. The positional information for the differentiating cells is typically provided by spatial concentration gradients of morphogen proteins. In the classical picture of morphogen-directed patterning, cells translate the morphogen concentration into spatial gene-expression domains via simple threshold-dependent readouts [50, 108, 109, 110]. Yet, while embryonic development is exceedingly precise, this mechanism is not very robust against intra- and inter-embryonic variations [52, 51, 30]: the spatial patterns of the target genes do not scale with the size of the embryo and the boundaries of the expression domains are susceptible to fluctuations in the morphogen levels and to the noise in gene expression. Intriguingly, the target genes of morphogens often mutually repress each other, as in the gap-gene system of the fruit fly *Drosophila* [111, 112, 113, 114, 115, 116, 117]. To elucidate the role of mutual repression in the robust formation of gene expression patterns, we have performed extensive spatially-resolved stochastic simulations of the gap-gene system of *Drosophila melanogaster*. Our results show that mutual repression between target genes can markedly enhance both the steepness and the precision of gene-expression boundaries. Furthermore, it makes them robust against embryo-to-embryo variations in the morphogen gradients.

The fruit fly *Drosophila melanogaster* (Fig. 5.1A) is arguably the paradigm of morphogenesis. During the first 90 minutes after fertilization it is a syncytium, consisting of a cytoplasm that contains rapidly diving nuclei, which are not yet encapsulated by cellular membranes. Around cell cycle 10 the nuclei migrate towards the cortex of the embryo and settle there to read out the concentration gradient of the morphogen protein Bicoid (Bcd), which forms from the anterior pole after fertilization [109]. One of the target genes of Bcd is the gap gene *hunchback* (*hb*), which is expressed in the anterior half of the embryo (Fig. 5.1B). In spite of noise in gene expression, the midembryo boundary of the *hb* expression domain is astonishingly sharp. By cell cycle

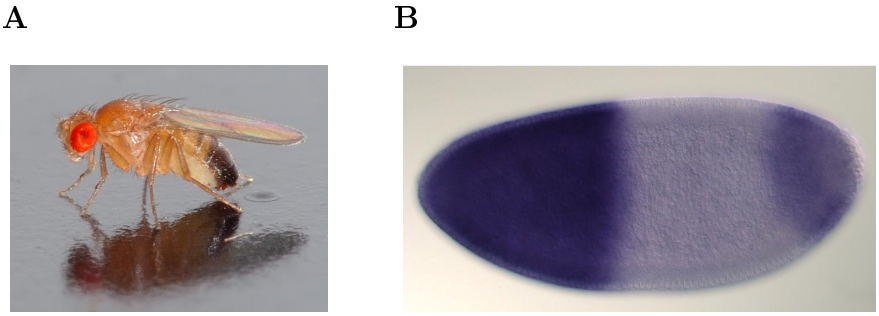

Figure 5.1: The fruit fly *Drosophila melanogaster*. (A) An adult fly. (B) The fly embryo ca. 90 min after fertilization. The anterior pole of the embryo is oriented towards the left. The cortical layer of nuclei is clearly visible. Expression of the gap gene *hunchback* (*hb*) is visualized via in-situ hybridization against its RNA (blue). The main expression domain of *hb* is localized to the anterior half of the embryo. See thesis appendix for image sources.

11, the *hb* mRNA boundary varies by about one nuclear spacing only [118, 119, 120], while by cell cycle 13 a similarly sharp boundary is observed for the protein level [52, 51, 121]. This precision is higher than the best achievable precision for a time-averaging based readout mechanism of the Bcd gradient [51]. Interestingly, the study of GREGOR *et al.* revealed that the Hb concentrations in neighboring nuclei exhibit correlations and the authors suggested that this implies a form of spatial averaging that enhances the precision of the posterior Hb boundary [51]. Two recent simulation studies suggest that the mechanism of spatial averaging is based on the diffusion of Hb itself [122, 123]; as shown analytically in [122], Hb diffusion between neighboring nuclei reduces the super-Poissonian part of the noise in its concentration. In essence, diffusion reduces noise by washing out bursts in gene expression. However, the mechanism of spatial averaging comes at a cost: it tends to lessen the steepness of the expression boundaries.

Bcd induces the expression of not only *hb*, but a number of gap genes, and pairs of gap genes tend to repress each other mutually. Interestingly, repression between directly neighboring gap genes is weak, whereas repression between non-adjacent genes is strong [124]. *hb* forms a strongly repressive pair with *knirps* (*kni*) which is expressed further towards the posterior pole; both genes play a prominent role in the later positioning of downstream pair-rule gene stripes [112]. It has been argued that mutual repression can enhance robustness to embryo-to-embryo variations in morphogen levels [115, 116, 117] and sharpen a morphogen-induced transition between the two mutually repressing genes in a non-stochastic background [125, 126]. However, mutual repression can also lead to bistability [127, 128, 129, 130, 131]. While bistablity may buffer against inter-embryo variations and rapid intra-embryo fluctuations in morphogen levels, it may also cause stochastic switching between distinct gene expression patterns, which would be highly detrimental. Therefore, the precise role of mutual repression in the robust formation of gene-expression patterns remains to be elucidated.

While the role of antagonistic interactions in the formation of gene-expression patterns has been studied using mean-field models [115, 131, 132, 133, 134], to address the question whether mutual repression enhances the robustness of these patterns against noise arising from the inherent stochasticity of biochemical reactions a stochastic model is essential. We have therefore performed large-scale stochastic simulations of a minimal model of mutual repression between *hb* and *kni*. Our model includes the stochastic and cooperative activation of *hb* by Bcd and of *kni* by the posterior morphogen Caudal (Cad) [135, 136]. Moreover, Hb and Kni can diffuse between neighboring nuclei and repress each other's expression, generating two separate spatial domains interacting at midembryo (see Fig. 5.2). We analyze the stability of these domains by systematically varying the diffusion constants of the Hb and Kni proteins, the strength of mutual repression and the Bcd and Cad activator levels. To quantify the importance of mutual repression, we compare the results to those of a system containing only a single gap gene, which is regulated by its morphogen only; this is the "system without mutual repression". While our model is simplified—it neglects, *e.g.*, the interactions of *hb* and *kni* with *krüppel* (*kr*) and *giant* (*gt*) [12]—it does allow us to elucidate the mechanism by which mutual repression can enhance the robust formation of gene expression patterns.

One of the key findings of our analysis is that mutual repression enhances the robustness of the gene expression domains against intra-embryonic fluctuations arising from the intrinsic stochasticity of biochemical reactions. Specifically, mutual repression increases the precision of gene-expression boundaries: it reduces the variation Δx in their positions due to these fluctuations. At the same time, mutual repression also enhances the steepness of the expression boundaries. To understand the interplay between steepness, precision and intra-embryonic fluctuations (biochemical noise), it is instructive to recall that the width Δx of a boundary of the expression domain of a gene g is, to first order, given by

$$\Delta x = \frac{\sigma_{\mathrm{G}}(x_{\mathrm{t}})}{|\langle G(x_{\mathrm{t}})\rangle'|} \tag{5.1}$$

where $\sigma_{\mathrm{G}}(x_{\mathrm{t}})$ is the standard deviation of the copy number G of protein G and $|\langle G(x_{\mathrm{t}})\rangle'|$ is the magnitude of the gradient of G at the boundary position x_{t} [51, 20, 122]. Steepness thus refers to the slope of the average concentration profile, $|\langle G(x_{\mathrm{t}})\rangle'|$, while precision refers to Δx, which is the standard deviation in the position at which G crosses a specified threshold value, here taken to be the half-maximal average expression level of G.

The simulations reveal, perhaps surprisingly, that mutual repression hardly affects the noise $\sigma_{\mathrm{G}}(x_{\mathrm{t}})$ at the expression boundaries of *hb* and *kni*. Moreover, mutual repression can strongly enhance the steepness $|\langle G(x_{\mathrm{t}})\rangle'|$ of these boundaries: the steepness of the boundaries in a system with mutual repression can, depending on the diffusion constant, be twice as large as that in the system without mutual repression. Together with Eq. (5.1), these observations predict that mutual repression can significantly enhance the precision of the boundaries, i.e. decrease Δx, which is indeed precisely what the simulations reveal. Interestingly, there exists an optimal diffusion constant that minimizes the boundary width Δx, as has been observed for a system without mutual repression [122]. While the minimal Δx of the system with mutual repression

is only marginally lower than that of the system without it, this optimum is reached at a lower value of the diffusion constant, where the steepness of the boundaries is much higher. We find that these observations are robust, i.e. independent of the precise parameters of the model, such as maximum expression level, size of the bursts of gene expression, and the cooperativity of gene activation.

Our results also show that mutual repression can strongly buffer against embryo-to-embryo variations in the morphogen levels by suppressing boundary shifts via a mechanism that is akin to that of [137, 138]. A more detailed analysis reveals that when the regions where Bcd and Cad activate *hb* and *kni* respectively overlap, bistability can arise in the overlap zone. Yet, the mean waiting time for switching is longer than the lifetime of the morphogen gradients, which means that the *hb* and *kni* expression patterns are stable on the relevant developmental time scales. This also means, however, that when errors are formed during development, these cannot be repaired. Here, our simulations reveal another important role for diffusion: without diffusion a spotty phenotype emerges in which the nuclei in the overlap zone randomly express either Hb or Kni; diffusion can anneal these patterning defects, leading to well-defined expression domains of Hb and Kni. Finally, we also study a scenario where *hb* and *kni* are activated by Bcd only. While this scheme is not robust against embryo-to-embryo variations in the morphogen levels, mutual repression does enhance boundary precision and steepness also in this scenario.

5.2 Results

5.2.1 Model

We consider the embryo in the syncytial blastoderm stage at late cell cycle 14, ca. 2 h after fertilization. In this stage the majority of the nuclei forms a cortical layer and *hb* and *kni* expression can be detected [114]. Our model is an extension of the one presented in [122]. It is based on a cylindrical array of diffusively coupled reaction volumes which represent the nuclei, with periodic boundary conditions in the angular (ϕ) and reflecting boundaries in the axial (x) direction. The dimensions of the cortical array are $N_x = N_\phi = 64$, with equal spacing of the nuclei $\ell = 8.5\mu$m in both directions. For a given embryo length L, this implies a cylinder radius $R = \frac{L}{2\pi} \simeq \frac{L}{6}$, which is close to the experimentally observed ratio. The resulting number of $N = 4096$ nuclei roughly corresponds to the expected number of cortical nuclei at cell cycle 14 if non-dividing polyploid yolk nuclei are taken into account [139] (see appendix section 5.A.1 for details); we also emphasize, however, that none of the results presented below depend on the precise number of nuclei.

In each nuclear volume we simulate the activation of the gap genes *hb* and *kni* by the morphogens Bcd and Cad, respectively, and mutual repression between *hb* and *kni* (see Fig. 5.2). In what follows, we will refer to Hb and Kni as repressors and to Bcd and Cad as activators. Our model of gene regulation bears similarities to those of [140, 141, 133, 134, 131], in the sense that it is based on a statistical mechanical model of gene regulation by transcription factors, allowing the computation of promoter-site occupancies. However, the models of [140, 141, 133, 134, 131] are mean-field models, which cannot capture the effect of intra-embryonic fluctuations due to biochemical

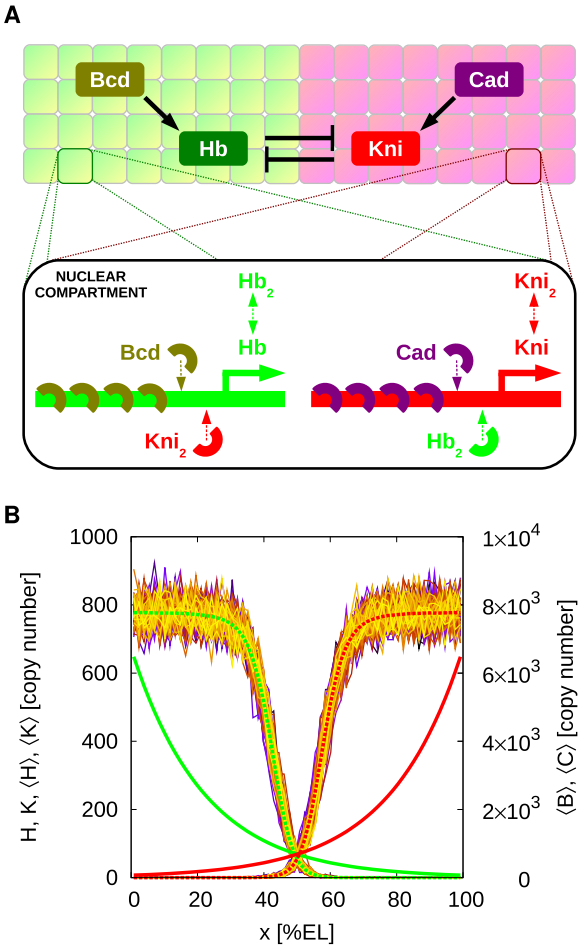

Figure 5.2: The model. (A) Cartoon of our model. Bcd activates *hb*, while its antagonist *kni* is activated by Cad. The gap genes *hb* and *kni* repress each other mutually. In each nuclear compartment we simulate the genetic promoters of both *hb* and *kni*. Activation is cooperative: In the default setting, 5 morphogen proteins have to bind to the promoter to initiate gene expression. Hb and Kni both form homodimers, which can bind to the other gene's promoter to totally block expression, irrespective of the number of bound morphogen proteins. Both dimers and monomers travel between neighboring nuclear compartments via diffusion. (B) Protein copy number profiles along the AP axis in a typical simulation in steady state, with parameter values as in Table S5.1 in the appendix. Plotted are the morphogen gradients Bcd ($\langle B \rangle$, solid green line) and Cad ($\langle C \rangle$, solid red line) and the resulting Hb (H) and Kni (K) total copy number profiles for different times. The dashed green and red lines show the Hb ($\langle H \rangle$) and Kni ($\langle K \rangle$) profiles averaged over time and the circumference of the (cylindrical) system.

noise arising from the inherent stochasticity of biochemical reactions. This requires a stochastic model; moreover, it necessitates a model in which the transitions between the promoter states are taken into account explicitly, since these transitions form a major source of noise in gene expression, as we will show. To limit the number of combinatorial promoter states, we have therefore studied a minimal model that only includes Bcd, Cad, Hb and Kni. Following [122], we assume that Bcd and Cad bind stochastically and cooperatively to $n_{\max}$ sites on their target promoters. To obtain a lower bound on the precision of the *hb* and *kni* expression domains, we assume that the activating morphogens Bcd and Cad bind to their promoters with a diffusion-limited rate $k_{\mathrm{on}}^{\mathrm{A}} = 4\pi\alpha D_{\mathrm{A}}/V$, where α is the dimension of a binding site, D_{A} is the diffusion constant of the morphogen, and V is the nuclear volume (see "Methods" section 5.4 for parameter values). Since the morphogen-promoter association rate is assumed to be diffusion limited, cooperativity of *hb* and *kni* activation is tuned via the dissociation rate $k_{\mathrm{off,n}}^{\mathrm{A}} = a/b^n$, which decreases with increasing number n of promoter-bound morphogen molecules. The baseline parameters are set such that the half-maximal activation level of *hb* and *kni* is at midembryo, and the effective Hill coefficient for gene activation is around 5 [122]; while we will vary the Hill coefficient, this is our baseline parameter. Again to obtain a lower bound on the precision of the gap-gene expression boundaries, transcription and translation is concatenated in a single step. Mutual repression between *hb* and *kni* occurs via binding of Hb to the *kni* promoter, which blocks the expression of *kni* irrespective of the number of bound Cad molecules, and vice versa. To assess the importance of bistability, Hb and Kni can homodimerize and bind to their target promoters only in their dimeric form, which is a prerequisite for bistability in the mean-field limit [127]. Both the monomers and dimers diffuse between neighboring nuclei and are also degraded; the effective degradation rate μ_{eff} is such that the gap-gene expression domains can form sufficiently rapidly on the time scale of embryonic development ($\approx 10-20$ min [139]). In the absence of mutual repression, our model behaves very similarly to that of [122], even though our model contains both monomers and dimers instead of only monomers.

Motivated by experiment [109, 52, 30], and in accordance with the diffusion-degradation model, we adopt an exponential shape for the stationary Bcd profile; we thus do not model the establishment of the gradient [142]. To elucidate the role of mutual repression, it will prove useful to take our model to be symmetric: the Cad profile is the mirror image of the Bcd profile, and *hb* and *kni* repress each other equally strongly. Diffusion of Bcd and Cad between nuclei induce fluctuations in their copy numbers on the time scale $\tau_{\mathrm{d}} = \ell^2/(4D_{\mathrm{A}}) \simeq 6$ s. Because τ_{d} is much smaller than the time scale for promoter binding, $1/k_{\mathrm{on}}^{\mathrm{A}} \simeq 360$ s, fluctuations in the copy number of Bcd and Cad are effectively averaged out by slow binding of Bcd and Cad to their respective promoters, *hb* and *kni* [122]. To elucidate the importance of the threshold positions for *hb* and *kni* activation, we will scale the morphogen gradients by a global dosage factor A; this procedure will also allow us to study the robustness of the system against embryo-to-embryo variations in the morphogen levels.

We simulate the model using the Stochastic Simulation Algorithm of GILLESPIE [53, 54]. Diffusion is implemented into the scheme via the next-subvolume method used in MesoRD [143, 144]. See http://ggg.amolf.nl for a public version of our code.

5.2.2 Characteristics of gap-gene expresson boundaries

Three key characteristics of gene expression boundaries are (1) the noise in the protein concentration at the boundary; (2) the steepness of the boundary; (3) the width of the boundary. While these quantities may make intuitive sense, their definitions are not unambiguous. Equally important, different definitions will reveal different properties of the system.

Decomposing the noise

Let us consider the variance in the copy number G of protein G at position x along the anterior-posterior (AP) axis. We define its mean copy number, averaged over all embryos, circumferential positions ϕ and all times, at the anterior-posterior position x as

$$\overline{\langle\langle G\rangle_\phi\rangle_{\rm e}}(x) \equiv \frac{1}{N_{\rm e}}\frac{1}{T}\frac{1}{N_\phi}\sum_{\rm e=0}^{N_{\rm e}-1}\sum_{\rm t=0}^{T-1}\sum_{\phi=0}^{N_\phi-1} G_{\rm e}(\phi,x,t), \tag{5.2}$$

where $G_{\rm e}(x,\phi,t)$ is the copy number of protein G in embryo e at position x and angle ϕ in the circumferential direction (perpendicular to the AP-axis) at time t. Here, we introduce the convention that the overline denotes an average in time, while the ensemble brackets with a subscript ϕ denote an average along the ϕ direction and that with a subscript e an average over all embryos. The variance in the copy number $G \equiv G_{\rm e}(x,\phi,t)$ is then given by

$$\sigma^2_{\rm G}(x) = \overline{\langle\langle (G - \overline{\langle\langle G\rangle_\phi\rangle_{\rm e}})^2\rangle_\phi\rangle_{\rm e}} \tag{5.3}$$

$$= \langle\overline{\langle G^2\rangle_\phi}\rangle_{\rm e} - \langle\overline{\langle G\rangle_\phi^2}\rangle_{\rm e} + \langle\overline{\langle G\rangle_\phi^2}\rangle_{\rm e} - \langle\overline{\langle G\rangle_\phi}^2\rangle_{\rm e} + \langle\overline{\langle G\rangle_\phi}^2\rangle_{\rm e} - \overline{\langle\langle G\rangle_\phi\rangle_{\rm e}}^2 \tag{5.4}$$

$$= \overbrace{\langle\overline{\sigma^2_{\rm G}}\rangle_{\rm e}(x) + \langle\sigma^2_{\langle{\rm G}\rangle_\phi}\rangle_{\rm e}(x)}^{\text{mean intra-embryonic noise}} + \overbrace{\sigma^2_{\langle\overline{\rm G}\rangle_\phi}(x)}^{\text{inter-embryonic variations}} \tag{5.5}$$

The total variance in the copy number can thus be decomposed into intra-embryonic fluctuations averaged over all embryos and inter-embryonic variations. The former can, furthermore, be decomposed into $\langle\overline{\sigma^2_{\rm G}}\rangle_{\rm e}(x)$, which is the time-averaged mean of the variance in G along the circumferential direction, $\overline{\sigma^2_{\rm G}}(x)$, averaged over all embryos, and $\langle\sigma^2_{\langle{\rm G}\rangle_\phi}\rangle_{\rm e}(x)$, which is the variance in time over the mean of G along the circumferential direction, $\sigma^2_{\langle{\rm G}\rangle_\phi}(x)$, again averaged over all embryos. These intra-embryonic terms capture different types of dynamics. If the expression boundary is rough but its average position does not fluctuate in time, then $\overline{\sigma^2_{\rm G}}(x)$ will be large yet $\sigma^2_{\langle{\rm G}\rangle_\phi}(x)$ will be small. Conversely, when the boundary is smooth but its average position does fluctuate in time, then $\overline{\sigma^2_{\rm G}}(x)$ will be small yet $\sigma^2_{\langle{\rm G}\rangle_\phi}(x)$ will be large. Naturally, a combination of the two is also possible. The third term, $\sigma^2_{\langle\overline{\rm G}\rangle_\phi}(x)$, captures

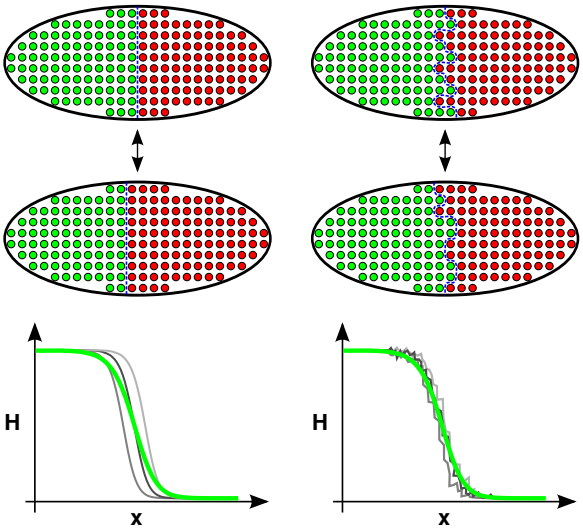

Figure 5.3: Two different contributions to the intra-embryonic variance in the boundary position. The total variance of the gap gene expression boundary position x_t due to intra-embryonic fluctuations, $\sigma^2_{x_t,\mathrm{intra}}$, can be decomposed into two contributions: $\sigma^2_{\langle x_t\rangle_\phi}$, the variance in time of the circumferential mean of x_t, and $\overline{\sigma^2_{x_t}}$, the time-average of the variance of x_t along the circumference of the embryo. The sketch illustrates two extremal cases: If the boundary is very smooth along the circumference at any moment in time, concerted movements of the boundary will dominate the total variance, i.e. $\sigma^2_{x_t,\mathrm{intra}} \simeq \sigma^2_{\langle x_t\rangle_\phi}$ (left side). If, in contrast, the boundary is rough but its mean position does not fluctuate much in time, then $\sigma^2_{x_t,\mathrm{intra}} \simeq \overline{\sigma^2_{x_t}}$ (right side). Naturally, a combination of the two types of fluctuations is possible.

the embryo-to-embryo variations in the average over time and ϕ of the protein-copy number. Similarly, we can decompose the fluctuations in the boundary position x_t as

$$\Delta x \quad = \sigma_{x_t} = \sqrt{\langle\overline{\sigma^2_{x_t}}\rangle_e + \langle\sigma^2_{\langle x_t\rangle_\phi}\rangle_e + \sigma^2_{\overline{\langle x_t\rangle_\phi}}} \tag{5.6}$$

The two different contributions to the intra-embryonic variance, $\langle\overline{\sigma^2_{x_t}}\rangle_e + \langle\sigma^2_{\langle x_t\rangle_\phi}\rangle_e$, are illustrated in Fig. 5.3. Here and in the next section, we will study the robustness of the system against intra-embryonic fluctuations, while in section 5.2.4 we study the robustness against inter-embryonic variations in the morphogen levels.

Intra-embryonic fluctuations

Fig. S5.2 in the appendix shows the decomposition of the noise in the Hb copy number H and the threshold position x_t of the Hb boundary, as a function of the diffusion constant. We show the intra-embryonic fluctuations for one given embryo (with the baseline parameter set); how Δx (the boundary variance originating from

intra-embryonic fluctuations) changes with embryo-to-embryo variations in the morphogen levels is addressed in section 5.2.4. Fig. S5.2 shows that by far the dominant contribution to the intra-embryonic noise in the copy number and threshold position is the time average of the variance in these observables along the circumferential direction; the variance in time of the ϕ-average of these quantities is indeed very small. The picture that emerges is that the expression boundary is rough, even when the diffusion constant D is large, i.e. $D = 1\ \mu\text{m}^2/\text{s}$. An analysis of the spatial correlation function at midembryo $\overline{\langle \delta H(0)\delta H(\phi)\rangle_\phi}(x_\text{t})$, where $\delta H(\phi) = H(x_\text{t}, \phi, t) - \overline{\langle H\rangle_\phi}$, revealed that the correlation length ξ_ϕ is on the order of a few nuclei, which corresponds to the diffusion length $\lambda = \sqrt{D/\mu_\text{eff}}$ a protein can diffuse with diffusion constant D before it is degraded with a rate μ_eff; the correlation length is thus small compared to the circumference. One possible source of coherent fluctuations in the mean copy number $\langle X\rangle_\phi$ and boundary position $\langle x_\text{t}\rangle_\phi$ are temporal variations of the morphogen profiles. However, in our model, these profiles are static—we argued that the morphogen fluctuations are fast on the timescale of gene expression, and are thus effectively integrated out. The small correlation length ξ_ϕ then indeed means that the varations in the mean over ϕ, $\langle \dots \rangle_\phi$, will be small. This leads to an interesting implication for experiments, which we discuss in the Discussion section (5.3).

The boundary steepness

Now that we have characterized the fluctuations in the copy number and the boundary position, the next question is how fluctuations in the copy number affect the steepness of the boundary. In particular, a gene-expression boundary can be shallow either because at each moment in time the interface is shallow, or because at each moment in time the interface is sharp yet the interface fluctuates in time, leading to a smooth profile. The question is thus how much the gradient of the mean concentration profile, $\overline{\langle G\rangle_\phi}'$, and the mean of the gradient, $\overline{\langle G'\rangle_\phi}$, differ (here the prime denotes the spatial derivative). Fig. S5.3 in the appendix shows both quantities as a function of the diffusion constant. It is seen that while the average of the gradient is larger than the gradient of the average (as it should), the difference is around a factor of 2. We thus conclude that the steepness of the expression boundary at each moment in time does not differ very much from the steepness of the average concentration profile.

In the rest of the manuscript, we will predominantly focus on the properties of individual embryos, and average quantities are typically averages over time and the circumference. For brevity, therefore, $\langle \dots \rangle = \overline{\langle \dots \rangle_\phi}$, unless stated otherwise.

5.2.3 Robustness to intra-embryonic fluctuations

Mutual repression shifts boundaries apart

Fig. 5.4A shows the average Hb and Kni steady-state profiles along the anterior-posterior (AP) axis as a function of their diffusion constant D for a system with mutual repression. The inset shows the morphogen-activation profiles, which are the spatial profiles of the probability that the *hb* and *kni* promoters have 5 copies of their respective morphogens bound. Without mutual repression, thus when Hb and Kni cannot bind to their respective target promoters, these profiles describe the probability that *hb* and *kni* are activated by their respective morphogens. Indeed, without mutual repression and without Hb and Kni diffusion, the Hb and Kni concentration profiles would be proportional to their respective morphogen-activation profiles [122], which means that they would precisely intersect at midembryo. In contrast, Fig. 5.4A shows that the Hb and Kni concentration profiles are shifted apart in the system with mutual repression. There is already a finite separation for $D = 0$, which increases further as D is increased.

In Fig. 5.4B we show the profile of the probability $\langle H_5^0 \rangle$ that the *hb* promoter is induced, meaning that it has 5 copies of Bcd bound to it and no Kni, and the profile of the likelihood $\langle H_5^1 \rangle$ that *hb* is activated by Bcd, yet repressed by Kni, in which case *hb* is not expressed. It is seen that repression by *kni* almost fully inhibits *hb* expression beyond the half-activation point, where *hb* would be expressed without *kni* repression (see inset Panel A). Indeed, mutual repression effectively cuts off protein production beyond midembryo. The production probability therefore changes more abruptly along the AP axis, leading to a higher steepness of the protein profiles near midembryo. For $D > 0$, repressor influx over the midplane increases, and as a result the regions of expression inhibiton are enlarged and the concentration profiles shift apart further.

Noise reduction via spatial averaging

Fig. 5.4C shows the standard deviation of the protein copy number along the AP axis for both Hb (σ_{H}) and Kni (σ_{K}). It is seen that the noise increases close to the half-activation point where promoter-state fluctuations are strongest [22, 41, 145]. This is also observed in Fig. 5.4D, which shows the normalized standard deviation $\sigma_{\mathrm{H}}/\langle H \rangle_{\max}$ versus the normalized mean $\langle H \rangle/\langle H \rangle_{\max}$ of the average Hb copy number; here, $\langle H \rangle_{\max}$ is the maximum average concentration of Hb. The noise maximum close to mid embryo diminishes with increasing D, approaching the Poissonian limit. Note that the Poissonian limit here is given by $\sigma_{\mathrm{P}} = \sqrt{(1 + f_{\mathrm{D}})\langle H \rangle}$, where $f_{\mathrm{D}} = 2\langle H_{\mathrm{D}} \rangle/\langle H \rangle$ is the fraction of dimerized Hb proteins with respect to the total Hb copy number (see appendix section 5.B.1 for details). Clearly, the spatial averaging mechanism described in [122, 123] reduces the noise also in our system, which differs from those in [122, 123] by the presence of both gap gene monomers and dimers instead of monomers only.

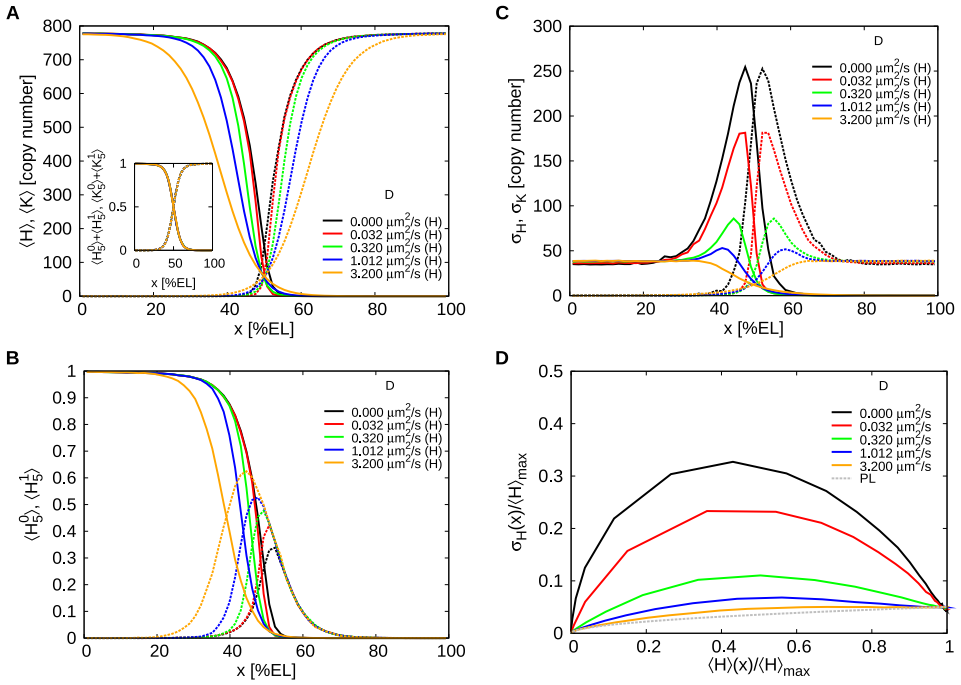

Figure 5.4: The effect of mutual repression on the average protein concentrations and their standard deviations. (A) Time- and circumference-averaged Hb ($\langle H \rangle$, solid lines) and Kni ($\langle K \rangle$, dashed lines) total protein copy number profiles along the AP axis for various diffusion constants D in a system with mutual repression. The inset shows for both the *hb* and the *kni* promoter the probability that the promoter binds 5 morphogen proteins irrespective of whether the antagonistic gap protein is bound to it (meaning that the promoter is activated by the morphogen, even though it may be repressed by the antogonistic gap protein); these "morphogen-activation" profiles are identical for all D values. (B) Profiles of the probability $\langle H_5^0 \rangle$ that the *hb* promoter is induced, meaning that it has 5 copies of Bcd bound to it and no Kni dimer (solid lines), and the probability $\langle H_5^1 \rangle$ that *hb* is activated by Bcd yet repressed by Kni, in which case *hb* is indeed not expressed (dashed lines). (C) AP profiles of the time- and circumference-averaged standard deviation of the total gap protein copy number for Hb (σ_{H}, solid lines) and Kni (σ_{K}, dashed lines). (D) Normalized standard deviation $\sigma_{\mathrm{H}}(x)/\langle H \rangle_{\max}$ versus the normalized mean $\langle H \rangle(x)/\langle H \rangle_{\max}$; $\langle H \rangle(x)$ is the averaged total Hb copy number at x and $\langle H \rangle_{\max}$ is the maximum of this average over all x. The grey dashed line represents the Poissonian limit (PL) given by $\sqrt{(1+f_{\mathrm{D}})\langle H \rangle(x)/\langle H \rangle_{\max}}$, where f_{D} is the fraction of proteins in dimers.

Mutual repression reduces the boundary width by increasing the steepness

Fig. 5.5 quantifies the impact of spatial averaging and mutual repression on the Hb boundary width Δx, comparing it to that of the system without mutual repression. To first order, the boundary precision Δx is related to the standard deviation in the protein copy number at the boundary, $\sigma_{\mathrm{H}}(x_{\mathrm{t}})$, and the steepness of the boundary, $|\langle H(x_{\mathrm{t}})\rangle'|$, via Eq. (5.1) [20, 51, 122]. The noise $\sigma_{\mathrm{H}}(x_{\mathrm{t}})$ decreases with increasing D due to spatial averaging in an almost identical manner for the systems with and without mutual repression (Fig. 5.5, top panel); indeed, perhaps surprisingly, mutual repression has little effect on the noise at the boundary. Increasing D also lessens the steepness of the protein profiles, thus reducing the slope $|\langle H(x_{\mathrm{t}})\rangle'|$ (Fig. 5.5, middle panel). While without mutual repression this reduction is monotonic, in the case with mutual repression the steepness first rises because increasing D increases the influx of the antagonistic repressor into the regions where the gap genes are activated by their respective morphogens, which, for low values of D, *steepens* the effective gene-activation profile $\langle H_5^1\rangle(x)$ by most strongly reducing gene expression near midembryo; after the steepness has reached its maximum at $D = 0.032\ \mu\mathrm{m}^2/\mathrm{s}$, it drops for higher diffusion constants, because the diffusion of the gap-gene proteins now flattens their concentration profiles. Most importantly, with mutual repression $|\langle H(x_{\mathrm{t}})\rangle'|$ reaches significantly higher values for all $D \leq 1.0\ \mu\mathrm{m}^2/\mathrm{s}$. At $D = 0.032\ \mu\mathrm{m}^2/\mathrm{s}$ the profile is roughly twice as steep as in the case without repression. Interestingly, for $D \lesssim 0.1\ \mu\mathrm{m}^2/\mathrm{s}$, our simulation results for the steepness of the profiles as normalized by their maximal values agree with those measured experimentally by SURKOVA *et al.* in cell cycle 14 [114]: In both simulation and experiment, the concentration drops from 90% to 10% of the maximal values over 5-10% of the embryo length.

Both with and without Hb-Kni mutual repression the trade-off between noise and steepness reduction leads to an optimal diffusion constant D_{min} that maximizes boundary precision, i.e. minimizes Δx (Fig. 5.5, lower panel). Mutual repression enhances the precision for $D \leq 1.0\ \mu\mathrm{m}^2/\mathrm{s}$ because in this regime decreasing D increases the steepness markedly while it has only little effect on the noise as compared to the system without mutual repression. Conversely, Δx is increased by mutual repression for $D \geq 10\ \mu\mathrm{m}^2/\mathrm{s}$ because it reduces the steepness. The minimum in the case with repression is marginally lower than that without ($D_{\mathrm{min,R}}/D_{\mathrm{min,NR}} \simeq 0.86$), but located at a lower D-value ($1.0\ \mu\mathrm{m}^2/\mathrm{s}$ vs. $3.2\ \mu\mathrm{m}^2/\mathrm{s}$). Most importantly, at $D = 0.32\ \mu\mathrm{m}^2/\mathrm{s}$, the system with mutual repression produces a profile that is twice as steep as that of the system without it at $D_{\mathrm{min,NR}} = 3.2\ \mu\mathrm{m}^2/\mathrm{s}$, whereas the precision Δx is essentially the same in both cases. Clearly, mutual repression can strongly enhance the steepness of gene-expression boundaries without compromising their precision.

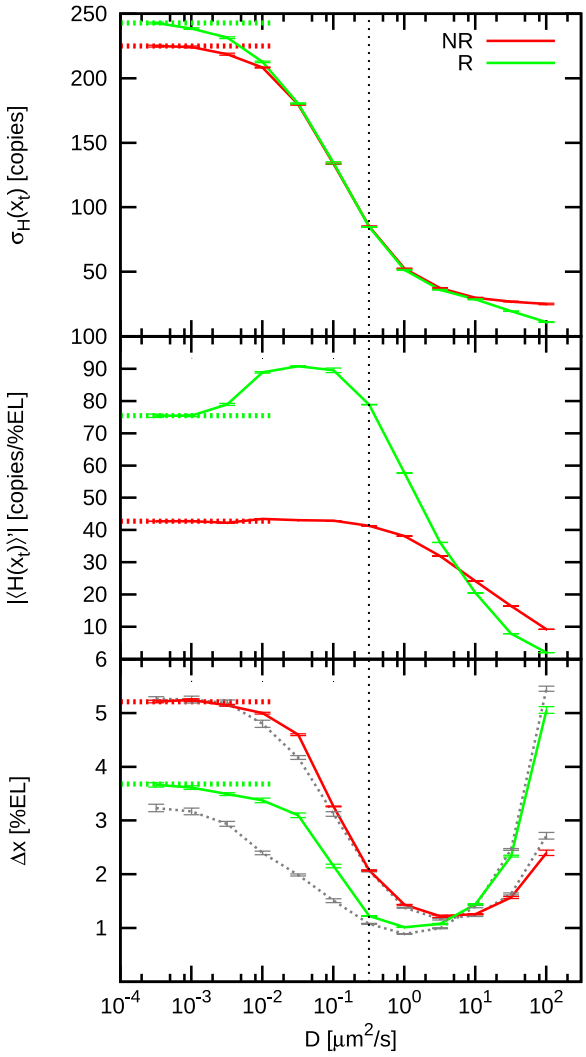

Figure 5.5: The effect of mutual repression on the precision and steepness of the Hb boundary. The figure shows the time- and circumference-average of the standard deviation of the total Hb copy number at the boundary $\sigma_{\mathrm{H}}(x_{\mathrm{t}})$ (upper panel), the slope of the total Hb copy number profile at the boundary $|\langle H\rangle'(x_{\mathrm{t}})|$ (middle panel) and the Hb boundary width Δx (lower panel) as a function of the diffusion constant D of the gap proteins. Red solid lines show the case without (NR) and green solid lines the case with mutual repression (R); the red and green dashed lines show the limiting values without diffusion of the gap proteins. The grey dashed lines in the boundary width plot are the values based on the approximation $\Delta x = \sigma_{\mathrm{H}}(x_{\mathrm{t}})/|\langle H(x_{\mathrm{t}})\rangle'|$. Note that for $D < 3.2\ \mu\mathrm{m}^2/\mathrm{s}$, mutual repression enhances the steepness of the boundary, which in turn enhances the precision of the boundary. The black dotted line marks the D-value where the boundary is both steep and precise due to mutual repression.

Influence of the Hill coefficient

A key parameter controlling the precision of the gap-gene expression boundaries, is the degree of cooperativity by which the gap genes are activated by their respective morphogens—this determines the profile steepness of the average gap-gene promoter activity. To investigate this, we have lowered the effective Hill coefficient from its baseline value of 5 by reducing the number $n_{\max}$ of morphogen molecules that are required to bind the promoter to activate gene expression. To isolate the effect of varying the *mean* gene-activation profiles $\langle H^0_{\mathrm{n}_{\max}}\rangle(x)$ and $\langle K^0_{\mathrm{n}_{\max}}\rangle(x)$, we varied, upon varying $n_{\max}$, the association and dissociation rates such that 1) the average gene activation probabilities near midembryo, $\langle H^0_{\mathrm{n}_{\max}}\rangle(L/2)$ and $\langle K^0_{\mathrm{n}_{\max}}\rangle(L/2)$, are unchanged and 2) the waiting-time distribution for the gene on-to-off transition is unchanged (since the average activation probability is fixed, the mean off-to-on rate is also unchanged, although the waiting-time distribution is not; see also Fig. S5.4 in the appendix). We observe that mutual repression markedly enhances the steepness of the gap-gene expression boundaries, also with a lower Hill coefficient for gene activation (Fig. S5.5 in the appendix). However, lowering the Hill coefficient reduces the steepness of the gene-activation profiles, causing the two antagonistic gene-activation profiles to overlap more. As a result, in each of the two gap-gene expression domains, more of the antagonist is present, which tends to increase the noise in gene expression by occassionally shutting off gene production. This, as explained in more detail later, is particularly detrimental when the diffusion constant is low. Indeed, when the effective Hill coefficient of gene activation is 3 or lower, mutual repression *increases* Δx when the diffusion constant is low, i.e. below approximately 0.1 $\mu\mathrm{m}^2/\mathrm{s}$. Nonetheless, the *minimal* Δx is still lower with mutual repression, and, consequently, also with a lower Hill coefficient for gene activation, mutual repression can enhance both the steepness and the precision of gene-expression boundaries.

Influence of the repression strength

As a standard we assume very tight binding of the Hb and Kni dimers, "the repressors", to their respective promoters. To test how this assumption affects our results we performed simulations in which we systematically varied the repressor-promoter dissociation rate $k^{\mathrm{R}}_{\mathrm{off}}$ in the range $[5.27 \cdot 10^{-4}/\mathrm{s}, 5.27 \cdot 10^{2}/\mathrm{s}]$, keeping the diffusion constant at $D = 1.0\ \mu\mathrm{m}^2/\mathrm{s}$ (the value that minimizes the boundary width at $k^{\mathrm{R}}_{\mathrm{off}} = 5.27 \cdot 10^{-3}/\mathrm{s}$) and all other parameters the same as before. Fig. 5.6 shows the noise, steepness and boundary precision as a function of the repressor-promoter dissociation rate. For high dissociation rates, these quantities equal those in the system without mutual repression (dashed lines). Yet, as the dissociation rate is decreased, the steepness rises markedly at $k^{\mathrm{R}}_{\mathrm{off}} = 1/\mathrm{s}$. In contrast, the noise $\sigma_{\mathrm{H}}(x_{\mathrm{t}})$ first decreases with decreasing $k^{\mathrm{R}}_{\mathrm{off}}$, passing through a minimum at $k^{\mathrm{R}}_{\mathrm{off}} = 0.1/\mathrm{s}$ before rising to a level that is higher than that in a system without mutual repression. This minimum arises because on the one hand increasing the affinity of the repressor (the antagonist) makes the operator-state fluctuations of the activator (the morphogen) less important—increasing repressor binding drives the concentration profiles of Hb and Kni away from midembryo, where the promoter-state fluctuations of the activators are strongest; on the other hand, when the repressor binds too strongly, then

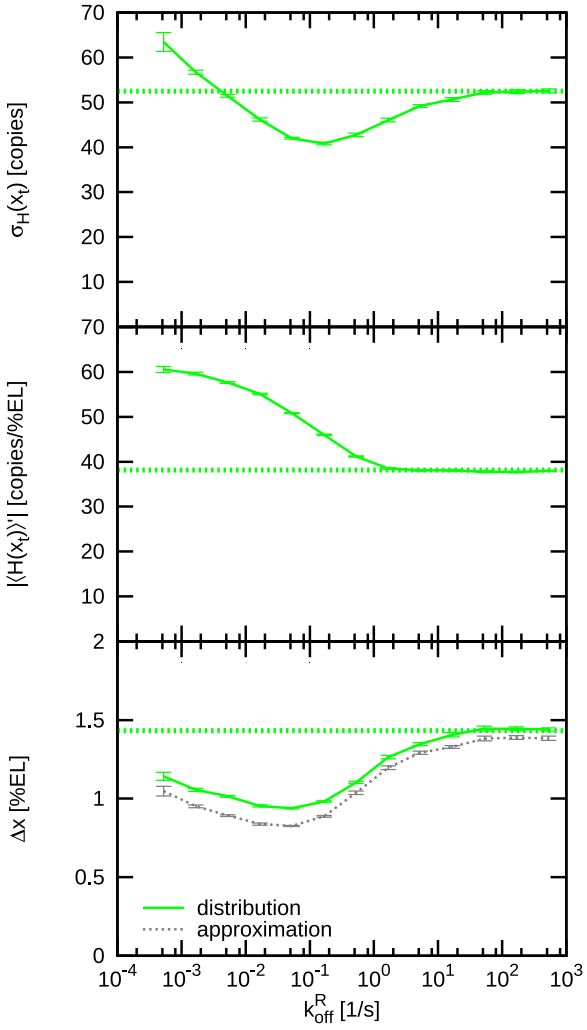

Figure 5.6: The effect of varying repression strength on the precision and steepness of the Hb boundary. Shown are the time- and circumference average of the standard deviation of the total Hb copy number at the boundary $\sigma_{\mathrm{H}}(x_{\mathrm{t}})$ (upper panel), the steepness of the boundary $|\langle H\rangle'(x_{\mathrm{t}})|$ (middle panel) and the Hb boundary width Δx (lower panel) as a function of $k^{\mathrm{R}}_{\mathrm{off}}$, the promoter-dissociation rate of Hb and Kni. The solid green line are values obtained from the boundary position distribution, the dashed grey line the ones calculated from the approximation $\Delta x = \sigma_{\mathrm{H}}(x_{\mathrm{t}})/|\langle H(x_{\mathrm{t}})\rangle'|$. Straight dashed lines mark the limits for the case without mutual repression ($k^{\mathrm{R}}_{\mathrm{on}} = k^{\mathrm{R}}_{\mathrm{off}} = 0$).

slow repressor unbinding leads to long-lived promoter states where gene expression is shut off, increasing noise in gene expression; this phenomenon is similar to what has been observed in Refs. [41] and [60], where slower binding of the gene regulatory proteins to the promoter increases noise in gene expression and decreases the stability of a toggle switch, respectively. The interplay between the noise and the steepness yields a marked reduction of the boundary width Δx; indeed, even in the limit of very tight repressor binding, mutual repression significantly enhances the precision of the boundary.

Influence of the expression level

Since the precise gap protein expression level is not known, we also varied the maximal protein copy number N by varying the maximal expression rate β (see appendix section 5.C.2). Fig. S5.7 in the appendix shows the output noise and slope at the boundary position, and the boundary precision Δx, as a function of the diffusion constant for three different expression levels. It is seen that for low diffusion constant, the precision is independent of N, while for higher diffusion constant it scales roughly with $1/\sqrt{N}$. This can be understood by noting that the steepness of the gene-expression boundary scales to a good approximation with N independently of D, while the noise σ scales with N when the diffusion constant is small, but with $\sqrt{N}$ when the diffusion constant is large (see also Eq. (5.1)). The scaling of the noise with N is due to the fact that for low D the noise in the copy number is dominated by the noise coming from the promoter-state fluctuations, which scales linearly with N, while for high D, diffusion washes out the expression bursts resulting from the promoter-state flucutations, leaving only the noise coming from the Poissonian fluctuations arising from transcription and translation, which scales with the square root of N [122]. In the appendix (section 5.C.2) we also study the importance of bursts arising in the transcription-translation step (see Fig. S5.8 in the appendix); however, we find that for a typical burst size, these bursts do not dramatically affect boundary precision.

5.2.4 Robustness to inter-embryonic variations

Although the Bcd copy number at midembryo has been determined experimentally [51], the measured value is not necessarily the half-activation threshold of *hb*. Indeed, in vivo the Hb profile is shaped by other forces, like mutual repression. In the *kni*-*kr* double mutant, the Hb boundary at midembryo shifts posteriorly [116]. Moreover, gap gene domain formation has been observed at strongly reduced Bcd levels, suggesting that Bcd might be present in excess [146]. Also from a theoretical point of view it is not obvious that a precisely centered morphogen-activation threshold is optimal, in terms of robustness against both intra-embryonic fluctuations and inter-embryonic variations. Here, we study the effect of changing the threshold position where *hb* and *kni* are half-maximally activated by their respective morphogens, Bcd and Cad. While the threshold positions could be varied by changing the threshold morphogen concentrations for half-maximal gap-gene activation (for example by changing the morphogen-promoter dissociation rates), we will vary these positions by changing the

amplitude of the morphogen profiles by a factor A. This procedure not only preserves the promoter-activation dynamics at the boundaries—a key determinant for the noise at the boundaries—but also allows us to study the importance of mutual repression in ensuring robustness against embryo-to-embryo variations. Indeed, we will examine not only how changing the threshold position affects the precision of the gap-gene expression boundaries, $\Delta x(A)$, but also how the average boundary positions vary with morphogen dosage, $x_{\mathrm{t}}(A)$, and how the latter gives rise to embryo-to-embryo variations in the boundary position $\Delta x_{\mathrm{t}}(\Delta A)$ due to embryo-to-embryo variations in the morphogen dosage ΔA.

Double-activation induces bistability

We first consider the scenario in which the amplitudes of both morphogens are scaled by the same factor A. When $A = 1$, the position at which *hb* and *kni* are half-maximally activated by their respective morphogens coincide at midembryo, meaning that the domains in which *hb* and *kni* are activated beyond half-maximum are adjoining, but do not overlap—this is the scenario discussed in the previous sections. When $A > 1$, the position at which *hb* is half-maximally activated by its morphogen is shifted posteriorly, while that of *kni* is shifted anteriorly, creating an overlap between the two regions where *hb* and *kni* are activated. In this "double-activated region" both *hb* and *kni* are activated by their respective morphogens, yet they also mutually repress each other. This may lead to bistability. To probe whether this is the case, we performed a bifurcation analysis of the mean-field chemical-rate equations of isolated nuclei, implying that $D = 0$ (see Fig. S5.1 in the appendix). In addition, we performed stochastic simulations of isolated nuclei with different morphogen levels corresponding to different positions along the AP axis. All other parameter values were the same as in the full-scale simulation. We recorded long trajectories of the order parameter $\Delta N \equiv H - K$, the difference between the total Hb and total Kni copy numbers, in the stationary state. From each trajectory we computed the distribution $P(\Delta N)$ of the probability that the system is in a state with copy number difference ΔN. This defines a "free energy" $G(\Delta N) \equiv -\ln P(\Delta N)$, with minima of $G(\Delta N)$ corresponding to maximally probable values of ΔN [129, 130]. For a bistable system, $G(\Delta N)$ resembles a double-well potential with minima located at a positive value of $\Delta N = \Delta N_{\mathrm{H}}$ and a negative value of $\Delta N = \Delta N_{\mathrm{K}}$, respectively. At midembryo the morphogen levels of Bcd and Cad are the same and hence the biochemical network in the nuclei in the midplane is symmetric, which means that, if this network is bistable, $G(\Delta N)$ resembles a symmetric double-well potential with $\Delta N_{\mathrm{H}} = -\Delta N_{\mathrm{K}}$ and $\Delta G \equiv G(\Delta N_{\mathrm{H}}) - G(\Delta N_{\mathrm{K}}) = 0$. Away from the middle, the morphogen levels differ, and one state will become more stable than the other; if the other state is, however, still metastable, then $G(\Delta N)$ will resemble an asymmetric double-well potential, with ΔG being negative if the *hb*-dominant state is more stable than the *kni*-dominant state, and vice versa. The emergence of such a "spatial switch" along the AP axis is also captured by our mean-field, bifurcation analysis (see appendix section 5.B.2) and was recently also shown in the mean-field analysis of PAPATSENKO and LEVINE for the same pair of mutually repressing genes [131].

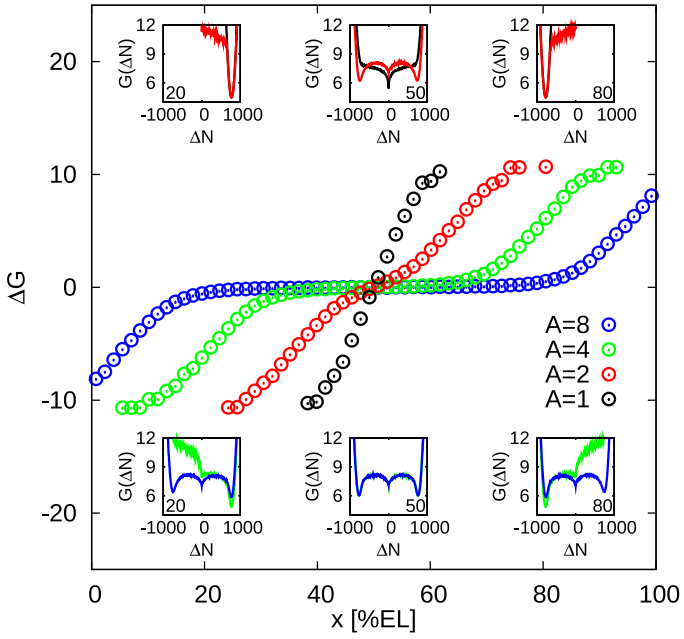

Figure 5.7: Emergence of bistability in double-activated regions. The "free energy" difference $\Delta G \equiv G(\Delta N_{\rm H}) - G(\Delta N_{\rm K})$ as a function of x, the distance of the nucleus from the anterior pole, for different amplitudes of the morphogen gradients A; here, $G(\Delta N) \equiv -\ln(P(\Delta N))$, where $P(\Delta N)$ is the stationary distribution of the order parameter $\Delta N = H - K$; $\Delta N_{\rm H} \simeq -\Delta N_{\rm K} \approx 800$ correspond to the minima of $G(\Delta N)$. Negative values of ΔG represent a strong bias towards the high-Hb state, while positive values correspond to high-Kni states. The insets shows $G(\Delta N)$ as a function of ΔN at the positions indicated by the numbers in their corners (values in [% EL]; colors correspond to main plot). The data is obtained from simulations of single nuclei with morphogen levels corresponding to the ones at position x in the full system; this is equivalent to the full system without diffusion between neighboring nuclei. Note the bistable behavior in a wide region of the embryo for higher A values.

Fig. 5.7 shows ΔG as a function of the position along the AP axis, for different amplitudes A of the morphogen gradients. The inset shows the energy profiles $G(\Delta N)$ for different positions along the AP axis. For $A = 1$, $G(\Delta N)$ always exhibits one minimum only, irrespective of the position along the AP axis; at midembryo, this minimum is located at $\Delta N = 0$, while moving towards the anterior (posterior) the energy minimum rapidly shifts to $\Delta N \approx +800(-800)$, reflecting that in the anterior (posterior) half of the embryo *hb* (*kni*) is essentially fully expressed. For $A = 2$, $G(\Delta N)$ develops into a double-well potential at midembryo, with two pronounced minima at $\Delta N \approx 800$ and $\Delta N \approx -800$, respectively. These two minima correspond to a state in which *hb* is highly expressed ($\langle H \rangle \approx 800$) and *kni* is strongly repressed ($\langle K \rangle \approx 0$) and another state in which *kni* is highly expressed and *hb* strongly re-

pressed, respectively. The fact that the two energy mimima are equal indicates that both of these states are equally likely. Moving away from midembryo, however, one gap-gene expression state rapidly becomes more stable than the other, and bistability is lost, yielding a potential with one minimum located at $\Delta N \approx 800$ in the anterior half and a potential with one minimum located at $\Delta N \approx -800$ in the posterior half of the embryo. Interestingly, for $A = 4$ and $A = 8$ a wide region of bistability develops around midembryo. In this region, $\Delta G \approx 0$, meaning that the high-*hb*—low-*kni* state and the low-*hb*—high-*kni* state are equally stable. These two states are equally likely because in this region both the *hb* and *kni* promoters are fully activated by their respective morphogens. It can also be seen that the width of this bistable region increases with the amplitude of the morphogen gradients, as expected.

Slow switching ensures a low noise level while diffusion avoids error locking

The bistability observed for $A > 1$ and $D = 0$ raises an important question, namely whether the nuclei can switch between the two gap-gene expression states on the time scale of embryonic development. This question is particularly pertinent for the higher morphogen amplitudes, where these two states are equally likely ($\Delta G \approx 0$) over a wide region of the embryo (Fig. 5.7): random switching between the two distinct gap-gene expression states in this wide region would then lead to dramatic fluctuations in the positions of the *hb* and *kni* expression boundaries, which clearly would be detrimental for development. We therefore computed [130] from the recorded switching trajectories the average waiting time for switching, τ_s, at midembryo ($\Delta G \simeq 0$) for different values of A; for $A \geq 2$, we find $\tau_s \simeq 6$ h (see Table S5.2 in the appendix). During cell cycle 14, approximately 2-3 hours after fertilization, the Bcd gradient disappears [147], suggesting that the spontaneous switching rate is indeed low on the relevant time scale of development.

With diffusion of Hb and Kni between neighboring nuclei ($D > 0$), the time scale for switching will be even longer. Diffusion couples neighboring nuclei, creating larger spatial domains with the same gap-gene expression state. This reduces the probability that a nucleus in the overlap region flips to the other gap-gene expression state. The latter can be understood from the extensive studies on the switching behavior of the "general toggle switch" [129, 130, 148, 149, 150, 60], which is highly similar to the system studied here—indeed, the toggle switch consists of two genes that mutually repress each other. These studies have revealed that the ensemble of transition states, which separate the two stable states, is dominated by configurations where both antagonistic proteins are present in low copy numbers. Clearly, the probability that in a given nucleus not only the minority gap protein, but also the majority gap protein reaches a low copy number, is reduced by the diffusive influx of that majority species from the neighboring nuclei, which are in the same gap-gene expression state. In essence, diffusion increases the effective system size, with its spatial dimension given by $\lambda = \sqrt{D/\mu_{\text{eff}}}$; in fact, since the stability of the toggle switch depends exponentially on the system size [129, 130], we expect the stability τ_s to scale with the diffusion constant as $\tau_s \sim e^D$. We thus conclude that random switching between the two gap-gene expression states, the high-*hb*—low-*kni* and low-*hb*—high-*kni* states, is not likely to occur on the time scale of early development.

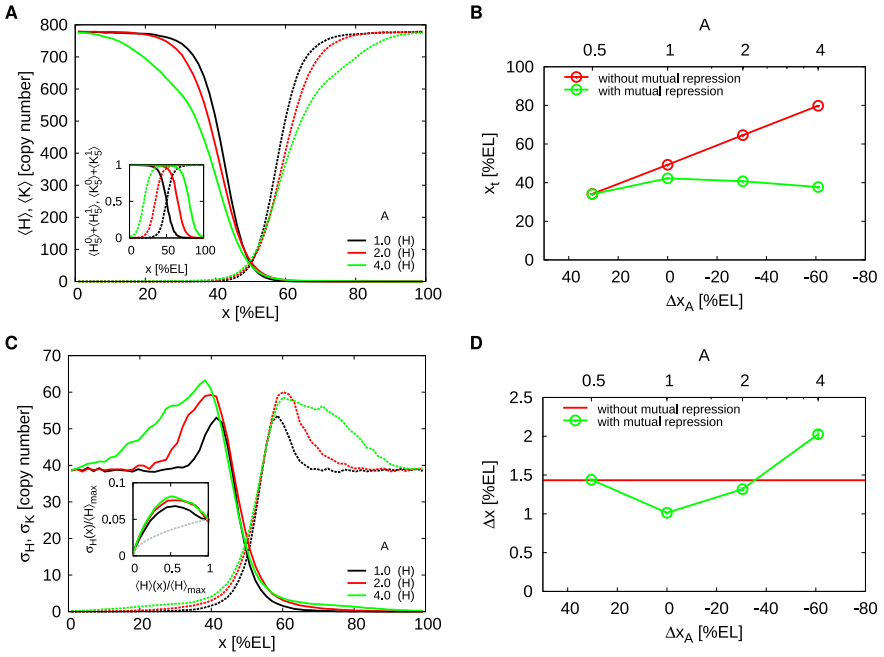

Figure 5.8: Mutual repression buffers against correlated variations in the activator levels. (A) Time- and circumference-averaged Hb ($\langle H \rangle$, solid lines) and Kni ($\langle K \rangle$, dashed lines) total copy-number profiles along the AP axis for various morphogen dosage factors A. Inset: the corresponding average occupancy of the promoter states with five bound morphogen molecules as a function of x. (B) The average Hb boundary position x_t as a function of Δx_A, the distance between the Hb and Kni boundaries without mutual repression, for the system with mutual repression (green,) and without it (red); Δx_A is varied by changing the morphogen dosage factor A. Note that mutual repression makes the gap-gene expression boundaries essentially insensitive to correlated changes in morphogen levels when $A > 1$. (C) AP profiles of the average standard deviation of the total Hb (σ_H, solid lines) and Kni (σ_K, dashed lines) copy numbers. Inset: $\sigma_H(x)/\langle H \rangle_{max}$ as a function of $\langle H \rangle(x)/\langle H \rangle_{max}$, where $\langle H \rangle(x)$ is the average Hb copy number at x and $\langle H \rangle_{max}$ its maximum over x. The grey dashed line represents the Poissonian limit. (D) The Hb boundary width Δx as a function of Δx_A with (green) and without (red) mutual repression. For $A = 4$, it was impossible to obtain a reliable error bar on Δx, because of the weak pinning force on the *hb* and *kni* expression boundaries.

The observation that the switching rate is low raises another important question: if errors are formed during development, can they be corrected? We observe in the simulations with $D = 0$ that when we allow the gap-gene expression patterns to develop starting from initial conditions in which the Hb and Kni copy numbers are both zero, in the overlap (bistable) region a spotty gap-gene expression pattern emerges, consisting of nuclei that are either in the high-*hb*—low-*kni* state or in the low-*hb*—high-*kni* state. When the diffusion constant of Hb and Kni is zero, then these defects

are essentially frozen in, precisely because of the low switching rate. Interestingly, however, we find in the simulations that a finite diffusion constant *can* anneal these defects. This may seem to contradict the statement made above that diffusion lowers the switching rate. The resolution of this paradox is that while diffusion lowers the switching rate for nuclei that are surrounded by nuclei that are in the same gap-gene expression state, it enhances the switching rate for nuclei that are surrounded by nuclei with a different gap-gene expression state; this is indeed akin to spins in an Ising system below the critical point. The mechanism for the formation of the gap-gene expression patterns, then, depends on the diffusion constant. When D is small yet finite, $0 < D < 0.1\mu\text{m}^2/\text{s}$, in the overlap region first small domains are formed consisting of nuclei that are in the same gap-gene expression state; these domains then coarsen analogously to Ostwald ripening of small crystallites in a liquid below the freezing temperature; ultimately, they combine with the *hb* or *kni* expression domains that have formed in the meantime outside the overlap region, where *hb* and *kni* are activated by their respective morphogens yet do not repress each other (see Videos S1 and S2, published online at http://www.ploscompbiol.org). For $D \gtrsim 0.1\mu\text{m}^2/\text{s}$, no "crystallites" are formed in the overlap region (both the Hb and Kni copy numbers are low yet finite and *hb* and *kni* simultatenously repress each other); instead, the *hb* and *kni* domains formed near the poles slowly invade the overlap region (see Videos S3 and S4, published online). Interestingly, even while in the absence of Hb and Kni diffusion $\Delta G \approx 0$ in the overlap region, the interface between the *hb* and *kni* expression domains does slowly diffuse towards midembryo when $D > 0$ and $A \leq 4$, due to the diffusive influx of Hb and Kni from the regions outside the overlap region. When $A = 8$, the *hb* and *kni* expression boundaries are not pinned to the middle of the embryo, and their positions exhibit slow and large fluctuations, presumably because the energetic driving force is small, and the diffusive influx of Hb and Kni from the regions near the poles is negligible. We will investigate this effect in more detail in a forthcoming publication.

Mutual repression inhibits boundary shifts

Fig. 5.8A shows the average gap-gene expression profiles for $A \in \{1, 2, 4\}$ and $D = 1.0\ \mu\text{m}^2/\text{s}$, which minimizes the boundary width Δx when $A = 1$ (see Fig. 5.5). While the morphogen-activation thresholds shift beyond midembryo as A is increased beyond unity, leading to an overlap of the domains where the gap genes are activated by their respective morphogens (see inset), the gap-gene expression boundaries overlap only marginally. This is quantified in panel B, which shows the Hb boundary position x_t as a function of A and as a function of $\Delta x_\text{A} \equiv x_{\text{A,Kni}} - x_{\text{A,Hb}}$, which is defined as the separation between the positions $x_{\text{A,Kni}}$ and $x_{\text{A,Hb}}$ where Kni and Hb are half-maximally activated by their respective morphogens; for $A = 1$, with adjoining morphogen activation regions, $\Delta x_\text{A} = 0$ and for $A > 1$, with overlapping activation regions, Δx_A is negative. Without mutual repression (red data), the Hb boundary position x_t tracks the shift of the *hb* activation threshold, as expected. In contrast, with mutual repression (green data) the boundary does not move beyond the position for $A = 1$ as A is increased. The same robustness was also observed for other values of the Hill coefficient of gap-gene activation (see Fig. S5.6 in the appendix).

Mutual repression enhances robustness to embryo-to-embryo variations

The fact that mutual repression can pin expression boundaries, dramatically enhances the robustness against embryo-to-embryo variations in the morphogen levels. We did not sample inter-embryo variations in A explicitly, but made an estimate using $\Delta x_t = (dx_t/dA)\Delta A$, where dx_t/dA was taken from Fig. 5.8B. A correlated symmetric variation $\delta_A \equiv \Delta A/A = 0.1$ of both morphogen levels then would lead to $\Delta x_t(\delta_A) \simeq 0.82$ %EL at $A = 1$ and $\Delta x_t(\delta_A) \simeq 0.25$ %EL at $A = 2$. Without mutual repression $\Delta x_{t,NR}(\delta_A) \simeq 2.2$ %EL. This analysis thus suggests that mutual repression reduces boundary variations due to fluctuations in the morphogen levels by almost a factor of 10 if the half-activation threshold is slightly posterior to midembryo (e.g. $A = 2$). If, on average, $A = 1$, then mutual repression still reduces Δx_t by inhibiting posterior shifts in those embryos in which $A > 1$. These results are consistent with those of [137, 117].

Overlap of morphogen activation domains does not corrupt robustness to intrinsic fluctuations

While mutual repression proves beneficial in buffering against embryo-to-embryo variations in morphogen levels, the question arises whether overlapping morphogen-activation domains does not impair robustness to intrinsic fluctuations arising from noisy gene expression and diffusion of gap gene proteins. We found that this depends on the Hill coefficient of gap-gene activation, which depends on the number n_{max} of morphogen binding sites on the promoter. Fig. 5.8C shows, for $n_{max} = 5$, that even though mutual repression increases the noise in gap-gene expression away from the boundaries, it has little effect on the noise at the boundaries when $A \leq 2$. For $A > 2$, the noise does increase significantly; in fact, it was impossible to obtain reliable error bars, because of the weak pinning force of the *hb-kni* interface. Moreover, overlapping morphogen activation domains decrease the steepness of the expression boundaries (panel A), and this increases the boundary width Δx (panel D). Indeed, when $n_{max} = 5$, mutual repression can enhance the precision of gene-expression boundaries, but only if the activation domains are adjoining ($A = 1$), or have a marginal overlap ($1 < A < 2$). For lower values of n_{max}, however, this enhancement of precision extends over a much broader range of A values; in fact, when $n_{max} < 3$, mutual repression enhances precision even up to $A = 4$ (see Fig. S5.6 in the appendix).

5.2.5 Boundaries shift upon uncorrelated variations in morphogen levels, yet intrinsic noise remains unaltered

Since correlated upregulation of both morphogen levels is a special case, we also studied the effect of uncorrelated activator scaling. To this end, only the Bcd level was multiplied by a global factor $A \in \{0.5, 1, 2, 3, 4\}$, while other parameters were left unchanged. Again we investigated the Hb boundary position x_t, its variance $\Delta x_t(\Delta A)$ due to extrinsic (embryo-to-embryo) variations in A and the variance due to intrinsic (intra-embryo) fluctuations $\Delta x(A)$. Results for $D = 1.0\ \mu\text{m}^2/\text{s}$ are summarized in Fig. 5.9.

The Hb boundary shifts less with mutual repression

Fig. 5.9A shows that the *hb* expression boundary shifts posteriorly with increasing A, in contrast to the case of correlated activator scaling. The Kni profile retracts in concert with the advance of the Hb domain. In Fig. 5.9B we compare the Hb boundary $x_t(A)$ to the data of HOUCHMANDZADEH et al. [52], assuming a 100% efficiency of the additional *bcd* gene copies. It is seen that the agreement between simulation and experiment is very good: while $x_t(A)$ of the simulations has a marginal offset as compared to the experimental data, the slope of $x_t(A)$ is essentially the same. Moreover, the slope is much lower than that obtained without mutual repression, showing that mutual repression can indeed buffer against uncorrelated variations in morphogen levels. These results parallel those of [137].

Robustness to inter-embryo fluctuations

To estimate the boundary variance due to inter-embryo variations in morphogen levels, we fitted a generic logarithmic function $x_{t,\text{fit}}(A) \equiv a \log(A) + b$ to the simulation data, giving $a \lesssim 15$ %EL for all values of D studied. Hence $\Delta x_t(\Delta A) \lesssim 15$ %EL $\Delta A/A$. A 10% variability in A around $A = 1$ thus would result in $\Delta x_t(\Delta A) \lesssim 1.5$ %EL, which is half as much as predicted by the model in [137] for that case. Nevertheless, it is yet too large to correspond to the experimental observations of MANU *et al.* that variations in the Bcd gradient of $\Delta A/A \approx 20\%$ correspond to variations in the Hb boundary position of $\Delta x_t(\Delta A) \lesssim 1.1$ %EL [116]. Our results therefore support their conjecture that higher levels of Bcd are correlated with upregulation of Kni and Cad.

Robustness to intra-embryo fluctuations

The output noise at the Hb boundary remains largely unaffected (Fig. 5.9C and inset) by Bcd upregulation, whereas the slope is reduced by approximately 10% per doubling of A (data not shown). As a result, the boundary width Δx stays close to 1 %EL for all considered A (green data; Fig. 5.9D), remaining lower than that obtained without mutual repression (red data; Fig. 5.9D).

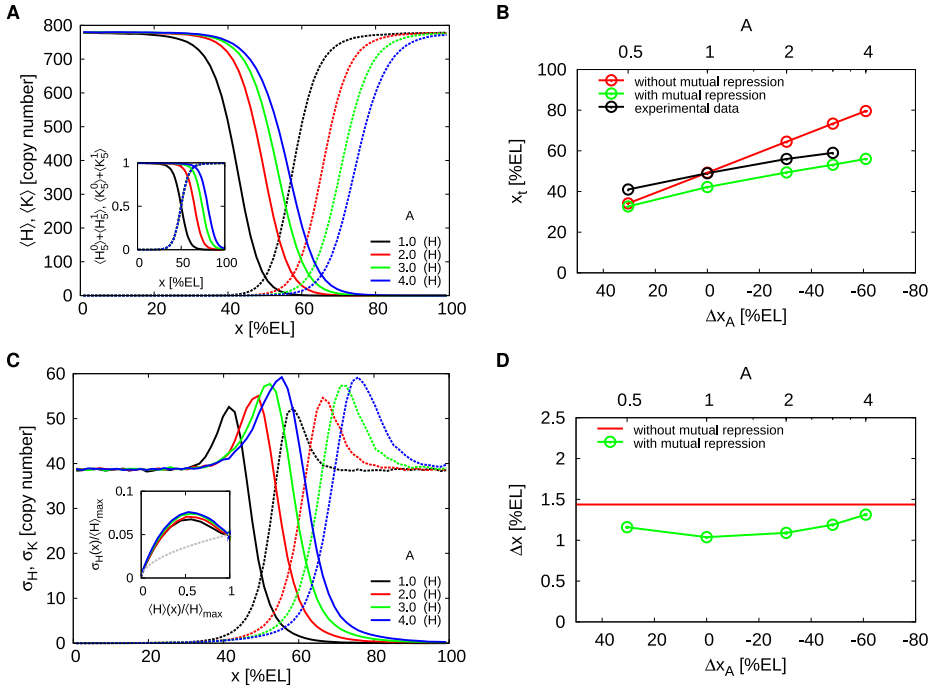

Figure 5.9: Robustness of the gap-gene expression boundaries to variations in the *bcd* gene dosage. (A) Time- and circumference-averaged Hb ($\langle H \rangle$, solid lines) and Kni ($\langle K \rangle$, dashed lines) total copy-nymber profiles along the AP axis for various *bcd* gene dosage factors $A_{\mathrm{Bcd}} = A \in \{0.5, 1, 2, 3, 4\}$ and $D = 1.0\ \mu\mathrm{m}^2/\mathrm{s}$. Inset: the average occupancy of the promoter states with five bound morphogen molecules as a function of x. (B) Comparison of the boundary position x_{t} as a function of A for $D = 1.0\ \mu\mathrm{m}^2/\mathrm{s}$ to values measured by Houchmanzadeh *et al.* [52] (black line). The red line shows the simulation results for the system without mutual repression. Note the good agreement between the experimental data and the simulation data of the system with mutual repression. (C) Profiles of the average standard deviation of the total Hb (σ_{H}, solid lines) and Kni (σ_{K}, dashed lines) copy number. Inset: $\sigma_{\mathrm{H}}(x)/\langle H \rangle_{\max}$ as a function of $\langle H \rangle(x)/\langle H \rangle_{\max}$. The grey dashed line represents the Poissonian limit. (D) The Hb boundary width Δx as a function of A and Δx_{A}, the separation between the Hb and Kni boundaries in a system without mutual repression, for the system with (green) and without (red) mutual repression. Δx_{A} is varied by multiplying the Bcd level by A_{Bcd}.

5.2.6 Mutual repression with one morphogen gradient

In the mutual repression motif discussed above, the two antagonistic genes were activated by independent morphogens, one emanating from the anterior and the other from the posterior pole. An alternative mutual repression motif is one in which the two genes are activated by the same morphogen, *e.g.* *hb* and *kni* both being activated by Bcd [125, 151].

We simulated a system in which *hb* and *kni* mutually repress each other, yet both are activated by Bcd, with *kni* having a lower Bcd activation threshold than *hb*. This generates a Hb and Kni domain, with the latter being located towards the posterior of the former (see Fig. S5.9 in the appendix). We systematically varied the mutual repression strength and the diffusion constant, to elucidate how mutual repression and spatial averaging sculpt stable expression patterns in this motif. Our analysis reveals that since *hb* and *kni* are both activated by the same morphogen gradient, *hb* should repress *kni* more strongly than vice versa: with equal mutual repression strengths either a spotty gap-gene expression pattern emerges in the anterior half, namely when the Hb and Kni diffusion constant are low ($D < 0.1\mu\text{m}^2/\text{s}$), or Kni dominates or even squeezes out Hb, namely when their diffusion constant is large. Nonetheless, for unequal mutual repression strengths and sufficiently high D, the repression of *hb* by *kni* does enhance the precision and the steepness of the Hb boundary, although the effect is smaller than in the two-gradient motif (Fig. S5.9 in the appendix). Clearly, while the one-morphogen-gradient motif cannot provide the robustness against embryo-to-embryo variations in morphogen levels that the two-morphogen-gradient motif can provide, mutual repression can enhance boundary precision also in this motif.

5.3 Discussion

Using large-scale stochastic simulations, we have examined the role of mutual repression in shaping spatial patterns of gene expression, with a specific focus on the *hb*-*kni* system. Our principal findings are that mutual repression enhances the robustness both against intra-embryonic fluctuations due to noise in gap-gene expression and embryo-to-embryo variations in morphogen levels.

To investigate the importance of mutual repression in shaping gene-expression patterns, we have systematically varied a large number of parameters: the strength of mutual repression, the diffusion constant of the gap proteins, the maximum expression level, the Hill coefficient of gap-gene activation, and the amplitude of the morphogen gradients. To elucidate how varying these parameters changes the precision of the gap-gene boundaries, we examined how they affect both the steepness of the gene-expression boundaries and the expression noise at these boundaries (see Eq. (5.1)). The effect on the steepness is, to a good approximation, independent of the noise, and would therefore be more accessible experimentally. We find that the steepness increases with decreasing diffusion constant, but increases with increasing strength of mutual repression, maximum expression level, and Hill coefficient of gap-gene activation. Moreover, mutual repression shifts the expression boundaries apart and makes the system more robust to embryo-to-embryo variations in the morphogen levels. In contrast, the noise at the expression boundaries decreases with increasing

diffusion constant, decreasing expression level, and decreasing Hill coefficient, while the dependence on the strength of mutual repression is non-monotonic, albeit not very large. The interplay between noise and steepness means that the precision of the gap-gene expression boundaries increases (i.e., Δx decreases) with increasing expression level. The dependence of Δx on the diffusion constant and the strength of mutual repression, on the other hand, is non-monotonic: there is an optimal diffusion constant and repression strength that maximizes precision. The effect of the Hill coefficient is conditional on the strength of mutual repression: without mutual repression, the precision slightly decreases with increasing Hill coefficient, while with mutual repression the precision increases with increasing Hill coefficient.

While mutual repression has only a weak effect on the noise in the expression levels at the gene-expression boundaries, it does markedly steepen the boundaries, especially when the diffusion constant is low. Indeed, mutual repression can enhance the precision of gene expression boundaries by steepening them. Nonetheless, even with mutual repression spatial averaging [123, 122] appears to be a prerequisite for achieving precise expression boundaries: without diffusion of the gap proteins, the width of the *hb* expression boundary is larger than that observed experimentally [51]. Hence, while previous mean-field analysis found diffusion not be important for setting up gene-expression patterns [131, 115], our analysis underscores the importance of diffusion in reducing copy-number fluctuations. In addition, diffusion can anneal patterning defects that might arise from the bistability induced by mutual repression. Diffusion is, indeed, a potent mechanism for reducing the effect of fluctuations, such that mean-field analyses can accurately describe mean expression profiles.

Interestingly, the minimum boundary width at the optimal diffusion constant in a system with mutual repression is not much lower than that in one without mutual repression. Yet, in the latter case the boundary width is already approximately one nuclear spacing, and there does not seem to be any need for reducing it further. However, with mutual repression, the same boundary width can be obtained at a lower diffusion constant, where the steepness of the boundaries is much higher, approximately twice as high as that without mutual repression. Our results thus predict that mutual repression allows for gap-gene expression boundaries that are both precise and steep. In fact, the width and steepness of the boundaries as predicted by our model are in accordance with values of these quantities measured experimentally [114].

Our observation that mutual repression increases the steepness of gene-expression boundaries without significantly raising the noise, makes the mechanism distinct from other mechanisms for steepening gene expression boundaries, such as lowering diffusion constants [122] or increasing the cooperativity of gene activation (see Fig. S5.5 in the appendix). These mechanisms typically involve a trade off between steepness and noise: lowering the diffusion constant or increasing the Hill coefficient of gene activation steepens the profiles but also raises the noise in protein levels at the expression boundary. In fact, increasing the Hill coefficient (without mutual repression) *decreases* the precision of gene-expression boundaries. This is because increasing the Hill coefficient increases the width of the distribution of times during which the promoter is off, leading to larger promoter-state fluctuations and thereby to larger noise in gene expression (see Fig. S5.4 in the appendix).

Another important role of mutual repression as suggested by our simulations is to buffer against inter-embryonic variations in the morphogen levels. HOUCHMANDZADEH *et al.* observed that in *bcd* overdosage experiments the Hb boundary does not shift as far posteriorly as predicted by the French flag model [52]. One possible explanation that has been put forward is that Bcd is inactivated in the posterior half of the embryo via a co-repressor diffusing from the posterior pole [137]. More recently, it has been proposed that gap gene cross regulation underlies the resilience of the gap-gene expression domains towards variations in the *bcd* gene dosage [116, 115]. Our analysis supports the latter hypothesis. In particular, our results show that when the regions in which *hb* and *kni* are acitvated by their respective morphogens overlap, the boundary positions are essentially insensitive to correlated variations in both morphogen levels, and very robust against variations of the Bcd level only, with the latter being in quantitative agreement with what has been observed experimentally [52]. Moreover, when this overlap is about 0-20% of the embryo length, mutual repression confers robustness not only against inter-embryonic variations in morphogen levels, but also intra-embryonic fluctuations such as those due to noise in gene expression.

MANU *et al.* found that in the *kr*;*kni* double mutant, which lacks the mutual repression between *hb* and *kni*/*kr*, the Hb midembryo boundary is about twice as wide as that in the wild-type embryo [116]. This could be due to a reduced robustness against embryo-to-embryo variations in morphogen levels, but it could also be a consequence of a diminished robustness against intra-embryonic fluctuations. The analysis of MANU *et al.* suggests the former [116, 115], and also our results are consistent with this hypothesis. However, our results also support the latter scenario: for $D \approx 0.3\mu\mathrm{m}^2/\mathrm{s}$, the Hb boundary width in the system without mutual repression is about twice as large as that in the system with mutual repression (Fig. 5.5, middle). Clearly, new experiments are needed to establish the importance of intra-embryonic fluctuations versus inter-embryonic variations in gene expression boundaries.

To probe the relative magnitudes of intra- vs inter-embryonic variations, one ideally would like to measure an ensemble of embryos as a function of time; one could then measure the different contributions to the noise in the quantity of interest following Eq. (5.5). This, however, is not always possible; staining, e.g., typically impedes performing measurements as a function of time. The question then becomes: if one measures different embryos at a given moment in time, are embryo-to-embryo variations in the mean boundary position or protein copy number (thus averaged over the circumference) due to intra-embryonic fluctuations in time or due to systematic embryo-to-embryo variations in e.g. the morphogen levels? Experiments performed on different embryos but at one time point cannot answer this question. Our analysis, however, suggests that the intra-embryonic fluctuations in the mean copy number or boundary position (i.e. averaged over ϕ) over time are very small, and that hence embryo-to-embryo variations in the mean quantity of interest are really due to systematic embryo-to-embryo variations; these variations then correspond to $\sigma^2_{\overline{\langle \mathrm{G} \rangle}_\phi}$ or $\sigma^2_{\overline{\langle \mathrm{x_t} \rangle}_\phi}$ in Eq. (5.5) or Eq. (5.6), respectively. The intra-embryonic fluctuations, $\langle \overline{\sigma^2_{\mathrm{G}}} \rangle_{\mathrm{e}}(x)$ or $\langle \overline{\sigma^2_{\mathrm{x_t}}} \rangle_{\mathrm{e}}(x)$, can then be measured by measuring the quantity of interest, G or x_t, as a function of ϕ, and averaging the resulting variance over all embryos. We expect that these observations, in particular the critical one that intra-embryonic fluctuations in

the mean quantity of interest are small, also hold for non-stationary systems, although this warrants further investigation.

Our model does not include self-activation of the gap genes. Auto-activation has been reported for *hb*, *kr* and *gt*, but there seems to be no evidence in case of *kni* [152, 12]. The self-enhancement of gap genes has the potential to steepen and sharpen expression domains even more by amplifying local patterns [153, 154]. Our results suggest, however, that auto-activation is not necessary to reach the boundary steepness and precision as observed experimentally.

Our results provide a new perspective on the WADDINGTON picture of development [155, 156]. WADDINGTON argued that development is "canalized", by which he meant that cells differentiate into a well-defined state, despite variations and fluctuations in the underlying biochemical processes. It has been argued that canalization is a consequence of multistability [116, 115, 131], which is the idea that cells are driven towards attractors, or basins of attraction in state space. To determine whether a given system is multistable, it is common practice to perform a stability analysis at the level of single cells or nuclei. Our results show that this approach should be used with care: diffusion of proteins between cells or nuclei within the organism can qualitatively change the energy landscape; specifically, a cell that is truly bistable without diffusion might be monostable with diffusion. Indeed, our results highlight that a stability analysis may have to be performed not at the single cell level, but rather at the tissue level, taking the diffusion of proteins between cells into account.

Finally, while our results have shown that mutual repression can stabilize expression patterns of genes that are activated by morphogen gradients, one may wonder whether it is meaningful to ask the converse question: do morphogen gradients enhance the stability of expression domains of genes that mutually repress each other? This question presupposes that stable gene expression patterns can be generated without morphogen gradients. Although it was shown that confined (though aberrant) gap gene patterns form in the absence of Bcd [157, 158, 159] and that Hb can partly substitute missing Bcd in anterior embryo patterning[160], it is not at all obvious how precise domain positioning could succeed in such a scenario. In particular, one might expect that with mutual repression only, thus without morphogen gradients, there is no force that pins the expression boundaries. Our results for the large overlapping morphogen-activation domains, with $A = 8$, illustrate this problem: in the overlap region, both *hb* and *kni* are essentially fully activated by their respective morphogens, as a result of which the morphogen gradients cannot determine the positions of the gap-gene boundaries within this region; indeed, mutual repression has to pin the expression boundaries of *hb* and *kni*. Yet, our results show that in this case the positions of the *hb* and *kni* expression boundaries exhibit large and slow fluctuations, suggesting that mutual repression alone cannot pin expression boundaries. Interestingly, however, with $A = 4$, the region in which both genes are activated is still quite large, about 50% of the embryo, and yet even though the underlying energy landscape is flat in this region, the interfaces do consistently move towards the middle of the embryo, due to diffusive influx of Hb and Kni from the polar regions. It is tempting to speculate that mutual repression and diffusion can maintain stable expression patterns, while morphogen gradients are needed to set these up, *e.g.* by breaking the symmetry between possible patterns that can be formed with mutual repression only.

5.4 Methods

In the following we describe details of our parameter choice and sampling technique. To unravel the mechanisms by which mutual repression shapes gene-expression patterns, it is useful to take the Cad-Kni-system to be a symmetric copy of the Bcd-Hb-system. Cad thus inherits its parameters from Bcd and Kni from Hb, if not otherwise stated. Table S5.1 in the appendix gives an overview of our standard parameter values. Data from experiments was used whenever possible. When it was unavailable we made reasonable estimates.

Binding rates are diffusion limited

We assume all promoter binding rates to be diffusion limited and calculate them via $k_{\mathrm{on}}^{\mathrm{X}} = 4\pi\alpha D_{\mathrm{X}}/V$. Here $\alpha = 10$ nm is the typical size of a binding site, D_{X} is the intranuclear diffusion constant of species X and $V = 143.8\ \mu\mathrm{m}^3$ is the nuclear volume. The precise values of D_{X} for the different species in our system are not known. GREGOR *et al.* have shown experimentally that the nuclear concentration of Bcd is in permanent and rapid dynamic equilibrium with the cytoplasm [30], suggesting that nuclear and cytoplasmic diffusion constants can be taken for equal. They have found $D_{\mathrm{Bcd}} \simeq 0.32\ \mu\mathrm{m}^2/\mathrm{s}$ by FRAP measurements. This value has been subject to controversy because it is too low to establish the gradient before nuclear cycle 10 ($\simeq$ 90 min) by diffusion and degradation only, prompting alternative gradient formation models [161, 162, 163, 164, 165, 166]. A more recent study revisited the problem experimentally via FCS, yielding significantly higher values for D_{Bcd} up to $10\ \mu\mathrm{m}^2/\mathrm{s}$ with a lower limit of $1\ \mu\mathrm{m}^2/\mathrm{s}$ [167]. We therefore have chosen a 10x higher value of $D_{\mathrm{Bcd}} = D_{\mathrm{Cad}} \equiv D_{\mathrm{A}} = 3.2\ \mu\mathrm{m}^2/\mathrm{s}$ as compared to the earlier choice in [122]. For simplicity, this value is taken for all binding reactions occuring in our model, except for the dimerization reaction rate $k_{\mathrm{on}}^{\mathrm{D}}$, which is taken to be higher by a factor of 2 to account for the fact that both reaction partners diffuse freely.

To model cooperative activation of *hb* and *kni* by their respective morphogens, the morphogen-promoter dissociation rate is given by $k_{\mathrm{off,n}}^{\mathrm{A}} = a/b^n/\mathrm{s}$, where n is the number of morphogen molecules that are bound to the promoter; for our standard cooperativity $n_{\mathrm{max}} = 5$ the values of $a = 410$ and $b = 6$ have been chosen such that the threshold concentration for promoter activation (in the absence of repression) equals the observed average number of morphogen molecules at midembryo (when $A = 1$, see below). n_{max} is varied in some simulations; we describe in appendix section 5.C.1 how a and b are chosen in these cases. The promoter unbinding rate of *hb* and *kni* (the repressor-promoter unbinding rate) $k_{\mathrm{off}}^{\mathrm{R}}$ is a parameter that we vary systematically. To study the potential role of bistability we decided to set $k_{\mathrm{off}}^{\mathrm{R}}$ to a value which ensures bistable behavior when both *hb* and *kni* are fully activated by their respective morphogens (meaning that all five binding morphogen-binding sites on the promoter are occupied). This requires tight repression, yielding dissociation constants $\sim 10^{-2}$ nM (but see also below). The dimer dissociation rate is set to be $k_{\mathrm{off}}^{\mathrm{D}} = k_{\mathrm{on}}^{\mathrm{D}}/V$, which is motivated by the choice for the toggle switch models studied in [129, 130] and [60], and asserts that at any moment in time the majority of the gap proteins is dimerized. This was found to be a precondition for bistability in the

mean-field limit in previous studies [127, 129, 130].

The parameters of the exponential morphogen gradients are chosen such that the number of morphogen molecules at midembryo and the decay length of the gradient are close to the experimentally observed values for Bcd, 690 and $\lambda = 119.5$ μm, respectively [51].

Production and degradation dynamics

The copy numbers of both monomers and dimers and the effective gap gene degradation rate μ_{eff} depend in a nontrivial manner on production, degradation and dimerization rates. However, for constant production rate β, without diffusion and neglecting promoter dynamics, an analytical estimate for the monomer and dimer copy numbers can be obtained from steady state solutions of the rate equations (see appendix section 5.A.2). Based on this we have made a choice for β and the monomeric (μ_{M}) and dimeric (μ_{D}) decay rates that leads to reasonable copy numbers and μ_{eff} (see Table S5.1 in the appendix). The latter is defined as the mean of μ_{M} and μ_{D} weighted by the species fractions. μ_{M} and μ_{D} are set such that $\mu_{\text{eff}} \simeq 4.34 \cdot 10^{-3}$ 1/s, which corresponds to an effective protein lifetime of ~ 4 min. This is close to values used earlier [137, 122] and allows for the rapid establishment of the protein profiles observed in experiments. The dimers have a substantially lower degradation rate than monomers, which enhances bistability [168]. The lower decay rate of the dimers may be attributed to a stabilizing effect of oligomerization (cooperative stability) [168].

Free parameters

One of the key parameters that we vary systematically is the internuclear gap gene diffusion constant D, which defines a nuclear exchange rate $k_{\text{ex}} = 4D/\ell^2$ (ℓ = internuclear distance). To study the effect of embryo-to-embryo variations in the morphogen levels, the latter are scaled globally by a dosage factor A. We considered two scenarios: scaling both gradients by the same A ("correlated variations") or scaling the Bcd gradient only ("uncorrelated variations"). To test how strongly the assumption of strong repressor-promoter binding affects our results, we also varied the repressor-promoter dissociation rate $k_{\text{off}}^{\text{R}}$. Moreover, to study the dependence of our results on the gap-gene copy numbers, we also increased the protein production rate β. These simulations are much more computationally demanding; therefore we limited ourselves to simulations with $\beta = 2\beta_0$ and $\beta = 4\beta_0$ where β_0 is our baseline value. Finally we also studied a system where both gap genes are activated by the same gradient (Bcd), varying both the diffusion constant D and the Kni repressor off-rate $k_{\text{off}}^{\text{R,Kni}}$, while keeping $k_{\text{off}}^{\text{R,Hb}}$ at the standard value.

Algorithmic details

All simulations are split into a relaxation and a measurement run. During the relaxation run we propagate the system towards the steady state without data collection. To reach steady state, as a standard we run $1 \cdot 10^9 - 3 \cdot 10^9$ GILLESPIE steps (ca. $2 \cdot 10^5 - 7 \cdot 10^5$ updates per nucleus). The measurement run is performed with twice the number of steps ($2 \cdot 10^9 - 6 \cdot 10^9$). The simulations are started from exponential

morphogen gradients and step profiles of the gap proteins; however, we verified that the final result was independent of the precise initial condition, and that the system reached steady state after the equilibration run. The results for $A = 4$ (Fig. 5.8) form, however, an exception: here it was impossible to obtain a reliable error bar, because of the weak pinning force on the *hb* and *kni* expression boundaries.

In steady state, we record for each row of nuclei and with a measurement interval of $\tau_\mathrm{m} = 100$ s the Hb boundary position x_t, i.e. the position where H drops to half of the average steady-state value measured at its plateau close to the anterior pole, which in our simulations is equal to the maximum average total Hb level $\langle H \rangle_\mathrm{max}$. From the corresponding histogram we obtain the boundary width Δx by computing the standard deviation. Additionally, after runtime we calculate an approximation for Δx from the standard deviation of H divided by the slope of the averaged H profile, both quantities taken at x_t, see Eq. (5.1) [51, 20, 122]. Further details of boundary measurement are described in appendix section 5.A.3.

Error bars for a given quantity are estimated from the standard deviation among $N_\mathrm{B} = 10$ block averages (block length $6 \cdot 10^8$) divided by $\sqrt{N_\mathrm{B} - 1}$, following the procedure described in [169]. We verified that estimates with smaller and larger block sizes yield similar estimates for a representative set of simulations.

5.5 Acknowledgements

This chapter is based on the following publication [170]:

Sokolowski T. R., Erdmann T. and ten Wolde P. R. (2012) Mutual Repression Enhances the Steepness and Precision of Gene Expression Boundaries.
PLoS Comput Biol **8**(8): e1002654. (doi:10.1371/journal.pcbi.1002654)

The author thanks A. HOFFMANN for a very thorough reading of this chapter.

5.A Appendix: Details of parameter choice and measurements

5.A.1 Number of cortical nuclei at cell cycle 14

The development of the Drosophila embryonic syncytium starts with a single nucleus. The first 9 nuclear divisions happen in the yolk. During cell cycles 7 to 10 a migration of the nuclei towards the cortex can be observed. However, approximately 200 polyploid nuclei stay behind in the yolk and stop dividing after their 10th cycle [139]. This quiescence persists during subsequent cell cycles, including cycle 14. As an effect of this, the number of nuclei at the cortex in cycle 14 is considerably lower than $2^{13} = 8192$. An estimate of the reduced number of cortical nuclei is given by:

$$N_{\text{cortex}} \simeq (2^9 - 200) \cdot 2^4 = 4992 \tag{S5.1}$$

This number indeed is closer to 2^{12} than to 2^{13}. Note that in our model the precise number of nuclei does not matter, rather it is the distance between the nuclear compartments and the diffusion correlation length that impact on the results. Our values for both the internuclear distance and the nuclear diameter correspond to the experimental values reported by GREGOR et al. [51, 30].

5.A.2 Predicted copy numbers and effective protein lifetime

Our main observables are the total copy numbers of Hb and Kni, defined as follows:

$$\begin{aligned} H &\equiv c^{\mathrm{m}}_{\mathrm{n,H}} = c^{\mathrm{m}}_{\mathrm{n,H_M}} + 2c^{\mathrm{m}}_{\mathrm{n,H_D}} + 2\sum_{\mathrm{j}=0}^{5} c^{\mathrm{m}}_{\mathrm{n,K^1_j}} \\ K &\equiv c^{\mathrm{m}}_{\mathrm{n,K}} = c^{\mathrm{m}}_{\mathrm{n,K_M}} + 2c^{\mathrm{m}}_{\mathrm{n,K_D}} + 2\sum_{\mathrm{j}=0}^{5} c^{\mathrm{m}}_{\mathrm{n,H^1_j}} \end{aligned} \tag{S5.2}$$

Here, for $G \in \{H, K\}$, $c^{\mathrm{m}}_{\mathrm{n,G^1_j}} = 1$ if the promoter of species G is binding j morphogen molecules and one (repressing) gap dimer; evidently, at any given moment in time $c^{\mathrm{m}}_{\mathrm{n,G^1_j}}$ can be equal to one for only one $j \in \{0..5\}$.

The ratio between the number of monomeric and the number of dimeric proteins is a nontrivial function of the monomer production rate, the monomer and dimer degradation rates and the parameters that determine the dimerization and dedimerization reactions. To obtain an estimate for the expected copy numbers of monomers and dimers of gene g we solved the mean-field rate equations for a simplified model which comprises monomer production, (de)dimerization and monomer and dimer degradation only, i.e. in which promoter state fluctuations and diffusion are neglected, in the steady state. We assume here that stochastic monomer production events can be accounted for by an effective mean-field production rate $\langle\beta\rangle = \beta\langle H^0_5\rangle$ for Hb and similarly for Kni, which depends on promoter (un)binding parameters and the particular morphogen and repressor levels. This yields the following prediction for the

copy number of monomers ($G_{\mathrm{M},\langle\beta\rangle}$) and dimers ($G_{\mathrm{D},\langle\beta\rangle}$):

$$G_{\mathrm{M},\langle\beta\rangle} = \frac{1}{4k^{\mathrm{D}}_{\mathrm{on}}\mu_{\mathrm{D}}}\Bigg\{2k^{\mathrm{D}}_{\mathrm{on}}\mu_{\mathrm{D}} - k^{\mathrm{D}}_{\mathrm{off}}\mu_{\mathrm{M}} - \mu_{\mathrm{M}}\mu_{\mathrm{D}} + \sqrt{8\langle\beta\rangle k^{\mathrm{D}}_{\mathrm{on}}\mu_{\mathrm{D}}\left(k^{\mathrm{D}}_{\mathrm{off}}+\mu_{\mathrm{D}}\right) + \left[\mu_{\mathrm{M}}\left(k^{\mathrm{D}}_{\mathrm{off}}+\mu_{\mathrm{D}}\right) - 2k^{\mathrm{D}}_{\mathrm{on}}\mu_{\mathrm{D}}\right]^2}\Bigg\}$$

$$G_{\mathrm{D},\langle\beta\rangle} = \frac{1}{8k^{\mathrm{D}}_{\mathrm{on}}\mu^2_{\mathrm{D}}}\Bigg\{k^{\mathrm{D}}_{\mathrm{off}}\mu^2_{\mathrm{M}} + \mu_{\mathrm{D}}\left[4\langle\beta\rangle k^{\mathrm{D}}_{\mathrm{on}} + \mu_{\mathrm{M}}\left(\mu_{\mathrm{M}} - 2k^{\mathrm{D}}_{\mathrm{on}}\right)\right] - \mu_{\mathrm{M}}\sqrt{8\langle\beta\rangle k^{\mathrm{D}}_{\mathrm{on}}\mu_{\mathrm{D}}\left(k^{\mathrm{D}}_{\mathrm{off}}+\mu_{\mathrm{D}}\right) + \left[\mu_{\mathrm{M}}\left(k^{\mathrm{D}}_{\mathrm{off}}+\mu_{\mathrm{D}}\right) - 2k^{\mathrm{D}}_{\mathrm{on}}\mu_{\mathrm{D}}\right]^2}\Bigg\} \tag{S5.3}$$

Here μ_{M} (μ_{D}) is the monomeric (dimeric) degradation rate and $k^{\mathrm{D}}_{\mathrm{on}}$ (k^{D}_{off}) are the dimerization forward (backward) rates, respectively. From this we calculate the total expected copy number $G_{\langle\beta\rangle} := 2G_{\mathrm{D},\langle\beta\rangle} + G_{\mathrm{M},\langle\beta\rangle}$ at effective production rate $\langle\beta\rangle$. In particular in the full-activation case, i.e. when the probability to be fully activated and unrepressed $\langle G^0_5\rangle \approx 1$ and therefore $\langle\beta\rangle \approx \beta$, the above estimates correspond to average values from our simulations very well.

We define the effective degradation as:

$$\mu_{\mathrm{eff}} = \mu_{\mathrm{eff}}(G_{\mathrm{M}}, G_{\mathrm{D}}) \equiv \frac{1}{G_{\mathrm{M}} + 2G_{\mathrm{D}}}\left(\mu_{\mathrm{M}}G_{\mathrm{M}} + 2\mu_{\mathrm{D}}G_{\mathrm{D}}\right) \tag{S5.4}$$

Our standard values result in $\mu_{\mathrm{eff}} \approx 4.34 \cdot 10^{-3}/\mathrm{s}$ with $G_{\mathrm{M}} = G_{\mathrm{M},\beta}$ and $G_{\mathrm{D}} = G_{\mathrm{D},\beta}$.

5.A.3 Measurement of the boundary width

By default we determine the boundary width in the following two ways:

Let $c^{\mathrm{m}}_{\mathrm{n,s}}$ be the copy number of species s in a nucleus with angular index $m < N_\phi$ and axial index $n < N_{\mathrm{x}}$, where N_ϕ is the number of rows around the circumference of the cylinder, and N_{x} is the number of colums in the axial direction along the AP axis. To compute the boundary width of the expression domain of a gap protein s, we compute for each row m $T^{\mathrm{m}}_{\mathrm{n,s}} = (c^{\mathrm{m}}_{\mathrm{n,s}} - \theta_{\mathrm{s}}) \cdot (c^{\mathrm{m}}_{\mathrm{n+1,s}} - \theta_{\mathrm{s}})$ as a function of n, where θ_{s} is half the copy number expected at full activation. A boundary position $x^{\mathrm{m}}_{\mathrm{t}} = x^{\mathrm{m}}(n_{\mathrm{t}} + \frac{1}{2})$ is defined as the position (nucleus) where $T^{\mathrm{m}}_{\mathrm{n_t,s}} < 0$. The values of $x^{\mathrm{m}}_{\mathrm{t}}$ are recorded in a histogram; here, the positions for the different rows m are put in the same histogram. The histogram is normalized at the end of the simulation, and the boundary width Δx is calculated as the standard deviation of this histogram.

Secondly, at the end of the simulation, the slope of the average, $\langle H(x_{\mathrm{t}})\rangle'$, and the standard deviation of the total Hb copy number $\sigma_{\mathrm{H}}(x_{\mathrm{t}})$ at the Hb boundary position x_{t} are calculated from the time- and ϕ-averaged profiles. From this, an approximation for the boundary width given by $\Delta x \approx \frac{\sigma(x_{\mathrm{t}})}{|\langle H(x_{\mathrm{t}})\rangle'|}$ is obtained, following [20, 51, 122]. To this end, first x_{t} is determined in the same way as in the runtime measurements, only now working on the (both time- and circumference-) averaged profile. We describe in the following section how the steepness $\langle H(x_{\mathrm{t}})\rangle'$ is measured.

5.A.4 Measurement of the profile steepness

In our discrete system the measurement of a local derivative at the boundary position x_t is a process prone to even small stochastic variations if a naive measurement technique is chosen. If the average boundary position x_t for a set of different samples with identical initial conditions always is in between two particular nuclear positions $x(n_0)$ and $x(n_0+1)$, then using linear differences to determine the steepness $\langle H(x_t)\rangle'$ at the boundary position may give a reasonable estimate. If, however, x_t fluctuates around a particular nuclear position $x(n_0)$ among different samples and $\langle H(x(n_0-1))\rangle - \langle H(x(n_0))\rangle$ significantly differs from $\langle H(x(n_0))\rangle - \langle H(x(n_0+1))\rangle$, the linear differences method will produce a large error bar and also markedly affect the mean of x_t among these samples. As a result both the measured steepness and the quality of that measurement for a given set of parameters depends on whether x_t accidently happens to predominantly vary in the interval between the same nuclear positions or not. To overcome this illness we measure the boundary steepness from the average protein profile by a two-step polynomial fitting procedure: First we fit a polynomial of 3rd degree to a region of the data around x_t that contains at least four points (nuclei). The derivative of the polynomial at x_t gives an initial estimate of the boundary slope, which we use this to calculate the approximative x-interval over which the profile falls from maximal to minimial expression level. If the latter is larger than the original fitting range (which usually is the case) we repeat the fitting on the enlarged interval. Since the profiles to a good approximation are sigmoidal functions this improves the quality of the fit. The measured boundary slope then is defined as the derivative of the polynomial function at x_t after the second fitting.

Parameter / Quantity	Symbol	Value	Unit	Remarks
Geometry				
Number of nuclei in axial direction x	N_{x}	64		
Number of nuclei in circumferential direction ϕ	N_{ϕ}	64		
Internuclear distance (lattice spacing)	l	8.5	μm	supported by [51]
- resulting embryo length	L	544	μm	
Nuclear radius	R	6.5	μm	supported by [30]
- resulting nuclear volume	V	143.8	$\mu\mathrm{m}^3$	assuming spherical shape
Morphogen / activator gradients				
Standard copy number at the poles	A_0	6720		varied in some simulations
- resulting copy number at half activation	$A_{\frac{1}{2}}$	690		supported by [51]
Morphogen diffusion length	λ	119.5	μm	supported by [51]
Activation dynamics				
Intranuclear activator diffusion constant	D_{A}	3.2	$\mu\mathrm{m}^2/\mathrm{s}$	supported by [167]
Activator binding site target size	α	10	nm	
- resulting activator binding rate	$k_{\mathrm{on}}^{\mathrm{A}}$	0.40	$\mu\mathrm{m}^3/\mathrm{s}$	diffusion limited, $k_{\mathrm{on}}^{\mathrm{A}} = 4\pi\alpha D_{\mathrm{A}}$
Activator unbinding rate	$k_{\mathrm{off,n}}^{\mathrm{A}}$	$410/6^n$	1/s	n = no. of bound activator molecules
Hill coefficient of activation	$\mathrm{n}_{\mathrm{max}}$	5		supported by [51]
Gap gene dynamics				
Gap protein monomer production rate	β_0	3.37	1/s	
Gap protein monomer degradation rate	μ_{M}	$3.37{\cdot}10^{-2}$	1/s	
Gap protein dimer degradation rate	μ_{D}	$3.37{\cdot}10^{-3}$	1/s	
Dimerization forward rate	$k_{\mathrm{on}}^{\mathrm{D}}$	0.80	$\mu\mathrm{m}^3/\mathrm{s}$	same as $2k_{\mathrm{on}}^{\mathrm{A}}$
Dimerization backward rate	$k_{\mathrm{off}}^{\mathrm{D}}$	$5.59{\cdot}10^{-3}$	1/s	
- predicted total Hb (Kni) copy number at full activation and $D = 0$	H_{β_0} (K_{β_0})	775		
Gap protein diffusion constant	D	varied		
Repression dynamics				
Repressing dimer binding rate	$k_{\mathrm{on}}^{\mathrm{R}}$	0.40	$\mu\mathrm{m}^3/\mathrm{s}$	same as $k_{\mathrm{on}}^{\mathrm{A}}$
Repressing dimer unbinding rate	$k_{\mathrm{off}}^{\mathrm{R}}$	$5.27{\cdot}10^{-3}$	1/s	equal to $0.1 \cdot k_{\mathrm{A},5}^{-}$; varied in some simulations

Table S5.1: The standard set of the most important parameters of the Drosophila embryo model.

5.B Appendix: Supplementary analysis

5.B.1 Poissonian limit with dimerization

In [122], it was shown that, when $D \to \infty$, the variance in the protein concentration becomes equal to the mean concentration: diffusion washes out bursts in gene expression, thus reducing the non-Poissonian part of the noise. However, in that model the proteins do not dimerize, in contrast to our model. With dimerization, a different limit for the variance in the total protein concentration is approached as $D \to \infty$. To derive this limit, first note that the total protein copy number G of a protein G is $G \approx 2G_\mathrm{D} + G_\mathrm{M}$. Assuming that $\langle G_\mathrm{D} G_\mathrm{M} \rangle \approx \langle G_\mathrm{D} \rangle \langle G_\mathrm{M} \rangle$ (our simulations indicate that this approximation is very accurate), we find that the variance σ^2_G in G is:

$$\sigma^2_\mathrm{G} \approx 4\sigma^2_{\mathrm{G_D}} + \sigma^2_{\mathrm{G_M}}, \tag{S5.5}$$

where $\sigma^2_{\mathrm{G_D}}$ is the variance in the dimer level G_D and $\sigma^2_{\mathrm{G_M}}$ is the variance in the monomer level G_M. Both monomers and dimers are subject to spatial averaging, and therefore their variances can be written in the form [122]:

$$\begin{aligned} \sigma^2_{\mathrm{G_M}} &= G_\mathrm{M} + \frac{1}{N}\left(\sigma^2_{0,\mathrm{G_M}} - G_\mathrm{M}\right) \\ \sigma^2_{\mathrm{G_D}} &= G_\mathrm{D} + \frac{1}{N}\left(\sigma^2_{0,\mathrm{G_D}} - G_\mathrm{D}\right) \end{aligned} \tag{S5.6}$$

Here N is the number of nuclei contributing to the averaging, which is proportional to D, and $\sigma^2_{0,\mathrm{G_{M/D}}}$ is the variance in the monomer and dimer levels in the absence of diffusion, respectively. The part preceded by $1/N$ represents the variance that can be reduced by spatial averaging. Plugging these expressions into the previous and using $G = 2G_\mathrm{D} + G_\mathrm{M}$ we arrive at:

$$\begin{aligned} \sigma^2_\mathrm{G} &= 4G_\mathrm{D} + G_\mathrm{M} + \frac{1}{N}\left[4\sigma^2_{0,\mathrm{G_D}} + \sigma^2_{0,\mathrm{G_M}} - 4G_\mathrm{D} - G_\mathrm{M}\right] \\ &= \left(1 + \frac{2G_\mathrm{D}}{G}\right) G + \frac{1}{N}\left[\sigma^2_{0,\mathrm{G}} - \left(1 + \frac{2G_\mathrm{D}}{G}\right) G\right] \\ &=: (1 + f_\mathrm{D})\, G + \frac{1}{N}\left[\sigma^2_{0,\mathrm{G}} - (1 + f_\mathrm{D})\, G\right] \end{aligned} \tag{S5.7}$$

Note that N is the same for both monomers and dimers because their diffusion constant does not differ in our model. Evidently, the lower bound for σ_G in the limit $N \to \infty$ is not $\sqrt{G}$ any more, but given by $\sqrt{(1 + f_\mathrm{D})\, G}$, where f_D is the fraction of proteins in the dimer state with respect to the total protein number (implying $f_\mathrm{D} \leq 1$). This is indeed what we observe in our data for σ_G. In our simulations the equilibrium is strongly shifted towards the dimerized state, so that $f_\mathrm{D} \approx 0.97$. We can understand the limit $N, D \to \infty$ intuitively by noting that in this limit there is no noise in the nuclear protein concentration due to the stochastic production and decay of molecules in each of the nuclei—this is because the synthesized molecules are immediately donated to a reservoir that is infinitely large; instead, there is only noise in the nuclear protein concentration due to the sampling of molecules from this reservoir, which obeys Poissonian statistics: $\sigma^2_{\mathrm{G_M}} = G_\mathrm{M}$ and $\sigma^2_{\mathrm{G_D}} = G_\mathrm{D}$. This yields, for $N, D \to \infty$, $\sigma^2_\mathrm{G} = 4\sigma^2_{\mathrm{G_D}} + \sigma^2_{\mathrm{G_M}} = 4G_\mathrm{D} + G_\mathrm{M} = (1 + f_\mathrm{D})G$.

5.B.2 Bifurcation analysis

In order to predict the regions in which bistability can be expected for different amplitudes A of the morphogen gradients we performed a deterministic mean-field bifurcation analysis for a simplified 1-dimensional version of our model of mutual repression between *hb* and *kni*. The analysis is based on the following two equations describing the change of the mean-field total copy number of Hb ($H(x)$) and Kni ($K(x)$) at position x:

$$\partial_t H(x) = \beta_H(x) \frac{K_R^2}{K_R^2 + [f_D K(x)]^2} - \mu_H H(x) \tag{S5.8}$$

$$\partial_t K(x) = \beta_K(x) \frac{K_R^2}{K_R^2 + [f_D H(x)]^2} - \mu_K K(x) \tag{S5.9}$$

Here β_H and β_K represent the protein synthesis rates, μ_H and μ_K the corresponding (effective) degradation rates, K_R is the dissociation constant of cooperative repressor binding to the promoter and f_D is the fraction of proteins in the dimerized state. Note that, since the intermediate step of dimerization is neglected here, we have to take $K_R = \sqrt{k_{off}^R / k_{on}^R}$ if k_{on}^R and k_{off}^R are the binding rates of the dimers. To facilitate calculations we make two further simplifying assumptions here:

1. We neglect activation dynamics and resulting promoter state fluctuations, i.e. we assume that certain constant levels of the activators at position x lead to average constant production rates $\beta_H = \beta([Bcd](x))$ and $\beta_K = \beta([\mathrm{Cad}](x))$, respectively. In our standard case $\beta([Act](x)) = [Act]^5(x)/([Act]^5(x) + 690^5)$ for both $[Act] = [Bcd]$ and $[Act] = [Cad]$.

2. In our simulations we have different degradation rates for monomers and dimers so that the effective total degradation rate depends on the monomer-to-dimer ratio, which in turn varies with the total copy number (see section 5.A.2). Thus, in principle, also f_D and μ_H and μ_K are functions of x, or the corresponding activator levels. Since this introduces further nonlinearities into the above equations and complicates their solution, we substitute the degradation rates μ_H and μ_K by a constant value μ_{eff}, which is the effective degradation rate for the maximal expression level (full activation). Also for f_D we take the constant value for full activation, $f_D \simeq 0.97$, which reflects that the dimerization equilibrium in our simulations is strongly shifted towards the dimerized state. The predictions concerning the bifurcation behavior only change marginally if μ_{eff} and f_D values for lower expression levels are used.

For each position x with local activator levels corresponding to the ones in the simulations we calculated fixed point solutions for the copy number pair $(H(x), K(x))$ starting from the steady-state assumption $\partial_t(H(x), K(x)) = (0, 0)$. The stability of the fixed points was determined starting from the Jacobian for the above ODE system:

$$J(H,K) = \begin{pmatrix} \partial_H[\partial_t H] & \partial_K[\partial_t H] \\ \partial_H[\partial_t K] & \partial_K[\partial_t K] \end{pmatrix} \tag{S5.10}$$

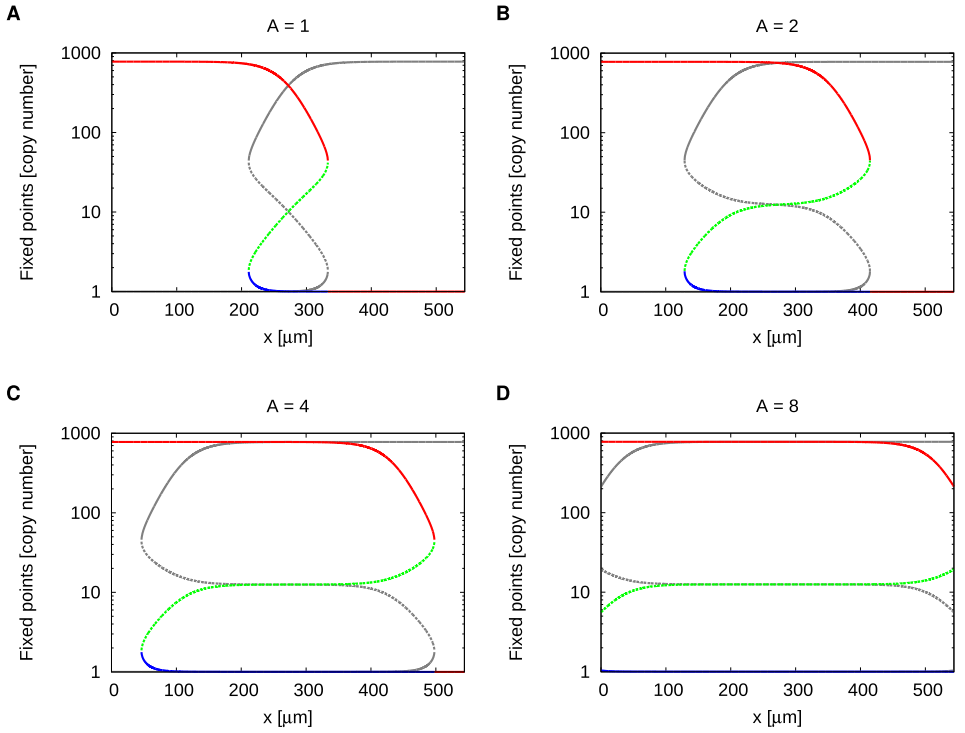

Figure S5.1: Bifurcation analysis of a one dimensional mean-field model of mutually repressing gap genes activated by morphogen gradients. Plotted are the stable (solid lines) and unstable (dashed lines) fixed points of the copy number of Hb (colored lines) and Kni (grey lines) as a function of the AP position x as predicted by a bifurcation analysis performed on a 1D mean-field model in which *hb* and *kni* are activated cooperatively by their respective morphogens and mutually repressing each other. Different colors correspond to different fixed points. The different panels show the solutions for activator amplitudes (A) A=1, (B) A=2, (C) A=4 and (D) A=8. All other parameters values are the standard values from Table S5.1. Activator concentrations at position x used in the mean-field analysis correspond to the ones in the 2D stochastic simulations. Away from midembryo each gap protein level has only one stable fixed point and one of the two levels is always zero. For all A there is a region around midembryo in which the protein levels have two stable and one unstable fixed points, implying bistability. In this region the analysis predicts bistable switching between the high-Hb–low-Kni and the low-Hb–high-Kni state. For clarity we color-code the Hb fixed points only. The Kni solutions are identical to the Hb solutions mirrored with respect to midembryo.

Within the relevant parameter regime we obtained fixed points with either two negative eigenvalues (i.e. stable fixed points) or one positive and one negative eigenvalue (i.e. saddle points). The determinant therefore completely characterizes the stability of the fixed points. If $\det J(H_0, K_0) < 0$, then (H_0, K_0) is a saddle point. Otherwise it is stable.

Fig. S5.1 shows the fixed point solutions for Hb and Kni as a function of x for different activator amplitudes A. Stable solutions are drawn with solid, unstable solutions with dashed lines. Depending on the A value, the system displays a saddle node bifurcation at a point towards the anterior (Hb) or posterior (Kni) from midembryo. Within the region confined by the bifurcation points two stable and one unstable fixed points exist for each gene, implying bistability. The region clearly widens for increasing A and spans almost the whole embryo length for $A = 8$. Our deterministic analysis therefore predicts the enlargement of the region of bistability as observed in our single nucleus simulations.

5.B.3 Estimation of switching times

To quantify the swiching times in the presence of bistability we performed simulations of isolated single nuclei featuring the same set of reactions and parameters as in the full scale simulation. To obtain estimates of switching times at different positions x along the AP axis we set the levels of Bcd and Cad in the given nucleus equal to the ones at x in the space-resolved simulations. The switching time was estimated by calculating from long time trajectories of the total Hb and Kni copy numbers the relaxation time t_s of the average correlation function

$$\langle C(t)\rangle_{t_0} \equiv \frac{\langle I_\mathrm{H}(t_0) I_\mathrm{K}(t)\rangle_{t_0}}{\langle I_\mathrm{H}(t_0)\rangle_{t_0}} \tag{S5.11}$$

where I_H (I_K) are indicator functions which are one if the difference in the total gap gene copy numbers $\Delta N = H - K$ is above (below) a certain threshold Θ_N ($-\Theta_\mathrm{N}$). Θ_N thus defines the regions within which the switch is considered to have switched to the Hb–high or Kni–high states, respectively, and serves to separate the stable attractor states from the transition region. We found that $\Theta_\mathrm{N} = 200$ is a reasonable choice for our set of parameters.

We determined the switching times from one long sample for different positions x and different activator amplitudes A and find that t_s is very similar within the double-activated bistable regions for high A. To obtain an error estimate we additionally calculated block averages of estimated switching times among 10 long samples for various A at midembryo ($x = L/2$). Table S5.2 shows our results from the latter procedure.

Note that for $A = 1$ the system is not truly bistable yet because for $A = 1$ we have half-activation at midembryo and due to the lack of diffusion large promoter-state fluctuations dominate over long-time switching potentially induced by mutual repression. Consequently, the given number does not reflect a switching time. We cite it here for completeness, however.

Activator amplitude A	Switching time $t_s[s]$
(1)	(6343.7 ± 17.2)
2	20302.5 ± 74.5
4	20957.3 ± 54.9
8	20994.7 ± 67.2

Table S5.2: Switching times at midembryo for different activator levels.

5.B.4 Analysis of statistical properties of the boundary

Our measures for both the boundary steepness and the variance of the boundary position are based on averages over both the time and the circumference of the embryo which were calculated during runtime. While the double-averaging procedure limits the amount of data that must be stored and facilitates rapid acquisition of good statistics, it also discards information about the microscopic properties of the boundary at a given time instance. Based on the average data it is impossible to determine whether the blurring of the boundary quantified by Δx is due to concerted stochastic movements of a steep and rather homogeneous instantaneous boundary or simply due to stochastic fluctuations of the boundary position in each nuclear row around a well-defined constant mean boundary position (or due to both). In the latter case the boundary will be rough at each given time instance, i.e. the time average of the boundary position variance in the cicumferential direction will be large, but the time variance of its circumferential mean will be negligible. The opposite will be the case in the other extreme. These quantities therefore can be used to distinguish the two hypothetical situations. The overall boundary width in both cases is given by the sum:

$$\Delta x^2 = \overline{\sigma^2_{\mathrm{x_t}(\phi)}} + \sigma^2_{\langle \mathrm{x_t} \rangle_\phi(\mathrm{t})} \tag{S5.12}$$

Here $\langle \dots \rangle_\phi$ denotes the average over the circumference, while the bar denotes the time average. An identical variance decomposition can be made for the fluctuations of the Hb copy number at any position x along the AP axis. Similarly, comparing the average of the profile steepness for a particular nuclear row and time instance to the steepness of the time- and circumference average of the copy number reveals whether the steepness of the average profile is due to concerted movements of similarly shallow instantaneous profiles or due to unconcerted fluctuations of steep instantaneous profiles.

In order to determine which of the portrayed blurring mechanisms is dominant in our system we performed the described variance decomposition for a set of 100 instantaneous outputs of the fully resolved 2D system in steady state, i.e. for 6400 different total Hb copy number profiles along the AP axis, for both the variances at the boundary and for the steepness at the boundary and for both the system with and without mutual repression. We focused on our standard parameter set (see Table S5.1) and a range of gap protein diffusion constants D.

At each time instance the boundary is rather rough

Fig. S5.2 shows for the systems with (Fig. S5.2A and C) and without (Fig. S5.2B and D) mutual repression the variance decomposition for the variance of the Hb copy number at the boundary (Fig. S5.2A and B) and for the variance of the boundary position x_t (Fig. S5.2C and D) as a function of the Hb protein diffusion constant D. As a control we compare the total variances calculated from the instantaneous profiles to the variances accumulated during runtime and, in case of Δx, to the value obtained from the approximation $\Delta x = \sigma_H(x_t)/|\langle H(x_t)\rangle'|$ (note that here $\langle \dots \rangle$ is the average over both time and ϕ). We see a good agreement between these quantities. The plots reveal that both for $\sigma_H(x_t)$ and Δx the variance over the circumference at a fixed time is by far the dominant contribution to the overall variance. This implies that in our system the boundary is indeed very rough at each time point and that concerted boundary movements do not occur.

At each time instance the profiles are slightly steeper than their average

The calculation of the variance decomposition is less straightforward for the slope. In particular for low D, when spatial averaging is still inefficient, the instantaneous profiles are very ragged and the boundary threshold value typically is crossed at multiple positions along the AP axis. This makes it impossible to uniquely define an instantaneous boundary position as required to calculate the instantaneous boundary slope. In order to perform the analysis at least on a subset of the data we introduced a protocol which only takes into account instantaneous profiles with a single boundary crossing, rejecting all other profiles. For low D, however, the rejection rates rise above 90%. We therefore decided to smoothen the profiles by computing running averages between a fixed number ν of nuclei along the AP axis before the analysis. The averaging lowers the rejection rate dramatically, however it also decreases the profile steepness and therefore manipulates the observable of interest. Nevertheless we can make a qualitative statement on the base of the results obtained for only slight smoothening of the profiles ($\nu = 3$). For simplicity and due to increased data abundance, in this analysis we used simple finite differences to determine the slope.

In Fig. S5.3 we plot the average of the instantaneous boundary steepness for different degrees of smoothening (averaging over $\nu = 3, 5, 7$ nuclei along the x-axis) as a function of D and compare to the steepness of the average Hb profile for the system with (S5.3A) and without (S5.3B) mutual repression. While the data for $\nu > 3$ clearly must be considered biased by the running averages, the values for $\nu = 3$ show that the instantaneous boundary slope on average is higher than the slope of the average profile, in particular for low diffusion constants.

The variance decomposition for the boundary position x_t shows that the variance of the circumference mean of the boundary position in time is very small. This implies that the steepness of the circumference-averaged profiles should be approximately equal to the steepness of the time- and circumference-averaged profile. As a control we therefore repeated the above analysis on the 100 ϕ-averaged instantaneous profiles of the same dataset. The averaging along the circumference significantly reduces the number of profiles with ambiguous boundary positions. We therefore were able to obtain reasonable estimates of the observable without pre-smoothening of the profiles

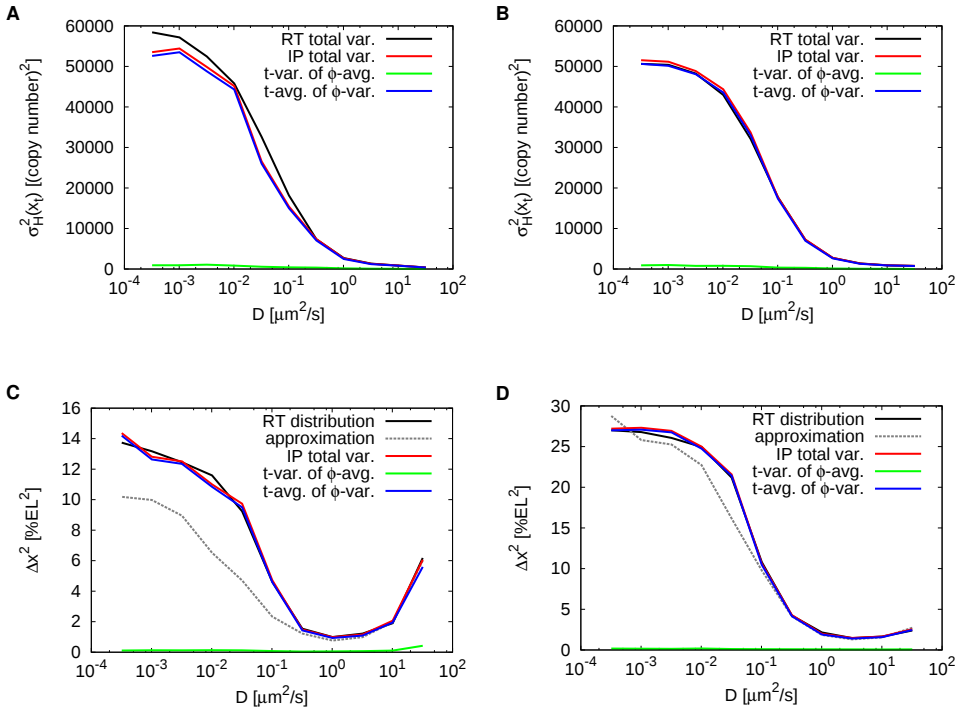

Figure S5.2: Decomposition of variances at the boundary. (A) Decomposition of the total Hb copy number variance at the average boundary position for the system with mutual repression as a function of the gap protein diffusion constant D. Plotted are: $\sigma^2_{\mathrm{H}}(x_\mathrm{t})$ the total (time- and circumference-) variance measured during runtime (RT, black), the same quantitity determined from a set of 6400 instantaneous profiles (IP, red, 64 AP rows at 100 different time points), $\sigma^2_{\langle \mathrm{H} \rangle_\phi}$ the variance in time of the circumference average of $H(x_\mathrm{t}, \phi)$ (green) and $\overline{\sigma^2_{\mathrm{H}}}$ the time average of the variance of $H(x_\mathrm{t}, \phi)$ over the circumference (blue). (B) The same as (A) for the system without mutual repression. (C) The same variance decomposition as in (A) for the Hb boundary position x_t instead of the copy number. The black line shows the Δx values measured as the standard deviation of the boundary position histogram accumulated during runtime (RT), the grey dashed line the corresponding values determined from the approximation $\sigma_{\mathrm{H}}(x_\mathrm{t})/|\langle H(x_\mathrm{t})\rangle'|$. (D) The same as in (C) for the system without mutual repression. In both cases, the main contribution to the total boundary variance $\sigma^2_{x_\mathrm{t}}$ comes from $\overline{\sigma^2_{x_\mathrm{t}}}$, implying that the blurring of the boundary is rather due to roughness than due to concerted boundary movements.

($\nu = 1$). The results are shown in Fig. S5.3C for the system with mutual repression and Fig. S5.3D for the system without mutual repression. In the system with mutual repression the average slope of the ϕ-averaged profiles for $\nu = 1$ agrees well with the slope of the both time- and ϕ-averaged Hb profile. In the system without mutual repression the ϕ-averaged profiles are slightly steeper than the average.

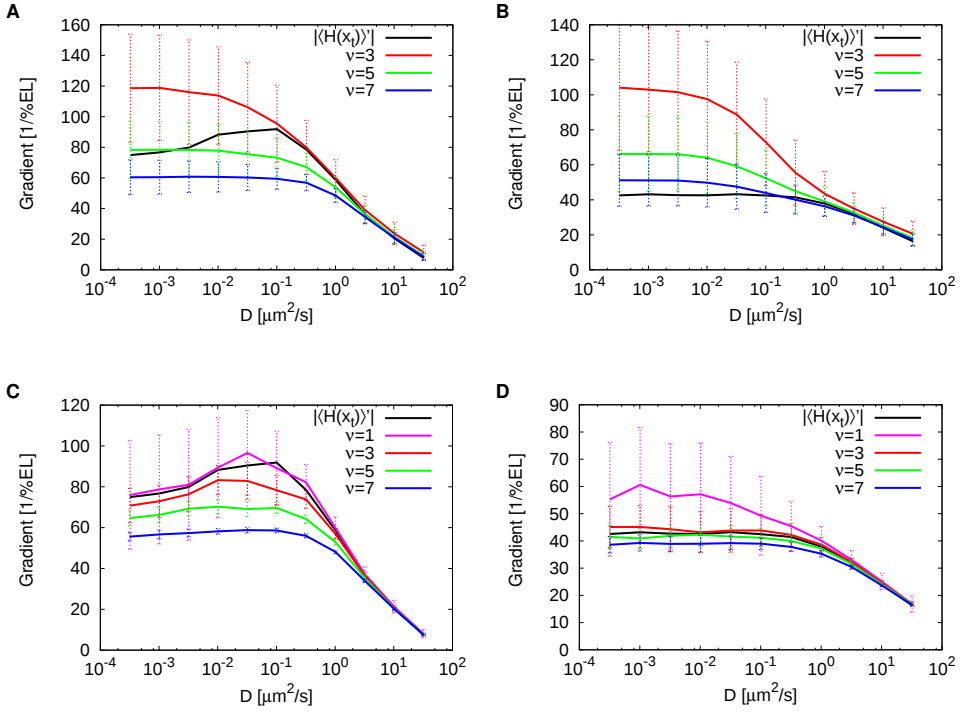

Figure S5.3: Microscopic properties of the boundary steepness. Panels (A) and (B) compare for different gap protein diffusion constants D the average Hb profile steepness at the boundary measured in a set of 6400 instantaneous profiles (64 AP rows at 100 different time points) to the steepness of the (time- and circumference-) average of the Hb profile ($|\langle H(x_t)\rangle'|$, black) for different numbers ν of neighboring data points used in calculating running averages over the instantaneous profiles for the system with (A) and without (B) mutual repression. Although for increasing ν the instantaneous profiles become less steep as a consequence of the smoothening, the values for $\nu = 3$ indicate that the profiles at a given row and time instance are slightly steeper than the average profile. In panels (C) and (D) we show results of the same analysis performed on the 100 circumference-averages of the instantaneous profiles, again for the system with (C) and without (D) mutual repression. Here $\nu = 1$ is the data obtained without calculating running averages (magenta). In both systems the steepness of the ϕ-averaged profiles agrees reasonably well with the steepness of the average profile $|\langle H(x_t)\rangle'|$.

5.C Appendix: Supplementary simulations

5.C.1 Influence of the Hill coefficient

To address the influence of changing activator cooperativity on our results we performed simulations with reduced number of activator binding sites $n_{\max}$. While in our model this is achieved by simply reducing the number of intermediate states between the empty promoter state and the producing promoter state, the binding parameters have to be rescaled with care to preserve the activation equilibrium at midembryo. Since we assume the activator binding rates to be diffusion limited, the necessary changes affect the unbinding rates $k^{\mathrm{A}}_{\mathrm{off,n}} = a/b^n$. However, even when preserving the equilibrium, the freedom in the choice of these parameters allows for altering the time scale of transitions between the different activation levels. In order to rescale the rates in a unique fashion upon lowering $n_{\max}$ we imposed the following constraints:

1. For all $n_{\max}$ the effective activator dissociation constant at midembryo $K^{\mathrm{A}}_{\mathrm{D}} = A_{1/2} = 690$ is preserved, which implies that for all $n_{\max}$ the average activation probability at midembryo is 1/2.

2. The waiting-time distribution for the unbinding from the producing state is the same for all $n_{\max}$ and, for comparison, equal to the one for the default cooperativity $n_{\max} = 5$, i.e. $\forall n : k^{\mathrm{A}}_{\mathrm{off,n_{max}}} = const = k^{\mathrm{A}}_{\mathrm{off},5}$.

3. The off-rate reduction per subsequent activator binding is always $1/b$, i.e. $\forall n : b(n) = b$.

Note that for $n_{\max} = 1$ the first two conditions can be met together only if $K^{\mathrm{A}}_{\mathrm{D}} k^{\mathrm{A}}_{\mathrm{on}} = k^{\mathrm{A}}_{\mathrm{off},5}$, which is not the case for our parameter set. We therefore restricted ourselves to $n_{\max} \in \{2, 3, 4, 5\}$. For each $n_{\max}$, the above constraints were used to uniquely determine the parameters a and b from the exact analytical solution for the average occupancy of the producing state, which was obtained from steady-state mean-field solutions of the chemical mass-action ODEs. Interestingly this results in only minor differences in a among the different $n_{\max}$ values, while the reduction per binding step $1/b_{\mathrm{n_{max}}}$ becomes significantly larger for lower $n_{\max}$. This fact has an important implication for the noise charactistics of the different promoters: If $a_{\mathrm{n_{max}}} \simeq a = const$ for all $n_{\max}$ then the unbinding rate from the state binding $(n_{\max} - 1)$ activator proteins (the "highest" non-producing activator state) is given by:

$$k^{\mathrm{A}}_{\mathrm{off},(\mathrm{n_{max}}-1)} \simeq a/b^{(n_{\max}-1)}_{\mathrm{n_{max}}} = b_{\mathrm{n_{max}}} k^{\mathrm{A}}_{\mathrm{off},5} \tag{S5.13}$$

Since $b_{\mathrm{n_{max}}}$ markedly increases with decreasing Hill coefficient the unbinding rate $k^{\mathrm{A}}_{\mathrm{off},(\mathrm{n_{max}}-1)}$ for low $n_{\max}$ will be higher than the corresponding rate for high $n_{\max}$. This will favor rapid returns to the producing state with $n_{\max}$ bound activator molecules for high Hill coefficients, whereas for low Hill coefficients the promoter is more likely to descent into the regime with less activator molecules bound. The fact that this is less likely for higher Hill coefficients is compensated by the fact that also the time to return to the producing state from the states binding low numbers

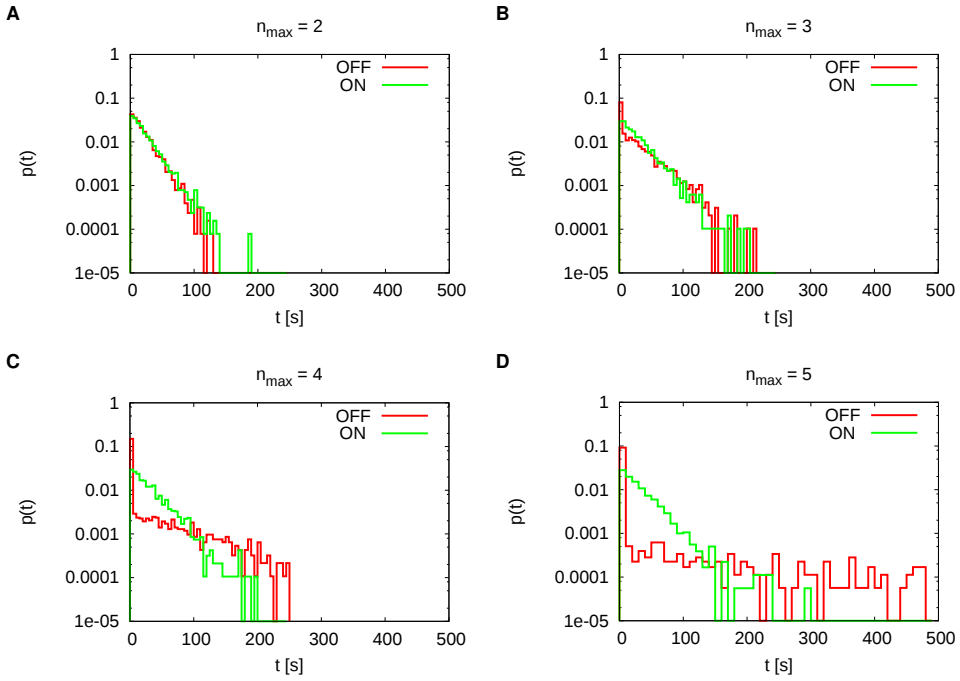

Figure S5.4: On- and off-times distributions of the *hb* promoter for different Hill coefficients $n_{\max}$ in a nucleus at midembryo. The panels show normalized histograms of the times spent in the producing ($n = n_{\max}$) promoter state ("ON", green) and of the times spent in the non-producing ($n < n_{\max}$) states ("OFF", red) for (A) $n_{\max} = 2$, (B) $n_{\max} = 3$, (C) $n_{\max} = 4$ and (D) $n_{\max} = 5$ (standard case). It can be seen that with increasing Hill coefficient $n_{\max}$ the off-times distribution changes from an exponential to a non-exponential distribution with high weight on very short off-times (implying fast returns to the producing state) and a with a long tail of long off-times. Since the off-rate from the producing state is kept the same for all $n_{\max}$ the on-times distributions remain unaltered. The on- and off-times have been determined from long time trajectories ($t_{\text{total}} = 10^5$ s) of the occupancy of the producing state with a sampling resolution of 0.5 s.

of activator molecules on average is longer for higher $n_{\max}$. Note that the mean off-time–just as the mean on-time–is the same for all $n_{\max}$. In short, for the promoters with higher Hill coefficients we expect an off-time distribution with high probability weight on short off-times and a long low-probability tail for long off-times, while the distribution for lower Hill coefficients should resemble an exponential.

In order to illustrate this effect we recorded long time-trajectories of the occupancy of the producing state in a single isolated nucleus close to midembryo for different $n_{\max}$ and without mutual repression nor diffusion. All other parameters were kept at the standard values. From these trajectories we determined the on- and off-times of the promoter and binned them into a histogram. The results are shown in Fig. S5.4. It can be seen that while for $n_{\max} = 2$ the two distributions are exponential

with approximately equal mean, the off-times distribution increasingly deviates from an exponential distribution as $n_{\max}$ is increased; more probability is shifted to very short off-times and very long off-times, causing the emergence of a long tail in the distribution.

Also for lower Hill coefficients mutual repression steepens profiles without corrupting boundary precision

The broadening of the off-times distribution is expected to result in higher output noise for high $n_{\max}$ as compared to low $n_{\max}$. This is confirmed by the simulations of the full-scale spatially resolved system for different $n_{\max}$. Fig. S5.5 shows $\sigma_{\mathrm{H}}(x_{\mathrm{t}})$, the average standard deviation of the total Hb copy number at the boundary position x_{t} (upper panels), the steepness $|\langle H(x_{\mathrm{t}})\rangle'|$ of the average Hb profile at x_{t} (middle panels) and the boundary width Δx (lower panels) as a function of the gap protein diffusion constant D for $n_{\max} \in \{2, 3, 4, 5\}$. $\sigma_{\mathrm{H}}(x_{\mathrm{t}})$ is indeed decreasing upon lowering $n_{\max}$, in particular in the regime of low diffusion constants. For higher diffusion constants the decrease is less pronounced: spatial averaging is efficient enough to lower the output noise down to the observed values irrespective of the width of the off-time distribution. The noise decreases less markedly for the systems with mutual repression. This is most likely due to the fact that lowering $n_{\max}$ also increases the probability of occasional repressor production beyond midembryo, which in turn increases the noise. The steepness plots reveal that, although the profiles naturally become less steep for lower $n_{\max}$, the steepness in the systems with mutual repression is markedly higher than the one in the system without mutual repression. In all systems the steepness as a function of D shows a very similar behavior: Upon increasing D the steepness in the systems with mutual repression first increases towards a maximum before it rapidly decreases. Since both $\sigma_{\mathrm{H}}(x_{\mathrm{t}})$ and $|\langle H(x_{\mathrm{t}})\rangle'|$ change with $n_{\max}$ in a similar fashion, in particular in the region around $D = 1\ \mu\mathrm{m}^2/\mathrm{s}$, the width Δx as a function of D also looks very similar in this region for all $n_{\max}$. In all cases the profiles in the system with mutual repression are more precise and markedly steeper as compared to the system without mutual repression at a D-value which is one order of magnitude less than the optimal value in the systems without mutual repression. Therefore the basic effect observed for $n_{\max} = 5$ also is observed in the simulations for lower Hill coefficients.

Figure S5.5: Boundary characteristics for reduced Hill coefficients $n_{\max}$. The standard deviation of the total Hb copy number at the boundary ($\sigma_{\mathrm{H}}(x_{\mathrm{t}})$, upper panels), the gradient of the average Hb total copy number gradient at the boundary ($|\langle H(x_{\mathrm{t}})\rangle'|$, middle panels) and the boundary width (Δx, lower panels) as a function of the gap protein diffusion constant D for the systems with (green) and without (red) mutual repression and Hill coefficients (A) $n_{\max} = 2$, (B) $n_{\max} = 3$, (C) $n_{\max} = 4$ and (D) $n_{\max} = 5$ (standard case). Grey dashed lines are values determined from the approximation $\Delta x = \sigma_{\mathrm{H}}(x_{\mathrm{t}})/|\langle H(x_{\mathrm{t}})\rangle'|$, solid lines are values calculated from the distributions of x_{t}. Broad dashed lines are the values for $D = 0$. Black dotted lines mark the D-value where the boundaries are both steep and precise due to mutual repression. ⟶

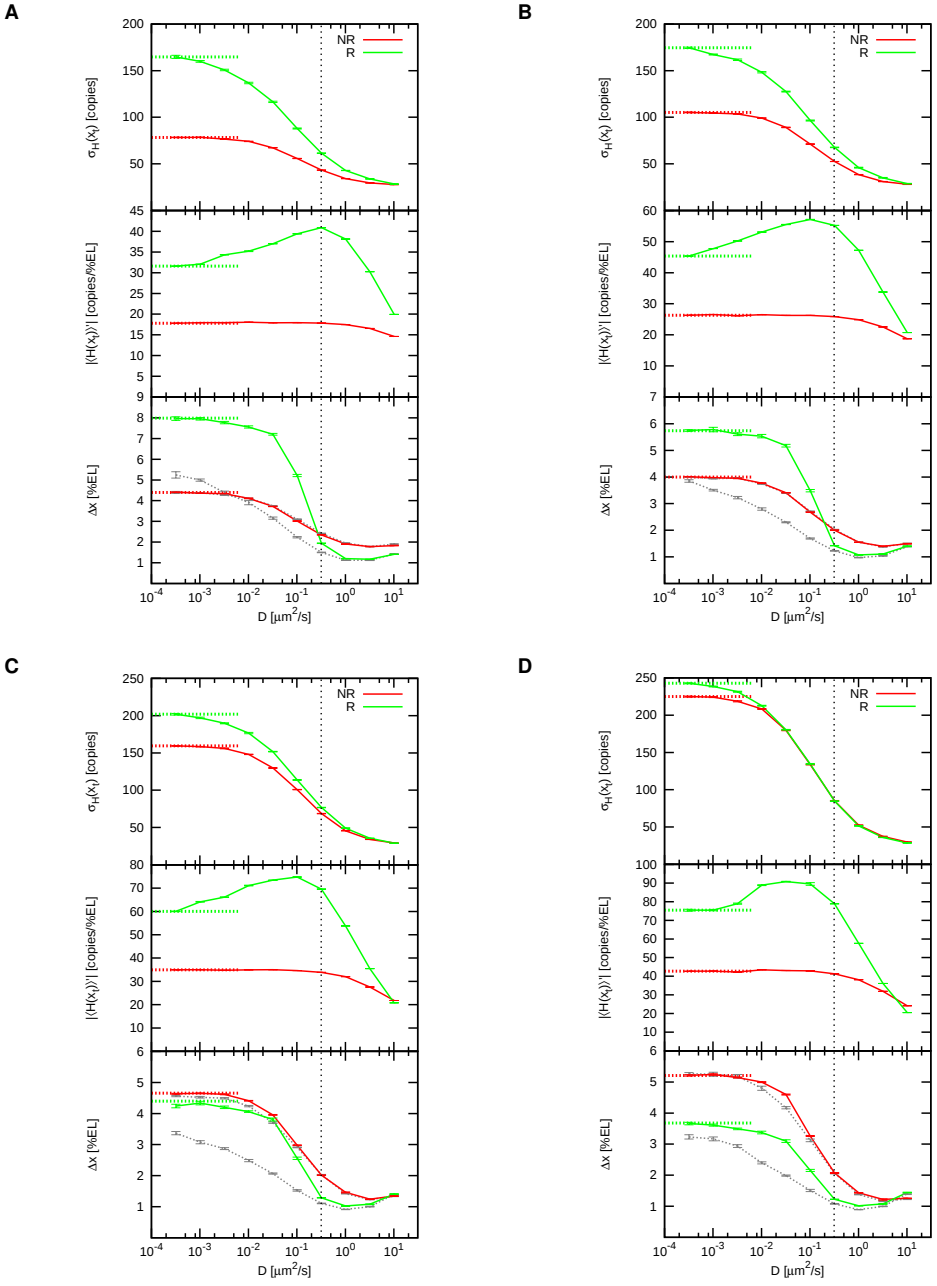
A
B
C
D
NR
R
σH(xf) [copies]
|⟨H(xf)⟩'| [copies/%EL]
Δx [%EL]
D [μm²/s]

Lower Hill coefficients allow for stronger morphogen level variations

Although lowering $n_{\max}$ in our system reduces the protein production noise it also markedly decreases the steepness of the gene activation profiles. An important implication of this is that for lower $n_{\max}$ the activation probability beyond midembryo increases. Lowering $n_{\max}$ thus is similar to increasing the activator amplitude A and, in principle, might result in the creation of a bistable region around midembryo already for lower A-values as compared to the system with $n_{\max} = 5$. We analysed how the results for Δx as a function of A for the case of correlated variations change as $n_{\max}$ is decreased. Fig. S5.6 shows $\Delta x(A)$ for $n_{\max} \in \{2, 3, 4, 5\}$ and $D = 1.0\ \mu\text{m}^2/\text{s}$ for systems with and without mutual repression. Overall, $\Delta x(A)$ is very similar for all considered $n_{\max}$. For $A \leq 2$ the width Δx in the systems with mutual repression is always lower than in the systems without mutual repression. The minimal Δx is attained at $A = 1$ in all cases. The main difference is in how Δx changes with A for $A > 1$: The lower $n_{\max}$, the slower the width increases with A. Thus, while lower Hill coefficients decrease the steepness of the profiles significantly, they may prove beneficial by extending the range over which extrinsic variations are successfully buffered without increasing intrinsic fluctuations of the boundary.

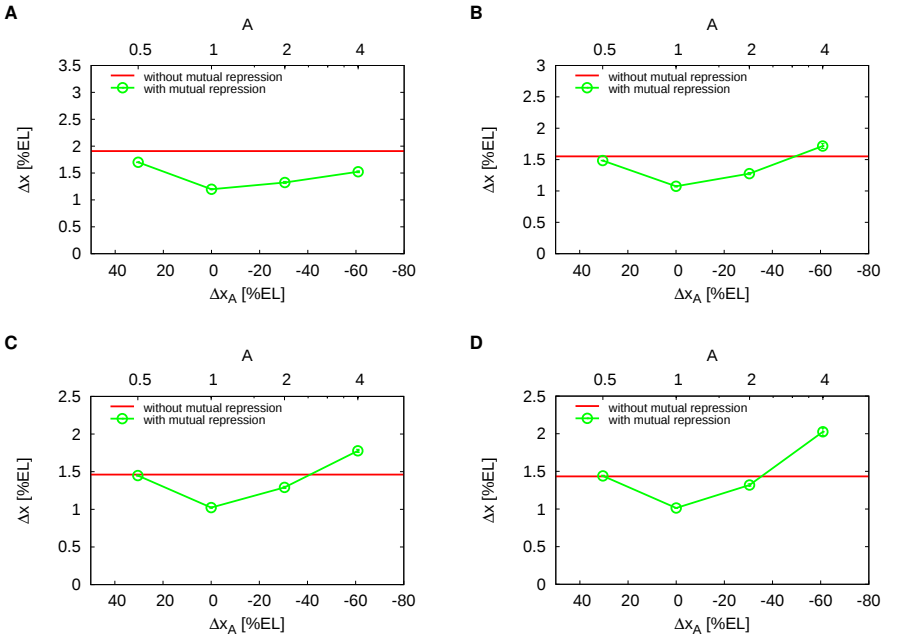

Figure S5.6: The effect of changing the activator amplitude A on the boundary precision for reduced Hill coefficients $n_{\max}$. Shown are the the boundary width Δx with (green) and without (red) mutual repression as a function of Δx_{A}, the separation between the Hb and Kni boundaries expected in the system without mutual repression, and the corresponding activator amplitude A for Hill coefficients (A) $n_{\max} = 2$, (B) $n_{\max} = 3$, (C) $n_{\max} = 4$ and (D) $n_{\max} = 5$ (standard case). In all cases $D = 1.0\ \mu\text{m}^2/\text{s}$.

5.C.2 Influence of the expression level

In order to examine the influence of a changed signal-to-noise ratio on our results we performed simulations with altered production dynamics. We did this by (1) by changing the production rate β (keeping the standard production burst size of one) and (2) introducing bursty production, i.e. producing 10 copies of the gap protein monomer at a time with a 10 times lower production rate ($\beta = \beta_0/10$). To preserve the binding equilibrium of the repression reaction at midembryo upon changing β we also changed the off-rate of the repressor dimers by a factor f_β^{D}, which is the ratio between the expected number of dimers at midembryo for the altered production rate β and the corresponding value for the standard production rate β_0. Note that, since in our system the copy numbers of both monomers and dimers depend on β in a nontrivial fashion (see section 5.A.2) the effective copy number increase typically does not correspond to the ratio β/β_0. Therefore $f_\beta^{\mathrm{D}} > \beta/\beta_0$ for $\beta > \beta_0$.

Increased production rates reveal different noise scaling behavior for different regimes of the diffusion constant

Upon increasing the production rate and consequently the total copy number of the gap proteins we may expect a relative decrease in the output noise, but only if the latter is purely Poissonian. In our system this corresponds to the limit of high gap protein diffusion constants. In that limit, we expect $\sigma_{\mathrm{G}} \propto \sqrt{G}$, where σ_{G} is the noise in the total gap gene copy number G. However, in the abscence of spatial averaging, i.e. for the limit $D \to 0$, non-Poissonian noise prevails and the expected scaling is $\sigma_{\mathrm{G}} \propto G$ [122]. If the copy number profile is scaled uniformly at each AP position x, which–to a good approximation–is the case in our system, we expect for the scaling of the gradient at midembryo $G'(x_{\mathrm{t}}) \propto G(x_{\mathrm{t}})$. The expected scaling for the boundary width Δx then is $\Delta x \propto 1$ for low diffusion constants and $\Delta x \propto 1/\sqrt{G}$ for high D. While the overall characteristics of the boundary are very similar to the system with $\beta = \beta_0$, a comparison roughly confirms the predicted scaling. Fig. S5.7 compares for Hb the standard deviation of the total copy number at the boundary (S5.7A), the steepness at the boundary (S5.7B) and the resulting boundary width (S5.7C) as a function of D for increased production rates $\beta = 2\beta_0$ and $\beta = 4\beta_0$ to the corresponding values for the sytem with production rate $\beta/2$. Thus, the values for $\beta = 4\beta_0$ are compared to $\beta = 2\beta_0$ and the values for $\beta = 2\beta_0$ are compared to β_0. Blue lines mark the expected change of the quantities as predicted by the scaling relations, where the corresponding copy number increase is given by the factor $f_2 \equiv f_{2\beta_0} = 2.22$ and $f_4 \equiv f_{4\beta_0}/f_{2\beta_0} = 2.16$. Here $f_\beta \simeq f_\beta^{\mathrm{D}}$ is the predicted *total* copy number at midembryo divided by the corresponding value for $\beta = \beta_0$.

The plots show that while the slope ratio is roughly equal to f_2 (f_4) for all D both in the system with (green) and without (red) mutual repression, the noise ratio depends on the diffusion constant and also slightly differs for the systems with and without mutual repression. Nevertheless the predicted scaling behavior is confirmed in both cases: in the low diffusion constant regime the noise ratio is roughly f_2 (f_4) and approaches $\sqrt{f_2}$ ($\sqrt{f_4}$) as D increases; together this leads to a boundary width ratio of one for low D which decreases towards $1/\sqrt{f_2}$ ($1/\sqrt{f_4}$) for higher D.

Bursty production has only a marginal influence on the boundary properties

In Fig. S5.8 we plot the standard deviation of the total Hb copy number at the boundary, the steepness of the total Hb copy number profile at the boundary and the boundary width Δx as a function of D for the system with bursty production (burst size 10). There is no significant difference as compared to the system with normal production (burst size 1, compare to Fig. S5.5(D) or Fig. 5.4 in the main text). For low D the production noise is marginally higher with bursty production, resulting in a slight increase of Δx in this regime; the effect of varying D, however, is much more important. This is most likely a consequence of the fact that for the given Hill coefficient $n_{\max} = 5$ promoter state fluctuations are already at a high level due to a very broad off-time distribution (see section 5.C.1).

Figure S5.7: The effect of increased copy number on the Hb boundary precision. Shown are the value ratios of important boundary properties for production rates $\beta > \beta_0$ as compared to $\beta/2$ for (A) the total Hb copy number noise $\sigma_{\mathrm{H}}(x_{\mathrm{t}})$ at the boundary, (B) the steepness of the average Hb profile at x_{t}, and (C) the resulting width Δx with (green) and without (red) mutual repression. Solid lines are for $\beta = 2\beta_0$, dashed lines for $\beta = 4\beta_0$. Blue lines depict the ratios as predicted from the expected scaling behavior for the limits of $D \to 0$ (upper line pairs) and $D \longrightarrow \infty$ (lower line pairs). The steepness is expected to scale precisely with the increased copy number in both limits. Note that the expected factor of copy number increase upon doubling β is not precisely two because of the nontrivial dependence of the monomer-dimer equilibrium on the production rate. $\longrightarrow$

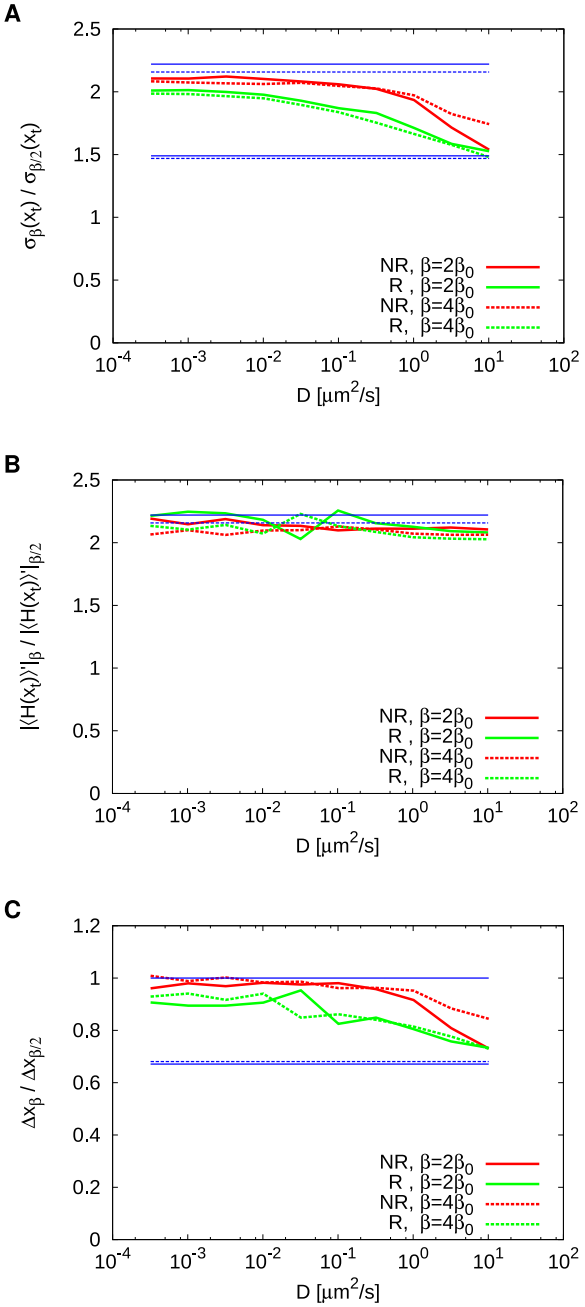
A
B
C
NR, β=2β0
R , β=2β0
NR, β=4β0
R, β=4β0
D [μm2/s]
σβ(xt) / σβ/2(xt)
⟨H(xt)⟩'|β / ⟨H(xt)⟩'|β/2
Δxβ / Δxβ/2

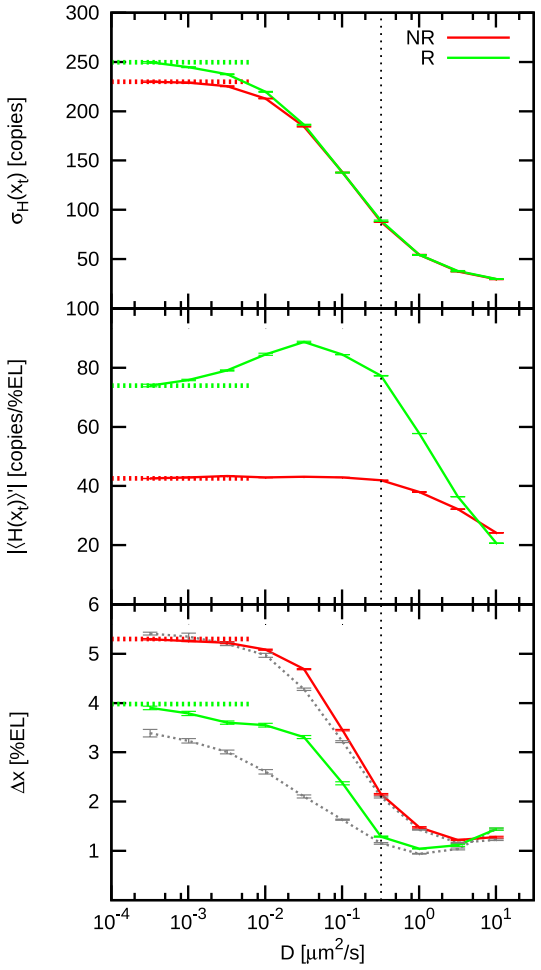

Figure S5.8: The effect of bursty gap protein production on the Hb boundary precision. The plot shows $\sigma_{\mathrm{H}}(x_{\mathrm{t}})$ the standard deviation of the total Hb copy number at the boundary, the steepness $|\langle H(x_{\mathrm{t}})\rangle'|$ of the average total Hb copy number profile at the boundary and the boundary width Δx with (green) and without (red) mutual repression as a function of the gap protein diffusion constant D for a system in which the gap proteins are produced in bursts of 10 at a time with decreased production rate $\beta = \beta_0/10$. The grey dashed lines are the values obtained from the approximation $\Delta x = \sigma_{\mathrm{H}}(x_{\mathrm{t}})/|\langle H(x_{\mathrm{t}})\rangle'|$. Thick dashed lines are values for $D = 0$. Error bars were obtained from block averages over 10 independent samples. The black dotted line marks the D-value where the boundary is both steep and precise due to mutual repression.

5.C.3 Activation of both gap genes by a single gradient

In the one-morphogen gradient scenario, both *hb* and *kni* are activated by the Bcd gradient. Here, *kni* is activated in the same way as *hb*, namely by 5-step cooperative binding, but with a lower activation threshold. This results in the induction of both genes in the anterior half of the embryo up to the posterior Hb boundary and of *kni* in an additional region posterior to the Hb boundary. Given that *hb* represses *kni* more strongly than vice versa in the double-activated bistable region, this parameter choice will result in the formation of two neighboring domains. We chose the *kni* activation threshold to be lower by a factor of 1/2, which causes an offset of its half-activation point by approximately 10 nuclei (83 μm) towards the posterior. We varied the protein diffusion coefficient D and $k_{\text{off}}^{\text{R,K}}$, the off-rate of the Kni repressor dimers from the *hb* promoter. The rate for dissociation of the Hb dimers from the *kni* promoter was kept at the standard value $k_{\text{off}}^{\text{R,H}} = 5.27 \cdot 10^{-3}$/s in all simulations.

The diffusion constant D of the gap proteins and the dissociation rate $k_{\text{off}}^{\text{R,K}}$ of Kni from the *hb* promoter are indeed key parameters. On the one hand, *hb* must repress *kni* more strongly than the other way around, because otherwise there will be only one *kni* domain. On the other hand, when $k_{\text{off}}^{\text{R,K}}$ is high, then *kni* is only significantly expressed when D is low, because *kni* represses *hb* more weakly than vice versa, which means that low amounts of invading Hb dimers are sufficient to shut off Kni production almost completely; indeed, in this regime, *kni* has hardly any effect on the precision of the *hb* expression domain. We found that when $k_{\text{off}}^{\text{R,H}}/k_{\text{off}}^{\text{R,K}}$ is roughly between 0.1 and 1, both *hb* and *kni* domains are formed robustly. In Fig. S5.9 we display the case for $k_{\text{off}}^{\text{R,H}}/k_{\text{off}}^{\text{R,K}} = 1/\sqrt{10} \approx 1/3$.

Fig. S5.9A shows that the maximum of the average Kni copy number is lower than that of Hb, even though for $x < 60$ %EL *kni* is essentially fully activated by Bcd (Fig. S5.9B). The lower maximum is due to the fact that *hb* represses *kni* more strongly than vice versa. Another point worthy of note is that the fluctuations in the Kni copy number in the Kni domain are higher than those of Hb in the Hb domain (Fig. S5.9C). This is essentially due to the small width of the Kni domain: *kni* is either fully activated by Bcd yet still repressed by Hb or not repressed by Hb yet stochastically activated by Bcd.

Panels D-F show, respectively, the noise in the Hb copy number at the *hb* expression boundary, the steepness of this boundary, and the width of this boundary, as a function of the diffusion constant D of the gap proteins. It is seen that the results are highly similar to those of the two-gradient motif. The noise in the Hb copy number at the boundary is not much affected by mutual repression (panel D), while the steepness, and consequently boundary precision, is markedly enhanced by mutual repression, especially when the diffusion constant is small. Note that while for the two-morphogen gradient scenario the approximation $\Delta x \approx \sigma_{\text{H}}(x_{\text{t}})/|\langle H(x_{\text{t}})\rangle'|$ is in very reasonable agreement with Δx as measured from the distribution of threshold crossings $p(x)$, here the agreement is much less. This is due to sporadic repression events in the anterior region where *hb* and *kni* are both fully activated, which leads to a long tail of $p(x)$ extending towards the anterior pole; while $p(x)$ in the tail is small, the fact that the tail is long does markedly increase the standard deviation Δx. Given that the approximation $\Delta x \approx \sigma_{\text{H}}(x_{\text{t}})/|\langle H(x_{\text{t}})\rangle'|$ works so well for all the other

cases, we consider this approximation, which does not suffer from sporadic but strong *hb* repression events in the anterior, to be more reliable. We therefore conclude that also in the one-morphogen gradient scenario, mutual repression can enhance both the steepness and the precision of gene-expression boundaries.

Figure S5.9: The effect of mutual repression in a system where both *hb* and *kni* are activated by the Bcd gradient. (A) Time- and circumference-averaged Hb ($\langle H \rangle$, solid lines) and Kni ($\langle K \rangle$, dashed lines) total copy-number profiles along the AP-axis for various Hb and Kni diffusion constants D. (B) AP profiles of the average standard deviation of the total gap gene copy number for Hb (σ_{H}, solid lines) and Kni (σ_{K}, dashed lines). Note that the noise in K in the Kni domain is larger than that in H in the Hb domain. (C) AP profiles of the probabilities $\langle H_5^0 \rangle + \langle H_5^1 \rangle$ and $\langle K_5^0 \rangle + \langle K_5^1 \rangle$ that the *hb* (solid lines) and *kni* (dashed lines) promoters have 5 Bcd molecules bound to them, respectively; in the absence of mutual repression between *hb* and *kni*, these profiles would directly determine the expression of *hb* and *kni*. (D) The noise in the Hb copy number at the *hb* expression boundary as a function of the Hb and Kni diffusion constant D. (E) The steepness of the *hb* expression boundary as a function of the diffusion constant of the gap proteins. (F) The width Δx of the *hb* expression boundary as a function of the Hb and Kni diffusion constant. The grey line corresponds to the approximation $\Delta x \approx \sigma_{\mathrm{H}}(x_{\mathrm{t}})/|\langle H(x_{\mathrm{t}}) \rangle'|$, which we consider to be more reliable than Δx as measured from the distribution of threshold crossings, $p(x)$; the latter suffers from sporadic but strong suppression events of *hb* by *kni* in the anterior, which leads to a long tail of $p(x)$, increasing Δx. It is seen that while mutual repression has hardly any effect on the noise in the copy number at the boundary, it does markedly enhance the steepness of the boundary, and thereby its precision. The ratio of the Hb–*kni*-promoter dissociation rate over the Kni–*hb*-promoter dissociation rate is $k_{\mathrm{off}}^{\mathrm{R,H}}/k_{\mathrm{off}}^{\mathrm{R,K}} = 1/3$. ⟶

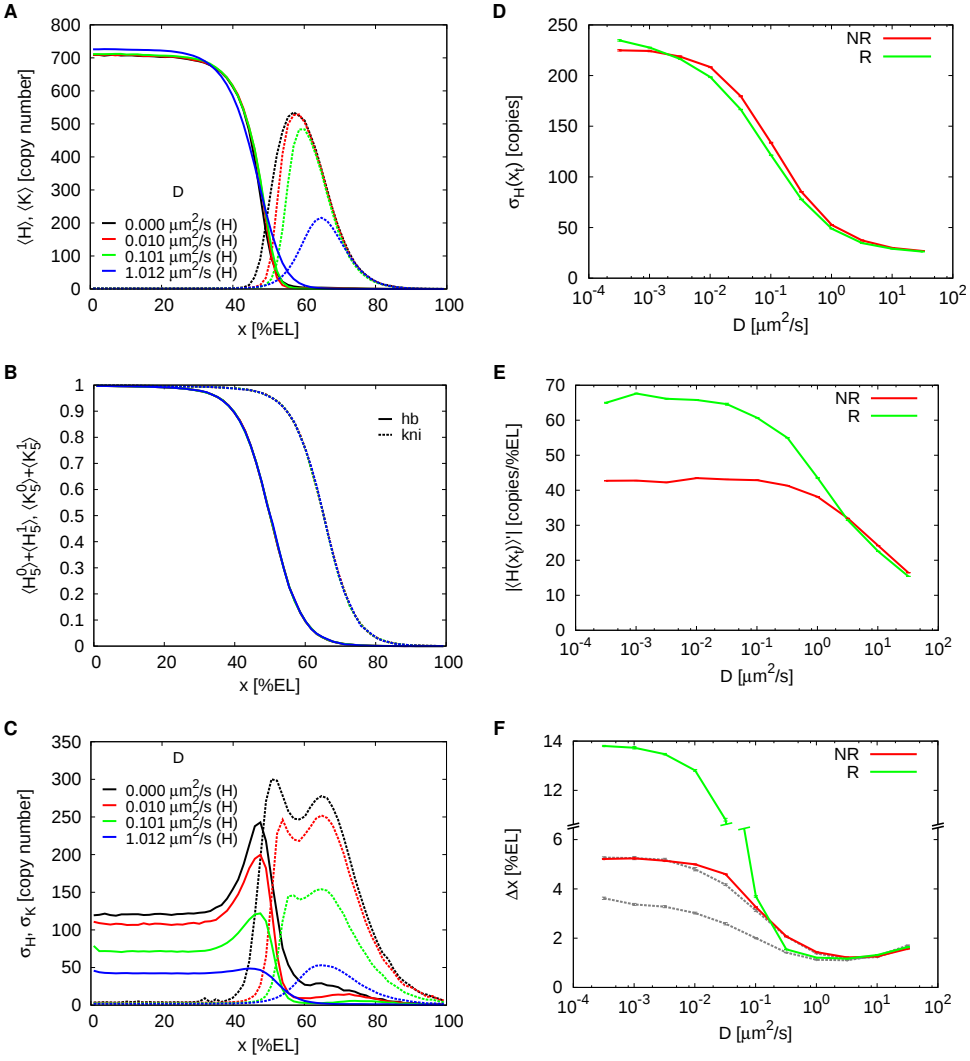
A
⟨H⟩, ⟨K⟩ [copy number]
x [%EL]
D
0.000 μm²/s (H)
0.010 μm²/s (H)
0.101 μm²/s (H)
1.012 μm²/s (H)
B
⟨H₅⁰⟩+⟨H₅¹⟩, ⟨K₅⁰⟩+⟨K₅¹⟩
x [%EL]
hb
kni
C
σH, σK [copy number]
x [%EL]
D
0.000 μm²/s (H)
0.010 μm²/s (H)
0.101 μm²/s (H)
1.012 μm²/s (H)
D
σH(xl) [copies]
D [μm²/s]
NR
R
E
|⟨H(xl)⟩'| [copies/%EL]
D [μm²/s]
NR
R
F
Δx [%EL]
D [μm²/s]
NR
R

Chapter 6

Robust gap gene patterns without morphogen gradients

6.1 Introduction

In embryogenesis, the stability of gene expression patterns is critical for correct development. In many developing organisms, stable patterns are established and maintained under the control of a single master regulator, whose spatial concentration profile results from production at a localized source, diffusion and degradation [171, 172, 173, 174]. However, reaction-diffusion systems of several interacting species offer an alternative strategy for robust developmental patterning [19, 175].

The embryo of the fruit fly *Drosophila melanogaster* is a paradigm of spatial patterning in embryogenesis. In its anterior half, the gradient of the morphogen Bicoid (Bcd) provides positional information [176, 109, 110, 177, 178, 179], and activates downstream gap genes which form stripes along the embryo cortex [166, 30, 180, 12]. The stability and precision of morphogen-controlled gap gene patterns has been extensively studied both in experiments [181, 147, 116, 114, 51, 113, 52] and theoretically [182, 183, 170, 184, 185, 151, 122, 123, 115, 186, 20, 137] in recent years. There is, however, increasing evidence suggesting that Bcd is not the main regulator of downstream targets in the posterior half of the embryo. For instance, gap gene stripes form in mutants with perturbed or knocked out *bcd* [146, 187, 188, 158, 177], and the same holds for embryos with knocked-out maternal genes that form posterior gradients [157]. In other species which lack *bcd*, well-ordered gap gene patterns similar to the ones seen in Drosophila emerge [189, 190, 191, 192, 193]. Moreover, in Drosophila the Bcd gradient is seen to disappear towards the end of developmental cycle 14, while fully-developed gap gene patterns remain intact [147].

An intriguing observation is that gap genes interact via mutual repression [112, 194, 124, 195, 196, 197, 158, 152, 111], with a peculiar feature of weak nearest-neighbor (NN) and strong next-nearest neighbor (NNN) repression [116, 115, 114, 113, 112, 12]. It has been suggested that alternating repression leads to stripe patterns which scale with embryo size [117]. Here we address the general question whether gap gene

patterns subject to gene expression noise can be maintained with high stability and precision in a self-organized way, purely by mutual repression of gap genes, i.e. in the absence of a master regulator.

Within this context, stability of an expression pattern can have two different meanings: In the WADDINGTON picture [155, 156, 198], development is seen as a succession of metastable states of gene expression. Taking this idea seriously, gene expression patterns in the developing Drosophila embryo would be true metastable states of the underlying dynamics, that is, basins of attraction in an "energy" landscape [115, 116, 199, 200, 201, 202, 203, 130, 204]. In such a scenario the breakdown of an established pattern is an activated process driven by intrinsic fluctuations in the system, and metastable states are separated by barriers that impose restoring forces on escaping trajectories. Alternatively, gene expression patterns may be stable over the required period of developmental time purely due to slow dynamics, without the need of restoring forces towards a metastable patterned state. An eventual breakdown of the pattern is not detrimental since by that time, downstream patterning mechanisms have taken control.

To address these questions we constructed a stochastic model for the pattern of the gap genes Hunchback (*hb*), Krüppel (*kr*), Knirps (*kni*) and Giant (*gt*) in the posterior half of the early Drosophila embryo. These genes repress each other mutually according to the experimentally observed pattern of alternating repression strength. We compared a setup in which Hb expression is pinned (i.e. not repressed) at the system boundaries to a system without Hb pinning. Pinning is motivated by the fact that the *hb* expression level at mid-embryo is strongly dictated by its activator Bcd [176, 52, 30], while in the posterior a second enhancer puts *hb* under activating control of the tightly localized protein Tailless (Tll) [205]. In this picture Bcd acts by setting boundary conditions for the pattern, rather than directly controlling expression of each gene, as would be the case in a purely threshold-based patterning mechanism. We conducted stochastic simulations of the pattern dynamics starting from a well-established stripe order, representing the posterior gap gene pattern in developmental cycle 14, and measured the time until pattern breakdown. Initial results demonstrated that for a well-tuned ratio of NN vs. NNN repression strength the gap gene patterns indeed remain stable for very long times. This stability prevented us from sampling destruction events by direct simulations and called for an enhanced sampling technique. Most well-established rare-event techniques such as transition-path sampling [206, 207], transition-interface sampling [208, 209, 210, 211, 212], metadynamics [213] and their descendants are limited to equilibrium systems. Several recent schemes including Forward Flux Sampling [214], non-equilibrium umbrella sampling [215] and the weighted-ensemble method [216, 217] address non-equilibrium systems. These methods rely on the existence of a kinetic barrier, which separates the initial and final state, making escape events effectively uncorrelated. Here, however, the existence of a barrier is part of the question; even the most stable patterns could gain their stability from slow, but transient dynamics. Some of us have recently developed Non-Stationary Forward Flux Sampling (NS-FFS) [218, 219] which enables efficient rare-event sampling in systems with transient dynamics. We used this technique to quantify gap gene pattern stability as a function of the mutual repression strength. The generated path ensemble allowed us to analyse the pathways to pattern destruc-

tion, which is essential to understand the origins of pattern stability.

We find that there is an optimal regime of intermediate NN repression strength, in which pattern persistence times are maximized and reach values that are more than sufficient to ensure stability over the biologically required time ($\simeq$ 2 h), in the absence of morphogen gradients. This stability arises from a combination of two effects: first, progress towards pattern destruction is intrinsically slow whenever NN repression is weak enough to allow for (partly) overlapping gap protein domains, but strong enough to suppress bistable switching at the interface between NNN expression domains. Second, in the pinned system in addition a restoring force towards the metastable stripe pattern strongly enhances stability.

6.2 Results

6.2.1 Pattern stability is maximized at intermediate nearest-neighbor repression strength

In order to assess whether and how gap gene patterns can be stable without an external morphogen gradient, we performed stochastic simulations of a spatial pattern of four gap genes that control each other via mutual repression, using NS-FFS. While Drosophila development is astonishingly precise and reproducible [52, 51, 30], the processes that drive it, in particular gene expression, are very stochastic. This prompted the search for mechanisms that attenuate gene expression noise in development, such as spatial averaging [122] and mutual regulatory interactions [170, 116]. Addressing this question requires a spatially resolved stochastic model. Here we opted for a minimal model of the posterior gap gene pattern in developmental cycle 14, shown in schematic Fig. 6.1. Nuclei at the outer surface of the embryo are represented as a cylindrical array of $N_z \times N_\phi$ well-stirred reaction volumes. Gap protein diffusion and nuclear exchange are modeled via hopping between neighboring compartments. To account for the radial symmetry of the embryo we impose periodic boundary conditions in the circumferential lattice direction, which enables diffusive hopping from lattice site (z, N_ϕ) to lattice site $(z, 1)$, and vice versa (here z and ϕ denote lattice indices in the axial and circumferential direction, respectively). In each nucleus, proteins of the gap genes *hb*, *kr*, *kni* and *gt* are produced from their corresponding promoters, dimerize and mutually repress each other by promoter binding. Each gene can repress the promoter of each other gene; however, the repression strength differs among different gene pairs, as discussed further below. Repression is non-competitive, i.e. each promoter has binding sites for each of the three other genes' dimers and is inactivated when at least one dimer is bound ("OR"-logics). Our model combines transcription and translation into one production step, and thus neglects some features of eukaryotic gene expression such as transcriptional bursts and enhancer dynamics; previous work has shown that this does not alter the results qualitatively [122, 170].

We fix ("pin") the expression level of Hb in the nuclei at the system boundaries by locally disallowing repression. This accounts for the fact that in the native pattern anterior Hb is in excess and under stringent control by Bcd [176], whereas in the posterior *hb* expression is driven by a second enhancer under the control of Tll [205], which in turn is directly controlled by the maternal terminal system and thus tightly

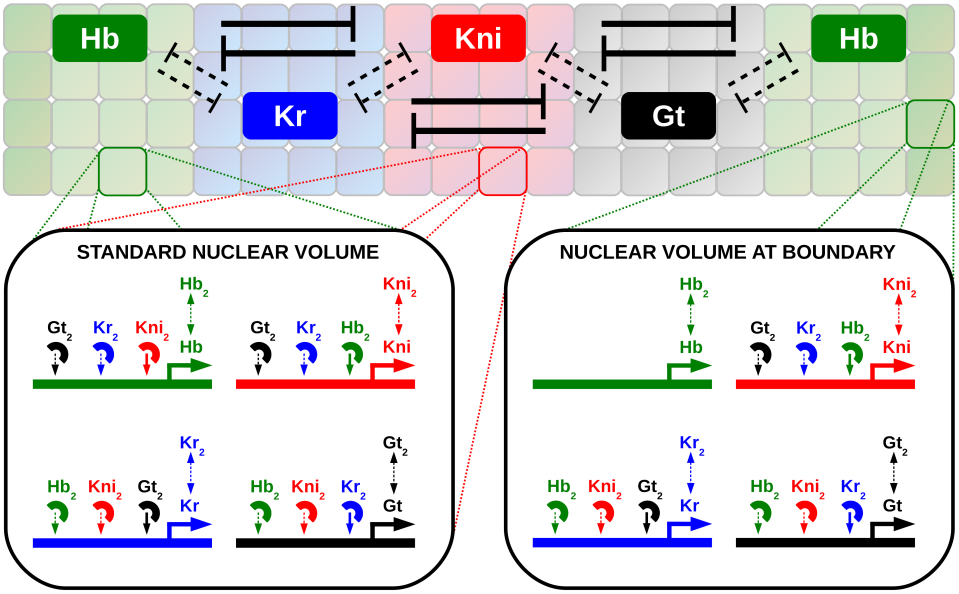

Figure 6.1: Schematic of our Drosophila embryo model. The posterior of the embryo in cycle 14 is modeled via a cylindrical lattice of reaction volumes that represent cortical nuclei. In each nuclear volume we simulate production, degradation, dimerization and mutual repression of the four gap genes Hb, Kr, Kni and Gt via the Gillsepie algorithm. Each gene is subject to repression by the protein dimers of the other genes, as indicated by the schematic promoters. Neighboring nuclei can exchange monomers and dimers via diffusive hopping. The system is initialized in a five-stripe pattern of expression domains in the experimentally observed order Hb–Kr–Kni–Gt–Hb. The strength of mutual repression varies among gap gene pairs: genes that have adjacent expression domains repress each other weakly, while next-nearest neighbors exhibit strong mutual repression. By default, the concentration of Hb is "pinned" at the system boundary where the set of modelled reactions differs from the rest of the system by the fact that the *hb* promoter can not be repressed. Note that this deliberately simplifying drawing does not depict the cylindrical model geometry in all details; these are fully described in the "Methods" section 6.4.

localized [220, 221]. To assess how this model assumption influences our results, we later compare to simulations in which *hb* is not not pinned. Further model details are given in the "Methods" section 6.4.

Initially, concentrations of the four gap gene proteins are arranged in five adjacent rectangular domains of equal size in the (anterior-posterior) order Hb-Kr-Kni-Gt-Hb, corresponding to the experimentally observed pattern in the posterior half of the embryo [116, 114, 113, 112, 12]. Within this arrangement the genes repress each other mutually via the characteristic pattern of strong next-nearest neighbor (NNN) and weaker nearest-neighbor (NN) repression [113, 112, 124, 195, 197, 158, 111]. More specifically, there are two pairs of strongly repressing genes, (*hb*,*kni*) and (*kr*,*gt*), and four pairs of genes that repress each other weakly ((*hb*,*kr*), (*kr*,*kni*), (*kni*,*gt*) and (*gt*,*hb*)). In our model the difference in repression strength is tuned via the unbinding

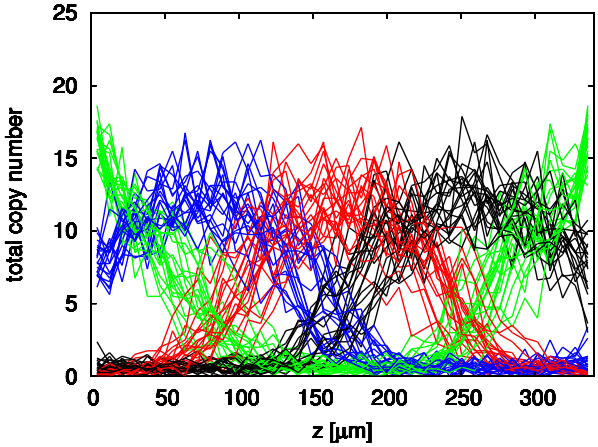

Figure 6.2: Typical simulation output. Here we show typical snapshots of the total copy numbers of all considered gap proteins as a function of the axial coordinate z of the cylinder, averaged over its circumference. Colors correspond to Fig. 6.1 (green = Hb, blue = Kr, red = Kni, black = Gt). Snapshots were taken every 60 min over a total simulated time of 20 h after an initial relaxation phase of 30 min, starting from rectangular domain profiles of equal length.

rate of the repressors from the repressed promoter. The strong repressor off-rate $k_{\text{off}}^{\text{NNN}}$ is chosen such that NNN pairs ((hb,kni) and (kr,gt)) are in a bistable regime, while the weak repressor off-rate $k_{\text{off}}^{\text{NN}}$ is varied; here bistability means that at the single-nucleus level only one of the two competing genes is significantly expressed. We then study gap gene stability as a function of the repression strength ratio κ, defined as

$$\kappa \equiv k_{\text{off}}^{\text{NN}} / k_{\text{off}}^{\text{NNN}} \ . \tag{6.1}$$

For $\kappa = 1$ also adjacent gene pairs are in the bistable regime, while in the limit $\kappa \to \infty$ NN pairs do not affect each other at all.

Figure 6.2 shows typical simulated gap protein profiles of an intact, relaxed pattern. To quantify pattern stability we measure the average time until at least one gap protein domain disappears as a function of κ. Note that in our system the shrinkage of the domain of gap protein G is always accompanied by the enlargement of the domain of G's strong interaction partner. This lead us to introduce the following two order parameters that measure the asymmetry for each of the two strongly antagonistic NNN pairs and track progress towards pattern destruction:

$$\lambda_{\text{x}} \equiv \max([\text{Hb}]_\Sigma, [\text{Kni}]_\Sigma)/N_\Sigma \tag{6.2}$$

$$\lambda_{\text{y}} \equiv \max([\text{Kr}]_\Sigma, [\text{Gt}]_\Sigma)/N_\Sigma \tag{6.3}$$

Here $[\text{G}]_\Sigma$ is the total copy number of G proteins (counting dimers twice). For convenience we normalize by $N_\Sigma = [\text{Hb}]_\Sigma + [\text{Kr}]_\Sigma + [\text{Kni}]_\Sigma + [\text{Gt}]_\Sigma$, the total protein number in the system.

In the well-ordered pattern each gap protein domain occupies roughly the same fraction of the system, so that $\lambda_{\text{x}} \approx \lambda_{\text{y}} \approx 0.25$. As expansion of a domain progresses

at the expense of its strong antagonist, $\lambda_{x(y)}$ is enlarged and reaches values around 0.5 when the shrinking domain ultimately is destroyed. The sum $\lambda = \lambda_x + \lambda_y$ thus is a natural choice for a progress coordinate towards pattern destruction, with values around 0.5 for intact patterns and values above 0.75 indicating their breakdown. In short, λ measures increasing asymmetry between strong repression partners as the system advances towards collapse.

Initial simulations revealed that the waiting times until destruction are long compared to the duration of the actual breakdown event, and are difficult to sample by direct simulation. A key question of this work is whether the intact gap protein pattern is protected by a barrier that separates it from the destroyed state. We thus cannot assume a priori that pattern destruction is an activated barrier-crossing process. This means that to investigate pattern breakdown the full history of the trajectories has to be taken into account; we cannot presuppose rapid equilibration within the basin of the initial state. We therefore resorted to NS-FFS which is uniquely suited to this non-equilibrium, transient rare event system. We used λ as the progress coordinate for NS-FFS, which resulted in a branched and weighted trajectory ensemble that samples the relevant λ-range uniformly; this allowed us to generate sufficient statistics of rare breakdown events even in the most stable regions of parameter space. Details of the setup are described in "Methods" section 6.4.

Figure 6.3 shows the reweighted histograms of simulated trajectories over the reduced phase space spanned by order parameters λ_x and λ_y at snapshot times $t \in [1\text{h}, 4\text{h}, 7\text{h}]$, for three different values of κ ranging from strong NN repression ($\kappa \simeq 3$) to the limit of non-interacting nearest neighbors ($\kappa = \infty$). Clearly, there exists a region of stable expression in phase space which is populated rapidly and then remains quasi-stationary, hinting at the existence of a metastable state, in particular for the case with moderate NN repression. Moreover, it can be seen that the speed with which the system escapes from the quasi-stationary region strongly depends on κ. The figure also reveals that there are two pathways to destruction: one in which either the Hb or Kni domain is destroyed first and one in which either the Gt or Kr domain is the first to vanish. Motivated by these observations we defined a "region of stable patterns" in terms of the order parameters via $R_S \equiv \{(\lambda_x, \lambda_y) | \lambda_x \leq 0.45 \text{ and } \lambda_y \leq 0.43\}$, see Fig. 6.3. States that lie outside of R_S are considered destroyed patterns. The survival probability $S(t) = \iint_{R_S} p(\lambda_x, \lambda_y, t) d\lambda_x d\lambda_y$ is the probability for the system to remain in the region of stable patterns until time t (re-entry into R_S is not observed). We find that $S(t)$ is well-described by an exponential decay, $S(t) \propto e^{-k_D t}$, for times t larger than a certain lag-time t_{lag}. k_D then defines a "destruction rate", which implies an average "pattern stability time" or mean time until pattern destruction via $\tau_D \equiv 1/k_D$ (see "Methods" section 6.4 for details).

Figure 6.4A reveals that pattern stability indeed depends strongly on the ratio of repression strenghts: there exists a sharp maximum of pattern persistence times τ_D as a function of κ at $\kappa_{opt} \simeq 31.6$, i.e. there is an optimal NN repression strength that maximizes pattern stability. Notably, while significantly less stable than at the optimum, patterns with considerable stability are possible in the limit of $\kappa \to \infty$, i.e. in the absence of NN repression. In contrast, in the limit $\kappa \to 1$, i.e. when NN and NNN repression have close to equal strength, patterns essentially collapse immediately.

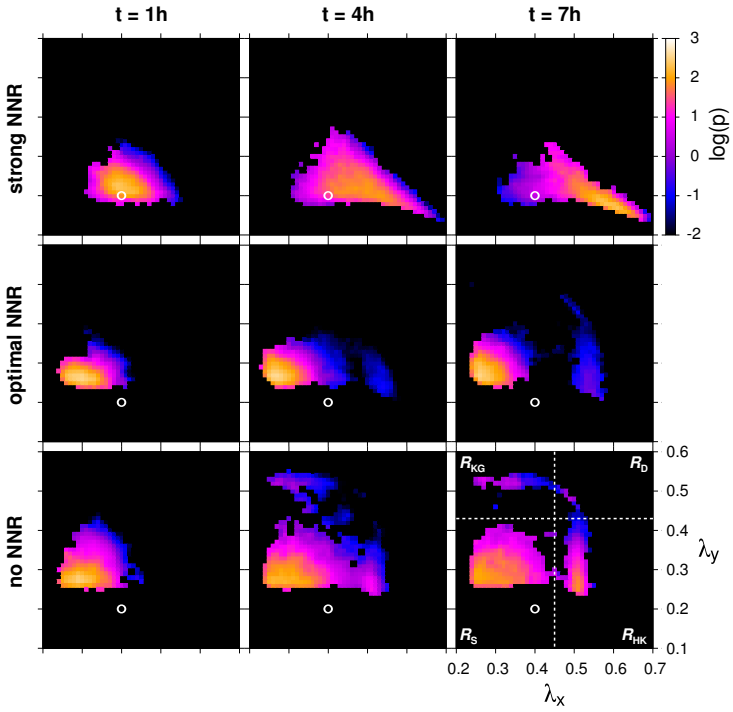

Figure 6.3: Pattern breakdown in the phase space spanned by λ_x and λ_y. The figure shows probability density snapshots of the phase space spanned by order parameters $\lambda_x = \max([\mathrm{Hb}]_\Sigma, [\mathrm{Kni}]_\Sigma)/N_\Sigma$ and $\lambda_y = \max([\mathrm{Kr}]_\Sigma, [\mathrm{Gt}]_\Sigma)/N_\Sigma$ at different times t after starting the simulation with an ordered pattern in the pinned system. (top row): for NNR (NN repression) almost as strong as NNNR (NNN repression) ($\kappa = 3.16$), system stability is low; (middle row) high stability for $\kappa = 31.6$; (bottom row) lower stability for NNNR only ($\kappa = \infty$). All plots are normalized histograms of reweighted (λ_x, λ_y)-points within $t \pm 5$ min. White circles indicate the starting point $(0.4, 0.2)$ of the initial rectangular pattern. In the middle and bottom rows we identify three densely populated regions: a broad region R_S centered around $(0.30, 0.30)$, which contains intact patterns, and two smaller regions close to $(0.55, 0.30)$ (R_{HK}) and $(0.30, 0.55)$ (R_{KG}), representing (partially) destroyed patterns (see "Methods" section 6.4 for detailed region definition). Ultimately trajectories will converge towards region R_D where two genes have been eliminated by their respective strong antagonists. Note the two different pathways to destruction, of which the one via R_{HK} is preferred over the one via R_{KG}.

The observation of a preferred phase space region in which system trajectories persist for long times raises the question whether this region constitutes a true metastable basin of attraction, addressed next. One way to determine whether there exists a basin that protects the pattern from destruction would be to compute the generalized free energy $F_g(\vec{\lambda}) = -\log \rho_{SS}(\vec{\lambda})$ from the stationary distribution $\rho_{SS}(\vec{\lambda})$, as in [130]. However, because the destroyed pattern effectively acts as a sink and the existence of a barrier which would allow for a quasi-stationary distribution within the basin

of intact patterns cannot be assumed a priori, we cannot meaningfully compute such a stationary distribution. We therefore pursued two complementary approaches: we analysed the transient behavior of perturbed patterns and computed the statistics of local phase space velocities.

6.2.2 In the maximally stable regime a restoring force exists

If enhanced phase space density in certain regions of the (λ_x, λ_y)-space is indeed due to the presence of a metastable basin, perturbations that transiently drive the system away from the stable pattern should be counteracted by restoring forces. To test this we perturbed intact patterns from the hypothetical basin by artificially enlarging regions in which one gap gene is dominant. Via brute-force simulations with higher time resolution we then checked whether the perturbed systems relax back into the basin region. We investigated two types of asymmetric perturbations: "Kni expansion", in which the central Kni domain is unidirectionally expanded at the expense of posterior Hb, and the converse "Hb expansion", in which the anterior Hb domain is enlarged at the expense of Kni (for details see "Methods" section 6.4). We found that for a gap protein G the center of mass z_G of its domain along the anterior-posterior axis is a good measure for characterizing the spatial properties of the gene expression domains. z_G captures alterations to gene expression domains in a robust way by avoiding ambiguity associated with defining and determining domain boundaries in the presence of gene expression noise. We calculated z_G separately for the anterior ($z_{\mathrm{Hb_A}}$) and posterior ($z_{\mathrm{Hb_P}}$) Hb domains.

Figure 6.5 shows, for $\kappa = \kappa_{\mathrm{opt}}$, time traces of z_G with $G \in \{\mathrm{Hb_A}, \mathrm{Kr}, \mathrm{Kni}, \mathrm{Gt}, \mathrm{Hb_P}\}$ for the two types of perturbations, averaged over 10 independent samples in each case. For both perturbations the average centers of copy number relax back to their original positions on a timescale $\sim 10\ h$. This demonstrates that for optimal repression strength ratio an effective restoring force counteracts deviations from the intact pattern, suggesting that in this case the region of high phase space density within R_S is a real metastable state confined by an underlying force field. Moreover, the timescale of relaxation is orders of magnitude shorter than the timescale of pattern collapse. Thus, for $\kappa = \kappa_{\mathrm{opt}}$ pattern destruction is a Markovian transition between metastable basins with transition waiting times much longer than the timescales of intra-basin dynamics.

In contrast, we could not observe clear restoring behavior in the systems with very weak or no nearest neighbor interaction (data not shown). Here perturbations of similar strength tend to result in almost immediate pattern destruction.

In summary, for the repression strengths ratio $\kappa_{\mathrm{opt}} \simeq 31.6$ that maximizes stability, pattern breakdown appears to be an activated process characterized by a restoring force towards the initial state.

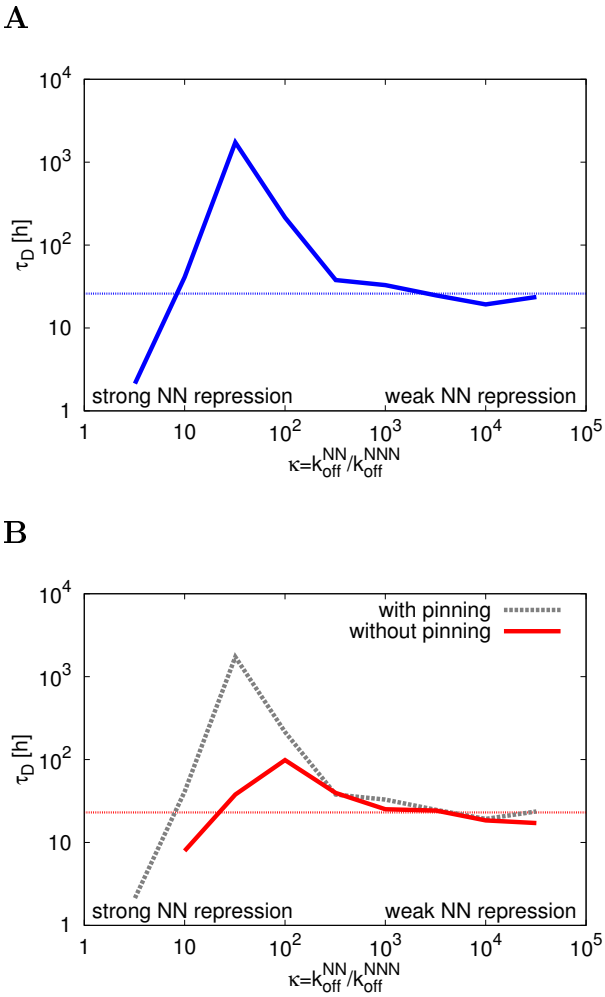

Figure 6.4: An optimal strength of nearest neighbor repression maximizes pattern stability. (A) Plotted is the mean time until pattern destruction τ_D as a function of κ, the ratio between the weak and strong repressor off-rate, for the system in which Hb is pinned at the boundaries. The dashed lines are the values for the completely uncoupled system, i.e. $\kappa = \infty$. We observe a pronounced maximum of the stability time when the weak repression is ca. 30 times weaker than the strong repression ($\kappa_{opt} \simeq 30$). (B) The same quantity for the system without pinning of Hb at the system boundaries. For comparison we replot the data for the system with pinning (gray dashed line). In the system without pinning stability is maximized at an optimal NN repression strength ratio as well. Note however that here the optimum slightly shifts towards weaker repression ($\kappa_{opt} \simeq 100$), while the optimal pattern persistence time is significantly reduced as compared to the case with pinning. Both curves agree well in the limit $\kappa \to \infty$.

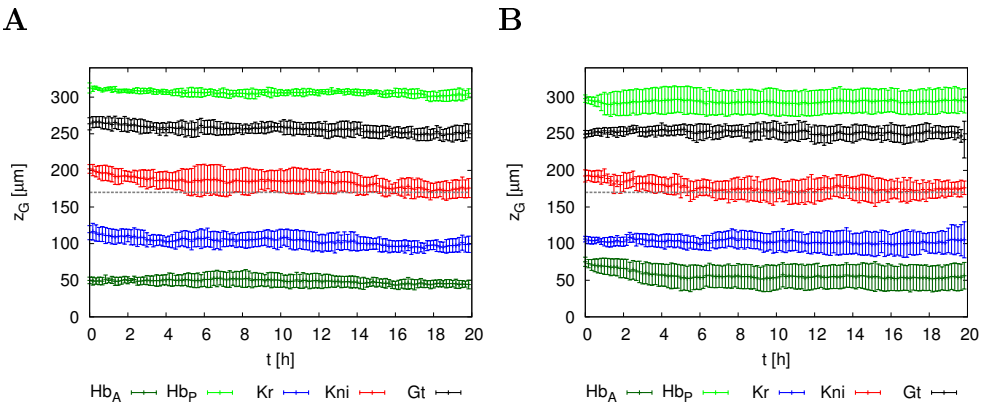

Figure 6.5: Perturbed trajectories are restored to their origin at optimal NN repression strength. Shown are averaged time traces of the copy number center-of-masses z_G for the five domains of the stable pattern (Hb_A = anterior Hb, Hb_P = posterior Hb) at $\kappa = \kappa_{opt}$ for two different perturbations: (A) "Kni expansion", i.e. prolongation of the central Kni domain by $\Delta = 8$ nuclei into the posterior and (B) "Hb expansion", i.e. prolongation of the anterior Hb domain by $\Delta = 8$ nuclei towards the center of the embryo. The gray-dashed line marks the center of the system. In both cases we observe a restoration of the metastable state on a timescale $\lesssim 10$ h.

6.2.3 The phase-space velocity field reveals a metastable basin

The existence of a true metastable basin should manifest itself also in the statistics of transient dynamics in phase space: forces that drive trajectories in phase space should translate into local mean phase space velocities with a clear bias towards basins of attraction.

To extract the velocity field for our system we modeled the coarse-grained pattern dynamics as overdamped diffusive motion in the $\vec{\lambda} \equiv (\lambda_x, \lambda_y)$ plane, assuming that these degrees of freedom capture the slowest time scales of the system and making a Markov approximation for the fast dynamics [222, 223]. This technique has been successfully applied in protein folding [224, 225, 226, 227]. The model equation is

$$\frac{d}{dt}\vec{\lambda} = \langle \vec{v}_\lambda \rangle (\vec{\lambda}) + \sqrt{2D_\lambda(\vec{\lambda})} d\vec{W} \tag{6.4}$$

where $\vec{W}$ is uncorrelated (2D) white noise with unit covariance. We estimated the local drift $\langle \vec{v}_\lambda \rangle (\vec{\lambda})$ and diffusion coefficient $D_\lambda(\vec{\lambda})$ from our reweighted simulated trajectories by averaging local displacements (see "Methods" section 6.4 and section 6.A.1 in the appendix for details). The same analysis was also conducted for the 2D spaces spanned by the single-gene components of λ_x and λ_y, i.e. for $\vec{\lambda}_{HK} \equiv ([Hb]_\Sigma/N_\Sigma, [Kni]_\Sigma/N_\Sigma)$ and $\vec{\lambda}_{KG} \equiv ([Kr]_\Sigma/N_\Sigma, [Gt]_\Sigma/N_\Sigma)$.

Note that the mean velocity $\langle \vec{v}_\lambda \rangle (\vec{\lambda})$ is different from the gradient of the log of the stationary density $\rho_{SS}(\vec{\lambda})$, which is not sampled in our simulations, and from the

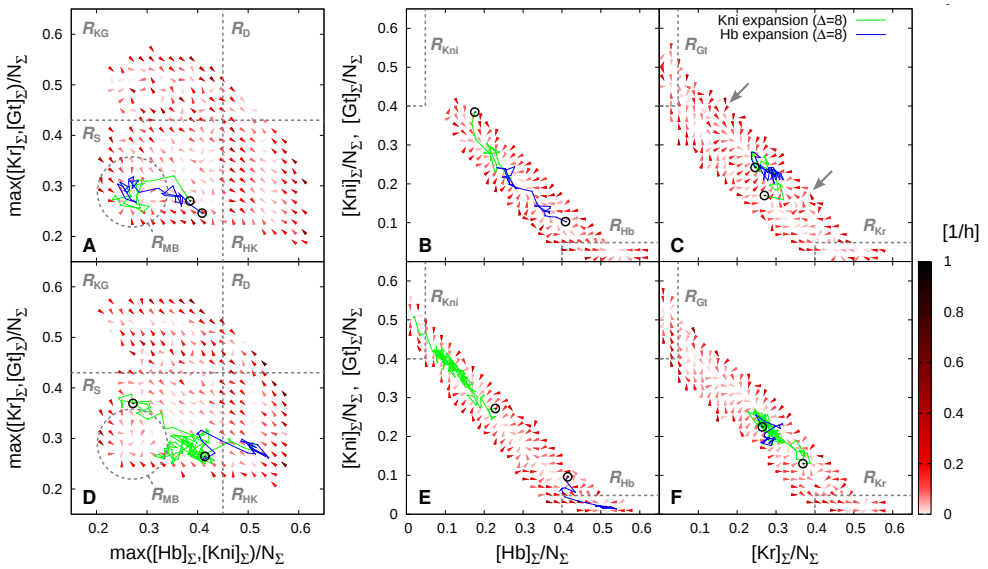

Figure 6.6: Phase space velocity fields reveal metastable basins. Here we show average phase space velocity fields for projections on different pairs of order parameters for the system with (A-C) and without (D-F) Hb pinning. Velocity fields were obtained by averaging displacements of all trajectories that exit the local bin on a lattice of 50×50 bins (see also "Methods" section 6.4); colors indicate magnitude. Green and blue lines show examples of relaxation trajectories for the two types of perturbations that we considered; starting points are marked by black bullets. Gray dashed lines indicate boundaries of phase space regions used for stability and flux analysis. Plots A and C for coordinates $\lambda_x = \max([\mathrm{Hb}]_\Sigma, [\mathrm{Kni}]_\Sigma)/N_\Sigma$ and $\lambda_y = \max([\mathrm{Kr}]_\Sigma, [\mathrm{Gt}]_\Sigma)/N_\Sigma$ (as in Fig. 6.3) show that regions of enhanced phase space density typically correspond to regions with low drift magnitude. In the lower-left part of R_S we identify a small subregion with concentrically inwards-pointing velocities (R_MB, dashed circle), towards which perturbed trajectories relax in the system with pinning (A). This is indicative of a metastable basin of intact patterns. The basin is much weaker in the unpinned system, as seen in (D) and in the two other coordinate systems (compare B to E and C to F). In particular, the concentric field region clearly visible in the Kr-Gt space in the system with pinning (C, gray arrows) is much less pronounced in the system without pinning (F). As expected, Hb pinning forbids the destruction pathway in which Kni is maximized (compare B to E).

probability flux in stationary state. Rather, it is proportional to the effective force acting at the reduced phase space point $\vec{\lambda}$ in the overdamped LANGEVIN model. The local mean velocity field $\vec{v}_\lambda(\vec{\lambda})$ is determined by the conditional transition probabilities $\pi(\vec{\lambda}, \vec{\lambda}')$ between states $\vec{\lambda}$ and $\vec{\lambda}'$, and thus can be extracted from our transient simulation data.

Figure 6.6 (A-C) shows a comparison of the average velocity field in different reduced phase space coordinates, for the optimal repression strength ratio ($\kappa \simeq 31.6$) in the system with Hb pinning. We also plot the relaxation of example trajectories starting from perturbed intact pattern states for the two considered perturbations and

indicate boundaries between different attractor regions (gray lines). In the (λ_x, λ_y)-space (panel A) one can identify two regions with low average velocities: one within the region of stable states R_S, the other within the region R_{HK} of states in which the Kni gene domain is destroyed (the corresponding region in which either Kr or Gt are destroyed, R_{KG}, is less clearly visible due to poor sampling) These low-drift "plateaus" are separated by a region with high velocity components towards R_{HK}, indicating that trajectories are quickly absorbed into this zone once they reach the edge of R_S. Notably, in the lower-left corner of the R_S plateau we notice a small region in which average velocities are significantly higher and all pointing inwards (R_{MB}, gray circle). This is indicative of a metastable basin around the ordered stripe pattern. Indeed, perturbed trajectories relax into this basin region after randomly exploring the diffusive plateau, and remain confined to the basin for later times (Fig. 6.6). The basin can be perceived more clearly in the $\vec{\lambda}_{HK}$-space (panel B) and in the $\vec{\lambda}_{KG}$-space (panel C). In both projections trajectories starting from perturbed states relax towards regions which are clearly enclosed by velocity vectors that point towards the centers of the regions, again indicating the existence of a metastable basin. This is in line with the WADDINGTON picture of "canalization" [155, 156], in which developmental stages are seen as successive attractors of the underlying dynamics; the ordered stripe pattern represents one such attractor.

In Figure S6.3 in the appendix we show the same set of velocity field plots for a case with weaker NN repression ($\kappa = 1000$). Here the velocity fields are even more plateau-like in R_S, and the characteristic concentric velocity pattern indicative of the basin in the optimal case cannot be clearly discerned any more. In accordance, trajectories starting from perturbed patterns fail to relax back and progress towards defective pattern states. Thus, canalization requires a minimum level of NN repression in this system.

Taken together, both the perturbation experiments and the velocity field analysis demonstrate that the long-time confinement of phase space trajectories close to the ordered pattern at optimal NN repression is due to the existence of a metastable basin which impedes progress towards destruction by restraining excursions from the basin. With decreasing strength of NN repression the basin gradually disappears, thus enhancing the probability of destruction.

6.2.4 Stability enhancement does not require pinning

To assess whether pinning of Hb domains is necessary for the observed stability enhancement at intermediate NN repression, we repeated our simulations and analysis also for a system without pinning. Here, Hb promoters in nuclei at the system boundaries were not exempted from mutual inhibition. Surprisingly, we find that also in the system that lacks pinning, stability is enhanced by the presence of weak interaction partners between two strongly repressing gap protein domains. In Figure 6.4B we again plot the mean destruction time τ_D against the ratio of the repressor off-rates κ for the system without pinning. The figure reveals high stability at an optimal repression strength ratio $\kappa_{opt} = 100$, which is close to the optimum in the system with pinning, albeit with about 10 times lower overall stability times.

6.2.5 Pinning introduces strong restoring forces

Perturbations of the same strength as in the system with pinning did not relax back even in the maximally stable case in the system without pinning (data not shown). This is elucidated by plotting the average local velocities in the unpinned system (Fig. 6.6D-F). While the mean velocity directions are very similar to the ones in the pinned system (Fig. 6.6A-C), inward-pointing velocities indicative of a metastable state are of significantly lower magnitude. This suggests that without pinning restoring forces are too weak to overcome fluctuations that drive the system out of the basin. Further support is provided by the fact that the diffusion coefficient in the plateau-like region of intact patterns R_S is very similar for all $\kappa \geq 10$ in both the system with and without pinning, as shown in Figure S6.1A of the appendix. This shows that the effective temperature is the same in both systems and that the differences between the pinned and unpinned system are indeed due to differences in their restoring forces, reflected in the velocity fields shown in Fig. 6.6. Specifically, the most important effect of pinning is that it removes the Hb destruction pathway which is accessible in the system without pinning (compare 6.6B to 6.6E), as discussed in more detail in the next section.

For the weakly coupled systems at $\kappa \gtrsim 1000$, pinning has almost no effect on the mean velocity fields, except for the fact that without pinning the Hb-destroyed states are apparent in the $([\mathrm{Hb}]_\Sigma/N_\Sigma, [\mathrm{Kni}]_\Sigma/N_\Sigma)$ space (compare Supporting Figure S6.5C to Figure S6.3C). Consistently, in this regime average stability times are very similar for the two considered system types. Most importantly, in the limit of weak NN interaction (large κ) stability seems to be the product of slow dynamics alone, both with and without pinning. Here the average times until destruction are of the same order of magnitude as the estimated times to diffuse through phase space from the region that corresponds to metastable states for optimal κ towards the edge of R_S, from which trajectories are quickly canalized into defective pattern states (see Supporting Figure S6.1B).

Thus, while in both the systems with and without pinning the overall effect of nearest-neighbor repression on pattern stability is very similar, we find that it can have two origins: for weak coupling, i.e. large κ values, stability originates from slow diffusive dynamics in phase space; for optimal NN coupling ($\kappa \simeq 10 - 100$) stability is additionally augmented by the creation of a metastable basin, which in turn can be significantly enhanced by pinning of Hb at the system boundaries.

6.2.6 Pathways to destruction

Both with and without pinning of Hb at the system boundaries, pattern stability is maximal at an optimal strength of NN repression. Stability times, however, are significantly higher in the system with pinning. In order to understand whether this is simply due to the fact that pinning prohibits destruction of the Hb domains or due to other pinning-induced effects, we compared the different pathways to destruction by computing probability fluxes through distinct reaction pathways (see "Methods" section 6.4 for details). The different reaction pathways are defined by the order in which gap gene domains are destroyed. In our system there are two major pathways: the Hb-Kni destruction pathway (either the Hb or the Kni domain vanishes first)

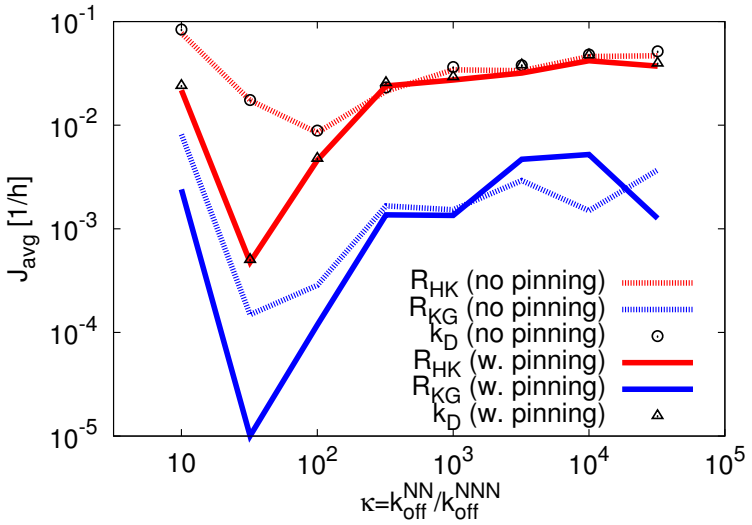

Figure 6.7: Pinning affects destruction pathways We plot here the average probability fluxes from the region of stable patterns R_S into the different remote basins identified in the (λ_x, λ_y) phase space as a function of the repression strength ratio κ for the systems with and without pinning. Here the flux is defined as the average increase per time of the total probability in the basin. Basin boundaries and flux quantities are described in detail in "Methods" (section 6.4). Shown are the flux into the basin R_{HK}, corresponding to destruction of either Hb or Kni (red lines), the flux into the basin R_{KG}, in which one of Kr or Gt is destroyed (blue lines), and the total outflux from R_S, which equals the pattern destruction rate k_D (black bullets). Solid lines and triangles show the data for the system with pinning, dashed lines and circles the values for the system without pinning. Clearly, in both with and without pinning and for all κ considered here, R_{HK} is the dominant fraction of the flux, reflecting that the dominant pathway to destruction is the one that starts with the disappearance of Hb or Kni. Pinning of *hb* expression at the system boundaries leads to a pronounced reduction of the flux through this pathway for $\kappa = 10 - 100$.

and the Kr-Gt destruction pathway (either the Kr or Gt domain vanishes first). The phase space histograms in Figure 6.3 demonstrate that simultaneous destruction of two domains, corresponding to trajectories that progress diagonally in λ_x-λ_y space, is highly improbable. We find that, while in general the Hb-Kni destruction pathway prevails, the fact that the Hb-destruction pathway is dominant for $\kappa \leq 100$ in the system without pinning accounts for the strong enhancement of pattern stability due to pinning.

In Figure 6.7 we plot for different repression strength ratios κ the magnitude of average fluxes from the region of intact patterns R_S in the λ_x-λ_y space into the respective neighboring regions that correspond to states in which one expression domain vanished. The figure reveals that for all κ the flux through the Hb-Kni destruction pathway is approximately ten times higher than the flux through the Kr-Gt pathway, for systems both with and without pinning. The figure also shows that pinning indeed reduces the flux through the dominant, i.e. Hb-Kni, pathway, most significantly for

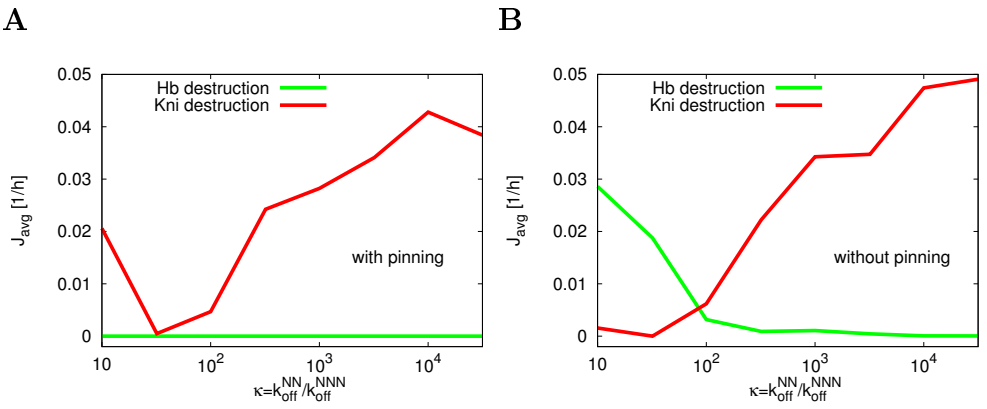

Figure 6.8: Pinning shifts the destruction flux balance in the dominant (Hb-Kni) pathway The figure shows the contributions of the Hb-destruction and Kni-destruction pathways to the outflux from R_S as a function of the repression strength ratio κ for the systems with (A) and without (B) pinning. See "Methods" section 6.4 for the definitions of basin boundaries and details of flux calculation. Without pinning and for strong NN repression, the preferred pathway to destruction is the one in which the Hb domains are destroyed first, while for weaker coupling (large κ) destruction begins via annihilation of the Kni domain. Interestingly, in both cases the flux through the Kni-destruction pathway is minimal at $\kappa \simeq 31.6$. Pinning forbids destruction via the Hb pathway and thus dramatically reduces the overall destruction flux for low κ, giving rise to the enhanced stability optimum at $\kappa \simeq 31.6$.

$\kappa \simeq 10 - 100$, i.e. around the optimal value κ_{opt}. This gives rise to the pronounced stability enhancement. The simultaneous reduction of the flux through the Kr-Gt pathway is not relevant for overall stability.

We analysed further the detailed composition of fluxes through the dominant (Hb-Kni) pathway by computing the average flux into the regions of destroyed states in $([\mathrm{Hb}]_\Sigma/N_\Sigma, [\mathrm{Kni}]_\Sigma/N_\Sigma)$ space (Figure 6.8). As expected, in the systems with pinning the entire flux through the dominant pathway goes into the Kni-destroyed state. Interestingly, this is also the case for the weakly coupled systems without pinning. Here the flux into the Hb-destroyed state is clearly dominant over the flux into the Kni-destroyed state for strong NN interaction. This explains why pinning, which prohibits exit through the Hb destruction pathway, increases stability in the $\kappa \lesssim 100$ regime. While the flux through the Kni destruction pathway is minimal at $\kappa = 31.6$ with or without pinning, in the system without pinning the accessibility of Hb destruction shifts the minimum of the combined flux through both pathways towards $\kappa = 100$ (Figure 6.7).

6.2.7 Fixed point analysis helps understanding the origin of domain stability

To better understand the mechanism behind pattern stability we performed a linear stability analysis for a deterministic system of two strongly repressing gene pairs (A,B) and (C,D), with weaker mutual repression across the pairs; (A,B) and (C,D) thus correspond to (Hb,Kni) and (Kr,Gt) in the simulated model. We first focused on a single well-mixed reaction volume in stationary state, neglecting diffusive coupling. This corresponds to either a single nucleus in the limit of zero diffusion constant or to a spatially homogenous steady state of the full system, i.e. infinitely fast diffusion. We additionally carried out an analysis that accounts for spatial coupling in a minimal way, as described further below. To compare to spatially resolved simulations, we calculated the set of fixed points (A, B, C, D), where letters denote total copy numbers, for different values of κ with all other parameters as in the full model. As in the simulations, κ was varied via the dissociation constant of the weak repression. For details of the analysis we refer to section 6.A.3 in the appendix.

Figure 6.9A shows a representative subset of the fixed point solutions (A, B, C, D) as a function of κ, for the well-mixed case. For weak NN repression, $\kappa \gtrsim \kappa_{\text{bif}} = 13$, two bistable pairs of genes exist in parallel, i.e. either gene of (A,B) can be coexpressed with either of (C,D). At $\kappa = \kappa_{\text{bif}}$, a bifurcation occurs towards a "monostable" regime for $\kappa \lesssim \kappa_{\text{bif}}$, where only one of the four genes can reach high expression levels. In other words, overlapping domains are impossible for strong NN repression. This gives a rationale for rapid pattern breakdown observed at $\kappa \lesssim \kappa_{\text{bif}}$ in the full system: because diffusion rapidly establishes NN overlap, no stable stripe pattern is possible.

We next included diffusive fluxes, mimicking the situation in a nucleus at one of the Hb-Kni interfaces. Flux values were estimated from simulations of intact patterns with $\kappa = \kappa_{\text{opt}}$ (the setup shown in Fig. 6.2). At these interfaces, both Hb and Kni are low and their effective influx is positive, while one weak repression partner (Kr or Gt) is high with a net outflux. How imposing these fluxes for the strong partners A and B and weak partner C affects the fixed point solutions is shown in Figure 6.9B: here, the only stable solution for $\kappa \gtrsim \kappa_{\text{bif}}$ is the one where C is high and both A and B low, thus inhibiting bistable switching between A and B, with expression levels in good quantitative agreement with those at the interface between the strong antagonists in the simulation. We do not find physically relevant fixed points for $\kappa \lesssim \kappa_{\text{bif}}$, again in line with simulations, where patterns rapidly collapse.

In summary, without diffusive coupling, for $\kappa \gtrsim \kappa_{\text{bif}}$ strongly repressing pairs in an interface nucleus form two independent bistable systems ((A,C) and (B,D)), whereas for $\kappa \lesssim \kappa_{\text{bif}}$ one species predominates. Spatial coupling with influx of A and B and outflux of C completely destabilizes solutions for $\kappa \lesssim \kappa_{\text{bif}}$; for $\kappa \gtrsim \kappa_{\text{bif}}$ it destroys bistability and results in coexistence of A and B at low expression levels, while C remains high. This suggests that the introduction of a weak interaction partner into the contact region of two strongly repressing gap gene domains acts as a stabilizing factor which impedes bistable switching, thereby slowing down interface dynamics and pattern breakdown. This mechanism works only for intermediate NN repression: for strong NN repression overlapping domains are unstable while for very weak NN repression bistability of strong partners is unhindered.

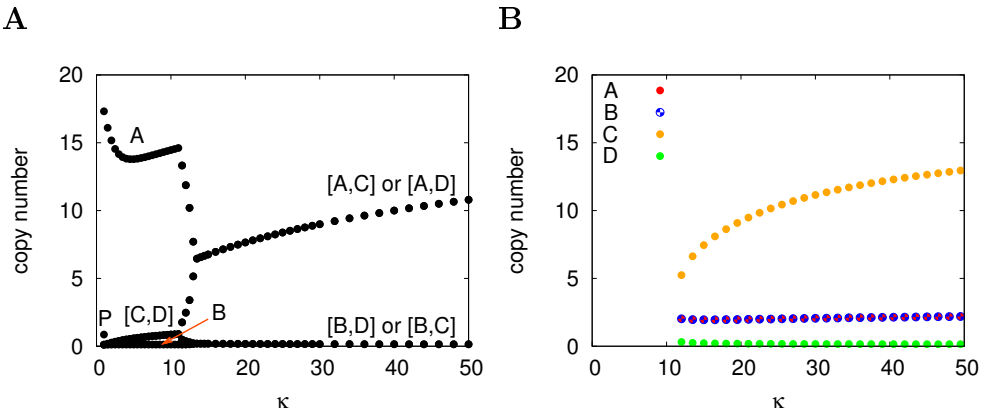

Figure 6.9: Linear stability analysis for two nested bistable pairs of mutually repressing genes. The figure shows fixed point solutions (A, B, C, D) for total copy numbers in a system of four mutually repressing genes. (A, B) and (C, D) constitute strongly repressing pairs, with repression between pairs weaker by a factor of κ ($\kappa \to \infty$ corresponding to no weak repression). We plot the solution branch in which gene A dominates. Equivalent solutions are obtained by permutations of {A, B, C, D} which preserve the weak/strong repression pattern. Panel (A) shows solutions for a spatially homogeneous system. The notation [A, C] means that A and C coexist with equal copy numbers. For $\kappa \lesssim \kappa_{\rm bif}$ only A is strongly expressed. Around $\kappa = \kappa_{\rm bif}$ a bifurcation occurs: for $\kappa \gtrsim \kappa_{\rm bif}$ two bistable pairs coexist, with two weakly interacting genes at high levels, while their respective strong antagonists are repressed. For $\kappa = 1$ in particular we find a solution in which all four genes are low (point P). In panel (B) we plot stable solutions for a system that mimics the situation in a nucleus exactly in the middle between A and B domains in the spatially resolved model. Diffusive coupling is accounted for by imposing influx of A and B and outflux of C, as described in the text. This selects a unique stable fixed point where C dominates, and A and B coexist at low levels, without bistable switching. For $\kappa \lesssim \kappa_{\rm bif}$ we do not find any physically relevant fixed points, indicating that the imposed domain configuration is unstable.

6.3 Discussion

In early embryogenesis, morphogen gradients provide a long-range positioning system by activating downstream patterning genes in a concentration-dependent manner. Indeed, many gap genes, which constitute the first layer of patterning genes in Drosophila, are known to be regulated by the morphogen gradient of Bicoid (Bcd) which spreads from the anterior embryo pole in the earliest stages of development [114, 113, 109, 110, 177, 178, 179]. This, however, raises the question how gap genes can establish expression domains in the posterior half of the embryo, where Bcd levels have been measured to be very low [51, 30] and therefore carry imprecise positional information. The fact that posterior gap gene stripes can form in flies with deficient maternal gradients [146, 158, 157] and that other insect species lack the Bcd gradient but display similar stripe patterns [189, 190, 191, 192, 193] raises further doubt on the importance of Bcd for posterior patterning.

An alternative view is that Bcd provides high-resolution positional information only in the anterior, up to a well-defined Hb expression domain boundary around mid-embryo, while in the posterior, patterning emerges in a self-organized way through mutual interactions of gap genes. Indeed, recent experimental and theoretical results suggest that mutual interactions between gap genes may play a prominent role in abdominal segmentation [181, 170, 183, 182, 115, 116, 114, 113], by establishing stable domains with slow effective dynamics [117]. However, it is not a priori clear how such a system could be robust given the stochastic nature of gene expression and regulation. In particular, copy number fluctuations can induce bistable switching at domain boundaries which may deteriorate expression patterns. Here we asked whether a system of mutually repressing gap gene stripes can indeed be stable over the required developmental time interval, and robust against perturbations, in the absence of any morphogen gradient.

We quantified the mean stability time of a five-stripe pattern of gap genes Hunchback (Hb), Krüppel (Kr), Knirps (Kni) and Giant (Gt) in a stochastic model of the posterior Drosophila embryo in cycle 14, as a function of the repression strength between neighboring stripes. Simulations of the breakdown of very stable patterns were made possible by the NS-FFS enhanced sampling scheme [218].

We find that for an optimal value of the repression strength between adjacent expression domains, the stability of the pattern is dramatically increased. This stability optimum can be traced back to the fact that bistable switching at the boundary between domains of strongly mutually repressing genes is inhibited by an intervening cushion domain of a gene that weakly represses both strong partners. This stabilizing mechanism works best if the spacer gene represses its nearest neighbors (NN) with moderate strength: very weak NN repression has no effect while strong NN repression globally destabilizes overlapping domains. At the optimal repression strength ($\kappa = \kappa_{\mathrm{opt}}$), the cushion thus tends to slow down the domain-boundary dynamics.

Stability is enhanced even more if expression of the outermost gene Hb is pinned at the system boundaries. We introduced pinning motivated by the fact that in wild-type embryos, Hb is under direct or indirect control of maternal cues, namely of Bcd in the anterior half and of Tailless (Tll) at the posterior pole of the embryo [205, 176]. We then find that intact patterns form a metastable attractor of the dy-

namics with a restoring force which counteracts perturbations, such as non-perfect initial conditions. Restoring forces are induced by pinning at the boundaries which effectively anchors the gene expression pattern. In the optimal stability regime, our observations are consistent with the WADDINGTON picture [155, 156] of development as canalization into successive metastable states; the ordered gap gene pattern represents one metastable state in this succession. Earlier work already demonstrated that developmental attractors may emerge as an intrinsic property of the created gene expression pattern via mutual interactions [115, 116]. Here, we demonstrate that also without morphogen gradients metastable basins arise, which protect stable patterns against stochastic fluctuations.

The present work leads to the interesting question how a properly ordered stripe pattern of mutually repressing genes is established initially. In particular, while pinning of Hb at the boundaries in principle would determine that Kni must form its domain in the center of the system, symmetry breaking between Kr and Gt requires additional control. The fact that Hb acts as an activator to Kr at low concentrations provides a possible mechanism [228, 194, 152]. Alternatively, the timing of the onset of gene expression for the different gap genes may determine their initial arrangement, which then gets frozen by mutual interaction.

The observed stability times appear sufficient for early embryogenesis ($\simeq 2h$ until cycle 14) for all NN repression strengths weaker than the optimal value, with or without pinning, even for the reduced system size considered here for computational feasibility. To assess the effect of system size, we have performed exemplary simulations in which we increased the gap gene production rate, the length of the system and its circumference, respectively (not shown). In all cases we find that while overall pattern stability is further increased, a stability maximum at intermediate NN repression strength persists. In a more realistic description, stability times will be modified due to the influence of system size and of features of gene regulation that were not included here (such as autoactivation and bursty translation); nevertheless we believe that the mechanisms of enhanced stability described here apply also in vivo. They provide an explanation for the persistence of the gap gene pattern after the Bcd gradient starts to disappear in developmental cycle 14 [147].

6.4 Methods

6.4.1 Details of the model

We model the early Drosophila embryo in its syncytial stage at cycle 14 with a cylindrical array of $N_z \times N_\phi$ nuclei coupled by diffusion of proteins. To capture the radial symmetry of the real embryo, we impose periodic boundary conditions in the "angular" lattice coordinate, denoted by lattice index ϕ; proteins thus can diffuse between lattice site (z, N_ϕ) and lattice site $(z, 1)$, where $z \in \{1, .., N_z\}$ is the "axial" index of the lattice site. Every nucleus contains four individual promoters for each of the gap genes hunchback (*hb*), krüppel (*kr*), knirps (*kni*) and giant (*gt*).

Each promoter can be repressed by the products of the three others with different affinities. We employ OR-logic, i.e. whenever one of the three repressor sites is occupied expression of the gene is completely blocked. There is no competition for repressor sites on the promoters. In the unrepressed state the promoters exhibit constitutive protein production, i.e. no external activator signal is required. This deliberately mimics a situation in which activation of the gap genes is not provided by external morphogen gradients but by either an omnipresent master activator or auto-activation with a low activation threshold. Consequently, our model explicitly does not include morphogen gradients. As a simplifying assumption, we treat the whole production process, i.e. transcription, elongation and translation, as one step governed by a single rate β. Proteins however can form (homo)dimers and dedimerize again [229, 230], and only in their dimeric form they act as repressors. This is to ensure that antagonistic genes form bistable pairs for sufficiently strong mutual repression.

Initially, all simulations are set up in a stripe pattern corresponding to the experimentally observed order in the embryo posterior, i.e. Hb-Kr-Kni-Gt-Hb [114, 113, 112]. This implies a fixed definition of "gene neighborhood" to which we refer throughout this paper: by nearest neighbors (NN) we mean the pairs (*hb*, *kr*), (*kr*, *kni*), etc., while the pairs (*hb*, *kni*) and (*kr*, *gt*) are considered next-nearest neighbors (NNN). A key ingredient of our model is that nearest-neighbor repression is weaker than repression between next-nearest neighbor domains (see paragraph "Parameter choice" for more details). By default we pin the expression of *hb* at the system boundaries, i.e. in nuclei on the two outermost rings of the cylinder the *hb* promoter is irrepressible, and therefore constitutively produces Hb proteins. This takes into accout that in the real system Hb is under strict control by Bcd throughout the anterior half [176], while in the posterior a second enhancer exposes Hb to positive regulation by the maternal terminal system [205, 220, 221]. We compare this system to a system in which there is no pinning and all nuclei are identical.

6.4.2 Simulations

To perform rare-event sampling of the spatially resolved system we integrate our "Gap Gene Gillespie" (GGG) simulator used in previous work [170, 122] with the recently developed NS-FFS scheme [218]. NS-FFS is used to monitor and process a progress coordinate written out by GGG at regular simulation interrupts, at which GGG trajectories are cloned and restarted in a way that sampling is enhanced in the direction of increased progress coordinate, i.e. towards pattern destruction.

Spatially resolved stochastic simulations (GGG)

In GGG, the model is implemented via the Stochastic Simulation Algorithm by GILLESPIE [53, 54] on a cylindrical 2D lattice of reaction volumes at constant distance $l = 8.5$ μm, with periodic boundary conditions in the circumferential direction of the array. An abstract graph of the reaction network that displays the set of reactions for any of the simulated promoters is shown in Figure S6.8 in the appendix. Diffusive chemical species (gap proteins and their dimers) hop between neighboring volumes via the next-subvolume method [144] which integrates diffusion into the GILLESPIE algorithm by annihilation of a species copy in the volume of origin and instantaneous insertion of that copy in a randomly chosen neighboring volume with a rate $k_{\text{diff}} = \frac{4D}{l^2}$. The source code of GGG with examples can be downloaded from http://ggg.amolf.nl.

Forward flux sampling

We employ the recently developed non-stationary forward flux sampling (NS-FFS) method [218, 219, 148] to enhance stochastic sampling of system realizations that increase a (reaction) progress coordinate λ while retaining correct statistical weight. NS-FFS achieves this by branching off multiple child trajectories upon crossing predefined interfaces in undersampled regions of (λ, t)-space and pruning trajectories that cross interfaces in oversampled regions. The NS-FFS scheme aims at equilizing the flux of simulated trajectories in the reaction coordinate direction among the time bins. The rate of branching and pruning is calculated from the temporal trajectory crossing statistics collected during runtime. To that purpose the time domain is subdivided into equidistant time intervals. For a detailed account of the reweighting procedure we refer to [218].

Progress coordinates

The choice of a suitable progress coordinate is a critical step of the FFS technique. Here, we seek to enhance progress of the simulated patterns towards their destroyed state. The destruction events are in particular characterized by the disappearance of one of the partners within each of the strongly repressing gap gene pairs. Progress towards destruction thus is accompanied by increasing pair asymmetry, which can be quantified for each pair separately by the following two order parameters:

$$\begin{aligned} \lambda_{\text{x}} &\equiv \max([\text{Hb}]_\Sigma, [\text{Kni}]_\Sigma)/N_\Sigma \\ \lambda_{\text{y}} &\equiv \max([\text{Kr}]_\Sigma, [\text{Gt}]_\Sigma)/N_\Sigma \end{aligned} \tag{6.5}$$

Here $[\text{G}]_\Sigma$ is the total copy number of G proteins (counting dimers twice) and $N_\Sigma = [\text{Hb}]_\Sigma + [\text{Kr}]_\Sigma + [\text{Kni}]_\Sigma + [\text{Gt}]_\Sigma$ the number of all proteins in the system. Based on this we define our progress coordinate, which increases whenever asymmetry among any of the pairs is augmented, via

$$\lambda \equiv \lambda_{\text{x}} + \lambda_{\text{y}} = \left[\max([\text{Hb}]_\Sigma, [\text{Kni}]_\Sigma) + \max([\text{Kr}]_\Sigma, [\text{Gt}]_\Sigma)\right]/N_\Sigma \,. \tag{6.6}$$

Since NS-FFS features multi-dimensional reaction coordinates we compared our standard choice to a setup in which the two components λ_x, λ_y of the reaction coordinate λ are treated as two separate reaction coordinates with an own set of interfaces each. While an orthogonal pair of reaction coordinates captures the principal reaction paths in our system more accurately, the acquisition of crossing statistics is prolongated because of the increased number of bins in these simulations, and we did not find any substantial advantage of this choice in terms of branching behavior. We therefore preferred the standard definition.

Combination of simulation methods

In order to wrap NS-FFS around the GGG simulator we run GGG for a predefined simulation time $t_{\mathrm{GGG}} = 60\,\mathrm{s}$. At the end of the simulation the reaction coordinates are calculated and passed on to the NS-FFS module, and the end state of the simulation is recorded. The NS-FFS module then determines whether an interface crossing has occured and, if so, decides on whether the trajectory shall be branched or pruned. In case of branching NS-FFS will prompt $n_{\mathrm{B}} \geq 1$ restarts of the GGG simulator with the recorded end state as initial condition, different random seeds and with new statistical weights. At each crossing and at measuring times spaced by a regular interval Δt the time, branch weight and reaction coordinate values are stored in a tree-like data structure that facilitates later analysis.

Trajectory trees are started from a standardized, regular-stripe initial condition passed to the first call of GGG. Propagation of the tree stops when all child branches have either reached the end of the time histogram or have been pruned. Subsequently a new tree is started with a different random seed. NS-FFS monitors the cumulative simulated time T_{cum} and terminates simulation when T_{cum} exceeds a predefined maximal simulation time T_{max} and the last trajectory tree has been propagated towards the end. Typically, $T_{\mathrm{max}} = 3 - 7\,\mathrm{h}$ and $T_{\mathrm{cum}} = 2 - 5 \cdot 10^7\ s$, which usually results in several thousand independent starts from the initial condition.

By default we start from an artificial pattern consisting of five non-overlapping stripes with rectangular profiles occupying an equal part of the total system length $L/5$ each and equal number of monomers (no dimers) in each nucleus close to the expected total copy numbers. We find that these initial patterns quickly relax towards typical metastable patterns, i.e. into the metastable main basin, which justifies our approach a posteriori.

6.4.3 Parameter choice

Repression

We are mainly concerned about the importance of distinct repression strength of nearest-neighbor (NN) as compared to next-nearest neighbor (NNN) interaction. We assume repressor binding-rates to be diffusion-limited via $k_{\mathrm{on}}^{\mathrm{R}} = 4\pi\sigma_{\mathrm{R}} D_{\mathrm{N}}$, where D_{N} is the intranuclear diffusion constant and σ_{R} an effective target radius. Repression strength therefore is varied by changing the unbinding rates of the repressing dimers. The main parameter in our simulations is $\kappa = k_{\mathrm{off}}^{\mathrm{NN}}/k_{\mathrm{off}}^{\mathrm{NNN}}$, the ratio between NN and NNN repressor off-rate. In this work only $k_{\mathrm{off}}^{\mathrm{NN}}$ is varied, while $k_{\mathrm{off}}^{\mathrm{NNN}}$ is chosen

sufficiently low to guarantee bistability between next-nearest neighbor genes, which is a precondition for the formation of individual stripe domains in the first place. For $\kappa = 1$ NN and NNN repressive interactions are equally strong, while for large κ values NN repression is much weaker than NNN repression. In the "uncoupled limit" $\kappa \to \infty$ the two bistable pairs coexist without sensing each other. We do not consider cases with $\kappa < 1$.

Dimerization

We set the dimerization forward rate $k_{\mathrm{on}}^{\mathrm{D}}$ to be equal to two times the diffusion-limited repressor binding rate, which is accounting for the fact that both reaction partners are diffusing. The dimerization backward rate is set via $k_{\mathrm{off}}^{\mathrm{D}} = k_{\mathrm{on}}^{\mathrm{D}}/V_{\mathrm{N}}$ (V_{N} = nuclear volume) as in [129, 130, 60, 170] to ensure that at any moment most of the proteins are dimerized.

Production and degradation

In our model both monomers and dimers are degraded. This leads to a nontrivial dependence of the total copy number on production, degradation and (de)dimerization rates, as we discuss with more detail in [170]. Since we did not find any experimental reports of gap protein lifetimes, we chose equal monomeric (μ_{M}) and equal dimeric degradation rate (μ_{D}) for all gap genes and set these quantities to values that lead to a reasonable effective lifetime of the gap proteins of $t_{\mathrm{eff}} \simeq 100$ s. The steady-state copy number is tuned via the production rate β. By default, we consider copy numbers as low as possible ($\simeq 15$) to minimize computational effort. The effect of increasing the average copy number is discussed in the "Discussion" section.

Geometry and internuclear transport

The choice of our geometric parameters, in particular of the lattice constant, is inspired by experimental measurements by Gregor et al. [51]. Information on the diffusion constants of proteins involved in early Drosophila patterning is scarce. The diffusion constant of the morphogen Bcd has been measured by several groups, yet its true value is still under debate [30, 167]. In our model we therefore set for all gap proteins an effective internuclear diffusion constant $D = 1\ \mu\mathrm{m}^2/\mathrm{s}$, which comprises both protein import/export and actual diffusion. This value is a reasonable cytoplasmic diffusion coefficient and well within the bounds reported for Bcd.

The simulated lattice is 40 nuclei long so that the total system length L roughly corresponds to the posterior 2/3 of the embryo in cycle 14. To reduce computation effort we simulate a system with smaller circumference (8 nuclei) as compared to the living embryo. This is justified by the fact that for our standard diffusion constant D and effective protein lifetime μ_{eff} the diffusive correlation length $l_{\mathrm{corr}} = \sqrt{D/\mu_{\mathrm{eff}}}$ is ≤ 2 nuclei. A larger circumference therefore is not expected to introduce new features into the system, but might alter the timescales of expression boundary movement and domain desintegration. We discuss the effect of reduced system size on measured stability times in the "Discussion" section.

For the specific numerical values of our parameters see the summary in Table S6.1.

6.4.4 Data analysis

Quantification of pattern stability

To analyse the destruction dynamics we produce two different 2D-histograms of the simulated trajectories: one histogram over the space spanned by the progress coordinate λ and the simulation time t and one over the reduced phase space spanned by the two components of the progress coordinate λ_x and λ_y. Trajectories are binned with the statistical weight assigned by NS-FFS, and in the end the histograms are normalized.

In the (λ_x, λ_y) phase space we can clearly identify several distinct regions that accumulate probability. Based on the most stable case we define rectangular boundaries that enclose the regions that correspond to different destruction states of the pattern:

- the metastable main basin of intact / undestroyed patterns: $R_S \equiv \{(\lambda_x, \lambda_y) | \lambda_x \leq 0.45 \wedge \lambda_y \leq 0.43\}$
- the basin in which either the Hb or Kni domain has vanished: $R_{HK} \equiv \{(\lambda_x, \lambda_y) | \lambda_x > 0.45 \wedge \lambda_y \leq 0.43\}$
- the basin in which either the Kr or Gt domain has vanished: $R_{KG} \equiv \{(\lambda_x, \lambda_y) | \lambda_x \leq 0.45 \wedge \lambda_y > 0.43\}$
- the destroyed end states basin in which either Hb or Kni and one of Kr or Gt have vanished: $R_D \equiv \{(\lambda_x, \lambda_y) | \lambda_x > 0.45 \wedge \lambda_y > 0.43\}$

Note that the location of the regions slightly changes for different values of κ. We found that the above boundary definitions constitute a good compromise. For each basin we compute the fraction of total probability as a function of time by integrating the weights of trajectories that are within the basin at time t. We define the survival probability of the pattern to be the integrated probability in R_S at time t after initialization: $S(t) = \iint_{R_S} p(t) d\lambda_x d\lambda_y$. As expected, $S(t)$ displays roughly exponential decay behavior after a certain lag phase that can be attributed to initial relaxation. To obtain the destruction rate of the pattern k_D we fit a function $f(x) \equiv \exp(-k_D(t - t_{lag}))$ to $S(t)$. This only yields satisfactory results if the fitting range is adapted accordingly, i.e. only $S(t)$ values for $t > t_{lag}$ are taken into account. Since t_{lag} itself is a fitting parameter we adopted the following protocol: Starting from a value of t_{start} that is clearly in the relaxation regime we perform the fit on the interval $[t_{start}, t_{end}]$ where t_{end} is the largest time recorded. We then choose the fitted values k_D and t_{lag} for which $|t_{lag} - t_{start}|$ is minimal. From this we compute the pattern stability time (average time until pattern destruction) via $\tau_D \equiv 1/k_D$. In most considered cases the patterns are very stable, i.e. k_D very small, and we can expand $S(t) \simeq 1 - k_D(t - t_{lag})$. As a control, we therefore also fitted $g(t) \equiv k_D(t - t_{lag})$ to $1 - S(t)$ for a fixed t_{lag} clearly in the exponential regime and obtained almost identical results.

Computation of average probability fluxes

To quantify which destruction pathways are dominant we computed the average fluxes J_{avg} into the regions of (partly) destroyed patterns. Here the average flux is defined as the average rate of increase in time of the fractional probability in the region and obtained by fitting a linear function $h(t) \equiv J_{\mathrm{avg}} t + P_0$ to $P_{\mathrm{R}}(t) \equiv \iint_{\mathrm{R}} p(t) d\lambda_{\mathrm{x}} d\lambda_{\mathrm{y}}$ for $R \in \{R_{\mathrm{HK}}, R_{\mathrm{KG}}, R_{\mathrm{D}}\}$ over the interval $[t_{\mathrm{start}}, t_{\mathrm{end}}]$ with t_{start} chosen such that $\partial_{\mathrm{t}} P_{\mathrm{R}}(t) \neq 0$ for $t > t_{\mathrm{start}}$. P_0 depends on the particular choice of t_{start} and is discarded.

Computation of average flux velocities

The average local drift velocity and diffusion constant of the trajectories in the $(\lambda_{\mathrm{x}}, \lambda_{\mathrm{y}})$ phase space are computed by averaging displacements $\Delta\lambda_{\mathrm{x(y)}} \equiv \lambda_{\mathrm{x(y)}}(t+\Delta t) - \lambda_{\mathrm{x(y)}}(t)$ and squared displacements $\Delta\lambda^2 \equiv \Delta\lambda_{\mathrm{x}}^2 + \Delta\lambda_{\mathrm{y}}^2$ on a two-dimensional lattice of bins covering the whole phase space. Displacements $\Delta\lambda_{\mathrm{x(y)}}$ are assigned to the bin at $\vec{\lambda} \equiv (\lambda_{\mathrm{x}}, \lambda_{\mathrm{y}})$, i.e. we are averaging outgoing displacements and the averaged vector $\langle\vec{\Delta\lambda}\rangle(\vec{\lambda})$ therefore will represent the average velocity with which trajectories leave this bin. The local phase space diffusion constant is calculated as $D_\lambda(\vec{\lambda}) \equiv \frac{1}{4\Delta t}\left[\langle\Delta\lambda^2\rangle(\vec{\lambda}) - \left(\langle\Delta\lambda_{\mathrm{x}}\rangle^2(\vec{\lambda}) + \langle\Delta\lambda_{\mathrm{x}}\rangle^2(\vec{\lambda})\right)\right]$. This is done in the same way for other combinations of phase space coordinates. The diffusion-drift decomposition is explained in more detail in the appendix.

6.4.5 Perturbation experiments

Simulations starting from perturbed initial conditions were performed directly via the GGG simulator. First the systems were relaxed to representative states within the metastable basin for a simulated time of $t_{\mathrm{relax}} = 30$ min. The final states of these runs then were post-modified according to the following two protocols:

1. "Kni expansion": starting from mid-embryo the central Kni domain was expanded as follows: the configurations in the nuclei just posterior to mid-embryo were copied and used to overwrite configurations in the subsequent Δ rows in the axial (z-) direction of the cylinder. The original configurations were stored and for each nucleus at row $z_{\mathrm{i}} > N_{\mathrm{z}}/2 + \Delta$ (counting from the anterior) the configuration was overwritten by the original configuration at $z_{\mathrm{i}} - \Delta$. The posterior-most nucleus was exempted from overwriting to preserve pinning.

2. "Hb expansion": here the anterior Hb domain was enlarged at the expense of Kni. To this purpose we applied the same copy-paste procedure as above starting form $z_{\mathrm{i}} = 5$, however only nuclei up to mid-embryo ($z_{\mathrm{i}} \leq N_{\mathrm{z}}/2$) were overwritten by the original configurations at $z_{\mathrm{i}} - \Delta$.

Δ quantifies the severity of perturbation. We found that $\Delta < 4$ results in changes to the pattern that were hard to distinguish from noise, while for $\Delta > 12$ perturbations were large enough to induce immediate pattern destruction with high probability. We therefore limited systematic tests to pertubations with $\Delta \in \{4, 8, 12\}$. Starting

from the perturbed initial conditions simulations were continued for $t_{\mathrm{sim}} = 20\ h$ and snapshots of the current configurations in all nuclei were written out with an acquisition interval of 10 min (simulated time). 10 samples starting from 10 different perturbed initial conditions were produced for each set of parameters.

In order to overcome the difficulties of boundary detection we quantified the motion of gap protein domains by tracking their center of mass (CoM) along the z-axis of the cylinder. For each gap gene G we define the CoM z_{G} as

$$z_{\mathrm{G}} \equiv \frac{\int_{\mathrm{z}} \int_{\mathrm{r}} z G_{\mathrm{tot}}(r,z) dr dz}{\int_{\mathrm{z}} \int_{\mathrm{r}} G_{\mathrm{tot}}(r,z) dr dz} \tag{6.7}$$

where $G_{\mathrm{tot}} = [G] + 2[G_2]$ is the total copy number. Since our system features two Hb domains we calculate z_{Hb} separately for the anterior ($\mathrm{Hb_A}$) and the posterior ($\mathrm{Hb_P}$) part of the embryo by restricting z-integration adequately. While the CoM remains unchanged upon symmetric changes of the domain boundaries or global copy number increase, it is well-suited to indicate relaxations from the asymmetric perturbations that we apply. To find general trends in the time-evolution of the domains CoM trajectories were averaged over the 10 samples.

6.5 Acknowledgements

This chapter is based on the forthcoming publication:

Sokolowski T. R., ten Wolde P. R. and Becker N. B. (2013) The Stability of Gap Gene Patterns without Morphogen Gradients.
Under review.

The author thanks N. TABERNER and A. HOFFMANN for critical reading.

6.A Appendix: Supplementary Information

6.A.1 Estimation of phase space diffusion coefficient from overdamped Langevin dynamics

Let $f(X,Y,t)$ be a twice differentiable real function depending on a two-dimensional diffusion-drift processes $\vec{X} = (X,Y)$ and time t (explicitly). In the overdamped LANGEVIN limit, i.e. assuming that the displacements of the random walker are goverened only by forces that stem from an underlying force field and by Gaussian noise, and that its accelerations and inertia are negligible, we can describe this random processes via

$$d\vec{X} = \vec{v}dt + \sigma d\vec{W} \tag{S6.1}$$

where $\vec{W}$ is a (two-dimensional) WIENER processes and $\vec{v} = (v_{\mathrm{X}}, v_{\mathrm{Y}})$ a (local) drift velocity resulting from the potential forces. Then we may calculate the differential of f with ITŌ's Lemma (employing TAYLOR expansion) as follows:

$$\begin{aligned} df(X,Y,t) = \sigma\frac{\partial f}{\partial X}dW_{\mathrm{X}} + \sigma\frac{\partial f}{\partial Y}dW_{\mathrm{Y}} \\ + \left[\frac{\partial f}{\partial t} + v_{\mathrm{X}}\frac{\partial f}{\partial X} + v_{\mathrm{Y}}\frac{\partial f}{\partial Y} + \frac{\sigma^2}{2}\frac{\partial^2 f}{\partial X^2} + \frac{\sigma^2}{2}\frac{\partial^2 f}{\partial Y^2} + \zeta\sigma^2\frac{\partial^2 f}{\partial X \partial Y}\right]dt \end{aligned} \tag{S6.2}$$

Here ζ measures the correlation between X and Y.

In order to apply this general formula to the specific diffusion-drift problem for the phase space coordinates $(\lambda_{\mathrm{x}}, \lambda_{\mathrm{y}})$ we set $X = \lambda_{\mathrm{x}}, Y = \lambda_{\mathrm{y}}$ and $f(X,Y,t) = f(\lambda_{\mathrm{x}}, \lambda_{\mathrm{y}}) = (\lambda_{\mathrm{x}} - \lambda_{\mathrm{x}_0})^2 + (\lambda_{\mathrm{y}} - \lambda_{\mathrm{y}_0})^2 \equiv \Delta\lambda^2$ (the squared displacement function).

Itō's Lemma now reads (note that the time and mixed derivatives vanish):

$$\begin{aligned} d(\Delta\lambda^2) &= d\left[(\Delta\lambda_{\mathrm{x}})^2 + (\Delta\lambda_{\mathrm{y}})^2\right] = d\left[(\lambda_{\mathrm{x}} - \lambda_{\mathrm{x}_0})^2 + (\lambda_{\mathrm{y}} - \lambda_{\mathrm{y}_0})^2\right] \\ &\simeq 2(\lambda_{\mathrm{x}} - \lambda_{\mathrm{x}_0})(v_{\lambda_{\mathrm{x}}}dt + \sigma dW_{\mathrm{x}}) + 2(\lambda_{\mathrm{y}} - \lambda_{\mathrm{y}_0})(v_{\lambda_{\mathrm{y}}}dt + \sigma dW_{\mathrm{y}}) \\ &\quad + \frac{\sigma^2}{2}2dt + \frac{\sigma^2}{2}2dt \end{aligned} \tag{S6.3}$$

To relate the above formula to the displacements sampled in our simulations with a fixed acquisition time interval Δt we shall integrate the infinitesimal contributions over this interval. At the same time we take the ensemble average to account for the averaging of independent samples, which causes the Gaussian terms σdW_{x} and σdW_{y} to vanish. We further assume that, to a good approximation, the drift velocities and diffusion coefficients are constant over the time interval Δt and diffusion isotropic in

λ_x and λ_y direction, i.e. $D_{\lambda_x} = D_{\lambda_y} = D_\lambda(\vec{\lambda})$. Finally, using $\sigma = \sqrt{2D_\lambda}$, we obtain:

$$\begin{aligned}
\left\langle \Delta\lambda^2 \right\rangle &= \left\langle \int_{\Delta t} d(\Delta\lambda^2) \right\rangle \\
&= \left\langle \int_0^{\Delta t} 2 \underbrace{\left[\lambda_x(t) - \lambda_x(0)\right]}_{\simeq \langle v_{\lambda_x} \rangle t} \underbrace{v_{\lambda_x}}_{\simeq \langle v_{\lambda_x} \rangle} dt \right\rangle + \left\langle \int_0^{\Delta t} 2 \underbrace{\left[\lambda_y(t) - \lambda_y(0)\right]}_{\simeq \langle v_{\lambda_y} \rangle t} \underbrace{v_{\lambda_y}}_{\simeq \langle v_{\lambda_y} \rangle} dt \right\rangle \\
&\quad + \left\langle \int_0^{\Delta t} 4 D_\lambda dt \right\rangle + \int_{\Delta t} \underbrace{\langle 2\Delta\lambda_x \sigma dW_x \rangle}_{0} + \int_{\Delta t} \underbrace{\langle 2\Delta\lambda_y \sigma dW_y \rangle}_{0} \\
&\simeq \left\langle \langle v_{\lambda_x} \rangle^2 \int_0^{\Delta t} 2t dt \right\rangle + \left\langle \langle v_{\lambda_y} \rangle^2 \int_0^{\Delta t} 2t dt \right\rangle + 4 \langle D_\lambda \rangle \Delta t \\
&\simeq \langle v_{\lambda_x} \Delta t \rangle^2 + \langle v_{\lambda_y} \Delta t \rangle^2 + 4 \langle D_\lambda \rangle \Delta t \\
&= \langle \Delta\lambda_x \rangle^2 + \langle \Delta\lambda_y \rangle^2 + 4 \langle D_\lambda \rangle \Delta t
\end{aligned} \tag{S6.4}$$

The final result shows that, knowing the average displacements $\langle \Delta\lambda_x \rangle$ and $\langle \Delta\lambda_x \rangle$ and average squared displacements $\langle \Delta\lambda^2 \rangle$ at $\vec{\lambda}$, we can compute the average diffusion coefficient $\langle D_\lambda \rangle (\vec{\lambda})$ via:

$$\langle D_\lambda \rangle (\vec{\lambda}) = \frac{1}{4\Delta t} \left[\langle \Delta\lambda^2 \rangle (\vec{\lambda}) - \left(\langle \Delta\lambda_x \rangle^2 (\vec{\lambda}) + \langle \Delta\lambda_y \rangle^2 (\vec{\lambda}) \right) \right] = \frac{1}{4\Delta t} \mathcal{V}_{\langle \lambda \rangle} (\vec{\lambda}) \tag{S6.5}$$

The bracket term containing the first moments corrects the mean squared displacement for the contributions coming from the deterministic drift and tends to zero as the process becomes purely diffusive.

6.A.2 Supplementary velocity field figures

Figures S6.2, S6.3, S6.4 and S6.5 show phase space velocity fields and trajectories starting from perturbed initial conditions for three different projections of the reaction coordinates, for the following cases:

- for the repression strength ratio $\kappa \simeq 31.6$ that optimizes pattern stability with pinning (Fig. S6.2)
- for weaker NN repression strength ($\kappa = 1000$) with pinning (Fig. S6.3)
- for the optimal repression strength ratio $\kappa = 100$ that optimizes pattern stability without pinning (Fig. S6.4)
- for weaker NN repression strength ($\kappa = 1000$) without pinning (Fig. S6.5)

A

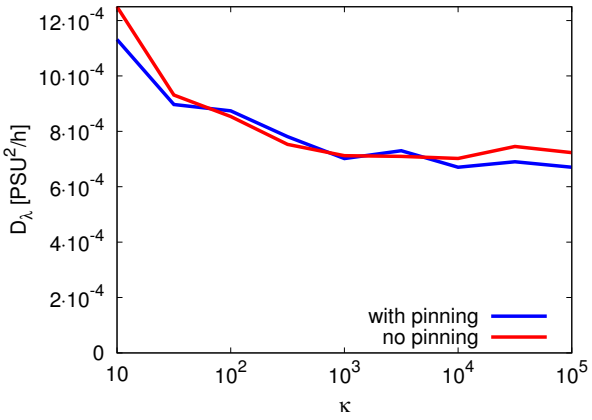

B

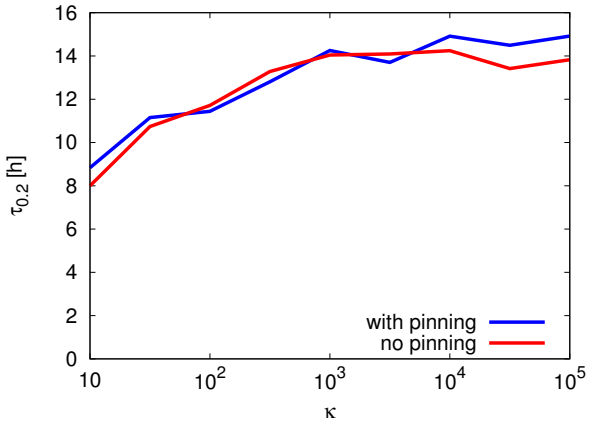

Figure S6.1: Average phase space diffusion coefficients as a function of κ. (A) shows the diffusion coefficient of phase space trajectories in the (λ_x, λ_y) space, as obtained from the overdamped LANGEVIN analysis described in section 6.A.1, averaged over the phase space region $R_P = [0.3, 0.4]^2$ (which is clearly part of the "diffusive plateau"), for different repression strength ratios κ (PSU = phase space units). In (B) we plot resulting approximate diffusion times from the phase space region of intact relaxed patterns, towards the edge of the diffusive plateau (from which trajectories are quickly absorbed into the regions of destroyed pattern states) as a function of κ, assuming a distance of 0.2 PSU for the initial phase space distance to the edge.

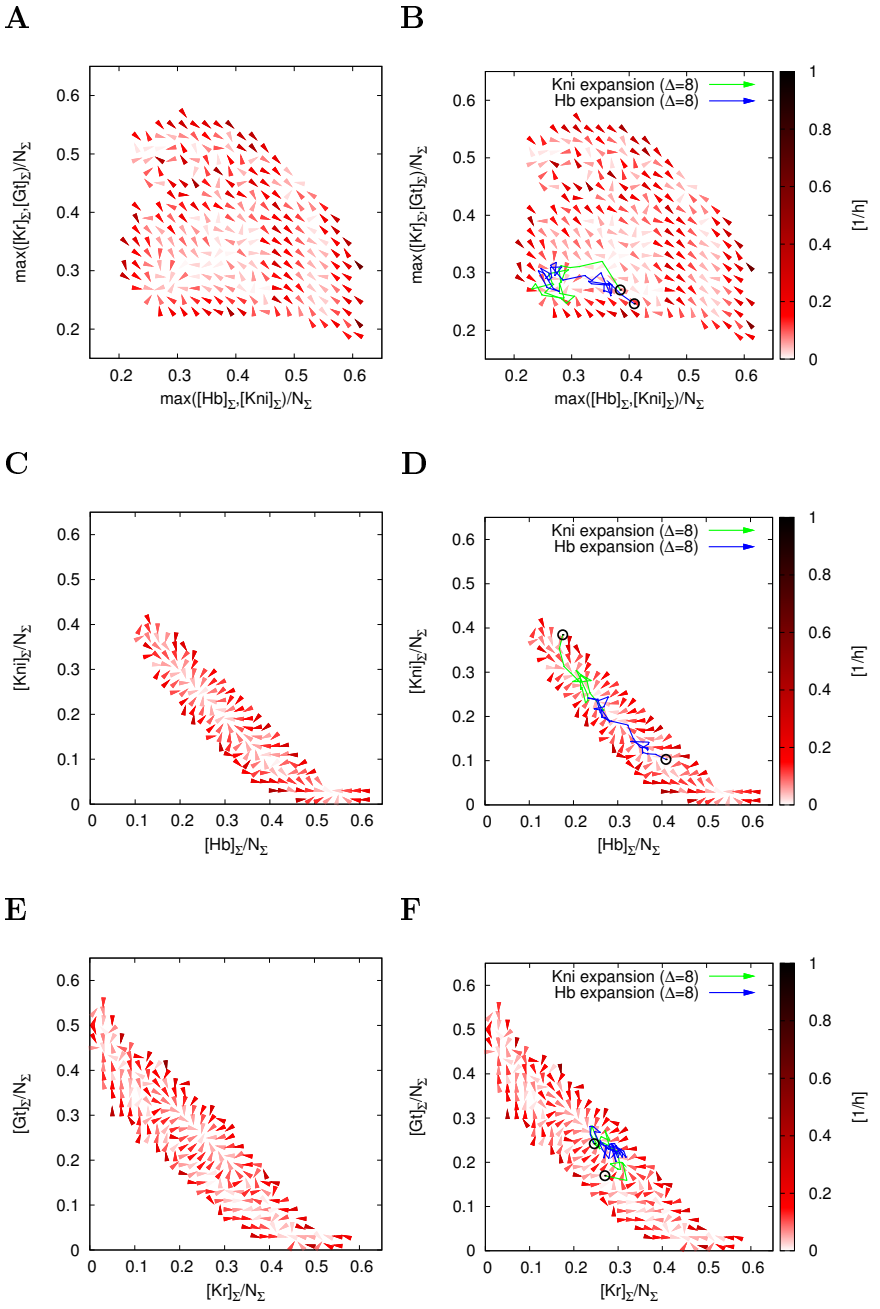

Figure S6.2: Average phase space velocities for the maximally stable system ($\kappa \simeq 31.6$) with pinning. Left plots (A, C, E) show local average phase space velocities, right plots (B, D, F) additionally show example trajectories for the two types of perturbations considered in the restoration experiments. Starting points are marked by black bullets.

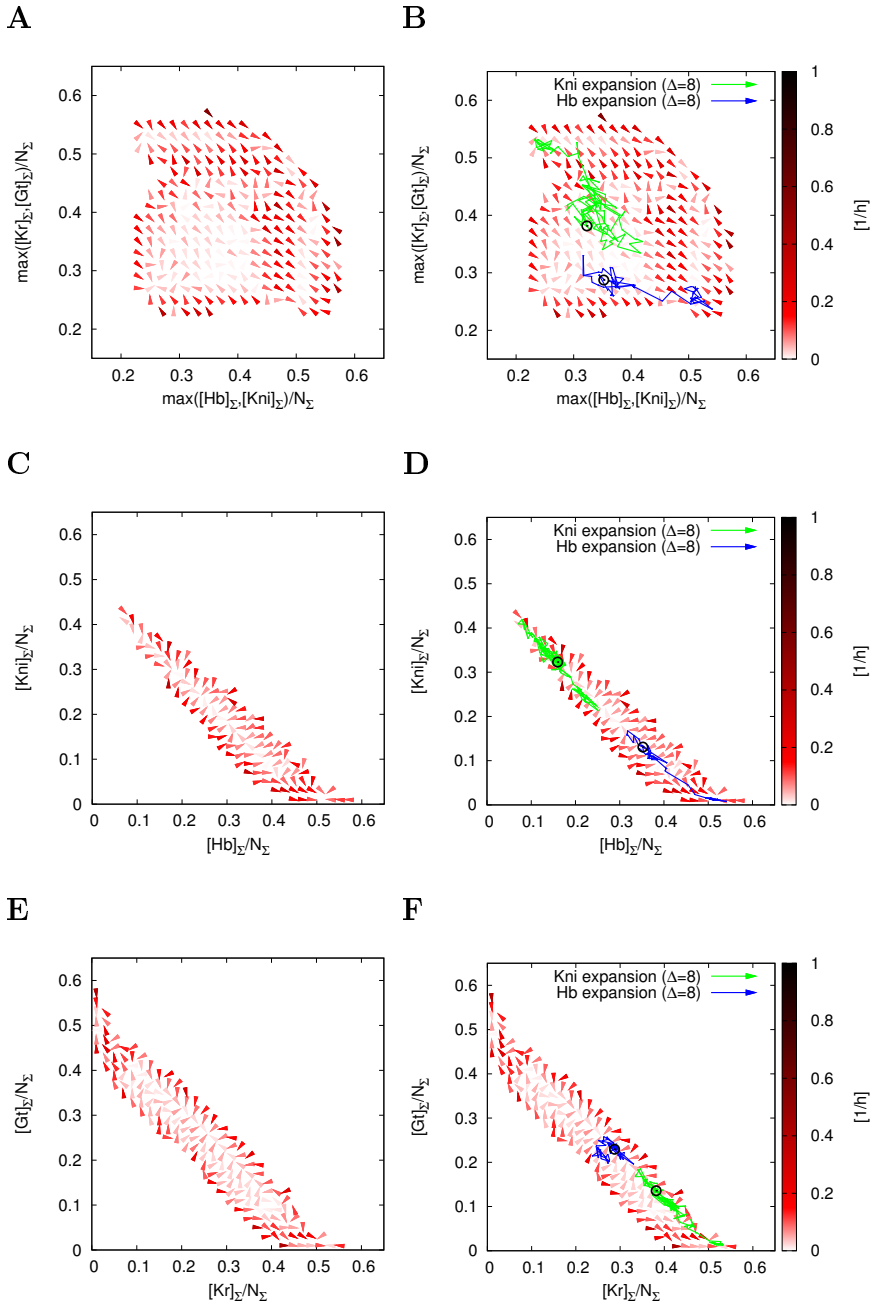

Figure S6.3: Average phase space velocities for weaker NN interaction ($\kappa = 1000$) in the system with pinning. Left plots (A, C, E) show local average phase space velocities, right plots (B, D, F) additionally show example trajectories for the two types of perturbations considered in the restoration experiments. Starting points are marked by black bullets.

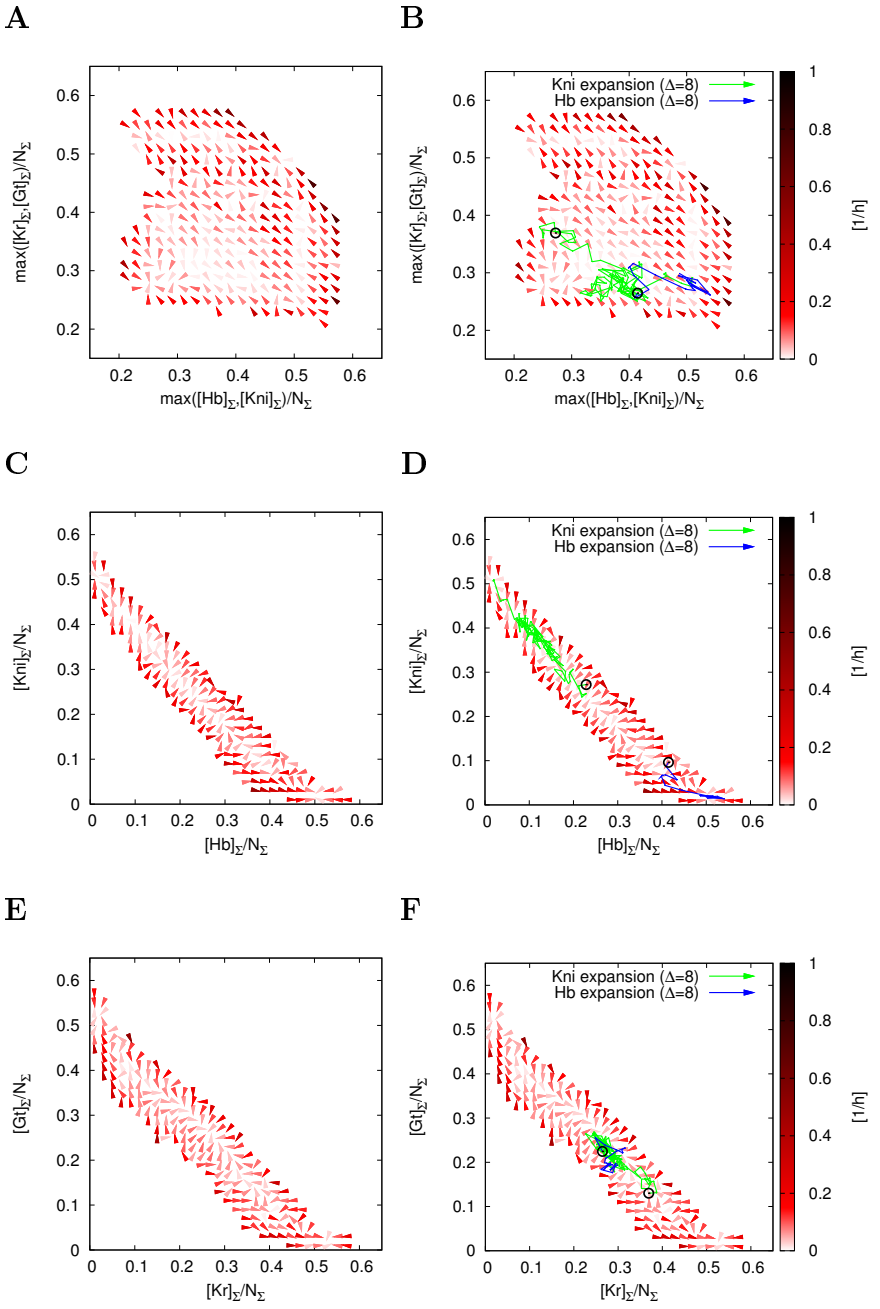

Figure S6.4: Average phase space velocities for the maximally stable system ($\kappa = 100$) without pinning. Left plots (A, C, E) show local average phase space velocities, right plots (B, D, F) additionally show example trajectories for the two types of perturbations considered in the restoration experiments. Starting points are marked by black bullets.

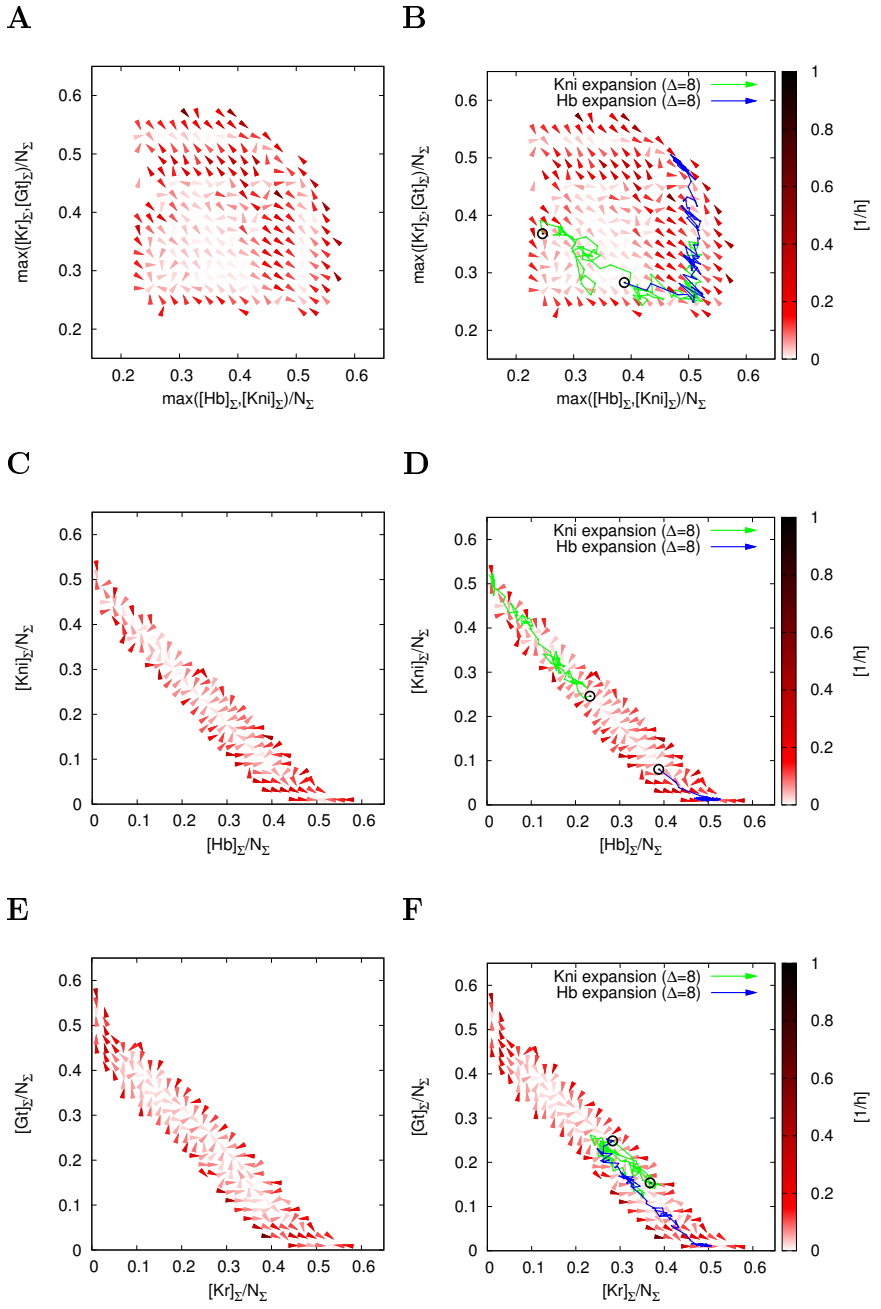

Figure S6.5: Average phase space velocities for weaker NN interaction ($\kappa = 1000$) in the system without pinning. Left plots (A, C, E) show local average phase space velocities, right plots (B, D, F) additionally show example trajectories for the two types of perturbations considered in the restoration experiments. Starting points are marked by black bullets.

6.A.3 Stability analysis of a mutually repressing four gene system

In order to elucidate the reason for the stabilization of an interface of two strongly antagonistic gene expression domains in the presence of further, weak interaction partners we conducted a linear stability analysis on a deterministic ODE system in steady state, which mimics the situation in a typical interface nucleus in our full-scale system. To model the particular situation in such a nucleus more accurately we introduce flux terms into the ODEs, which–in an approximative fashion–take into account the diffusive exchange of particles with neighboring nuclei.

We analysed the following set of 8 equations that describe the production, degradation and (de)dimerization of four mutually repressing genes A, B, C and D:

$$\partial_t A_1 = \frac{\beta}{(1+B_2/K_\mathrm{s})(1+C_2/K_\mathrm{w})(1+D_2/K_\mathrm{w})} - \mu_\mathrm{M} A_1 - k^\mathrm{D}_\mathrm{on} A_1^2 + k^\mathrm{D}_\mathrm{off} A_2 = 0$$

$$\partial_t A_2 = k^\mathrm{D}_\mathrm{on} A^2 - (k^\mathrm{D}_\mathrm{off} + \mu_\mathrm{D}) A_2 + j_{\mathrm{A}_2} = 0$$

$$\partial_t B_1 = \frac{\beta}{(1+A_2/K_\mathrm{s})(1+C_2/K_\mathrm{w})(1+D_2/K_\mathrm{w})} - \mu_\mathrm{M} B_1 - k^\mathrm{D}_\mathrm{on} B_1^2 + k^\mathrm{D}_\mathrm{off} B_2 = 0$$

$$\partial_t B_2 = k^\mathrm{D}_\mathrm{on} B^2 - (k^\mathrm{D}_\mathrm{off} + \mu_\mathrm{D}) B_2 + j_{\mathrm{B}_2} = 0$$

$$\partial_t C_1 = \frac{\beta}{(1+D_2/K_\mathrm{s})(1+A_2/K_\mathrm{w})(1+B_2/K_\mathrm{w})} - \mu_\mathrm{M} C_1 - k^\mathrm{D}_\mathrm{on} C_1^2 + k^\mathrm{D}_\mathrm{off} C_2 = 0$$

$$\partial_t C_2 = k^\mathrm{D}_\mathrm{on} C^2 - (k^\mathrm{D}_\mathrm{off} + \mu_\mathrm{D}) C_2 + j_{\mathrm{C}_2} = 0$$

$$\partial_t D_1 = \frac{\beta}{(1+C_2/K_\mathrm{s})(1+A_2/K_\mathrm{w})(1+B_2/K_\mathrm{w})} - \mu_\mathrm{M} D_1 - k^\mathrm{D}_\mathrm{on} D_1^2 + k^\mathrm{D}_\mathrm{off} D_2 = 0$$

$$\partial_t D_2 = k^\mathrm{D}_\mathrm{on} D^2 - (k^\mathrm{D}_\mathrm{off} + \mu_\mathrm{D}) D_2 + j_{\mathrm{D}_2} = 0 \tag{S6.6}$$

Here capital letters X_1 denote monomer numbers, while capital letters with index X_2 describe dimer numbers; the total copy number is defined as $X = X_1 + 2X_2$. The (monomer) production rate β, the monomeric and dimeric degradation rates μ_M and μ_D and the dimerization forward and backward rates k^D_on and $k^\mathrm{D}_\mathrm{off}$ are equal for all four species, in correspondence to our full-scale model. The four genes thus have identical properties, except for the strength by which a gene is repressed by the other genes, which is tuned via two repression threshold parameters (dissociation constants) K_s

and K_w. Here K_s stands for strong, K_w for weaker mutual repression, i.e. $K_s < K_w$. The ratio $\kappa = K_w/K_s$ corresponds to the repression strength ratio parameter κ in the main text. For each gene X the term j_{X_2} represents an effective dimeric flux into or out of the considered nucleus due to dimer exchange with neighboring nuclei. To facilitate calculations we assume that in steady state these fluxes are constant; flux magnitudes are estimated from our spatially resolved simulations, as explained further below. As a further simplification we neglect the monomeric fluxes. This is justified by the fact that in our model the monomer degradation rate is one order of magnitude higher than the dimer degradation rate, translating into a significantly shorter diffusion length for the monomers.

The analysis was performed by numerically solving the above steady-state equations for fixed point solutions. Stability was determined by calculating the eigenvalues of the corresponding Jacobian at the fixed point to discriminate between stable (all eigenvalues with negative real part), unstable (at least one eigenvalue with positive real part) and oscillatory solutions. All parameter values were chosen in correspondence to the full scale model (see Table S6.1), while κ was varied via K_w as in the simulations.

We first analysed the system without dimeric fluxes, i.e. $j_{X_2} = 0$ for $X \in \{A, B, C, D\}$. Figure S6.6 shows 3D plots of two different 2D projections of the four-dimensional fixed point solutions for the total copy numbers (A, B, C, D) as a function of κ, the ratio between weak and strong repression threshold. Here we employ the fact that, due to the repeating interaction symmetry, the change of 4D attractor locations with κ can be understood by looking at the change of attractor locations in the 2D spaces spanned by the components of two strongly and two weakly repressing species, respectively. In Figure S6.7A-D we additionally plot 1D projections of the four single components, which, in this case, are identical. The plots reveal two principal fixed point regimes: A "monostable regime" in which only one of four genes can attain high expression levels for low κ and a "coexistence regime" of two bistable pairs in which each state of one bistable pair can coexist with each state of the other bistable pair. The two regimes are separated by a bifurcation that occurs around $\kappa \simeq \kappa_{bif}$. Note that when A is high on the weak partners branch (blue) in Fig. S6.6 (and its weak partner C therefore low) within the monostable regime ($\kappa \lesssim \kappa_{bif}$), the corresponding points on the strong partners branch (red) are the ones in the low-expression regime close to zero, and vice versa. Interestingly, at $\kappa = 1$ we find an additional stable fixed point at which all four genes have very low expression levels ($A = B = C = D \simeq 1$), meaning that when all genes suppress each other equally strongly one possible outcome is that none of them can reach significant expresssion levels. Taken together this demostrates that for $\kappa \lesssim \kappa_{bif}$ solutions in which two genes are expressed at significant levels are unstable. Given a certain minimal domain size required in a system with finite repressor diffusion length this implies instability of the whole partly overlapping five-stripe pattern and thus provides an explanation for fast pattern destruction in the strong coupling regime.

As a second step we repeated the stability analysis with nonzero dimer fluxes, in order to mimic the situation in a nucleus at the Hb-Kni expression boundaries interface. To this end we imposed a dimer influx for the two strong antagonists A and B and a dimer outflux for C, which is a weak partner of both A and B, with

flux magnitudes approximately equal to average fluxes estimated on the base of time- and circumference-averaged stationary profiles from simulations of the system with pinning at optimal κ. These fluxes were estimated by first finding the nuclear row N_{i} at the Hb – Kni interface, computing the stationary copy number gradients ΔN_- and ΔN_+ with respect to the preceding and subsequent rows via finite differences and then multiplying their difference with the diffusive hopping rate, i.e.:

$$j_{\mathrm{est}} \equiv (\Delta N_+ - \Delta N_-)\frac{4D}{l^2} \tag{S6.7}$$

where l is the (constant) distance between nuclei.

Figure S6.7E-H demonstrates that imposing dimeric fluxes as described has a dramatic effect on the fixed point solutions of the system. Here we could not find any physically meaningful stable fixed points for $\kappa \lesssim 12$. For higher values of κ we find that there is only one stable solution: Maybe contrary to expectation, an influx of A and B dimers results in a significant reduction of the expression levels of these genes, while gene C, in spite of the assumed outflux, reaches high expression levels. Consequently, production of D is strongly suppressed. The total copy numbers at the fixed points are in good agreement with typical copy numbers at the interface between strongly repressing gene domains in our simulations.

In summary, our analysis predicts that when all genes repress each other with close to equal strength ($\kappa \lesssim \kappa_{\mathrm{bif}}$) patterns with overlapping gap gene domains are intrinsically unstable. It further indicates that a small net influx of two strongly repressing partners A and B and outflux of one of their weak interaction partners C may result in the counterintuitive effect that the expression level of A and B will be significantly reduced while C is stabilized at higher levels.

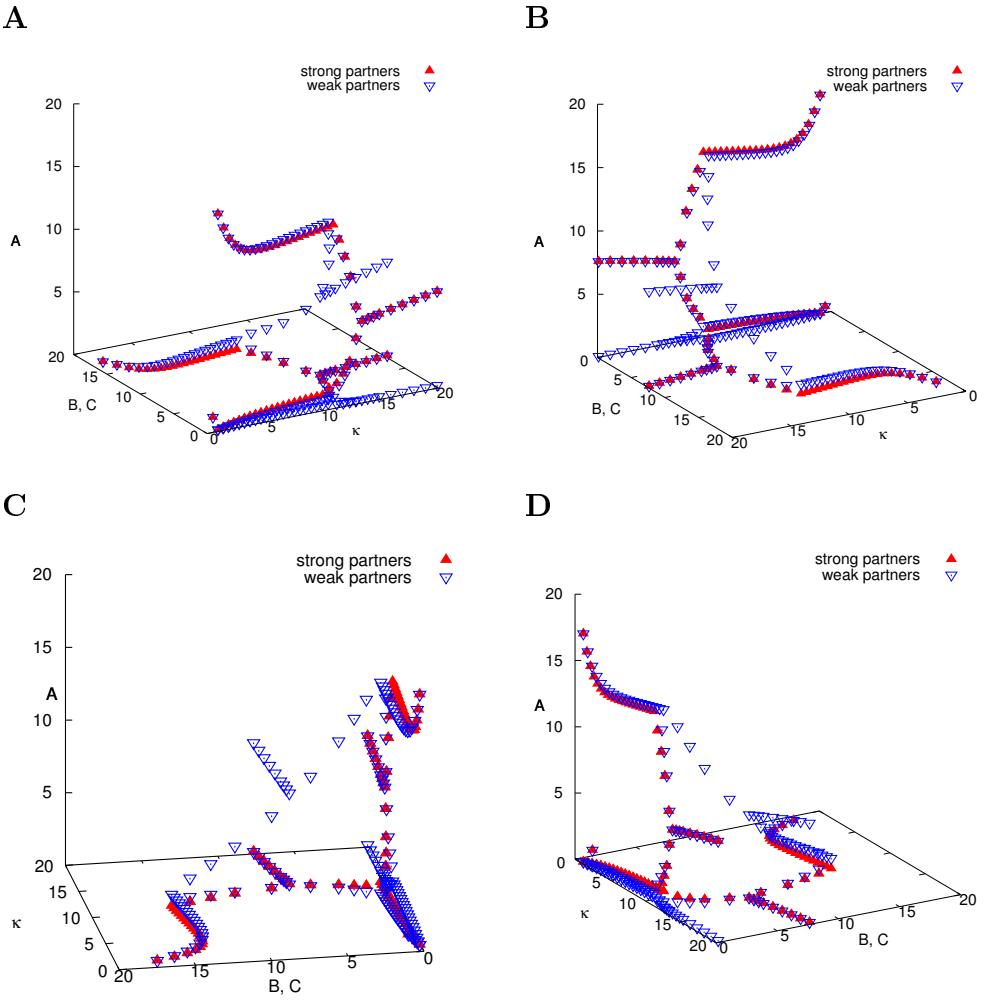

Figure S6.6: Steady state stability analysis with zero dimer fluxes. Shown are 2D projections of stable fixed point solutions (A, B, C, D) for the total copy numbers (monomers + dimers) of the considered mutually repressing four-gene system as a function of κ, the ratio between weak and strong repression thresholds. Each plot contains data for two different projections: (A, B), i.e. strong interaction partners (red triangles), and (A, C), i.e. weak interaction partners (blue triangles). Note that for the analysed system projections (A, B) and (C, D) and projections (A, C), (A, D), (B, C) and (B, D) are identical for symmetry reasons. Panels A-D display the same data in different viewing perspective.

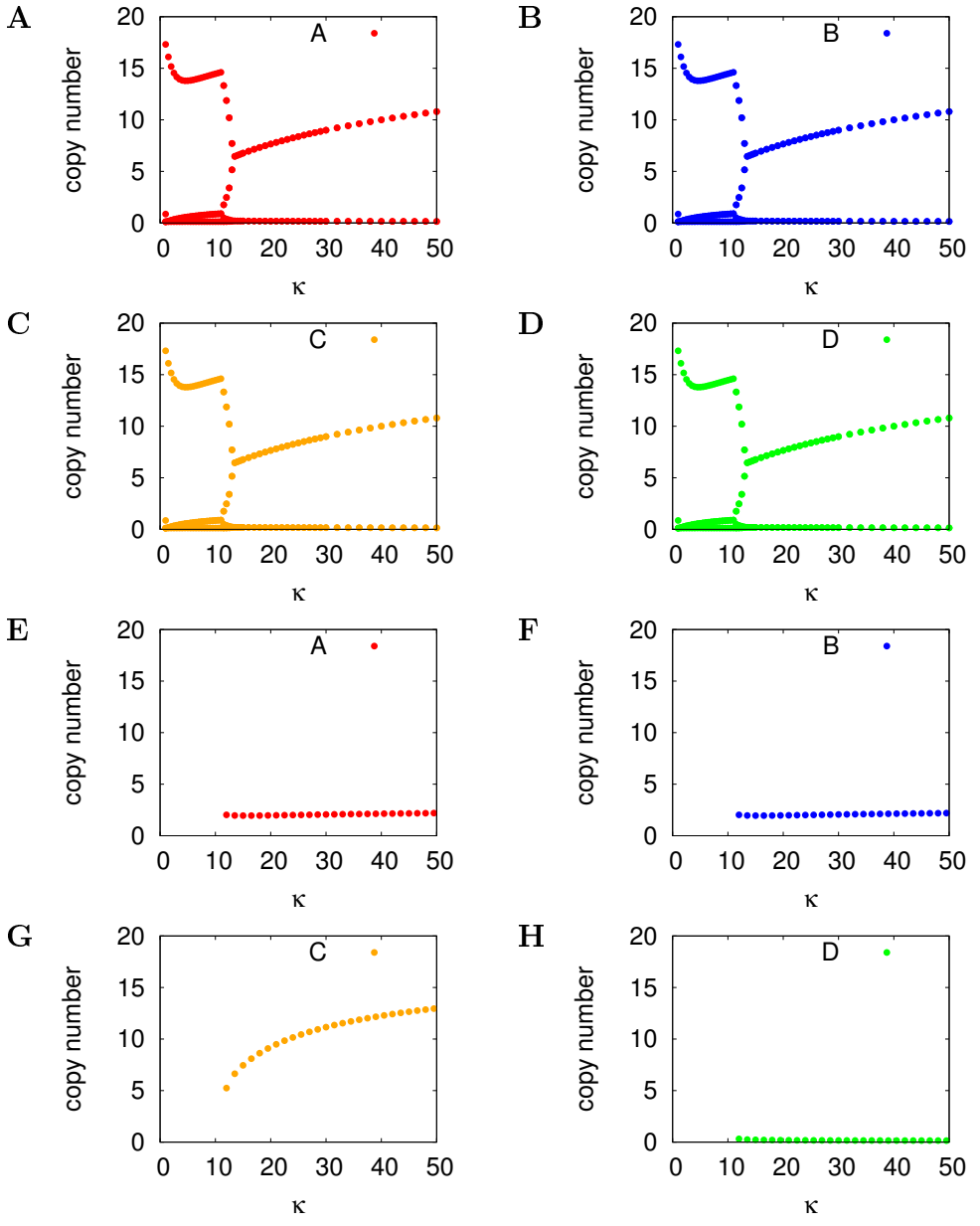

Figure S6.7: Steady state stability analysis with zero and nonzero dimer fluxes. Shown are the projected single components of stable fixed point solutions (A, B, C, D) for the total copy numbers (monomers + dimers) of the considered mutually repressing four-gene system as a function of κ, the ratio between weak and strong repressor off-rate, for the well-mixed system without dimer fluxes (A-D) and for the system with dimer fluxes (E-H), mimicking the situation at an interface nucleus in the simulations.

Quantity	Symbol	Value	Unit
Geometry			
Nuclear radius	r_{N}	2.5	μm
Nuclear volume	V_{N}	65.4	$\mu\mathrm{m}^3$
No. of nuclei in axial direction	N_{z}	40	
- resulting system length	L	340	μm
No. of nuclei in circumferential direction	N_{ϕ}	8	
Production / degradation			
Protein production rate	β	0.20	s^{-1}
Monomer degradation rate	μ_{M}	0.05	s^{-1}
Dimer degradation rate	μ_{D}	0.005	s^{-1}
- resulting effective degr. rate	μ_{eff}	0.0095	s^{-1}
Binding / unbinding			
Intranuclear diffusion const.	D_{N}	3.2	$\mu\mathrm{m}^2/s$
Repressor target site radius	σ_{R}	0.5	μm
- resulting (diff. ltd.) repressor on-rate	$k_{\mathrm{on}}^{\mathrm{R}}$	20.1	$\mu\mathrm{m}^3/s$
Standard (strong) repressor off-rate	$k_{\mathrm{off}}^{\mathrm{NNN}}$	0.06	s^{-1}
Weak repressor off-rate	$k_{\mathrm{off}}^{\mathrm{NN}}$	varied	$\geq k_{\mathrm{off}}^{\mathrm{R,s}}$
Monomer protein radius	σ_{M}	0.05	μm
- resulting (diff. ltd.) dimerization forward rate	$k_{\mathrm{on}}^{\mathrm{D}}$	4.0	$\mu\mathrm{m}^3/s$
Dimerization backward rate	$k_{\mathrm{off}}^{\mathrm{D}}$	0.062	$\mu\mathrm{m}^3/s$
Internuclear diffusion			
Standard internuclear diffusion const.	D	1.0	$\mu\mathrm{m}^2/s$
Internuclear lattice distance	l	8.5	μm

Table S6.1: The standard parameters of the simulated model of the posterior *Drosophila* embryo with four mutually repressing gap genes.

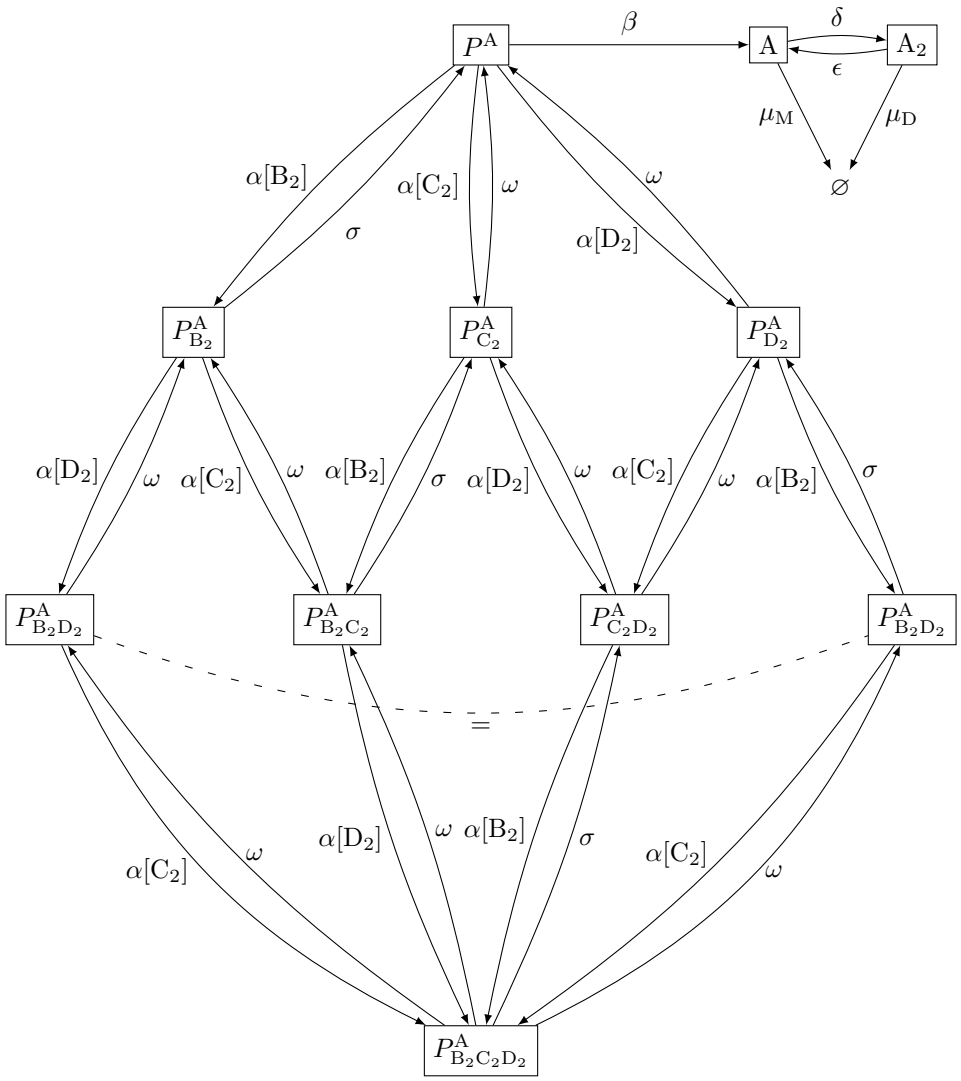

Figure S6.8: Reaction network. This schematic shows the set of reactions that affect production and degradation of a single gap gene species A. The strong repressor of A is denoted by B, the weak interaction partners by C and D. For each species, X denotes the monomer, X_2 the dimer. For easy readability here we abbreviate: $\alpha \equiv k^{\mathrm{R}}_{\mathrm{on}}$ = diffusion limited repressor binding rate; $\sigma \equiv k^{\mathrm{NNN}}_{\mathrm{off}}$ = next-nearest neighbor / strong repressor unbinding rate; $\omega \equiv k^{\mathrm{NN}}_{\mathrm{off}}$ = nearest-neighbor / weak repressor unbinding rate; $\delta \equiv k^{\mathrm{D}}_{\mathrm{on}}$ = dimerization forward rate; $\epsilon \equiv k^{\mathrm{D}}_{\mathrm{off}}$ = dimerization backward rate. In our model the shown set of reactions is defined for all combinations $(\mathrm{A},\mathrm{B},\mathrm{C},\mathrm{D}) \in \{(\mathrm{Hb},\mathrm{Kni},\mathrm{Kr},\mathrm{Gt}),(\mathrm{Kni},\mathrm{Hb},\mathrm{Kr},\mathrm{Gt}),(\mathrm{Kr},\mathrm{Gt},\mathrm{Hb},\mathrm{Kni}),(\mathrm{Gt},\mathrm{Kr},\mathrm{Hb},\mathrm{Kni})\}$.

References

[1] Avery OT, MacLeod CM, McCarty M (**1944**) Studies on the Chemical Nature of the Substance Inducing Transformation of Pneumococcal Types: Induction of Transformation by a Desoxyribonucleic Acid Fraction Isolated from Pneumococcus Type III. *J Exp Med* **79**:137–158.

[2] Watson JD, Crick FH (**1953**) A Structure for Deoxyribose Nucleic Acid. *Nature* **171**:737–738.

[3] Jacob F, Monod J (**1961**) Genetic regulatory mechanisms in the synthesis of proteins. *J Mol Biol* **3**:318–356.

[4] Hermsen R, Tans S, ten Wolde PR (**2006**) Transcriptional regulation by competing transcription factor modules. *PLoS Comput Biol* **2**:e164 1-9.

[5] Wadhams GH, Armitage JP (**2004**) Making sense of it all: bacterial chemotaxis. *Nat Rev Mol Cell Biol* **5**:1024–1037.

[6] Demir M, Salman H (**2012**) Bacterial Thermotaxis by Speed Modulation. *Biophys J* **103**:1683–1690.

[7] Gluch MF, Typke D, Baumeister W (**1995**) Motility and Thermotactic Responses of *Thermotoga maritima*. *J Bacteriol* **177**:5473–5479.

[8] Mehta P, Goyal S, Long T, Bassler BL, Wingreen NS (**2009**) Information processing and signal integration in bacterial quorum sensing. *Mol Syst Biol* **5**:325.

[9] Reading NC, Sperandio V (**2006**) Quorum sensing: the many languages of bacteria. *FEMS Microbiol Lett* **254**:1–11.

[10] Edery I (**2000**) Circadian rhythms in a nutshell. *Physiol Genomics* **3**:59–74.

[11] Gilbert SF (**2006**) Developmental Biology. Sinauer Associates, 8th edition.

[12] Jaeger J (**2011**) The gap gene network. *Cell Mol Life Sci* **68**:243–274.

[13] Davidson EH, Rast JP, Oliveri P, Ransick A, Calestani C, Yuh CH, Minokawa T, Amore G, Hinman V, Arenas-Mena C, Otim O, Brown CT, Livi CB, Lee PY, Revilla R, Rust AG, jun Pan Z, Schilstra MJ, Clarke PJC, Arnone MI, et al. (**2002**) A Genomic Regulatory Network for Development. *Science* **295**:1669–1678.

[14] McAdams HH, Arkin A (**1997**) Stochastic mechanisms in gene expression. *Proc Natl Acad Sci USA* **94**:814–819.

[15] Thattai M, van Oudenaarden A (**2001**) Intrinsic noise in gene regulatory networks. *Proc Natl Acad Sci USA* **98**:8614–8619.

[16] Elowitz MB, Levine AJ, Siggia ED, Swain PS (**2002**) Stochastic Gene Expression in a Single Cell. *Science* **297**:1183–1186.

[17] Ozbudak EM, Thattai M, Kurtser I, Grossman AD, van Oudenaarden A (**2002**) Regulation of noise in the expression of a single gene. *Nature Genetics* **31**:69–73.

[18] Schrödinger E (**1944**) What Is Life? : The Physical Aspect of the Living Cell. http://whatislife.stanford.edu/LoCo_files/What-is-Life.pdf.

[19] Turing AM (**1952**) *Phil Trans R Soc London B* **237**:37–72.

[20] Tostevin F, ten Wolde PR, Howard M (**2007**) Fundamental Limits to Position Determination by Concentration Gradients. *PLoS Comput Biol* **3**:e78.

[21] Walczak AM, Mugler A, Wiggins CH (**2009**) A stochastic spectral analysis of transcriptional regulatory cascades. *Proc Natl Acad Sci USA* **106**:6529–6534.

[22] Tkačik G, Gregor T, Bialek W (**2008**) The Role of Input Noise in Transcriptional Regulation. *PLoS ONE* **3**:e2774.

[23] Tkačik G, Walczak AM, Bialek W (**2009**) Optimizing information flow in small genetic networks. *Phys Rev E* **80**:031920.

[24] Walczak AM, Tkačik G, Bialek W (**2010**) Optimizing information flow in small genetic networks. II. Feed-forward interactions. *Phys Rev E* **81**:041905.

[25] Tkačik G, Walczak AM, Bialek W (**2012**) Optimizing information flow in small genetic networks. III. A self-interacting gene. *Phys Rev E* **85**:041903.

[26] Tostevin F, de Ronde W, ten Wolde PR (**2012**) Reliability of frequency- and amplitude-decoding in gene regulation. *Phys Rev Lett* **108**:108104 1-5.

[27] de Ronde W, Tostevin F, ten Wolde PR (**2011**) Multiplexing biochemical signals. *Phys Rev Lett* **107**:048101.

[28] Berg HC, Purcell EM (**1977**) Physics of chemoreception. *Biophys J* **20**:193–219.

[29] Grecco HE, Schmick M, Bastiaens PI (**2011**) Signaling from the Living Plasma Membrane. *Cell* **144**:897–909.

[30] Gregor T, Tank DW, Wieschaus EF, Bialek W (**2007**) Probing the Limits to Positional Information. *Cell* **130**:153–164.

[31] Shaw AS, Filbert EL (**2009**) Scaffold proteins and immune-cell signalling. *Nat Rev Immunol* **9**:47–56.

[32] Burack WR, Shaw AS (**2000**) Signal transduction: hanging on a scaffold. *Curr Opin Cell Biol* **12**:211–216.

[33] Andrews SS, Addy NJ, Brent R, Arkin AP (**2010**) Detailed Simulations of Cell Biology with Smoldyn 2.1. *PLoS Comput Biol* **6**:e1000705.

[34] Andrews SS, Bray D (**2004**) Stochastic simulation of chemical reactions with spatial resolution and single molecule detail. *Phys Biol* **1**:137.

[35] Franks KM, Bartol TM, Sejnowski TJ (**2002**) A Monte Carlo Model Reveals Independent Signaling at Central Glutamatergic Synapse neuromuscular junction. *Biophys J* **83**:2333–2348.

[36] Stiles JR, van Helden D, Bartol TM, Salpeter EE, Salpeter MM (**1996**) Miniature endplate current rise times <100 microseconds from improved recordings can be modeled with passive acetylcholine diffusion from a synaptic vesicle. *Proc Natl Acad Sci USA* **93**:5747–5752.

[37] Plimpton SJ, Slepoy A (**2005**) Microbial cell modeling via reacting diffusing particles. *J Phys Conf Ser* **16**:305–309.

[38] Dobrzyński M, Rodríguez JV, Kaandorp JA, Blom JG (**2007**) Computational methods for diffusion-influenced biochemical reactions. *Bioinformatics* **23**:1969–1977.

[39] van Zon JS, ten Wolde PR (**2005**) Green's-function reaction dynamics: a particle-based approach for simulating biochemical networks in time and space. *J Chem Phys* **123**:234910 1–16.

[40] van Zon JS, ten Wolde PR (**2005**) Simulating biochemical networks at the particle level and in time and space: Green's function reaction dynamics. *Phys Rev Lett* **94**:128103 1–4.

[41] van Zon JS, Morelli MJ, Tănase-Nicola S, ten Wolde PR (**2006**) Diffusion of Transcription Factors Can Drastically Enhance the Noise in Gene Expression. *Biophys J* **91**:4350 - 4367.

[42] Takahashi K, Tănase-Nicola S, ten Wolde PR (**2010**) Spatio-temporal correlations can drastically change the response of a MAPK pathway. *Proc Natl Acad Sci USA* **107**:2473-2478.

[43] Hachet O, Bendez FO, Martin SG (**2012**) Fission yeast: in shape to divide. *Curr Opin Cell Biol* **24**:858–864.

[44] Brunner D, Nurse P (**2000**) CLIP170-like tip1p Spatially Organizes Microtubular Dynamics in Fission Yeast. *Cell* **102**:695–704.

[45] Sawin KE, Nurse P (**1998**) Regulation of Cell Polarity by Microtubules in Fission Yeast. *J Cell Biol* **142**:457–471.

[46] Mugler A, Gotway Bailey A, Takahashi K, ten Wolde PR (**2012**) Membrane clustering and the role of rebinding in biochemical signaling. *Biophys J* **102**:1069-1078.

[47] de Ronde W, ten Wolde PR, Mugler A (**2012**) Protein logic : a statistical mechanical study of signal integration at the single-molecule level. *Biophys J* **103**:1097–1107.

[48] Nüsslein-Volhard C, Wieschaus E (**1987**) Mutations affecting segment number and polarity in Drosophila. *Nature* **287**:795–801.

[49] Lewis EB (**1978**) A gene complex controlling segmentation in Drosophila. *Nature* **276**:565–570.

[50] Wolpert L (**1969**) Positional information and the spatial pattern of cellular differentiation. *J Theor Biol* **25**:1–47.

[51] Gregor T, Wieschaus EF, McGregor AP, Bialek W, Tank DW (**2007**) Stability and Nuclear Dynamics of the Bicoid Morphogen Gradient. *Cell* **130**:141–152.

[52] Houchmandzadeh B, Wieschaus E, Leibler S (**2002**) Establishment of developmental precision and proportions in the early Drosophila embryo. *Nature* **415**:798–802.

[53] Gillespie D (**1976**) A general method for numerically simulating the stochastic time evolution of coupled chemical reactions. *J Comput Phys* **22**:403–434.

[54] Gillespie D (**1977**) Exact stochastic simulation of coupled chemical reactions. *J Chem Phys* **81**:2340–2361.

[55] Opplestrup T, Bulatov VV, Gilmer GH, Kalos MH, Sadigh B (**2006**) First-Passage Monte Carlo Algorithm: Diffusion without All the Hops. *Phys Rev Lett* **97**:230602.

[56] Gibson MA, Bruck J (**2000**) Efficient Exact Stochastic Simulation of Chemical Systems with Many Species and Many Channels. *J Phys Chem A* **104**:1876–1889.

[57] Carslaw HS, Jaeger JC (**1959**) Conduction of Heat in Solids. Oxford University Press, 2nd edition.

[58] Özışık MN (**2002**) Boundary Value Problems of Heat Conduction. Dover Publications, 1st edition.

[59] Beck JV, Cole KD, Haji-Sheikh A, Litkouhl B (**1992**) Heat Conduction Using Green's Function. Taylor & Francis, 1st edition.

[60] Morelli MJ, ten Wolde PR (**2008**) Reaction Brownian dynamics and the effect of spatial fluctuations on the gain of a push-pull network. *J Chem Phys* **129**:054112 1–11.

[61] Paijmans J (**2012**) The fundamental lower bound of the noise in transcriptional regulation. Master's thesis, Univeristy of Amsterdam.

[62] Halford SE, Marko JF (**2004**) How do site-specific DNA-binding proteins find their targets? *Nucleic Acids Res* **32**:3040–3052.

[63] Shimamoto N (**1999**) One-dimensional Diffusion of Proteins along DNA. *J Biol Chem* **274**:15293–15296.

[64] von Hippel PH, Berg OG (**1989**) Facilitated target location in biological systems. *J Biol Chem* **264**:675–678.

[65] Hirokawa N, Noda Y, Tanaka Y, Niwa S (**2009**) Kinesin superfamily motor proteins and intracellular transport. *Nature Rev Mol Cell Biol* **10**:682–696.

[66] Vale RD (**2003**) The molecular motor toolbox for intracellular transport. *Cell* **112**:467–80.

[67] Higuchi H, Endow SA (**2002**) Directionality and processivity of molecular motors. *Curr Op Cell Biol* **14**:50–57.

[68] Smoluchowski M (**1915**) Über Brownsche Molekularbewegung unter Einwirkung äußerer Kräfte und den Zusammenhang mit der verallgemeinerten Diffusionsgleichung. *Ann Phys* **353**:1103–1112.

[69] Smoluchowski M (**1916**) Drei Vorträge über Diffusion, Brown'sche Molekularbewegung und Koagulation von Kolloidteilchen. *Physik Z* **17**:557–551 and 587–599.

[70] Lamm G, Schulten K (**1983**) Extended Brownian dynamics. II. Reactive, nonlinear diffusion. *J Chem Phys* **78**:2713–2734.

[71] Galjart N, Perez F (**2003**) A plus-end raft to control microtubule dynamics and function. *Curr Opin Cell Biol* **15**:48–53.

[72] Sawin KE (**2000**) Microtubule dynamics: The view from the tip. *Curr Biol* **10**:R860–R862.

[73] Etienne-Manneville S (**2010**) From signaling pathways to microtubule dynamics: the key players. *Curr Opin Cell Biol* **22**:104–111.

[74] van der Vaart B, Akhmanova A, Straube A (**2009**) Regulation of microtubule dynamic instability. *Biochem Soc Trans* **37**:1007–1013.

[75] Janson ME, de Dood ME, Dogterom M (**2003**) Dynamic instability of microtubules is regulated by force. *J Cell Biol* **161**:1029–1034.

[76] Mitchison T, Kirschner M (**1984**) Dynamic instability of microtubule growth. *Nature* **312**:237–242.

[77] Gardner MK, Charlebois BD, Jánosi IM, Howard J, Hunt AJ, Odde DJ (**2011**) Rapid Microtubule Self-assembly Kinetics. *Cell* **146**:582–592.

[78] Brun L, Rupp B, Ward JJ, Nédélec F (**2009**) A theory of microtubule catastrophes and their regulation. *Proc Natl Acad Sci USA* **106**:21173–21178.

[79] Dogterom M, Yurke B (**1998**) Microtubule Dynamics and the Positioning of Microtubule Organizing Centers. *Phys Rev Lett* **81**:485–488.

[80] Dogterom M, Leibler S (**1993**) Physical aspects of the growth and regulation of microtubule structures. *Phys Rev Lett* **70**:1347–1350.

[81] Tischer C, Brunner D, Dogterom M (**2009**) Force- and kinesin-8-dependent effects in the spatial regulation of fission yeast microtubule dynamics. *Mol Syst Biol* **5**:250.

[82] Sawin KE, Snaith HA (**2004**) Role of microtubules and tea1p in establishment and maintenance of fission yeast cell polarity. *J Cell Sci* **117**:689–700.

[83] Behrens R, Nurse P (**2002**) Roles of fission yeast tea1p in the localization of polarity factors and in organizing the microtubular cytoskeleton. *J Cell Biol* **157**:783–793.

[84] Alberts B, Johnson A, Lewis J, Raff M, Roberts K, Walter P (**2002**) Molecular Biology of the Cell. Garland Science, 4th edition.

[85] Auerbach D, Thaminy S, Hottiger MO, Stagljar I (**2002**) The post-genomic era of interactive proteomics: facts and perspectives. *Proteomics* **2**:611–623.

[86] Goffeau A, Barrell B, Bussey H, Davis R, Dujon B, Feldmann H, Galibert F, Hoheisel J, Jacq C, Johnston M, Louis E, Mewes H, Murakami Y, Philippsen P, Tettelin H, Oliver S (**1996**) Life with 6000 Genes. *Science* **274**:546, 563–567.

[87] Watson GN (**1962**) A treatise on the theory of Bessel functions. Cambridge University Press, 2nd edition.

[88] Bowman F (**1958**) Introduction to Bessel functions. Dover Publications (New York), 1st edition.

[89] Bossen L (**2010**) Integrating membranes into the enhanced Green's Function Reaction Dynamics algorithm. Master's thesis, University of Amsterdam.

[90] Chang F, Martin SG (**2009**) Shaping Fission Yeast with Microtubules. *Cold Spring Harb Perspect Biol* **1**:a001347.

[91] Martin SG (**2009**) Microtubule-dependent cell morphogenesis in the fission yeast. *Trends Cell Biol* **19**:447–454.

[92] Mitchison JM, Nurse P (**1985**) Growth in cell length in the fission yeast Schizosaccharomyces pombe. *J Cell Sci* **75**:357–76.

[93] Das M, Drake T, Wiley DJ, Buchwald P, Vavylonis D, Verde F (**2012**) Oscillatory Dynamics of Cdc42 GTPase in the Control of Polarized Growth. *Science* **337**:239–243.

[94] Tatebe H, Nakano K, Maximo R, Shiozaki K (**2008**) Pom1 DYRK Regulates Localization of the Rga4 GAP to Ensure Bipolar Activation of Cdc42 in Fission Yeast. *Curr Biol* **18**:322–330.

[95] Feierbach B, Verde F, Chang F (**2004**) Regulation of a formin complex by the microtubule plus end protein tea1p. *J Cell Biol* **165**:697–707.

[96] Busch KE, Hayles J, Nurse P, Brunner D (**2004**) Tea2p Kinesin Is Involved in Spatial Microtubule Organization by Transporting Tip1p on Microtubules. *Dev Cell* **6**:831–843.

[97] Busch KE, Brunner D (**2004**) The Microtubule Plus End-Tracking Proteins mal3p and tip1p Cooperate for Cell-End Targeting of Interphase Microtubules. *Curr Biol* **14**:548–559.

[98] Mata J, Nurse P (**1997**) tea1 and the Microtubular Cytoskeleton Are Important for Generating Global Spatial Order within the Fission Yeast Cell. *Cell* **89**:939–49.

[99] Verde F, Mata J, Nurse P (**1995**) Fission yeast cell morphogenesis: identification of new genes and analysis of their role during the cell cycle. *J Cell Sci* **131**:1529–1538.

[100] Browning H, Hayles J, Mata J, Aveline L, Nurse P, , McIntosh JR (**2000**) Tea2p Is a Kinesin-like Protein Required to Generate Polarized Growth in Fission Yeast. *J Cell Biol* **151**:15–28.

[101] Castagnetti S, Novák B, Nurse P (**2007**) Microtubules offset growth site from the cell centre in fission yeast. *J Cell Sci* **120**:2205–2213.

[102] Snaith HA, Sawin KE (**2003**) Fission yeast mod5p regulates polarized growth through anchoring of tea1p at cell tips. *Nature* **423**:647–651.

[103] Bicho CC, Kelly DA, Snaith HA, Goryachev AB, Sawin KE (**2010**) A catalytic role for Mod5 in the formation of the Tea1 cell polarity landmark. *Curr Biol* **20**:1752–1757.

[104] Tatebe H, Shimada1 K, Uzawa S, Morigasaki S, Shiozaki K (**2005**) Wsh3/Tea4 is a novel cell-end factor essential for bipolar distribution of Tea1 and protects cell polarity under environmental stress in S. pombe. *Curr Biol* **15**:1006–1015.

[105] Martin SG, McDonald WH, Yates JR, Chang F (**2005**) Tea4p Links Microtubule Plus Ends with the Formin For3p in the Establishment of Cell Polarity. *Dev Cell* **8**:479–491.

[106] Varga V, Leduc C, Bormuth V, Diez S, Howard J (**2009**) Kinesin-8 Motors Act Cooperatively to Mediate Length-Dependent Microtubule Depolymerization. *Cell* **138**:1174–1183.

[107] Saunders TE, Pan KZ, Angel A, Guan Y, Shah JV, Howard M, Chang F (**2012**) Noise reduction in the intracellular pom1p gradient by a dynamic clustering mechanism. *Dev Cell* **22**:558–572.

[108] Wolpert L (**1994**) Positional information and pattern formation in development. *Dev Genet* **15**:485–490.

[109] Driever W, Nüsslein-Volhard C (**1988**) A gradient of bicoid protein in Drosophila embryos. *Cell* **54**:83–93.

[110] Driever W, Nüsslein-Volhard C (**1988**) The bicoid protein determines position in the Drosophila embryo in a concentration-dependent manner. *Cell* **54**:95–104.

[111] Jäckle H, Tautz D, Schuh R, Seifert E, Lehmann R (**1986**) Cross-regulatory interactions among the gap genes of Drosophila. *Nature* **324**:668–670.

[112] Clyde DE, Corado MSG, Wu X, Pare A, Papatsenko D, Small S (**2003**) A self-organizing system of repressor gradients establishes segmental complexity in Drosophila. *Nature* **426**:849–853.

[113] Jaeger J, Blagov M, Kosman D, Kozlov KN, Manu, Myasnikova E, Surkova S, Vanario-Alonso CE, Samsonova M, Sharp DH, Reinitz J (**2004**) Dynamical Analysis of Regulatory Interactions in the Gap Gene System of Drosophila melanogaster. *Genetics* **167**:1721–1737.

[114] Surkova S, Kosman D, Kozlov K, Manu, Myasnikova E, Samsonova AA, Spirov A, Vanario-Alonso CE, Samsonova M, Reinitz J (**2008**) Characterization of the Drosophila segment determination morphome. *Dev Biol* **313**:844–862.

[115] Manu, Surkova S, Spirov AV, Gursky VV, Janssens H, Kim AR, Radulescu O, Vanario-Alonso CE, Sharp DH, Samsonova M, Reinitz J (**2009**) Canalization of Gene Expression and Domain Shifts in the Drosophila Blastoderm by Dynamical Attractors. *PLoS Comput Biol* **5**:e1000303.

[116] Manu, Surkova S, Spirov AV, Gursky VV, Janssens H, Kim AR, Radulescu O, Vanario-Alonso CE, Sharp DH, Samsonova M, Reinitz J (**2009**) Canalization of Gene Expression in the Drosophila Blastoderm by Gap Gene Cross Regulation. *PLoS Biol* **7**:591–603.

[117] Vakulenko S, Manu, Reinitz J, Radulescu O (**2009**) Size Regulation in the Segmentation of Drosophila: Interacting Interfaces between Localized Domains of Gene Expression Ensure Robust Spatial Patterning. *Phys Rev Lett* **103**:168102.

[118] Porcher A, Abu-Arish A, Huart S, Roelens B, Fradin C, Dostatni N (**2010**) The time to measure positional information: maternal Hunchback is required for the synchrony of the Bicoid transcriptional response at the onset of zygotic transcription. *Development* **137**:2795–2804.

[119] He F, Ren J, Wang W, Ma J (**2011**) A Multiscale Investigation of Bicoid-Dependent Transcriptional Events in Drosophila Embryos. *PLoS ONE* **6**:e19122.

[120] Perry MW, Boettiger AN, Levine M (**2011**) Multiple enhancers ensure precision of gap gene-expression patterns in the Drosophila embryo. *Proc Natl Acad Sci USA* **108**:13570 –13575.

[121] He F, Wen Y, Deng J, Lin X, Lu LJ, Jiao R, Ma J (**2008**) Probing Intrinsic Properties of a Robust Morphogen Gradient in Drosophila. *Dev Cell* **15**:558–567.

[122] Erdmann T, Howard M, ten Wolde PR (**2009**) Role of Spatial Averaging in the Precision of Gene Expression Patterns. *Phys Rev Lett* **103**:258101.

[123] Okabe-Oho Y, Murakami H, Oho S, Sasai M (**2009**) Stable, Precise, and Reproducible Patterning of Bicoid and Hunchback Molecules in the Early Drosophila Embryo. *PLoS Comput Biol* **5**:e1000486.

[124] Kraut R, Levine M (**1991**) Mutually repressive interactions between the gap genes giant and Kruppel define middle body regions of the Drosophila embryo. *Development* **111**:611–621.

[125] Saka Y, Smith JC (**2007**) A mechanism for the sharp transition of morphogen gradient interpretation in Xenopus. *BMC Dev Biol* **7**:47.

[126] Ishihara S, Shibata T (**2008**) Mutual interaction in network motifs robustly sharpens gene expression in developmental processes. *J Theor Biol* **252**:131–144.

[127] Cherry JL, Adler FR (**2000**) How to make a biological switch. *J Theor Biol* **203**:117–133.

[128] Kepler TB, Elston TC (**2001**) Stochasticity in transcriptional regulation: origins, consequences, and mathematical representations. *Biophys J* **81**:3116–3136.

[129] Warren PB, ten Wolde PR (**2004**) Enhancement of the Stability of Genetic Switches by Overlapping Upstream Regulatory Domains. *Phys Rev Lett* **92**:128101.

[130] Warren PB, ten Wolde PR (**2005**) Chemical Models of Genetic Toggle Switches. *J Phys Chem B* **109**:6812–6823.

[131] Papatsenko D, Levine M (**2011**) The Drosophila Gap Gene Network Is Composed of Two Parallel Toggle Switches. *PLoS ONE* **6**:e21145.

[132] Ishihara S, Fujimoto K, Shibata T (**2005**) Cross talking of network motifs in gene regulation that generates temporal pulses and spatial stripes. *Genes Cells* **10**:1025–1038.

[133] Zinzen RP, Senger K, Levine M, Papatsenko D (**2006**) Computational Models for Neurogenic Gene Expression in the Drosophila Embryo. *Curr Biol* **16**:1358–1365.

[134] Zinzen RP, Papatsenko D (**2007**) Enhancer Responses to Similarly Distributed Antagonistic Gradients in Development. *PLoS Comput Biol* **3**:e84.

[135] Rivera-Pomar R, Lu X, Perrimon N, Taubert H, Jäckle H (**1995**) Activation of posterior gap gene expression in the Drosophila blastoderm. *Nature* **376**:253–256.

[136] Schulz C, Tautz D (**1995**) Zygotic caudal regulation by hunchback and its role in abdominal segment formation of the Drosophila embryo. *Development* **121**:1023–1028.

[137] Howard M, ten Wolde PR (**2005**) Finding the Center Reliably: Robust Patterns of Developmental Gene Expression. *Phys Rev Lett* **95**:208103.

[138] Morishita Y, Iwasa Y (**2009**) Accuracy of positional information provided by multiple morphogen gradients with correlated noise. *Phys Rev E* **79**:061905.

[139] Foe VE, Alberts BM (**1983**) Studies of nuclear and cytoplasmic behaviour during the five mitotic cycles that precede gastrulation in Drosophila embryogenesis. *J Cell Sci* **61**:31–70.

[140] Bolouri H, Davidson EH (**2003**) Transcriptional regulatory cascades in development: Initial rates, not steady state, determine network kinetics. *Proc Natl Acad Sci USA* **100**:9371 –9376.

[141] Janssens H, Hou S, Jaeger J, Kim A, Myasnikova E, Sharp D, Reinitz J (**2006**) Quantitative and predictive model of transcriptional control of the Drosophila melanogaster even skipped gene. *Nat Genet* **38**:1159–1165.

[142] Sample C, Shvartsman SY (**2010**) Multiscale modeling of diffusion in the early Drosophila embryo. *Proc Natl Acad Sci USA* **107**:10092–10096.

[143] Elf J, Ehrenberg M (**2004**) Spontaneous separation of bi-stable biochemical systems into spatial domains of opposite phases. *Syst Biol (Stevenage)* **1**:230–236.

[144] Hattne J, Fange D, Elf J (**2005**) Stochastic reaction-diffusion simulation with MesoRD. *Bioinformatics* **21**:2923–2924.

[145] So L, Ghosh A, Zong C, Sepúlveda LA, Segev R, Golding I (**2011**) General properties of transcriptional time series in Escherichia coli. *Nat Genet* **43**:554–560.

[146] Ochoa-Espinosa A, Yu D, Tsirigos A, Struffi P, Small S (**2009**) Anterior-posterior positional information in the absence of a strong Bicoid gradient. *Proc Natl Acad Sci USA* **106**:3823–3828.

[147] Drocco JA, Grimm O, Tank DW, Wieschaus E (**2011**) Measurement and Perturbation of Morphogen Lifetime: Effects on Gradient Shape. *Biophys J* **101**:1807–1815.

[148] Allen RJ, Warren PB, ten Wolde P (**2005**) Sampling Rare Switching Events in Biochemical Networks. *Phys Rev Lett* **94**:018104.

[149] Lipshtat A, Loinger A, Balaban NQ, Biham O (**2006**) Genetic Toggle Switch without Cooperative Binding. *Phys Rev Lett* **96**:188101.

[150] Loinger A, Lipshtat A, Balaban NQ, Biham O (**2007**) Stochastic simulations of genetic switch systems. *Phys Rev E* **75**:021904.

[151] Cotterell J, Sharpe J (**2010**) An atlas of gene regulatory networks reveals multiple three-gene mechanisms for interpreting morphogen gradients. *Mol Syst Biol* **6**:425.

[152] Treisman J, Desplan C (**1989**) The products of the Drosophila gap genes hunchback and Kruppel bind to the hunchback promoters. *Nature* **341**:335–337.

[153] Lopes FJP, Vieira FMC, Holloway DM, Bisch PM, Spirov AV (**2008**) Spatial Bistability Generates hunchback Expression Sharpness in the Drosophila Embryo. *PLoS Comput Biol* **4**:e1000184.

[154] Holloway DM, Lopes FJP, da Fontoura Costa L, Travençolo BAN, Golyandina N, Usevich K, Spirov AV (**2011**) Gene Expression Noise in Spatial Patterning: hunchback Promoter Structure Affects Noise Amplitude and Distribution in Drosophila Segmentation. *PLoS Comput Biol* **7**:e1001069.

[155] Waddington CH (**1942**) Canalization of Development and the Inheritance of Acquired Characters. *Nature* **150**:563–565.

[156] Waddington CH (**1959**) Canalization of Development and Genetic Assimilation of Acquired Characters. *Nature* **183**:1654–1655.

[157] Hülskamp M, Schröder C, Pfeifle C, Jäckle H, Tautz D (**1989**) Posterior segmentation of the Drosophila embryo in the absence of a maternal posterior organizer gene. *Nature* **338**:629–632.

[158] Hülskamp M, Pfeifle C, Tautz D (**1990**) A morphogenetic gradient of hunchback protein organizes the expression of the gap genes Kruppel and knirps in the early Drosophila embryo. *Nature* **346**:577–580.

[159] Struhl G, Johnston P, Lawrence PA (**1992**) Control of Drosophila body pattern by the hunchback morphogen gradient. *Cell* **69**:239–249.

[160] Simpson-Brose M, Treisman J, Desplan C (**1994**) Synergy between the hunchback and bicoid morphogens is required for anterior patterning in Drosophila. *Cell* **78**:855–865.

[161] Bergmann S, Sandler O, Sberro H, Shnider S, Schejter E, Shilo B, Barkai N (**2007**) Pre-Steady-State Decoding of the Bicoid Morphogen Gradient. *PLoS Biol* **5**:e46.

[162] Bialek W, Gregor T, Tank DW, Wieschaus EF (**2008**) Response: Can We Fit All of the Data? *Cell* **132**:17–18.

[163] Barkai N, Shilo B (**2009**) Robust Generation and Decoding of Morphogen Gradients. *Cold Spring Harb Perspect Biol* **1**:a001990.

[164] Spirov A, Fahmy K, Schneider M, Frei E, Noll M, Baumgartner S (**2009**) Formation of the bicoid morphogen gradient: an mRNA gradient dictates the protein gradient. *Development* **136**:605–614.

[165] Hecht I, Rappel W, Levine H (**2009**) Determining the scale of the Bicoid morphogen gradient. *Proc Natl Acad Sci USA* **106**:1710–1715.

[166] Porcher A, Dostatni N (**2010**) The bicoid morphogen system. *Curr Biol* **20**:R249–R254.

[167] Abu-Arish A, Porcher A, Czerwonka A, Dostatni N, Fradin C (**2010**) High Mobility of Bicoid Captured by Fluorescence Correlation Spectroscopy: Implication for the Rapid Establishment of Its Gradient. *Biophys J* **99**:L33–L35.

[168] Buchler NE, Gerland U, Hwa T (**2005**) Nonlinear protein degradation and the function of genetic circuits. *Proc Natl Acad Sci USA* **102**:9559–9564.

[169] Frenkel D, Smit B (**2001**) Understanding Molecular Simulation: From Algorithms to Applications. Academic Press, second edition. ISBN 0122673514.

[170] Sokolowski TR, Erdmann T, ten Wolde PR (**2012**) Mutual Repression Enhances the Steepness and Precision of Gene Expression Boundaries. *PLoS Comput Biol* **8**:e1002654.

[171] Wartlick O, Kicheva A, González-Gaitán M (**2009**) Morphogen Gradient Formation. *Cold Spring Harb Perspect Biol* **1**:a001255.

[172] Rogers KW, Schier AF (**2011**) Morphogen gradients: from generation to interpretation. *Annu Rev Cell Dev Biol* **27**:377–407.

[173] Ashe HL, Briscoe J (**2006**) The interpretation of morphogen gradients. *Development (Cambridge, England)* **133**:385–394.

[174] Gurdon JB, Bourillot PY (**2001**) Morphogen gradient interpretation. *Nature* **413**:797–803.

[175] Meinhardt H (**1982**) Models of Biological Pattern Formation. Academic Press, London.

[176] Driever W, Nüsslein-Volhard C (**1989**) The bicoid protein is a positive regulator of hunchback transcription in the early Drosophila embryo. *Nature* **337**:138–143.

[177] Frohnhöfer HG, Nüsslein-Volhard C (**1986**) Organization of anterior pattern in the Drosophila embryo by the maternal gene bicoid. *Nature* **324**:120–125.

[178] Struhl G, Struhl K, Macdonald PM (**1989**) The gradient morphogen bicoid is a concentration-dependent transcriptional activator. *Cell* **57**:1259–1273.

[179] Macdonald PM, Struhl G (**1986**) A molecular gradient in early Drosophila embryos and its role in specifying the body pattern. *Nature* **324**:537–545.

[180] Crauk O, Dostatni N (**2005**) Bicoid Determines Sharp and Precise Target Gene Expression in the Drosophila Embryo. *Current Biology* **15**:1888–1898.

[181] Dubuis JO, Samanta R, Gregor T (**2013**) Accurate measurements of dynamics and reproducibility in small genetic networks. *Mol Syst Biol* **9**:639.

[182] Crombach A, Wotton KR, Cicin-Sain D, Ashyraliyev M, Jaeger J (**2012**) Efficient Reverse-Engineering of a Developmental Gene Regulatory Network. *PLoS Comput Biol* **8**:e1002589.

[183] Kozlov K, Surkova S, Myasnikova E, Reinitz J, Samsonova M (**2012**) Modeling of Gap Gene Expression in Drosophila *Kruppel* Mutants. *PLoS Comput Biol* **8**:e1002635.

[184] Bieler J, Pozzorini C, Naef F (**2011**) Whole-Embryo Modeling of Early Segmentation in Drosophila Identifies Robust and Fragile Expression Domains. *Biophys J* **101**:287–296.

[185] Hengenius JB, Gribskov M, Rundell AE, Fowlkes CC, Umulis DM (**2011**) Analysis of Gap Gene Regulation in a 3D Organism-Scale Model of the Drosophila melanogaster Embryo. *PLoS One* **6**:e26797.

[186] Fomekong-Nanfack Y, Postma M, Kaandorp JA (**2009**) Inferring Drosophila gap gene regulatory network: a parameter sensitivity and perturbation analysis. *BMC Syst Biol* **3**:94.

[187] Lucchetta EM, Vincent ME, Ismagilov RF (**2008**) A Precise Bicoid Gradient Is Nonessential during Cycles 11–13 for Precise Patterning in the Drosophila Blastoderm. *PLoS ONE* **3**:e3651.

[188] Lucchetta EM, Lee JH, Fu LA, Patel NH, Ismagilov RF (**2005**) Dynamics of Drosophila embryonic patterning network perturbed in space and time using microfluidics. *Nature* **434**:1134–1138.

[189] Wimmer EA, Carleton A, Harjes P, Turner T, Desplan C (**2000**) Bicoid-Independent Formation of Thoracic Segments in Drosophila. *Science* **287**:2476–2479.

[190] Schröder R (**2003**) The genes orthodenticle and hunchback substitute for bicoid in the beetle Tribolium. *Nature* **422**:621–625.

[191] Goltsev Y, Hsiong W, Lanzaro G, Levine M (**2004**) Different combinations of gap repressors for common stripes in Anopheles and Drosophila embryos. *Dev Biol* **275**:435–446.

[192] Ben-David J, Chipman AD (**2010**) Mutual regulatory interactions of the trunk gap genes during blastoderm patterning in the hemipteran Oncopeltus fasciatus. *Dev Biol* **346**:140–149.

[193] García-Solache M, Jaeger J, Akam M (**2010**) A systematic analysis of the gap gene system in the moth midge Clogmia albipunctata. *Dev Biol* **344**:306–318.

[194] Schulz C, Tautz D (**1994**) Autonomous concentration-dependent activation and repression of Krüppel by hunchback in the Drosophila embryo. *Development* **110**:3043-3049.

[195] Kraut R, Levine H (**1991**) Spatial regulation of the gap gene giant during Drosophila development. *Development* **111**:601–609.

[196] Zuo P, Stanojević D, Colgan J, Han K, Levine M, Manley JL (**1991**) Activation and repression of transcription by the gap proteins hunchback and Krüppel in cultured Drosophila cells. *Genes Dev* **5**:254–264.

[197] Eldon ED, Pirrotta V (**1991**) Interactions of the Drosophila gap gene giant with maternal and zygotic pattern-forming genes. *Development* **111**:367–378.

[198] Huang S (**2012**) The molecular and mathematical basis of Waddington's epigenetic landscape: A framework for post-Darwinian biology? *BioEssays* **34**:149–157.

[199] Huang S (**2009**) Reprogramming cell fates: reconciling rarity with robustness. *BioEssays* **31**:546–560.

[200] Huang S, Guo YP, May G, Enver T (**2007**) Bifurcation dynamics in lineage-commitment in bipotent progenitor cells. *Dev Biol* **305**:695–713.

[201] Wang J, Zhang K, Xu L, Wang E (**2011**) Quantifying the Waddington landscape and biological paths for development and differentiation. *Proc Natl Acad Sci USA* **108**:8257–8262.

[202] Wang J, Xu L, Wang E, Huang S (**2010**) The Potential Landscape of Genetic Circuits Imposes the Arrow of Time in Stem Cell Differentiation. *Biophys J* **99**:29–39.

[203] Wang J, Xu L, Wang E (**2008**) Potential landscape and flux framework of nonequilibrium networks: Robustness, dissipation, and coherence of biochemical oscillations. *Proc Natl Acad Sci USA* **105**:12271–12276.

[204] Walczak AM, Onuchic JN, Wolynes PG (**2005**) Absolute rate theories of epigenetic stability. *Proc Natl Acad Sci USA* **102**:18926–18931.

[205] Margolis JS, Borowsky ML, Steingrímsson E, Shim CW, Lengyel JA, Posakony JW (**1995**) Posterior stripe expression of hunchback is driven from two promoters by a common enhancer element. *Development* **121**:3067–3077.

[206] Bolhuis PG, Chandler D, Dellago C, Geissler PL (**2002**) Transition path sampling: throwing ropes over rough mountain passes, in the dark. *Annu Rev Phys Chem* **53**:291–318.

[207] Dellago C, Bolhuis PG, Geissler PL (**2002**) Transition Path Sampling. *Adv Chem Phys* **123**:1–84.

[208] van Erp TS, Moroni D, Bolhuis PG (**2003**) A novel path sampling method for the calculation of rate constants. *J Chem Phys* **118**:7762.

[209] Bolhuis PG (**2003**) Transition-path sampling of β-hairpin folding. *Proc Natl Acad Sci USA* **100**:12129–12134.

[210] Moroni D, Bolhuis PG, van Erp TS (**2004**) Rate constants for diffusive processes by partial path sampling. *J Chem Phys* **120**:4055–4065.

[211] Moroni D, van Erp TS, Bolhuis PG (**2004**) Investigating rare events by transition interface sampling. *Physica A* **340**:395–401.

[212] van Erp TS, Bolhuis PG (**2005**) Elaborating transition interface sampling methods. *J Comp Phys* **205**:157–181.

[213] Laio A, Parrinello M (**2002**) Escaping free-energy minima. *Proc Natl Acad Sci USA* **99**:12562 –12566.

[214] Allen RJ, Frenkel D, ten Wolde P (**2006**) Simulating rare events in equilibrium or nonequilibrium stochastic systems. *J Chem Phys* **124**:024102.

[215] Warmflash A, Bhimalapuram P, Dinner AR (**2007**) Umbrella sampling for nonequilibrium processes. *J Chem Phys* **127**:154112.

[216] Zhang BW, Jasnow D, Zuckerman DM (**2007**) Efficient and verified simulation of a path ensemble for conformational change in a united-residue model of calmodulin. *Proc Natl Acad Sci USA* **104**:18043–18048.

[217] Huber GA, Kim S (**1996**) Weighted-ensemble Brownian dynamics simulations for protein association reactions. *Biophys J* **70**:97–110.

[218] Becker NB, Allen RJ, ten Wolde PR (**2012**) Non-stationary forward flux sampling. *J Chem Phys* **136**:174118–174118-18.

[219] Becker NB, ten Wolde PR (**2012**) Rare switching events in non-stationary systems. *J Chem Phys* **136**:174119–174119-15.

[220] Casanova J (**1990**) Pattern formation under the control of the terminal system in the Drosophila embryo. *Development* **110**:621–628.

[221] Weigel D, Jürgens G, Klingler M, Jäckle H (**1990**) Two gap genes mediate maternal terminal pattern information in Drosophila. *Science* **27**:495–498.

[222] Zwanzig R (**1961**) Memory Effects in Irreversible Thermodynamics. *Phys Rev* **124**:983–992.

[223] Mori H (**1965**) Transport, Collective Motion, and Brownian Motion. *Prog Theor Phys* **33**:423–455.

[224] Yang S, Onuchic JN, Levine H (**2006**) Effective stochastic dynamics on a protein folding energy landscape. *J Chem Phys* **125**: 054910.

[225] Kopelevich DI, Panagiotopoulos AZ, Kevrekidis IG (**2005**) Coarse-grained kinetic computations for rare events: Application to micelle formation. *J Chem Phys* **122**:044908.

[226] Hummer G, Kevrekidis IG (**2003**) Coarse molecular dynamics of a peptide fragment: Free energy, kinetics, and long-time dynamics computations. *J Chem Phys* **118**:10762.

[227] Plotkin SS, Wolynes PG (**1998**) Non-Markovian Configurational Diffusion and Reaction Coordinates for Protein Folding. *Phys Rev Lett* **80**:5015–5018.

[228] Papatsenko D, Levine MS (**2008**) Dual regulation by the Hunchback gradient in the Drosophila embryo. *Proc Natl Acad Sci USA* **105**:2901–2906.

[229] McCarty AS, Kleiger G, Eisenberg D, Smale ST (**2003**) Selective Dimerization of a C2H2 Zinc Finger Subfamily. *Mol Cell* **11**:459–470.

[230] Sauer F, Jäckle H (**1993**) Dimerization and the control of transcription by Krüppel. *Nature* **364**:454–457.

Summary

A Computational Study of Robust Formation of Spatial Protein Patterns

The blueprint of all living organisms is contained in their genes. On the single cell level, genetic information determines growth, shape and function, which on the level of a whole organism specifies its development and behavior. Since the discovery of DNA and gene regulatory mechanisms it became more and more evident that cells process their genetic information in a way comparable to a computer that runs a specific program. This requires the establishment of information flow and "logical wiring". In biological cells this is achieved via proteins that are expressed from certain genes and transported elsewhere to specifically activate (or suppress) the expression of other genes (thus acting as "transcription factors"), or to accomplish other signalling tasks. As a well-known example, distinct development of different body parts is typically controlled by localized concentration patterns of specific proteins in the respective regions. However, in contrast to man-made information-processing devices, cells are highly stochastic systems: both gene expression and intracellular transport, predominantly occuring via diffusion, are random processes, and typical protein concentrations very low, making cellular information processing prone to noise. Nevertheless, cellular signalling and organism development appear exceedingly robust and reliable on the macroscopic scale. The mechanisms that cells employ to control their intrisic stochasticity recently have been the subject of numerous experimental and theoretical studies. Although it is increasingly recognized that spatial aspects chiefly affect biochemical noise control, space often is not explicitly taken into account in theoretical models of cellular information processing. The leading question of this work is how cells control noise in gene expression in order to establish well-defined spatial protein patterns that, on a larger scale, produce behavior that appears deterministic and reproducible.

A major methodic difficulty arises here: Due to typically low protein numbers, mean-field analysis largely fails to describe such systems accurately, while particle-based approaches usually are demanding, both mathematically and computationally. In the last years *enhanced Green's Function Reacton Dynamics* (eGFRD) was developed as an elegant and powerful stochastic simulation scheme that closes the gap

between accuracy and efficiency: Using exact analytical solutions, it implements an event-driven stochastic algorithm that retains spatial information of individual particles at a markedly lower computational cost than classical simulation techniques, such as Brownian Dynamics. However, until now eGFRD was limited to simulations of biochemical particle ensembles in unbounded 3D space, whereas in vivo intracellular transport in lower dimensions and spatial confinement play an important role. In the first part of this thesis (chapter 2 and chapter 3) we present work that extends eGFRD in a way that includes 1D and 2D transport on finite structures, binding of particles to these structures and reactions of particles both on and in between structures of different dimensionality. Continuing on the main theme of this thesis, as an example application in chapter 4 the extended eGFRD scheme is used to simulate a particle-based stochastic model of growth factor polarization in fission yeast. A different model organism is the subject of chapter 5 and chapter 6: Here we study how a specific gene regulation motif, mutual repression, contributes to noise-control in the early development of the fruit fly *Drosophila melanogaster*, a paradigm of embryogenesis. In the following, the three content blocks are described in more detail separately.

eGFRD in all dimensions and different transport modes

The main idea of eGFRD is to separate the space into simple (protective) subdomains that contain at most two biochemically interacting particles, thus breaking down the many-particle problem into a number of one- and two-particle problems. This makes it possible to exactly calculate the transient analytical solution (Green's function) of the reaction-diffusion problem for each of the subdomains individually. The Green's functions are used to sample next-event times and expected new particle positions in order to setup an event-driven Monte Carlo simulation. The analytical calculation of the Green's functions thus is the–oftentimes challenging–key task in eGFRD development. Moreover, a specific Green's function has to be determined essentially from scratch for each dimension, each coordinate system and each new boundary condition.

One of the main achievements of this work is the analytical derivation of the Green's function for the reaction-diffusion problem in 1D for various mathematical boundary conditions, which is presented in chapter 2. Importantly, as an additional feature, the derived solutions take into account active, drift-like transport in 1D, which is a widespread mode of intracellular transport along linear polymer tracks in vivo. We used the new Green's functions to implement transport on finite 1D structures into eGFRD, introducing several new protective domain types. As a special case, we also derived the Green's function for a particle that diffuses in 1D and with a certain rate binds to a reactive site ("sink") along its way, modelling the diffusive search of a transcription factor for its binding site on the DNA.

Similarly, we obtained the Green's functions describing diffusion and interparticle reactions in 2D, as well as binding of particles from 3D two lower-dimension structures, which is the subject of chapter 3. To treat the binding of a particle diffusing in 3D to a 2D particle that diffuses on a plane ("direct binding") we derived a coordinate transform which converts the anisotropic diffusion of the interparticle vector to a coordinate-rescaling problem, enabling the use of previously known Green's functions

for that case. Again, these solutions together with newly defined protective domain types were used to implement transport and reactions in 2D into eGFRD. Finally, we implemented transition domains into eGFRD, which handle transfer of diffusing particles between orthogonal planes, allowing for the creation of a simulation box completely bounded by reactive 2D structures.

Establishment of polarized growth factor concentrations in fission yeast

The newly implemented eGFRD features enabled us to simulate a stochastic model of the polarization of growth factor proteins in fission yeast, described in chapter 4. Fission yeast forms rod-like shapes by virtue of growing in an elongated fashion from two opposite cell poles exclusively. This growth localization is maintained by accumulating growth factor proteins on the cell membrane at the poles. Experiments have shown that proper growth factor polarization relies on a combination of (1) active 1D transport of the growth factors on linear polymer tracks (microtubules) reaching outwards from the cell center with (2) 2D diffusion of a membrane-bound reaction-partner that acts as a recruiting agent for the formation of slowly diffusing membrane-bound growth factor complexes. The mechanistic details of this interplay however remain unknown. In our simulations we quantified how efficiently the growth factors are polarized along the long axis of the yeast cell as a function of key system parameters and comparing different models for binding of the growth factors to the membrane-bound anchoring agent (direct binding from 3D to 2D vs. two-step binding, i.e. binding to the membrane first, followed by diffusive search for the reaction partner). First, we find that–at equal footing–the system with direct binding displays better polarization properties than the two-step binding system. This is traced back to the fact that in the two-step binding model growth factors are depleted from the bulk by membrane binding much more than in the direct-binding model and therefore less likely to be directed outwards by binding to microtubules, giving a rationale for the presence of the membrane-bound anchoring agent in the first place. Second, we discover that–in the system with direct binding–there is an optimal lifetime of the membrane-bound growth factor complexes which maximizes a combined score defined as the product of our polarity measure and the complex surface density at the cell poles; this reflects a trade-off between these two factors arising upon variation of the complex lifetime.

The benefits of mutual repression in embryo development

The early embryonic development of the fruit fly *Drosophila melanogaster* is a widely studied paradigm of developmental biology. Specification of different body segments along the long axis of the egg-shaped embryo is driven by emergent protein stripe-patterns in which distinct genes are expressed. These "gap genes" typically are activated in a concentration-dependent manner by upstream transcription factors that form (morphogen) gradients along the embryo axis. This way the concentration signal is converted into positional information. In this setting, the reliability with which different body parts are specified directly depends on the reproducibility and stability of the protein-stripe boundaries. Intriguingly, experimental measurements of

gap protein noise levels have revealed that –in spite of the stochastic nature of gene expression–the boundary variance not only is surprisingly low, but even reduced with progressing development, suggesting hidden noise-control mechanisms. As presented in the second part of this thesis (chapter 5 and chapter 6), we studied–in a spatially-resolved stochastic model–the noise-control properties of a gene regulatory motif that is prominent among gap genes: mutual repression. In the context of gene regulation mutual repression means that the protein produced from one gene suppresses the production (transcription) of another gene and vice versa. Indeed we identified several beneficial roles of mutual repression in the given context.

In chapter 5 we focus on a minimal model of two mutually repressing gap genes, activated by two upstream activator gradients, respectively. We performed extensive stochastic simulations of a model that explicitly comprises the several thousand individual cell nuclei that constitute the embryo at that particular stage of development, measuring the boundary variance of the activated gap protein patterns for different values of important system parameters. We find that mutual repression indeed plays a useful role in limiting the boundary variance: In synergy with spatial averaging, at an optimal gap protein diffusion constant mutual repression allows for protain domain boundaries which are sharp and steep simulateously, facilitating downstream readout of the spatially confined patterning protein signal. Moreover, this beneficial effect turns out to be very robust against varying key system parameters, such as the average level of the activator gradient: In the regime of slight activator overexpression, mutual repression is found to buffer against extrinsic fluctuations, i.e. fluctuations in the concentration levels of the activator gradients, without hampering control of the intrinsic noise. The origin of this additional benefit is traced back to bistability emerging from mutual repression.

The observation of a weakend role for the activator gradients in the abovementioned regime lead us to the question: Is the gradient-based activation of the gap genes critical for correct stripe patterning in the first place, or can a stable gap gene pattern also be maintained without morphogen gradients, i.e. only by mutual gap gene interactions? This question was additionally motivated by the fact that most gap gene stripes form in the posterior half of the embryo, where the concentration of the morphogen that is commonly considered their master regulator is low. Most intriguingly, the posterior gap genes repress each other mutually with a characteristic pattern of alternating repression strength: while nearest-neighbor stripes interact only weakly, mutual repression between next-nearest neighbor stripes is strong. Conducting stochastic simulations of the posterior gap gene system, aided by a novel rare-event sampling technique, we quantified the pattern stability as a function of the weak repression strength (chapter 6). We demonstrate that there is an optimal weak repression strength for which the stability of the whole pattern is dramatically enhanced, reaching persistence times way beyond the biologically relevant regime. Our results further indicate that–in the optimal setting–a restoring force is created which counteracts fluctuations away from the stable pattern state. Finally, performing a stability analysis we show that the introduction of a weak repression partner between two stripes of strongly repressing genes can suppress bistable switching at their interface, thus attenuating interface fluctuations and stabilizing the whole pattern.

Samenvatting

Een numerieke studie naar de robuuste vorming van ruimtelijke eiwit patronen

De blauwdruk van alle organismen is gecodeerd in hun genen. Deze genetische informatie bepaalt de groei, vorm en functie op het niveau van een enkele cel, wat de ontwikkeling en het gedrag van het gehele organisme bepaalt. Sinds de ontdekking van het DNA en de mechanismen die genexpressie regelen werd het steeds duidelijker dat cellen hun genetische informatie verwerken op een manier die sterke gelijkenissen vertoont met hoe een computer een programma uitvoert. Dit leid tot de vraag hoe in een biologische cel de benodigde "logische schakelingen" opgebouwd zijn. Een cel neemt een "logische beslissing" door de gereguleerde expressie van eiwitten en het transport van deze eiwitten binnen de cel. Hier kunnen de eiwitten de transcriptie van bepaalde genen regelen (ze zijn dus werkzaam als transcriptiefactoren) of bepaalde signaaltaken verrichten. Een bekend voorbeeld is de vorming van lichaamsdelen. Dit wordt geregeld door de concentratie van regel eiwitten op bepaalde locaties van de cel te verhogen. Echter, in tegenstelling tot informatie verwerkende systemen gemaakt door de mens, zijn cellen hoogst stochastische systemen. Het gedrag van genexpressie en intracellulair vervoer, dat doorgaans plaatsvindt door middel van diffusie, wordt overheerst door willekeurige gebeurtenissen, waardoor bij de verwerking van informatie in een cel rekening gehouden moet worden met ruis. Het is dus verrassend dat de macroscopische ontwikkeling van een organismen zo robuust is. Recent zijn de mechanismen die cellen gebruiken om hun inwendige stochasticiteit te beheersen onderworpen aan talrijke experimentele en theoretische studies. Hoewel in toenemende mate wordt herkend dat de ruimtelijke aspecten van grote invloed zijn op het controleren van ruis, wordt dit vaak niet meegenomen in modellen die de informatieverwerking in een cel beschrijven. De voornaamste vraag in dit werk is hoe de ruis in genexpressie voldoende beheerst wordt om de deterministisch en reproduceerbaar ogende ruimtelijke eiwit patronen in organismen te produceren.

Nu blijkt het modelleren van de ruimtelijke aspecten binnen een cel uitdagend te zijn: omdat eiwitten vaak in lage concentraties in de cel aanwezig zijn geeft een meanfield-analyse vaak een inadequate beschrijving van het systeem, terwijl een gedetailleerde beschrijving van alle deeltjes zowel mathematisch als numeriek ondoenlijk

is. Recent is *enhanced Green's Function Reaction Dynamics* (eGFRD) ontwikkeld als een elegante en krachtige stochastische simulatie methode dat het gat dicht tussen nauwkeurigheid en efficiëntie. Gebruik makend van exacte oplossingen van de diffusievergelijking, implementeert het een gebeurtenis-aangedreven stochastisch algoritme dat de posities van alle deeltjes in het systeem beschrijft bij een opvallend lagere numerieke prijs dan klassieke simulatietechnieken zoals Brownian Dynamics. Sinds kort was eGFRD gelimiteerd tot de simulatie van biochemische deeltjes in een driedimensionale (3D) ruimte met periodieke randvoorwaarden, terwijl intracellulair actief transport juist in lagere dimensies plaatsvindt en de ruimtelijke beperking hier een belangrijke rol spelen. In het eerste deel van deze scriptie (hoofdstuk 2 en hoofdstuk 3) presenteren we een uitbreiding op eGFRD dat het mogelijk maakt één- en tweedimensionaal vervoer op eindige structuren te simuleren. Verder maken we het mogelijk dat deeltjes vanuit het cytoplasma binden met deze structuren, en kunnen reageren met andere deeltjes op hetzelfde structuur of met deeltjes uit het cytoplasma. Voortbordurend op het hoofdthema van deze scriptie presenteren we in hoofdstuk 4 een toepassing van de uitgebreide mogelijkheden van eGFRD: een op deeltjes gebaseerd stochastisch model van groeifactor polarisatie in gistcellen. Een ander modelorganisme, de fruitvlieg Drosophila melanogaster, is het onderwerp van hoofdstuk 5 en hoofdstuk 6: hier bestuderen we hoe een specifiek motief van wederzijdse onderdrukking in genregulatie bijdraagt aan ruiscontrole in een vroeg stadium in de ontwikkeling van de vlieg: een paradigma van embryogenese. Hieronder gaan we dieper in op de drie hoofdonderwerpen van de scriptie.

eGFRD in alle dimensies en verschillende manieren van transport

De hoofdgedachte van eGFRD is om de ruimte onder te verdelen in simpele subdomeinen die hooguit twee deeltjes bevatten. Hierdoor wordt het veel-deeltjes probleem opgebroken in een aantal één- en tweedeeltjesproblemen. Voor het diffusieprobleem geldend in elk van deze subdomeinen bestaan analytische oplossingen in de vorm van Green's functies. De Green's functies worden gebruikt om het tijdstip van de volgende gebeurtenis en de verwachte nieuwe posities van de deeltjes te berekenen zodat een gebeurtenis-gedreven Monte Carlo simulatie ontstaat. De analytische afleiding van de Green's functies is dus een belangrijke en uitdagende stap in de ontwikkeling van eGFRD. Bovendien moet een specifieke Green's functie in wezen opnieuw worden afgeleid voor elke dimensie, elk coördinatensysteem en elke nieuwe randvoorwaarde.

Een belangrijk resultaat van dit werk is de analytische afleiding van de Green's functie voor het reactie-diffusie probleem in 1D met verschillende randvoorwaarden. We geven de afleiding en resultaten in hoofdstuk 2. Een belangrijke eigenschap van de oplossingen is dat ze rekening houden met actieve, driftachtig vervoer in 1D, wat een wijdverspreide manier is van intracellulair vervoer langs lineaire polymeren. We gebruiken de nieuwe Green's functies om vervoer op eindige 1D structuren te implementeren in eGFRD. Verder hebben we het mogelijk gemaakt om in eGFRD de zoektocht van een transcriptiefactor naar zijn promotor op het DNA te simuleren. De Green's functie hiervoor beschrijft de 1D diffusie van een deeltje dat, als het langs een specifieke plek (de promotor) diffundeert, met een kans bind.

Op een vergelijkbare wijze hebben we de Green's functies verkregen die de diffusie en de reacties tussen deeltjes in het vlak (2D) beschrijven, zowel voor de binding van deeltjes van het cytoplasma (3D) op lagere dimensionale structuren, wat het onderwerp is van hoofdstuk 3. Om de reactie van een deeltje dat in 3D diffundeert, met een deeltje dat in 2D diffundeert ("directe binding") te beschrijven hebben we een coördinatietransformatie afgeleid. Deze transformatie stelt ons in staat de anisotropische diffusie van de vector tussen de deeltjes om te zetten naar een het reeds bekende probleem van isotrope diffusie, zodat we het kunnen simuleren met de eerder afgeleide Green's functies. We gebruiken deze oplossingen in combinatie met de nieuwe domeinen voor 2D diffusie om het transport en de reacties in 2D te implementeren in eGFRD. Tot slot hebben we zogenaamde overgangsdomeinen geïmplementeerd in eGFRD, die de diffusie van deeltjes tussen orthogonale vlakken behandelen, waardoor de diffusie over de zijden van een doos mogelijk wordt.

De vorming van polarisatie in de concentratie van groeifactor eiwitten in gistcellen

De nieuwe functies van eGFRD stellen ons in staat een stochastisch model te simuleren van de polarisatie van de concentratie van groeifactor eiwitten in gistcellen, wat we beschrijven in hoofdstuk 4. Gist heeft een staafachtige vorm door exclusief langs één as te groeien vanuit de twee tegenover elkaar liggende polen. Deze lokalisatie van groei wordt in stand gehouden door de ophoping van groeifactoren op het celmembraan bij de polen. Experimenten hebben laten zien dat deze polarisatie veroorzaakt wordt door een combinatie van (1) actief 1D transport van de groeifactoren langs de lineaire polymeren (microtubuli) naar de polen, en (2) 2D diffusie van een membraangebonden reactiepartners (ankereiwitten) van de groeifactoren. Als het membraan gebonden eiwit en de groeifactor een binding aangaan vormen zij een zeer langzaam diffunderent membraangebonden groeifactorcomplex. Hoe deze mechanismen leiden tot de polarisatie van de groeifactoren is echter onbekend. In onze simulaties kwantificeren we hoe efficiënt de groeifactoren zijn gepolariseerd langs de lange as van de gistcel, als een functie van de belangrijkste parameters van het systeem en vergelijken we de verschillende modellen voor de binding van de groeifactoren aan het membraangebonden ankereiwit. Verschillende modellen voor interacties zijn de directe binding van 3D naar 2D of een binding in twee stappen; i.e. eerst bind de groeifactor aan het membraan, gevolgd door een zoektocht op het membraan naar zijn reactiepartner. We vinden ten eerste dat het model met directe binding betere polarisatie eigenschappen laat zien dan het model met binding in twee stappen. Dit komt omdat bij het tweede model de groeifactoren grotendeels aan het celmembraan geboden zijn en nauwelijks nog in het cytoplasma aanwezig zijn. Hierdoor binden ze minder met de microtubuli die voor het actieve transport naar de celpolen zorgen en is de concentratie van het eiwit bij de polen dus lager. Dit illustreert de noodzaak voor een membraangebonden ankermiddel. Ten tweede ontdekken we dat er in het systeem met directe binding een optimale levensduur bestaat van de membraangebonden groeifactorcomplexen. Bij deze levensduur is het product van de polarisatiegraad en de concentratie van de groeifactoren bij de polen optimaal. Dit optimum weerspiegelt een afweging tussen deze twee factoren bij het variëren van de levensduur van het complex.

De voordelen van wederzijdse onderdrukking bij genexpressie in de embryonale ontwikkeling

De vroegste stadia in de embryonale ontwikkeling van de fruitvlieg *Drosophila melanogaster* gelden als een paradigma in de ontwikkelingsbiologie. De lichaamssegmenten waaruit de fruitvlieg is opgebouwd worden in de eerste stadia van ontwikkeling gevormd langs de lange as van het embryo. De locatie van de segmenten wordt bepaalt door een aantal regel genen die in een gestreept patroon langs de as van het embryo actief zijn. De activiteit van deze zogenaamde kloofgenen (gap genes) is afhankelijk van de concentratie van transcriptiefactoren. De concentratie valt af langs de as van het embryo en vormt zo een morfogene gradiënt. Hierdoor geeft de concentratie van de transcriptiefactoren in een cel informatie over de positie van deze cel langs de embryonale as. De nauwkeurigheid waarmee de positie en de specificatie van een lichaamsdeel bepaald wordt hangt direct af van hoe scherp de grenzen tussen de gebieden met verschillende actieve genen van het embryo zijn. De gemeten niveaus van ruis in de kloofeiwit concentraties in het embryo laten zien dat, ondanks de stochastische aard van genexpressie, de variantie in de positie van de grensgebieden niet alleen verrassend laag is, maar zelfs afneemt met de ontwikkeling van de fruitvlieg. Dit suggereert de aanwezigheid van mechanismen voor ruiscontrole. In het tweede deel van deze scriptie (hoofdstuk 5 en hoofdstuk 6), bestuderen we–in een ruimtelijk opgelost stochastisch model–de eigenschappen van ruiscontrole met een motief van genregulatie dat veel voorkomt onder kloofgenen: wederzijdse onderdrukking. Bij genregulatie betekend wederzijdse onderdrukking dat het eiwit behorend bij een bepaald gen de productie (transcriptie) van een ander gen onderdrukt en vice versa. We vinden dat het motief van wederzijdse onderdrukking de nauwkeurigheid van de positie van de grensgebieden sterk verbetert.

In hoofdstuk 5 behandelen we een minimaal model van twee zich wederzijdse onderdrukkende kloofgenen, die geactiveerd worden door twee gradiënten van transcriptiefactoren. We voeren uitgebreide stochastische simulaties uit van een model met een duizendtal individuele celkernen waaruit het embryo bestaat. We meten de variantie op de grens van de patronen van geactiveerde kloofeiwitten bij verschillende waarden van de systeemparameters. We vinden dat wederzijdse onderdrukking een belangrijke rol speelt in het verminderen van de variantie van de positie van het grensgebied. Samen met de ruimtelijke middeling van eiwitconcentraties laat een wederzijdse onderdrukking bij een optimale diffusieconstante van het kloofeiwit eiwitgrenzen toe die tegelijk scherp en steil zijn. Hierdoor ontstaat het robuuste ruimtelijke patroon in de embryo. Het blijkt dat het fenomeen van scherpe grensgebieden persistent is bij variatie van de systeemparameters. Bijvoorbeeld als we de activatorgradiënt veranderen: indien sprake is van een te hoge expressie van het activator gen, treedt de wederzijdse onderdrukking op als een buffer tegen extrinsieke schommelingen, i.e. schommelingen in de concentratieniveaus van de activatorgradiënten, zonder de controle over de intrinsieke ruis te belemmeren. Dit mechanisme dankt zijn werking aan de bistabiliteit door de wederzijdse onderdrukking.

De observatie dat de activatorgradiënten minder belangrijk zijn voor de bepaling van het grensgebied leidt tot de volgende vraag: is de activatie van de kloofgenen door het morfogen essentieel voor het robuuste streeppatroon, of is het patroon van

kloofgenen ook stabiel met alleen onderlinge interacties tussen de kloofgenen? Deze vraag wordt nog extra gemotiveerd door de observatie dat de meeste kloofgenstrepen vormen in het achterdeel van het embryo, waar de concentratie van het morfogen zo laag is dat het onwaarschijnlijk is dat het nog voor celdifferentiatie zorgt. Fascinerend is dat de kloofgenen elkaar onderling onderdrukken met een karakteristiek patroon van afwisselende sterkte van interactie: terwijl de eiwitten in grenzende gebieden elkaars expressie slechts zwak onderdrukken, is de onderlinge onderdrukking tussen de gebieden naast de buren zeer sterk. We hebben de stabiliteit van dit systeem van kloofgen interactie onderzocht als functie van de zwakke interactie door middel van stochastische simulaties in combinatie met een nieuwe techniek die geoptimaliseerd is voor de simulatie van zeldzame gebeurtenissen (hoofdstuk 6). We laten zien dat er een zwakke interactie van onderdrukking bestaat, waarbij de stabiliteit van het hele patroon gemaximaliseerd is, en de levensduur van het patroon vele malen langer is dan biologische relevante tijdschalen. Onze resultaten wijzen bovendien uit dat in het optimale regime een corrigerende kracht ontstaat die schommelingen die wegleiden van het stabiele patroon tegen gaat. Ten slotte laten we door middel van een stabiliteitsanalyse zien dat de introductie van een zwakke onderdrukkingspartner tussen twee gebieden van sterk onderdrukkende genen de bistabiliteit van de eiwitconcentraties in het grensgebied onderdrukt en daarmee de fluctuaties in de positie van het grensgebied verzwakken, wat de stabiliteit van het hele patroon versterkt.

Index

Bessel equation, 68
Bessel function, 68, 83
Bicoid, 99, 155
bifurcation analysis, 135, 170, 188
bistability, 100, 102, 104, 115, 117, 124, 128, 159, 170, 172, 174, 177
Bromwich integral, 30, 69
Brownian Dynamics, 16
bulk structure, 19
burst horizon, 49
burst radius, 49
bursting, 9, 12

canalization, 126, 166, 173
cap, 37
Cap Interaction, 37
Caudal, 101
Cdc42, 90
Center of Mass Escape, 13
collision detection, 52
CoM Escape, 13, 15
combined score, 94
Cylindrical Surface Cap Growth, 55
Cylindrical Surface Catastrophy, 55
Cylindrical Surface Growing Cap Interaction, 57
Cylindrical Surface Growing Cap Single, 57
Cylindrical Surface Growth event, 55
Cylindrical Surface Interaction, 20
Cylindrical Surface Sink, 37

detailed balance, 16
direct binding, 60, 62
disk, 37
Disk Surface Single, 37
domain, 7, 8
domain making, 47
Drosophila melanogaster, 99, 155
dynamic instability, 37, 55
dynamical cylinders, 55

eGFRD, 8

fixed point analysis, 135, 170, 188
forward flux sampling, 156, 157, 175
fruit fly, 99, 155

gap gene, 99, 155
Gap Gene Gillespie, 174
GFRD, 7
GGG, 174
Giant, 101, 156
Gillespie algorithm, 4, 105, 175
Green's function, 9
growth domain, 55
growth event, 55
growth factors, 90
growth volume, 55

Hankel function, 83
Hunchback, 99, 156
hypergeometric function, 83

Interaction, 19
Interaction domain, 19
intruder, 50
irregular Bessel function, 83
IV Escape, 14, 15
IV Interaction, 62

Knirps, 100, 156
Krüppel, 101, 156

Mal3, 90
microtubule catastrophy, 55
Mixed Pair 1D-Cap, 37

Mixed Pair 1D/Growing Cap, 57
Mixed Pair 2D-3D, 62
Mod5, 90
modified Bessel function, 68
monomolecular reaction, 11, 15
morphogen, 4, 99, 155, 172, 177
morphogen gradient, 4, 99, 155, 172, 177
Multi, 16, 52
Multi domain, 16
Multi horizon, 49
Multi partner horizon, 49
multi-shell factor, 16, 48
mutual bursting, 47
mutual repression, 100, 155

NETO, 90
next-event time, 12
next-subvolume method, 105, 175
Non-Interaction Single, 19
Non-Stationary Forward Flux Sampling, 5, 157, 175
NS-FFS, 5, 157, 175

overdamped Langevin dynamics, 164, 181

Pair, 11, 13
Pair domain, 11, 13
pair horizon, 49
Pair Reaction, 14, 15
planar surface, 60
Planar Surface Interaction, 60
Planar Surface Pair, 63
Planar Surface Single, 63
Planar Surface Transition, 63
Planar Surface Transition Pair, 65
polarity, 94
polarity factors, 90
polarity markers, 90
polarization score, 94
Pom1, 98
premature bursting, 47
progress coordinate, 160, 175
propensity function, 12
protective domain, 8

rare-event sampling, 157, 174
reaction, 19
reaction coordinate, 160, 175
reaction horizon, 49
reaction length, 16
reaction volume, 16
regular Bessel function, 83
residue formula, 31

scale angle, 53
scale aspect ratio, 53
scale center, 53
shellmaking, 47
Single, 11
Single domain, 11
Single Escape, 11
Single Reaction, 11
single-shell factor, 48
slowdown factor, 91
Smoluchowski equation, 23, 24
social upsizing, 47
SSA, 4, 105, 175
stability analysis, 135, 170, 188
Stochastic Simulation Algorithm, 4, 105, 175
structure, 19
surface, 19
surface horizon, 49
survival probability, 12

Tailless, 156, 157
Tea1, 90
Tea2, 90
Tea4, 90
test shell, 52
Tip1, 90
Transition, 19, 60
Transition domain, 19
transition-interface sampling, 157
transition-path sampling, 157

Waddington picture, 126, 156, 173
wedge domain, 72, 81

zero-shell, 50
Zero-Single, 50

List of abbreviations

Abs	absorbing
Bcd / *bcd*	Bicoid protein / gene
BD	Brownian Dynamics
Cad / *cad*	Caudal protein / gene
CDF	cumulative distribution function
Cyl	cylindrical
eGFRD	enhanced Green's Function Reaction Dynamics
FCS	fluorescence correlation spectroscopy
FFS	forward flux sampling
FRAP	fluorescence recovery after photobleaching
GFRD	Green's Function Reaction Dynamics
GGG	Gap Gene Gillespie
Gt / *gt*	Giant protein / gene
Hb / *hb*	Hunchback protein / gene
Inf	infinite
Kni / *kni*	Knirps protein / gene
Kr / *kr*	Krüppel protein / gene
NETO	new end take-off
NN	nearest neighbor
NNN	next-nearest neighbor
Nos / *nos*	Nanos protein / gene
NS-FFS	Non-Stationary Forward Flux Sampling

ODE	ordinary differential equation
PDE	partial differential equation
PDF	probability density function
PSU	phase space unit
Rad	radiating, radiative
SSA	Stochastic Simulation Algorithm
Sym	symmetric
TIS	transition interface sampling
Tll / *tll*	Tailless protein / gene
TPS	transition path sampling
WLOG	without loss of generality

List of persons

In this appendix for the interested reader we present some information about some of the persons behind the names mentioned in different places throughout this book.

Friedrich Wilhelm Bessel (∗1784 in Minden, Westfalen Province, Prussia; †1846 in Königsberg, East Prussia). German mathematician and astronomer. After an apprenticeship in a trade company, he turned towards astronomy, working at Lilienthal observatory near Bremen. His work attracted widespread attention. In spite of lacking university education, at the age of 25 he was appointed director of the Royal Prussian Observatory in Königsberg. In the course of studying many-body gravitational systems he developed the theory of Bessel functions, today commonly used throughout classical and quantum physics.

George Green (∗1793 in Sneinton, England; †1841 in Nottingham, England). British mathematician and physicist. Born as a wealthy baker's son, he received some school education. He started his career as a miller, later inheriting half of his father's business. His economic success increasingly allowed him to turn towards science. At the age of 39 he enrolled for undergraduate studies in Cambridge and finished with a BA degree. His famous contributions to integral calculus first remained largely unknown to the scientists of his time. Only after his death their use became commonplace in physics and mathematics.

Hermann Hankel (∗1839 in Halle an der Saale, Saxony Province, Prussia; †1873 in Schramberg, Württemberg). German mathematician. He grew up in a physics professor's family in Leipzig, Saxony. After studying mathematics with Möbius, Riemann (in Göttingen), Weierstrass and Kronecker (in Berlin), he became a professor in Erlangen, Bavaria. He made important contributions to integration theory, complex analysis and the theory of special functions, being most known for the development of the Hankel transform. Having suffered from various diseases early on, he died at a young age.

Marian Smoluchowski, Ritter von Smolan (∗1872 in Vorderbrühl, Austria; †1917 in Cracow, Poland). Austro-Hungarian / Polish physicist. Born into an aristocrat family, he grew up in larger Vienna, where he studied physics with Exner and Štefan. After working in Paris, Glasgow and Berlin, he first became a professor in Lwów / Lviv, Galicia in 1900, then in 1912 in Cracow. Influenced by Boltzmann's ideas, he co-pioneered statistical physics. He described Brownian motion independently of Einstein and provided the first theory of diffusion in a force field. He died in an dysentry epidemy in 1917.

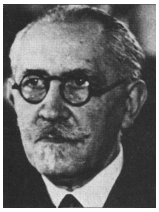

Paul Langevin (∗1872 in Paris, France; †1946 ibid.). French physicist. He commenced his studies at École de Physique et Chimie and ENS in Paris, later continuing in Cambridge. He obtained his PhD at the Sorbonne with P. Curie in 1902, only to become a physics professor at Collège de France in 1904. He became director of the École de Physique et Chimie in 1926 and member of the Académie des Sciences in 1934. As an anti-fascist, he was removed from his position during the German occupation (1940–44). He developed groundbreaking mathematical methods for the stochastic description of molecular systems (Langevin dynamics).

Oswald Theodore Avery (∗1877 in Halifax, Nova Scotia, Canada; †1955 in Nashville, Tennessee, USA). Canadian-American physician and medical researcher. He was born in Canada, but moved to New York City at young age, later studying medicine at Colgate and Columbia University. After graduating in 1904 he practiced as a physician, entering medical research in 1907. The major part of his work was done at Rockefeller University. Together with MacLeod and McCarty, Avery is credited with the discovery that DNA is the carrier of genetic information. Though outstandingly important, their work was never awarded the Nobel-prize.

Erwin Schrödinger (∗1887 in Vienna; †1961 ibid.). Austrian-Irish physicist. He studied physics in Vienna with Hasenöhrl and Exner. In 1921 he became professor at the (then German) University of Breslau, later moving to Zürich. He succeeded Planck on his chair in Berlin in 1927, but left Germany for England when the Nazis took power, only to receive the Nobel Prize and return to Austria shortly afterwards. Fleeing the Nazis again in 1939, he finally became Theoretical Physics Director in Dublin. He was first to describe quantum mechanics as an eigenvalue problem, spearheading essentially all of subsequent quantum theory.

Conrad Hal Waddington (∗1905 in Evesham, England; †1975 in Edinburgh, Scotland). British biologist, paleontologist and philosopher. Born in England, he spent his early years in Southern India, before being sent back to England for schooling at the age of 4. He studied natural sciences and philosophy in Cambridge. After World War II he became a professor in Edinburgh. He made important contributions to genetics, developmental biology and evolution theory. In particular, he is credited with introducing the concept of the epigenetic landscape as a thinking model for progressing organism development.

Colin Munro MacLeod (∗1909 in Port Hastings, Nova Scotia, Canada; †1972). Canadian-American geneticist. He entered medicine studies at McGill University, Montreal, already at the age of 16, finishing at the age of 23. After a short stay at Montreal General Hospital, he joined the research group of Avery at Rockefeller University in 1934. There he contributed to demonstrate that DNA is the carrier of genetic information. Later he turned towards immunology and epidemiology. He was chiefly involved in international programs fighting cholera in South East Asia and, from 1961 onwards, life sciences advisor of several US presidents.

Maclyn McCarty (∗1909 in South Bend, Indiana, USA; †2005 in New York City, USA). American biochemist and geneticist. He studied biochemistry in Stanford and medicine at Johns Hopkins University, graduating in 1937. After specializing as a pediatrician, he joined Avery's research at Rockefeller University in 1941. Together with MacLeod they showed that DNA is the carrier of genetic information. He was at Rockefeller University for almost 60 years, becoming leader of the bacteriology and immunology lab in 1946, later physician-in-chief of the university hospital. He helped to elucidate how streptococci cause rheumatic fever.

Jacques Lucien Monod (∗1910 in Paris, France; †1976 in Cannes, France). French biochemist. Son of a French mother and an American father, he grew up in Cannes. He studied biology at the Sorbonne. During the war he was an active member of the Résistance. As one of the first propagators of quantitative and molecular biology, he chiefly contributed to genetics, enzymology and bacteriology. Together with Jacob and Lwoff he received the Nobel prize for their work on the lac operon, the first discovered example of a gene regulation. He also coined the term diauxie to characterize two distinct growth modes.

Alan Turing (∗1912 in London, England; †1954 in Wilmslow, England). British mathematician, physicist and computer scientist. He was brought up in England while his parents partly worked in India. He studied mathematics in Cambridge and Princeton, quickly displaying his extraordinary skills. His work on computation theory and cryptology today forms the base of computer science. During World War II he lead the team that broke the German Enigma cipher machine, decisively contributing to the allied victory. Studying pattern formation in biochemical systems, he also pioneered mathematical biology.

Kiyoshi Itō (∗1915 in Hokusei, Mie, Honshū, Japan; †2008 in Kyōto, Japan). Japanese mathematician. In 1938 he graduated in Mathematics from the University of Tokyo, receiving his PhD in 1945. During World War II he worked for the national statistical office, where he started to develop his new ideas on stochastic processes. Becoming a professor in Kyōto in 1952, he had numerous stays abroad, in Stanford, Princeton, Cornell and Aarhus. His novel way of describing stochastic processes today is well-known as Itō calculus, widely applied in science and economy. He wrote in Japanese, Chinese, German, French and English.

Francis Harry Compton Crick (∗1916 in Weston Favell, England; †2004 in San Diego, California, USA). British molecular biologist, biophysicist and neuroscientist. Growing up in Northampton area, he studied physics at University College, London. There he also began his PhD project, which however was interrupted by a lab bombing during World War II. After the war he changed towards biology. In 1949 he started to work on X-ray christallography of DNA in Cambridge. As a 35-year old graduate student, in 1953 he resolved the structure of DNA together with Watson (Nobel prize 1962). Later he lead an own institute in La Jolla.

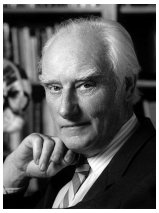

Edward B. Lewis (∗1918 in Wilkes-Barre, Pennsylvania, USA; †2004). American geneticist. Having spent his youth in Pennsylvania, he studied biostatistics at the University of Minnesota. He obtained his PhD in 1942, working on Drosophila genetics with Sturtevant at Caltech. In World War II he served as a US Air Force meteorologist. He is considered a founding father of developmental genetics. For his studies on Drosophila development he received the Nobel Prize in Medicine in 1995, together with Nüsslein-Volhard and Wieschaus. He also contributed to radiology, studying the effect of nuclear fallout on cancer formation.

François Jacob (∗1920 in Nancy, France). French geneticist. Born into a merchant's family, he enjoyed education in prestigeous schools. He demonstrated a high talent in mathematics and physics, but decided to enrol for medical studies. During the war he escaped to Britain to join the allied cause. He finished his studies and became a medical doctor in 1947 only to turn towards microbiology research shortly afterwards, later working with Monod. Together with Lwoff they received the Nobel prize in 1967 for their groundbreaking work on transcriptional regulation of enzyme expression in *E. coli*.

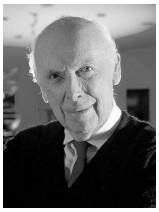

James Dewey Watson (∗1928 in Chicaco, Illinois, USA). American molecular biologist, geneticist and zoologist. Fascinated by bird-watching from his childhood, he initially aimed at becoming an ornithologist. However, after reading Schrödinger's book *What Is Life?*, he decided to study genetics in Chicago and at Indiana University, receiving his PhD in 1950. He first worked in Copenhagen, but changed to Cavendish Laboratory (Cambridge) only 1 year later. In 1953, together with Crick, he elucidated the structure of DNA (Nobel prize 1962). Later he became a professor in Harvard and directed the Cold Spring Harbor Laboratory.

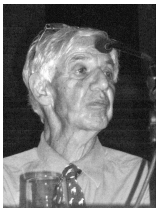

Lewis Wolpert (∗1929 in Johannesburg, Republic of South Africa). South-African biologist, scientific author and broadcaster. Originally trained as a construction engineer, he moved to London to become a developmental biology researcher. Today he is member of the Royal Society and professor emeritus of the University College London. Wolpert is known for introducing the "French flag model", one of the first explanations for how genetic information is converted into positional information to specify distinct development of body parts, into developmental biology.

Daniel Thomas Gillespie (∗1938 in Missouri, USA). American physicist. He was born in Missouri and grew up in Oklahoma. He studied at Rice University and obtained his PhD at Johns Hopkins University with a dissertation in experimental elementary particle physics. From 1971 to 2001, he worked as a civilian scientist at the Naval Weapons Center in China Lake, California. There he developed his famous algorithm for next-event driven stochastic simulation of biochemical systems. Since 2001 he is a private consultant in computational biochemistry, co-working with research groups at various Californian universities.

Christiane Nüsslein-Volhard (∗1942 in Magdeburg, Sachsen-Anhalt, Germany). German biochemist. Though born in Magdeburg, she grew up in Frankfurt / Main, where she started to study biology, later also biochemistry in Tübingen, where she completed her PhD. In 1978 she became a group leader at the EMBL in Heidelberg. Here she conducted her famous work on the genetic regulation of fly embryogenesis together with Wieschaus, for which (with Lewis) they received the Nobel Prize. Later she directed the MPI for developmental biology in Tübingen. She is a guest professor at numerous universities.

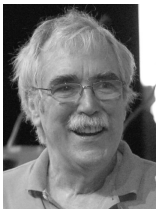

Eric F. Wieschaus (∗1947 in South Bend, Indiana, USA). American biologist. He spent most of his youth in Alabama. After his studies at the University of Notre Dame and in Yale, he went for his first postdoc to the EMBL in Heidelberg, working on the genetic basis of fruit fly embryogenesis with Nüsslein-Volhard. For this groundbreaking experimental work they received the Nobel Prize in Physiology or Medicine together with Lewis. Today Wieschaus teaches molecular biology and biochemistry in Princeton and the University of Medicine and Dentistry of New Jersey.

Image references

Coverwork

- Windmill picture: "Overzicht met molens nabij Schermerhorn", Wikimedia Commons, Creative Commons Attribution-Share Alike 3.0 Netherlands license, by Rijksdienst voor het Cultureel Erfgoed.
- Drosophila melanogaster: Wikimedia Commons, Creative Commons Attribution 2.5 Generic license, photo by André Karwath aka Aka.
- Fission yeast: Wikimedia Commons, released into public domain given that copyright holder is credited, from "The Cell Cycle. Principles of Control" by David O. Morgan.
- AMOLF: By Grace Joseph (AMOLF), released into public domain on Wikimedia Commons.
- eGFRD domains: by the author of this book.

Quote page

- "Panorama Beskidu Żywieckiego z Pilska", Wikimedia Commons, Creative Commons Attribution-Share Alike 3.0 Unported license, by Wiktor Baron.

Chapter 5

- Drosophila melanogaster: see above.
- Hunchback in-situ hybridization: cut from picture published at Wikimedia Commonsunder Creative Commons Attribution 2.5 Generic license by user Nina.

List of Persons

- Friedrich W. Bessel: Wikimedia Commons, copyright-free.
- George Green: old painting, copyright-free.
- Hermann Hankel: Wikimedia Commons, copyright-free.
- Marian Smoluchowski: Wikimedia Commons, copyright-free.

- Paul Langevin, Wikimedia Commons, copyright-free.
- Oswald T. Avery, Wikimedia Commons, copyright-free.
- Erwin Schrödinger, Wikimedia Commons, copyright-free.
- Colin M. MacLeod, Wikimedia Commons, copyright-free.
- Maclyn McCarty, Wikimedia Commons, Creative Commons Attribution 2.5 Generic license, by Marjorie McCarty, first published in: Lederberg J, Gotschlich EC (2005) A Path to Discovery: The Career of Maclyn McCarty. PLoS Biol **3**(10): e341.
- Jacques L. Monod: Wikimedia Commons, copyright-free.
- Alan Turing: Wikimedia Commons, copyright-free.
- Kiyoshi Itō: Wikimedia Commons, Creative Commons Attribution-Share Alike 2.0 Germany license, by Konrad Jacobs, Erlangen.
- Francis H. C. Crick: Wikimedia Commons, Creative Commons Attribution 2.5 Generic license, photo by Marc Lieberman, first published in: Siegel RM, Callaway EM (2004) Francis Crick's Legacy for Neuroscience: Between the α and the Ω. PLoS Biol **2**(12): e419.
- François Jacob: Wikimedia Commons, copyright-free.
- James D. Watson: Wikimedia Commons, public domain.
- Lewis Wolpert: Wikimedia Commons, Creative Commons Attribution-Share Alike 2.0 Generic license, originally posted on Flickr by user jmerelo.
- Christiane Nüsslein-Volhard: Wikimedia Commons, Creative Commons Attribution-Share Alike 2.0 France license, by user Rama.
- Eric F. Wieschaus: Wikimedia Commons, released into public domain under Creative Commons CC0 1.0 Universal Public Domain Dedication license.

Acknowledgements

More than four years passed since I came to settle down at Science Park Amsterdam, heading down MacGillavrylaan on unfinished sidewalks on a foggy January afternoon. Finishing the very last parts of this book with the fantastic new AMOLF building charming with its bright-green interior to my side, I am looking back with delight and gratitude on these years.

My foremost thanks are dedicated to my supervisor, Pieter Rein. His constant readiness to advise and criticize, but also his willingness to himself learn during our conversations, allowed me to turn the initial random walk of my PhD into the more directed progress that was required to accomplish this work. His immense passion for science and the sharp focus with which he approaches problems were a guiding ideal for me during my time at AMOLF, and will remain so in future. In particular I would like to thank him for his patience and understanding in those situations in which the circumstances of life were harder than the challenges of work.

Nils, if Pieter Rein is my "Doktorvater", as they use to say in German, you must be called something like my "Doktoronkel". During your time at AMOLF, and most so when we were working together on destroying gap gene patterns, I have not only considered you a good friend of mine, but also a constant source of skill and knowledge that inspired me to tackle problems in a better way and more efficiently, which largely contributed to give my PhD efforts the right spin.

Pierre, thank you so much for our collaboration on yeast, which–maybe as an interesting example of science valorization– ended up in running a private brewery, and for all the joyful discussions connected to this. J'espère qu'on va, quand même, continuer de quelque manière! Of course, at this point I shall not forget to thank Hinco for supporting our experiments with the necessary lab equipment.

Laurens, if there is something that I should thank you most for, than it is to be sort-of the antipole to the germanized Pole coming along with the attitude and (over-?) motivation to get things done with some proper Gründlichkeit as schnell as possible. Thanks for the sweet salt that fell on me from your salero, and of course for all the technical magic that you casted on me to keep Bessel Inc. alive.

Filipe, I would like to thank you for being the presto-log that dragged me out of my office and "back to the present" on Friday evening, while during the week, in particular during my first months at AMOLF, you provided me with many insights into what I increasingly realized is supposed to be my work, constantly reminding me, with your charming British politeness, that I am not necessarily at the target yet.

Wiet, it seems that I cannot remember a topic on which we did not have an intense discussion. Thank you for constantly challenging me in a nice way, for being my scientific teddybear oftentimes, and also for all the practical help that I received from you.

Jeanette, thank you for being such an ideal roommate, for all the moments of mutual humor and fatalism that we shared in a cordial way, and of course for translating my summary to Dutch and Limburgs. Most importantly, with your help I had the important insight that the PhD is like putting an infinetly long sausage on a barbeque.

Joris, although these few lines of amateur patheticism not in any way can be compared to the roaring sound of a South German sportscar, please be assured that I am truly thankful to you for polishing the samenvatting with an outstanding, maybe even fanatic commitment. I would also like to thank you for the occasional inspiring races on the autobahnen of Dutch-Anglo-German poetry, which certainly contributed to activate hidden synapses.

José and Sarah, thanks for the good times that we spent collaborating on such important projects as getting dutchified, re-inventing the wheel, and organizing smashing building-destruction parties and small-scale olympics in Amsterdam.

Many thanks to my groupmates Thomie, Andrew, Chris, Martijn, Aimee, Nicola, Anton, Marlo, of whom I hope that he will reappear one day, David and Mark for attending my occasionaly maybe unappropriately prepared Wednesday morning talks and for more than one prolific discussions; this includes some special thanks to Thorsten for our mutual effort on mutual repression.

Kuba and Albertas, thank you for successfully filling up some of my weekends with inspiring nightly random walks through Utrecht, powered by inimitable and indestructible Eastern-European ATP.

For making my stay at AMOLF a time that I will happily remember throughout my life I would like to thank Nuria, Ioana, Sophie, Philippe, Chris, Feng, Björn, Eva, Maga, Svenja, Milena, Florian, Stef, François, Georges, Nicola, Jacopo, Katja, Noreen, Sebastian, Iza & Łukasz, Kamila & Sana, Marina, Marjon, Daan, Koos, Simon, Nienke, Paige, Liedewij, Alireza, Fatemeh, Stephen, David, Martin, Jochen, Bela, Jeroen, Tom, Ana, Sanne, Paolo, Gianluca, and all the other people that make AMOLF such a great place to be.

At this point I would also like to thank my good old friends Milan, Jascha, Christian, Christoph, ΦM, Koen, Romina, Samuel, Florian and Johannes, who since ever have been enriching my life with fruitful conversations.

I wish to send my special thanks to my family, in particular to my parents, who throughout their lives have always been examples for me in terms of diligence and studiousness, and to my brother, for being a reliable partner in the challenging moments that we both faced in the passed years.

My biggest thank goes to Annegret, whom I would like to thank not only for succumbing to the idea of living 4 years in the big gray DUWO, but also for sustaining for the year-long process of a crazy physicist becoming a crazy scientist–thank you for all your love, patience and support, and for the daily smile that made our life here even more joyful.

Thomas R. Sokolowski, April 2013